

**University of
Reading**

Pharmacological Investigation of Nox2-NADPH
Oxidase Inhibitors and p47^{phox} Redox-signalling in
Angiotensin II-induced Cardiac Hypertrophy in Mice

By

Fangfei Liu

Thesis submitted for the degree of Doctor of Philosophy

School of Biological Science

SEPTEMBER 2020

Acknowledgement

First and foremost, I would like to express my gratitude to my supervisor, Prof. Jian-Mei Li, for providing me with the chance to work with her on this project. She has empowered me not only just as a scientist but also as a person. I thank her for being there with me through thick and thin. Nothing about this PhD would be possible without her. I would also like to thank my co-supervisor, Dr Katrina Bicknell. She went the extra mile to spend her valuable time to encourage and care for me when things are getting tight, especially during the last two years of this journey and the thesis submission.

Also, a big thank you to the JML research group, especially my senior colleague Dr Li Geng who taught me the lab techniques and helped me adapt to my PhD life at the beginning. My thanks also go to other members in the group, colleagues Ms Naureen Bhatti, Dr Junjie Du, and Dr Angshumonik Angbohang, for their help, advice and support.

I would also like to thank the CAF technical support, Mr Nicolas Michael and Dr. John McKendrick, who supported my research with expertise and patience.

Special thanks go to my better half Mr Matt Woolven, who are always there to put up with my stress and care for my wellbeing. The deepest gratitude would go to my parents, who made coming to Britain for this PhD possible for me, and without whom I would never be able to accomplish any of these. It would not be possible without your endless support in the good and bad times in my life. This thesis is dedicated to you, and I love you.

Contents

Acknowledgement	2
List of Tables	9
List of Figures	10
List of Publications and Presentations	14
Publications.....	14
Presentations	15
List of Abbreviations	16
Abstract.....	19
Chapter 1.....	21
General Introduction	21
1.1 Cardiovascular Diseases (CVDs).....	21
1.1.1 Prevalence	21
1.1.2 Pathogenesis of CVDs	22
1.2 Reactive Oxygen Species (ROS)	25
1.2.1 Generation, interconversion and elimination of ROS.....	27
1.2.2 Exogenous source	28
1.2.3 Enzymatic source	29
1.3 NADPH Oxidase.....	32
1.3.1 Nox1.....	33
1.3.2 Nox2.....	34
1.3.3 Nox4.....	35
1.3.4 Nox5.....	37
1.4 Nox2 structure and its activation	39
1.4.1 Nox subunits	41
1.4.2 p47 ^{phox}	45
1.5 p47 ^{phox} signalling in cardiac disorders	50
1.5.1 p47 ^{phox} signalling in apoptosis	50
1.5.2 p47 ^{phox} signalling in cardiac pathological hypertrophic growth	52
1.5.3 p47 ^{phox} signalling in cardiomyocyte survival.....	55
1.5.4 p47 ^{phox} signalling in coronary arterial endothelial dysfunction	57
1.5.5 Role of p47 ^{phox} in contractile dysfunction	60
1.6 Nox inhibitors and antioxidants	63
1.6.1 Small molecule inhibitors	63
1.6.2 Peptide-based inhibitors.....	65

1.6.3 Antioxidants.....	66
1.7 Hypothesis and aim.....	68
Chapter 2.....	70
Materials and Methods.....	70
2.1 Chemicals and reagents.....	70
2.2 Animals.....	70
2.3 Sample collection and preparation for pharmacokinetics (PK) analysis.....	71
2.4 HPLC-MS/MS.....	73
2.4.1 Equipment and instrument settings.....	74
2.4.2 Quantification.....	76
2.5 PK analysis.....	77
2.5.1 Non-compartmental analysis (NCA).....	78
2.5.2 Compartmental analysis using a non-linear mixed effect (NLME) model.....	86
2.6 Lucigenin chemiluminescence assay.....	92
2.7 Dihydroethidium (DHE) assay.....	93
2.8 Malondialdehyde (MDA) assay.....	95
2.9 Amplex Red assay.....	96
2.10 Western blot.....	97
2.9.1 Sample preparation.....	98
2.9.2 Gel preparation.....	98
2.9.3 Sample loading.....	100
2.9.4 Protein separation.....	100
2.9.5 Transfer.....	101
2.9.6 Detection.....	101
2.11 Immunofluorescence.....	102
2.11.1 Section preparation.....	103
2.11.2 Fixation.....	104
2.11.3 Blocking.....	104
2.11.4 Application of primary antibody.....	105
2.11.5 Application of secondary antibody.....	105
2.11.6 Application of 4', 6-diamidino-2-phenylindole (DAPI) to visualise the nuclei.....	106
2.11.7 Mounting and observation.....	106
2.12 Statistics.....	107
2.13 Randomisation and blinding.....	108

Chapter 3.....	109
Pharmacokinetics (PK) Studies and Evaluation of Apocynin in Reducing Tissue Oxidative Stress in Mice.....	109
3.1 Introduction.....	109
3.1.1 Aims and objectives.....	112
3.2 Materials and methods.....	113
3.2.1 Chemicals and reagents.....	113
3.2.2 Animal Models.....	113
3.2.3 Calibration standards preparation	116
3.2.4 Sample processing.....	117
3.2.5 HPLC-MS/MS method specific to apocynin detection.....	119
3.2.6 PK analysis of apocynin.....	119
3.2.7 Tissue distribution of apocynin.....	120
3.2.8 Effect of apocynin on tissue ROS production.....	120
3.3 Results.....	121
3.3.1 Establishment of HPLC-MS/MS method for apocynin and phenacetin detection.....	121
3.3.2 Tissue distribution of apocynin in different organs post iv bolus injection.....	128
3.3.3 Characterisation of apocynin PK parameters by non-compartmental analysis (NCA) and non-linear mixed-effects (NLME) model.....	131
3.3.4 The effect of apocynin on reducing organ O ₂ ⁻ production.....	136
3.3.5 The effect of apocynin on reducing organ lipid peroxidation.....	141
3.3.6 The effect of apocynin on reducing brain O ₂ ⁻ production in dietary-induced middle-aged obesity murine model.....	143
3.4 Discussion.....	146
Chapter 4.....	151
Chemical Properties and <i>in vivo</i> Pharmacokinetic (PK) Analysis of LMH001 by HPLC-MS/MS.....	151
4.1 Introduction.....	151
4.1.1 Aims and objectives.....	153
4.2 Materials and methods.....	154
4.2.1 Chemical properties and fragmentation analysis of LMH001.....	154
4.2.2 Chemicals and reagents.....	154
4.2.3 Animal model.....	154
4.2.4 Calibration standards preparation.....	156
4.2.5 HPLC-MS/MS methods for detecting LMH001.....	157

4.2.6 Method for extracting LMH001 from plasma and urine	158
4.2.7 Plasma protein binding	160
4.2.8 The detection of LMH001 in simulated gastric and intestinal fluids.....	160
4.2.9 PK analysis of LMH001.....	163
4.3 Results.....	165
4.3.1 Chemical properties of LMH001	165
4.3.2 Predicted fragmentation pattern of LMH001.....	169
4.3.3 Development of HPLC-MS/MS method for LMH001 detection	170
4.3.4 Plasma protein binding of LMH001	172
4.3.5 The detection of LMH001 in simulated gastric and intestinal fluids.....	173
4.3.6 LMH001 distribution in the plasma and urine.....	179
4.3.7 Characterisation of LMH001 PK parameters by non-compartmental analysis (NCA) and non-linear mixed-effects (NLME) model	180
4.4 Discussion.....	192
Chapter 5.....	200
Evaluation of LMH001 in Reducing Oxidative Stress Angiotensin II (AngII)-stimulated H9C2 cells.....	200
5.1 Introduction.....	200
5.1.1 Aims and objectives.....	201
5.2 Materials and Methods.....	202
5.2.1 Cell culture.....	202
5.2.2 Protein concentration measurement.....	205
5.2.3 Effect of LMH001 on ROS production <i>in vitro</i>	206
5.2.4 Effect of LMH001 on p47 ^{phox} and Nox expression, and the activation of the MAPK signalling pathway.....	208
5.3 Results.....	209
5.3.1 Effect of LMH001 on O ₂ ⁻ production in AngII-stimulated H9C2 cells, examined by lucigenin chemiluminescence.....	209
5.3.2 PD analysis and modelling of LMH001 in AngII-stimulated H9C2 cells.....	211
5.3.3 Effect of LMH001 on ROS production in AngII-stimulated H9C2 cells, examined by Amplex red and DCFH-DA	214
5.3.4 Effect of LMH001 on the expression of p47 ^{phox} and Noxes in AngII-stimulated H9C2 cells, examined by western blot	218
5.3.5 Effect of LMH001 on the activation of MAPK/ERK signalling pathway in AngII-stimulated H9C2 cells, examined by western blot.....	220
5.4 Discussion.....	222
Chapter 6.....	227

The Role of p47 ^{phox} in Angiotensin II (AngII)-induced Cardiac Hypertrophy in Mice	227
6.1 Introduction.....	227
6.1.1 Aims and objectives.....	230
6.2 Materials and Methods.....	232
6.2.1 Chemicals and reagents.....	232
6.2.2 AngII-induced cardiac hypertrophy and cardiac samples from wild-type and p47 ^{phox} KO mice.....	232
6.2.3 Measurement of cardiac hypertrophy by cross-sectional cardiomyocyte size..	235
6.2.4 Sample preparation	236
6.2.5 Protein concentration measurement.....	237
6.2.6 ROS measurement	237
6.2.7 Western blot.....	237
6.2.8 Immunofluorescence.....	238
6.3 Results.....	239
6.3.1 The effect of AngII infusion on the blood pressure	239
6.3.3 The effect of AngII infusion and targeting p47 ^{phox} on the cardiac <i>in situ</i> O ₂ - production measured by DHE fluorescence	242
6.3.4 The effect of AngII infusion and targeting p47 ^{phox} on the cardiac O ₂ - production measured by lucigenin chemiluminescence.....	244
6.3.5 The effect of AngII infusion and targeting p47 ^{phox} on the cardiac H ₂ O ₂ production measured by Amplex Red fluorescence	246
6.3.6 The effect of AngII infusion and targeting p47 ^{phox} on the cardiac p47 ^{phox} and Nox expression examined by western blot	248
6.3.7 The effect of AngII infusion and targeting p47 ^{phox} on the activation of the MAPK signalling pathway examined by western blot	250
6.3.8 The effect of AngII infusion and targeting p47 ^{phox} on phosphorylation of H2AX and ASK1.....	252
6.4 Discussion.....	257
Chapter 7.....	262
General Discussion and Future Work.....	262
7.1 General Discussion	262
7.2 Future Work.....	268
Appendix.....	271
Appendix I: List of Reagents	271
Appendix II: List of antibodies	273
Appendix III: List of equipment	274
Appendix IV: R Script for NCA Analysis	275

Appendix V: Phase-contrast of H9C2 cells	278
Appendix VI: Full-gel Western Blot Images for H9C2 cell Analysis	279
Appendix VII: Full-gel Western Blot Images for WT and KO Cardiac Homogenates	281
Reference	285

List of Tables

Chapter 1

Table 1. 1 Isoforms of NADPH oxidase and their functional mechanisms.....	38
Table 1. 2 p47 ^{phox} KO studies on mediating cardiac functioning and redox signalling pathways.	49

Chapter 2

Table 2. 1 Column defining settings for the data in Phoenix WinNonlin 8.1.....	80
Table 2. 2 Reagents for separating gel preparation.....	99
Table 2. 3 Reagents needed for stacking gel preparation.	99

Chapter 3

Table 3. 1 Log BB of apocynin.....	131
Table 3. 2 Plasma NCA PK profile of apocynin by Phoenix WinNonlin 8.1.....	132
Table 3. 3 Model fit of apocynin using compartmental models by WinNonlin 8.1. .	133
Table 3. 4 NLME model parameters of apocynin one compartmental analysis by Phoenix WinNonlin 8.1.	134

Chapter 4

Table 4. 1 Recipe for the fasted state simulated intestinal (FaSSIF) and the fasted state gastric intestinal (FaSSGF).	161
Table 4. 2 Chemical properties of LMH001.	165
Table 4. 3 Plasma protein binding of LMH001 in murine plasma.	173
Table 4. 4 Curve fit and NCA PK calculation of LMH001 by R 4.0.1, with PKNCA package.	183
Table 4. 5 Curve fit and NCA PK calculation of LMH001 by Phoenix WinNonlin 8.1.	185
Table 4. 6 Curve fit by Excel and NCA PK calculation of LMH001 by hand.	187
Table 4. 7 Compartmental analysis of LMH001 by WinNonlin 8.1.	189
Table 4. 8 Model diagnostic parameters of LMH001 compartmental analysis, fitted with NLME model.	190

Chapter 5

Table 5. 1 Model details for the PD analysis of LMH001 in AngII-stimulated H9C2 cells.	206
Table 5. 2 Calculated PD parameters of LMH001 in reducing O ₂ ⁻ production in AngII-stimulated H9C2 cells.	212

List of Figures

Chapter 1

Figure 1. 1 Distribution of Cardiovascular disease mortality: Age-standardised death rate per 100,000 population, both sexes in 2015 (Roth et al., 2017).	21
Figure 1. 2 A diagram for the generation, inter-conversion and elimination of ROS. 27	
Figure 1. 3 Production of NO by NOS.	29
Figure 1. 4 Production of H ₂ O ₂ by XO.	30
Figure 1. 5 The schematic presentation of the structure of Nox1 when it is activated.	33
Figure 1. 6 The schematic presentation of the structure of Nox4.	35
Figure 1. 7 The schematic presentation of the structure of Nox5.	37
Figure 1. 8 Schematic diagram of the translocation of Nox2 regulatory subunits (p40 ^{phox} , p47 ^{phox} and p67 ^{phox}) during the activation of Nox2.	41
Figure 1. 9 The structure of the functional elements of p40 ^{phox}	42
Figure 1. 10 The structure of the functional elements of p67 ^{phox}	43
Figure 1. 11 A multiple-sequence alignment in p47 ^{phox} of different species.	46
Figure 1. 12 A schematic of interactions between p67 ^{phox} , p47 ^{phox} , and p40 ^{phox}	48
Figure 1. 13 A schematic of interactions between p47 ^{phox} and cortactin.	62

Chapter 2

Figure 2. 1 Thermo Scientific Accela HPLC and LTQ-Orbitrap XL mass spectrometer.	75
Figure 2. 2 Settings of apocynin Identification in User Peak Detection Settings, Thermo Xcalibur Quan Browser.	76
Figure 2. 3 Settings of apocynin ICIS Integration in User Peak Detection Settings, Thermo Xcalibur Quan Browser.	77
Figure 2. 4 The organisation and import of raw data.	79
Figure 2. 5.1 The process of one-compartmental analysis by Phoenix WinNonlin 8.1: selecting phoenix model.	88
Figure 2. 6 General principles of Western Blot.	98
Figure 2. 7 Precision Plus Protein™ Dual Colour Standards for molecular weight estimation of the protein of interest.	100
Figure 2. 8 The wiping of the slides. The numbers are used for indicating the order of wiping.	105

Chapter 3

Figure 3. 1 The non-invasive mouse restraint (A) and tail vein injection (B).	114
Figure 3. 2 A schematic diagram of the design and workflow of PKPD characterisation of apocynin.	114
Figure 3. 3 A schematic diagram of the establishment and the analysis of the middle-age diet-induced obesity murine model.	116
Figure 3. 4 Workflow of apocynin extraction from different biological samples for HPLC-MS/MS analysis.	118
Figure 3. 5 Representative HPLC-MS/MS of phenacetin (IS) in different samples.	122
Figure 3. 6 Representative HPLC-MS/MS of apocynin in different samples.	123

Figure 3. 7 Representative mass spectrum of apocynin.....	124
Figure 3. 8 Representative mass spectrum of diapocynin, showing prominent parent ion at m/z 329.1068.....	125
Figure 3. 9 Representative selected-reaction-monitoring HPLC-MS/MS chromatograms of diapocynin detection in (A) plasma, (B) brain and (C) liver from the same CD1 mice PK model.	126
Figure 3. 10 Linearity of apocynin by HPLC-MS/MS.	128
Figure 3. 11 Kinetic change of apocynin concentration in different tissue organs....	130
Figure 3. 12 Time-dependent elimination of apocynin in the plasma.	132
Figure 3. 13 Diagnostic scatter plots of one-compartmental NMLE model fit of apocynin using Phoenix WinNonlin 8.1.	135
Figure 3. 14 O ₂ .- production in brain homogenates detected by lucigenin chemiluminescence.	137
Figure 3. 15 O ₂ .- production in the liver homogenates detected by lucigenin chemiluminescence.	138
Figure 3. 16 O ₂ .- production in the heart homogenates detected by lucigenin chemiluminescence.	139
Figure 3. 17 <i>in-situ</i> O ₂ .- production in brain sections by detected by DHE.	140
Figure 3. 18 Lipid peroxidation by MDA assay in (A) brain, (B) liver and (C) heart.	142
Figure 3. 19 The effect of apocynin in dietary-induced middle-aged obesity murine model.....	145

Chapter 4

Figure 4. 1 Design and workflow of PK characterisation of LMH001.	156
Figure 4. 2 Workflow of LMH001 extraction from different biological samples for HPLC-MS/MS analysis.	159
Figure 4. 3 Possible structural change of LMH001 after the derivatisation by BSFTA + TMCS.	162
Figure 4. 4 HP (Agilent) 6890-5973 GC-MS System.	163
Figure 4. 5 3D structure and the pKa values calculated by ChemOffice 19.0.....	168
Figure 4. 6 Proposed fragmentation pattern of LMH001 in negative ionisation, result from Mass Frontier™ Spectral Interpretation Software.	169
Figure 4. 7 Representative selective-reaction-monitoring HPLC-MS/MS chromatograms of LMH001 in mobile phase A in negative ionisation mode.....	171
Figure 4. 8 Linearity of LMH001 quantification by HPLC-MS/MS.....	172
Figure 4. 9 Detected LMH001 in different fluids.....	174
Figure 4. 10 Representative chromatograms of LMH001 in fasted state simulated intestinal fluid (FaSSIF) before and after 60 min.	175
Figure 4. 11 Representative chromatograms of LMH001 in fasted state simulated gastric fluid (FaSSIF) before and after 60 min.	177
Figure 4. 12 Representative chromatograms of LMH001 in methanol before and after 60 min.	178
Figure 4. 13 Kinetic changes of LMH001 from 1 min to 24 h post iv bolus (10 mg/kg) in male CD1 mice (12-week of age, 26-30 g) in plasma and urine (from 5 min to 24 h).	180

Figure 4. 14 NCA analysis by R 4.0.1, including the R Script (A) and Console (B).	182
Figure 4. 15 Curve fit of LMH001 plasma concentration against time (0.017 h to 0.5 h) generated by Phoenix WinNonlin 8.1	185
Figure 4. 16 The non-compartmental analysis of LMH001 by Excel and hand calculation.	186
Figure 4. 17 Schematic illustrations of one, two and three compartmental models.	189
Figure 4. 18 One-compartmental NLME model fit of LMH001 using Phoenix WinNonlin 8.1	191
Figure 4. 19 The predicted hydrolysis of LMH001 in simulated intestinal and gastric fluid.	194
Figure 4. 20 The comparison between the logarithmic (black) and linear (red) trapezoidal method in calculating AUC.	198

Chapter 5

Figure 5. 1 Outline of the experiments carried out to study the effect of LMH001 <i>in vivo</i> and <i>in vitro</i> .	208
Figure 5. 2 O ₂ ⁻ production in saline and AngII treated H9C2 cells.	210
Figure 5. 3 Non-linear regression analysis of LMH001 in reducing 100 nM AngII-stimulated H9C2 cells.	211
Figure 5. 4 PD analysis and residue distribution of LMH001 on the inhibition of O ₂ ⁻ production in 100 nM-stimulated H9C2 cells.	213
Figure 5. 5 H ₂ O ₂ production in H9C2 cells in response to AngII examined by Amplex red fluorescence.	215
Figure 5. 6 The effect of LMH001 in reducing AngII-stimulated oxidative stress, examined by DCFH-DA fluorescence.	217
Figure 5. 7 The p47 ^{phox} , and Nox expression in 24 h control, AngII-stimulated and LMH001-treated H9C2 cells.	219
Figure 5. 8 The ERK1/2 and p38 MAPK phosphorylation in 24 h control, AngII-stimulated and LMH001-treated H9C2 cells.	221

Chapter 6

Figure 6. 1 CODA non-invasive murine blood-pressure measurement system, its application on conscious mice, and the representative blood pressure trace.	234
Figure 6. 2 Set-up of 2-week AngII-infused middle-age WT and p47 ^{phox} KO murine model and the biochemical and molecular experiments for the assessment.	235
Figure 6. 3 Cardiovascular functions of WT and p47 ^{phox} KO mice after 2-week infusion of AngII or saline, measured by blood pressure and heart/body weight ratio.	241
Figure 6. 4 <i>In situ</i> cardiac cross-sectional area and O ₂ ⁻ production in AngII or saline-infused WT and p47 ^{phox} KO mice.	243
Figure 6. 5 O ₂ ⁻ production in AngII or saline-infused WT and p47 ^{phox} KO mouse heart.	245
Figure 6. 6 H ₂ O ₂ production in saline or AngII infused WT and p47 ^{phox} KO mouse heart.	247
Figure 6. 7 Protein expression level of p47 ^{phox} , Nox1, Nox2 and Nox4 in AngII or saline-infused WT and p47 ^{phox} KO mice.	249

Figure 6. 8 Protein phosphorylation of ERK1/2, MKK3/6 and p38MAPK in saline or AngII infused WT and p47^{phox} KO mice.251

Figure 6. 9 γ H2AX detection in the AngII and saline-infused WT and p47^{phox} KO mice by western blot.253

Figure 6. 10 γ H2AX detection in the AngII and saline-infused WT and p47^{phox} KO mice by immunofluorescence.254

Figure 6. 11 Phosphorylation of ASK1 and Nox2 expression in the AngII and saline-infused WT and p47^{phox} KO mice, examined by immunofluorescence.....256

List of Publications and Presentations

Publications

Fangfei Liu, Lampson M. Fan, Nicholas Michael, and Jian-Mei Li. "In vivo and in silico characterization of apocynin in reducing organ oxidative stress: A pharmacokinetic and pharmacodynamic study." *Pharmacology Research & Perspectives* 8, no. 4 (2020): e00635.

Li Geng, Lampson M. Fan, **Fangfei Liu**, Colin Smith, and Jian-Mei Li. "Nox2 dependent redox-regulation of microglial response to amyloid- β stimulation and microgliosis in aging." *Scientific Reports* 10, no. 1 (2020): 1-11.

Lampson M. Fan, Li Geng, Sarah Cahill-Smith, **Fangfei Liu**, Gillian Douglas, Chris-Anne Mckenzie, Colin Smith, Gavin Brooks, Keith M. Channon, and Jian-Mei Li. "Nox2 contributes to age-related oxidative damage to neurons and the cerebral vasculature." *The Journal of Clinical Investigation* 129, no. 8 (2019): 3374-3386.

Fangfei Liu, and Jian-Mei Li. " p47^{phox} dependent Redox regulation of Angiotensin II-induced Cardiac Hypertrophy: 260" *Free Radical Biology and Medicine* 145 (2019). (Abstract)

Fangfei Liu and Jian-Mei Li. "In Vivo PKPD Evaluation and Computer Modelling of Apocynin in Reducing Organ Superoxide Production: 37." *Free Radical Biology and Medicine* 145 (2019). (Abstract)

Fangfei Liu and Jian-Mei Li. "BS24 Pharmacokinetic analysis and evaluation of apocynin in reducing cardiac superoxide production." *Heart* 105, no. Suppl 6(2019): A156-A156. (Abstract)

Fangfei Liu, Junjie Du, and Jian-Mei Li. "218 Knockout p47^{phox} reduces angiotensin ii-induced cardiac oxidative stress and hypertrophy." *Heart* 103, no. Suppl 5 (2017): A142-A143. (Abstract)

Presentations

Annual Meeting: Society for Redox Biology and Medicine, 20-23 November 2019, Las Vegas, USA: "p47^{phox} dependent Redox regulation of Angiotensin II-induced Cardiac Hypertrophy" (*poster presentation*) and " In Vivo PKPD Evaluation and Computer Modelling of Apocynin in Reducing Organ Superoxide Production " (*poster presentation*)

Annual Meeting: British Atherosclerosis Society and British Society for Cardiovascular Research, 03-04 Jun 2019, Manchester, United Kingdom: "Pharmacokinetic Analysis and Evaluation of Apocynin in Reducing Cardiac Superoxide Production" (*poster presentation*)

Annual Meeting: Society for Redox Research Australasia, 13-16 December 2018, Auckland, New Zealand: "Redox-regulation of AngII-induced Cardiac Hypertrophy and Apoptosis: A Study Using p47^{phox} Knockout Mice" and "Pharmacokinetic Analysis (*oral presentation*) and Evaluation of Apocynin in Reducing Brain Superoxide Production" (*poster presentation*)

Annual Meeting: British Atherosclerosis Society and British Society for Cardiovascular Research, 03-04 Jun 2017, Manchester, United Kingdom: "Knockout p47^{phox} reduces angiotensin ii-induced cardiac oxidative stress and hypertrophy" (*poster presentation*)

List of Abbreviations

AA	amino acid
ACE2	AngII converting enzyme 2
AIC	Akaike's information criterion
AICc	corrected version of AIC
AIR	auto-inhibitory region
AngII	angiotensin II
ANOVA	one-way analysis of variance
APS	ammonium persulfate
ASK1	apoptosis signal-regulating kinase 1
AUC	area under the curve
BIC	Bayesian information criterion
CGD	chronic granulomatous disease
CL	clearance
COX	cyclooxygenase
CVDs	cardiovascular diseases
Cy3	Cyanine-3
DAPI	4', 6-diamidino-2-phenylindole
DHE	Dihydroethidium
DPI	diphenyleneiodonium
Duox1	dual oxidase 1
Duox2	dual oxidase 2
EDTA	ethylenediaminetetraacetic acid
EGF	epidermal growth factor
ERK1/2	extracellular regulated kinase1/2
FAD	flavin adenine dinucleotide
FITC	fluorescein isothiocyanate
H ₂ O ₂	hydrogen peroxide
HBSS	Hanks' balanced salt solution
HESI	heated electrospray ionization

HFD	high-fat diet
HPLC-MS/MS	high performance liquid chromatography tandem mass spectrometry
JNK	c-Jun N-terminal kinases
KO	knockout
LDL	low-density lipoprotein
L-NAME	N ^G -Nitro-arginine methyl ester
LOX	lipoxygenase
MAPK	mitogen-activated protein kinase
MDA	Malondialdehyde
MI	myocardial infarction
MMP2	matrix metalloproteinase 2
NADH	nicotinamide adenine dinucleotide
NADPH	nicotinamide adenine dinucleotide phosphate
NCA	non-compartmental analysis
Ncf1	neutrophil cytosolic factor 1
neo	neomycin resistance
NFκB	nuclear factor kappa-light-chain-enhancer of activated B cells
NLME	non-linear mixed effect
NO	nitric oxide
NOS	nitric oxide synthase
Nox	NADPH oxidase
OCT	optimal cutting temperature compound
OD	optical density
PB1	one phox and Bem1
PBS	phosphate buffered saline
PD	pharmacodynamics
PEG-SOD	polyethylene glycol-superoxide dismutase
PI3K	phosphatidylinositol 3-kinase
PK	pharmacokinetics
PKC	protein kinase C

PMA	phorbol-12-myristate-13-acetate
PRR	proline-rich region
PVDF	polyvinylidene fluoride
PX	phox homology
ROS	reactive oxygen species
SD	standard deviation
SDS	sodium lauryl sulfate
SH3	Src homology 3
SOD	superoxide dismutase
SRM	selected reaction monitoring
TBA	2-thiobarbituric acid
TBST	Tris buffered saline-Tween
TNF α	tumour necrosis factor α
TPRs	tetratricopeptide repeats
VEGF	vascular endothelial growth factor
VSMCs	vascular smooth muscle cells
XDH	xanthine dehydrogenase
XO	xanthine oxidase

Abstract

Reactive oxygen species (ROS) are involved in the signal transduction and cell defence in mammalian cells. However, excessive ROS derived under pathophysiological conditions are associated with the development of a wide range of diseases including cardiovascular, metabolic, neurodegenerative diseases and cancer. gp91^{phox}-containing NADPH oxidase (Nox2) was found to be one of the primary enzymatic sources of ROS and p47^{phox} is its key regulator.

LMH001 was developed in this lab as an inhibitor of Nox2 targeting p47^{phox}, but its chemical properties and preclinical pharmacokinetics and pharmacodynamics (PK/PD) have not been studied. At the same time, the role of p47^{phox} and its signalling pathways under pathophysiological conditions remained unclear. Therefore, the overall aim of this study is to characterise the PK/PD properties of LMH001 and understand its mechanism in depth by knockout (KO) of p47^{phox} in Angiotensin II (AngII)-induced oxidative stress and cardiac hypertrophy model.

The plasma concentration of LMH001 showed a mono-exponential decline pattern with a $t_{1/2} = 0.042$ h and a clearance = 5682.63 mL/h/kg, and its effect in reducing AngII-stimulated H9C2 (a rat myoblast cell line) ROS production showed an $IC_{50} = 124.00 \pm 42.6$ ng/ml. In the AngII-induced hypertrophic models, wild type (WT) mice displayed significantly raised systolic blood pressure (SBP) and induced cardiac hypertrophy after AngII-infusion. In contrast, p47^{phox} KO mice only demonstrated a mild increase in SBP without hypertrophy. There was also phosphorylation of ERK1/2, p38 MAPK and MAPK kinase 3/6 (MKK3/6). Apoptosis was suggested by increased levels of γ H2AX and apoptosis signal-regulating kinase 1 (ASK1) phosphorylation.

In conclusion, p47^{phox} plays a crucial role in AngII-induced cardiac oxidative stress and hypertrophy. Its signalling through MKK3/6, p38MAPK and ERK1/2 phosphorylation are essential in γ H2AX and ASK1 phosphorylation and cardiomyocyte apoptosis. This study also provided vital information on the chemical properties, PK/PD, and pharmacological efficacy of LMH001. Its potential as a drug candidate for oxidative stress-related diseases was discussed, and future experiments on the development of LMH drugs were suggested.

Chapter 1

General Introduction

1.1 Cardiovascular Diseases (CVDs)

1.1.1 Prevalence

Cardiovascular diseases (CVDs) are disorders in the heart and vascular system. They include coronary heart disease, cerebrovascular disease, peripheral arterial disease, rheumatic heart disease, congenital heart disease and deep vein thrombosis and pulmonary embolism. In 2016, the estimated number of people who died from CVDs was 17.9 million (31% of global death), in which 85% were caused by coronary heart disease and stroke. **Figure 1.1** demonstrated the mortality (age-standardised death rate per 100,000 people in both genders) distribution of CVDs in 2015 throughout the world.

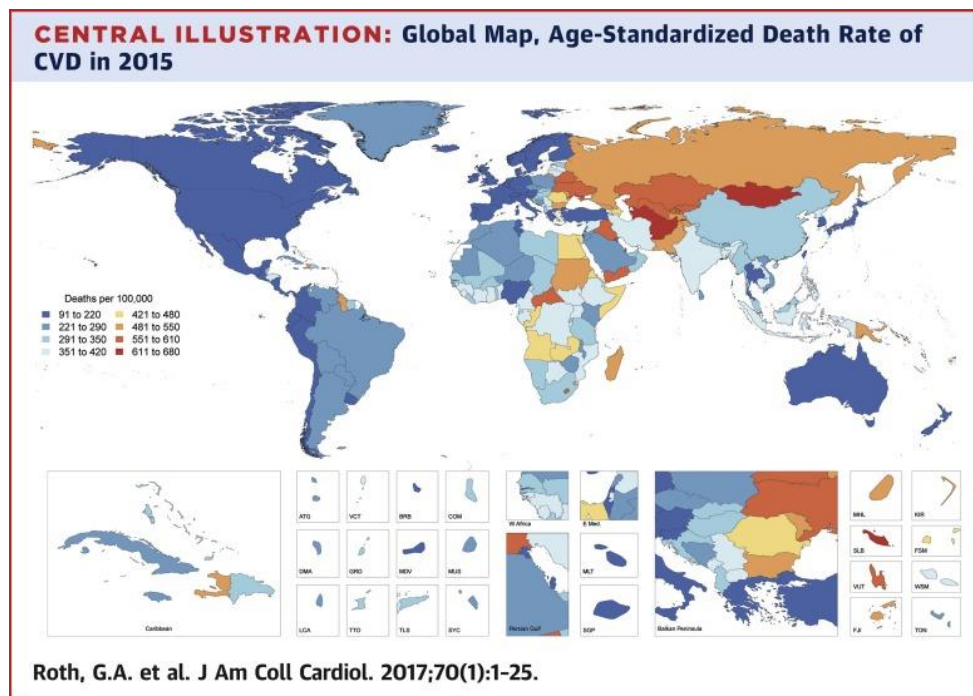


Figure 1. 1 Distribution of Cardiovascular disease mortality: Age-standardised death rate per 100,000 population, both sexes in 2015 (Roth et al., 2017).

In Europe, more than 85 million people were living with CVDs, and they are the cause of 3.9 million death each year in 2015 (Timmis et al., 2018). In the UK, before the COVID-19 pandemic, it was reported that 7.4 million people were living with the CVDs and they caused 170,000 death each year, accounting for 28% of all deaths. Given the high prevalence and mortality rate of the CVDs, much emphasis has been put on the research aiming towards improving the human circulatory system in the UK and globally.

1.1.2 Pathogenesis of CVDs

Beating approximately 70 times per minute in resting state, human heart pumps blood with oxygen and nutrients to the rest part of the body and its muscle is supplied with blood through another system called coronary arteries. A human heart consists of several parts including atrium (left and right atrium), ventricle (left and right ventricle), valves (mitral, aortic, pulmonary and tricuspid valves) and it connects to several veins and arteries containing vena cava (superior vena cava and inferior vena cava), pulmonary artery, pulmonary vein and aorta. CVDs in heart include coronary heart disease which is the damage in coronary arteries resulting in failure of providing sufficient blood to heart muscles, rheumatic heart disease which is disorders in heart muscle and valves due to rheumatic fever, and congenital heart disease which is malformations of heart structure at the stage of birth (Bhatt & Pashkow, 2008).

Vessels in human body include 1) arteries which take the blood from the heart to organs in need of oxygen and nutrition, 2) veins which carry the blood to the heart and 3) capillaries which are small and thin vessels connected to both arteries and veins delivering the oxygen-saturated blood to each cell in organs. These three types of vessels make up for the human vascular system. As an example, a normal human brain gets the blood supply from the heart through two arteries running left and right side of

the neck and capillaries, thus enabling not only intellectual but also normal brain functions. Disorders involving blood vessels supplying the brain are classified as cerebrovascular disease. Most vascular diseases are related to atherosclerosis and these include cerebrovascular disease, peripheral arterial disease which results in insufficient blood supplying to arms and legs and deep vein thrombosis and pulmonary embolism, which is a disease caused by clots formed in legs moving to the lung or the heart (Samson, 2008).

Atherosclerosis is a pathological condition which lipid plaques gradually build up in the vessels. This process involves a long term immunoinflammatory responses possibly from endothelial cells, leukocytes, and intimal smooth muscle cells, and can affect coronary, cerebral, and peripheral arteries and the aorta (Falk, 2006). Under normal conditions, low-density lipoprotein would be able to pass through endothelial cells by transcytosis and be taken up by receptor-mediated endocytosis. The pathological processes begin with a damaged endothelial wall with exposed adhesion molecules which would capture leukocytes and develops because the captured leukocytes would then undergo morphological changes and squeeze through endothelium and entre tunica intima, produce reactive oxygen species (ROS) and oxidise the un-regulated LDL through the damaged endothelial wall. The oxidised LDL would then attract more white blood cells (and intimal smooth muscle cells), produce more ROS and therefore form a positive feedback and lead to the accumulation of foam cells (Goncharov et al., 2015). The foam cell would eventually die, which attract more white blood cells to form a lipid core, and eventually form a plaque (Falk, 2006). With the endothelial cells covering the plaque, and calcium salt and other dead cell debris accumulating, the plaque hardens.

In some scenarios, the endothelial cells which over the plaque could get compromised, activate the coagulation cascade and eventually it would lead to the formation of fibrin-rich blood clots, and sometimes reach out to the vessel lumen and form thrombus (Capra et al., 2014). This process is thrombosis, and since the blood clot could then break down and travel in the blood vessels, the most devastated consequences of atherosclerosis and thrombosis can be ischemic (thrombotic) stroke or myocardial infarction.

Ischemic or thrombotic stroke could happen when the blood clot, formed by thrombosis, block the blood supply in cerebral artery to the brain. Since the brain does not store oxygen or glucose, within a very short time (minutes), the brain starts dying. The immediate responses of the brain include the ion imbalance, such as the $\text{Na}^+ - \text{K}^+$ pump dysfunction and calcium overload, the metabolic response include the disrupted phosphatase activity, decrease of ATP levels and pH, and ROS production and increase of oxidative stress, which would then lead to further responses such as apoptosis and autophagy (Rodrigo et al., 2013). Similarly, myocardial infarction is often linked with coronary thrombosis (Palasubramaniam, Wang & Peter, 2019). With the rupture of the blood clot in the vessel, and the blockage of blood supply, the systolic function of the myocardium was compromised, thus leading to ion imbalance, increase of oxidative stress, mitochondrial alterations and eventually, apoptosis and necrosis of cardiomyocytes and cardiac tissues (Frangogiannis, 2015). During the current COVID-19 pandemic, complications of acute myocardial infarction in COVID-19 patients without any cardiac history or implication of clear atherosclerosis were discovered (Tedeschi et al., 2020). Possibly, due to the severe effects of COVID-19, high levels of proinflammatory mediators diffused coronary thrombosis without cardiac histories.

Unlike ischemic stroke, haemorrhagic stroke is caused by internal bleeding of the brain, and accounts for about 25% of all strokes. It could happen due to the rupture of an aneurysm stemmed from a weakened artery wall, long-standing hypertension, a major trauma, genetics or physical forces. Haemorrhagic stroke could also come from arteriovenous malformation (Linfante & Wakhloo, 2007). It could induce the expression of inflammatory factors such as tumour necrosis factor tumour necrosis factor α (TNF α), interleukin 6 (IL-6) and nuclear factor-kappa B (NF- κ B) in the brain and the spleen (Lee et al., 2008). However, the immunological and biochemical changes induced by haemorrhagic stroke remain insufficiently studied (Saand et al., 2019).

Risk factors for atherosclerosis and thrombosis, and in general, CVDs, include endothelial damage and dysfunction, which largely involves oxidative stress and ROS production, this include high blood cholesterol (Xu, Liu & Liu, 2013), raised blood pressure (Kokubo & Kamide, 2009), high blood glucose level (Aguiar, Duarte & Carvalho, 2019), smoking (Ramotowski et al., 2019) and complications under severe COVID-19 conditions. At the same time, patients with chronic cardiovascular conditions are considered high risk groups for COVID-19.

1.2 Reactive Oxygen Species (ROS)

ROS are free radicals and molecules derived from oxygen. They are involved in the signal transduction of many physiological processes such as immune responses (Williams & Kwon, 2004), metabolism and inflammation (Forrester et al., 2018), differentiation (Arakaki et al., 2013), proliferation (Ruiz-Gines et al., 2000) (Lopez-Acosta et al., 2018), adhesion (Lopez-Acosta et al., 2018; Maulucci et al., 2010), apoptosis (Fan et al., 2019; Li et al., 2007) and cell cycle regulation (Tickner et al., 2011; Verbon, Post & Boonstra, 2012). Some of the examples of ROS are H₂O₂, O₂⁻, OH \cdot , ONOO⁻ and so on. ROS act as a mediator in various reduction-oxidation (redox)

signalling transduction pathways. For example, in mammalian cells, pathways involving the regulation of cell cycle and differentiation, such as p53 (Li et al., 2007), peroxisome proliferator-activated receptor- γ (Tickner et al., 2011), γ H2AX (Fan et al., 2019) and activates apoptosis signal-regulating kinase 1 (ASK1) (Matsukawa et al., 2004), are redox-sensitive. Under pathophysiological conditions, these redox-sensitive signalling pathways could mediate a self-protective or clearing mechanism when activated by upstream stress signalling pathways in response to the oxidative stress.

ROS are also responsible for microbial removal and essential for maintaining the normal functioning of the immune system. The importance of ROS production can be reflected by a genetic disease called chronic granulomatous disease (CGD). CGD is a primary immunodeficiency that was caused by the mutation in NADPH oxidase subunits (Pollock et al., 1995). Nox2 mutation could result in X-linked recessive CGD (XR-CGD), while mutations on the genes coding for p22^{phox}, p47^{phox}, p67^{phox} and p40^{phox} cause the autosomal recessive CGD (Chiriaco et al., 2016). With these conditions, a bacterial and fungal infection could develop at a very early stage of life, thus making it hard to survive until adulthood if not diagnosed promptly.

1.2.1 Generation, interconversion and elimination of ROS

Figure 1.2 illustrates the generation, inter-conversion and elimination of ROS.

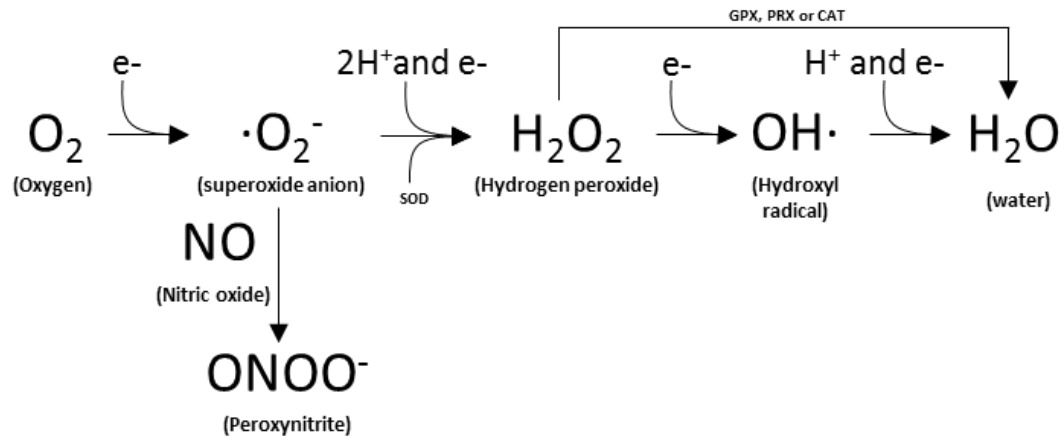


Figure 1. 2 A diagram for the generation, inter-conversion and elimination of ROS.

H^+ : Hydrogen ion, e^- : electron, SOD: superoxide dismutase, GPX: glutathione peroxidase, PRX: peroxiredoxin and CAT: catalase.

Oxygen is essential for eukaryote aerobic cellular respiration and the generation of ROS (Nohl et al., 2003). During the phosphorylation of the electron transport chain, the oxygen receives electrons from the reduced form of nicotinamide adenine dinucleotide (NADH) and flavin adenine dinucleotide (FADH₂). It then reacts with hydrogen to produce water (Bartolome & Abramov, 2015). In the presence of some hormones, such as angiotensin II (AngII) (Massey et al., 2012) or abnormal high-energy factors, such as radiation that can release electrons from the environment (Rodriguez & Redman, 2005), the oxygen transforms into superoxide anion (O_2^-). Under healthy physiological conditions in vascular endothelial cells, the nitric oxide synthase (NOS) can generate nitric oxide ($\cdot NO$) to interact with O_2^- and produce peroxynitrite ($ONOO^-$) as a mid-product. Without molecular targets, it would isomerise to nitrate (NO_3^-), a stable product (Forstermann, Xia & Li, 2017). This process was also discovered in neurotransmission and immune system, and NOS was found to present in three different

isoforms including endothelial NOS (eNOS), inducible-NOS (iNOS) and neuronal NOS (nNOS) (Marletta, 1994). The O_2^- can also be converted to hydrogen peroxide by superoxide dismutase (SOD). This reaction results in the formation of hydrogen peroxide (H_2O_2). Furthermore, by accepting an electron from iron ions, H_2O_2 produces hydroxyl radical (OH^\cdot), which is also involved in the health homeostasis (Lipinski, 2011; Lyngsie et al., 2018). Under physiological conditions, ROS production/elimination is regulated by redox signalling reactions involving SOD, glutathione peroxidase, peroxiredoxin and catalase (**Figure 1.2**). By contrast, during pathological conditions, excessive free radical molecules are resulting in an oxidative stress-induced imbalance of the cellular homeostasis. Therefore, this can ultimately lead to redox-dependent pathophysiological responses such as vascular endothelial damage thus exposing cells to a long-term inflammatory process, which could lead to disorders such as thrombosis, atherosclerosis and vascular remodelling (Fearon & Faux, 2009).

1.2.2 Exogenous source

The environment such as smoking, pollution, (deleted HFD, referenced the rest) and ionising radiation (specifically, the organic and inorganic radioactive chemicals) can also be a source of ROS (Kelly, 2003; Peluffo et al., 2009; Smith et al., 2012). For example, smoking (cigarette smoke extract as was used in the study) could increase O_2^- and $ONOO^-$ production (Peluffo et al., 2009). Also, heavy metals including cadmium were shown to inhibit the growth and viability of yeasts, demonstrated by higher levels of malondialdehyde (MDA) and glutathione production, as well as the increased activities of catalase, SOD and glutathione peroxidase in the cadmium-exposed cells (Muthukumar & Nachiappan, 2010).

1.2.3 Enzymatic source

Several different enzymes also produce ROS in mammalian cells. These enzymes include NOS, xanthine oxidase (XO) and xanthine dehydrogenase (XDH), cyclooxygenase (COX) and lipoxygenase (LOX), mitochondrial electron transport chain and nicotinamide adenine dinucleotide phosphate (NADPH) oxidase (Nox).

1.2.3.1 Nitric oxide synthase (NOS)

In the cardiovascular system, eNOS can produce NO from L-arginine in response to increased shear stress caused by increased blood pressure (Tejero & Stuehr, 2013; Omanwar et al., 2014), thus plays a role in reducing the blood pressure. The production of NO by NOS is demonstrated in **Figure 1.3**, which involves two oxygens being reduced to NO catalysed by NOS at the presence of NADPH, an electron donor.

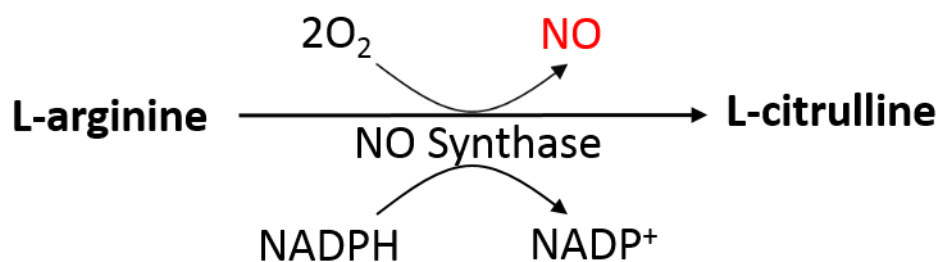


Figure 1. 3 Production of NO by NOS.

The uncoupling of NO caused by excessive O₂⁻ can result in the generation of peroxynitrite (ONOO⁻), which can then oxidise tetrahydrobiopterin, an essential cofactor for eNOS functioning (Alp & Channon, 2004) and induce endothelial dysfunction. The uncoupling of NO is closely related to the development of many cardiovascular disorders such as myocardial infarction (Masano et al., 2008), cardiac hypertrophy and fibrosis (Leiva et al., 2016), development of atherosclerosis in the

new-born during pregnancy (Moens et al., 2008) and vascular endothelial dysfunction in diabetes (Thum et al., 2007).

1.2.3.2 Xanthine oxidoreductase (XO)

Xanthine Oxidoreductase exists in two forms, XO and XDH, interconvertible to each other. XO catalyses xanthine or hypoxanthine to produce uric acid, and hydrogen peroxide at the presence of oxygen and XDH undergoes the same reaction but requires the participation of NAD^+ to produce NADH. The reactions are illustrated in **Figure 1.4**.

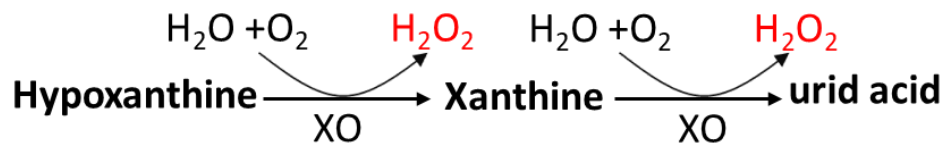


Figure 1. 4 Production of H_2O_2 by XO.

It is well established that XO plays a vital role in activating cell defence mechanisms in T cells and neutrophils while it was less addressed in ROS production in terms of cell/tissue damage (Chung et al., 1997). Xanthine oxidase was also found to induce hydrogen peroxide production under inflammatory conditions, yet it was defined as an insignificant contributor towards ROS generation in human vascular endothelium (Palermartinez et al., 1994).

1.2.3.3 Cyclooxygenase (COX) and lipoxygenase (LOX)

COX and LOX function by catalysing arachidonic acid as a substrate upon the activation of phospholipase A_2 and producing ROS through their metabolites. These metabolites that are associated with ROS production from LOX pathways include cytosolic leukotriene B_4 and cytosolic phospholipase A_2 (Kim, Kim & Kim, 2008), and

from COX include prostaglandin G2 and prostaglandin H2 (PGH2) (Cho, Seo & Kim, 2011).

However, these metabolites, instead of producing cell/tissue-damaging ROS directly, they mediate the activation of several signalling pathways that can induce Nox-dependent ROS production. In addition, in a study of AngII-induced hypertension, excessive Nox/mitochondria-derived-ROS and COX2 have been reported to have a complicated relationship. However, although COX2 could be one source of ROS, in this study, it was more likely that Nox-derived ROS were dominantly participating in the development of vascular dysfunction (Martinez-Revelles et al., 2013). Similar metabolic procedures happen with LOX. Accumulating evidence is showing that both Cox and LOX can induce Nox-based ROS generation and it was Nox-derived ROS that plays a significant part of the development of cardiovascular diseases (Cho, Seo & Kim, 2011).

1.2.3.4 Mitochondrial electron transport chain

ROS can be produced in electron transport chains in mitochondria. In mitochondria, oxygen is produced by converting NADH or FADH₂. Since some of the electrons can escape this process and get caught by the oxygen, ROS could be generated. ROS production from this process predominantly is spotted from mitochondrial complex I, and this is a coenzyme Q (CoQ)/CoQH₂, proton motive force (Δp) and NADH/NAD⁺ dependent process (Murphy, 2009).

In cardiomyocytes, a drug, diclofenac, has been discovered to have a side effect of inducing ROS-dependent cardiotoxicity through this physiological process (Ghosh et al., 2016). However, the damage ROS make under pathophysiological conditions is closely linked to the activation of NADPH oxidase. Studies showed that mitochondrial

ROS generation participated in the process of mitogen-activated protein kinase (MAPK) activation upon AngII stimulation, yet it did not contribute to AngII induced vasoconstriction (Kimura et al., 2005a). Ischaemic reperfusion injury-induced AngII could also have an effect on electron transport chain in mitochondria, yet the real ROS were enhanced through the activation of NADPH oxidase, which was induced through c-Jun N-terminal kinases (JNK) and MAPK signalling pathways (Kimura et al., 2005b).

1.3 NADPH Oxidase

Nox is multi-unit cellular membrane-associated proteins that locate on the cell membrane and transfer the electrons from the cytoplasm to both intracellular compartments such as nuclei, mitochondria, endosomes, phagosomes and extracellular compartments such as an extracellular matrix. NADPH is the reduced form of nicotinamide adenine dinucleotide phosphate (NADP⁺). Generated by glucose-6-phosphate dehydrogenase in the cytosol, it carries an electron and can donate the electron in several physiological processes such as lipid and nucleic synthesis and innate immunity in phagocytes. Nox is involved in the latter process. Upon activation, NADPH serves as an electron donor and oxygen accepts the electron. The function of NADPH oxidase is to transfer the electron donated by NADPH through its catalytic subunits and transmembrane components to oxygen and generate O₂^{-•}. Nox include Nox1, Nox2, Nox3, Nox4, Nox5, dual oxidase 1 (Duox1) and dual oxidase 2 (Duox2). There are four isoforms, i.e. Nox1, Nox2, Nox4 and Nox5 that have been found in the human cardiovascular system (Lassegue & Griendling, 2010).

NADPH oxidase is one of the significant sources of O₂^{-•} generation in mammalian cells. Under normal conditions, these enzymes generate O₂^{-•} to promote the process of microbial killing in the innate immune system (Segal, 2008). Because these enzymes are sensitive to a wide range of stimuli, their activation is involved in

many physiological processes. For example, in the central nerve system (CNS), Nox is essential in the process of neuronal signalling transduction, memory, central cardiovascular homeostasis (Infanger, Sharma & Davisson, 2006) and inflammation (Sorce & Krause, 2009). Also, in the cardiovascular system, $O_2^{\cdot-}$ production in an NADH/NADPH oxidase-dependent manner can also be induced by AngII, a circulating vasoconstrictor acting locally as paracrine and autocrine hormone (Rajagopalan et al., 1996), which is beneficial short-term in maintaining cardiovascular homeostasis. However, under pathophysiological conditions, thiol-reactive stable compounds from cigarette smoke can also activate Nox to produce $O_2^{\cdot-}$ and cause endothelial dysfunction, and this eventually might lead to vascular toxicity (Jaimes et al., 2004).

1.3.1 Nox1

In the cardiovascular system, Nox1 was found in the arterial endothelial cells (Ago et al., 2005) and vascular smooth muscle cells (VSMCs) (Zhang et al., 2013). The structure of Nox1 is shown in **Figure 1.5**.

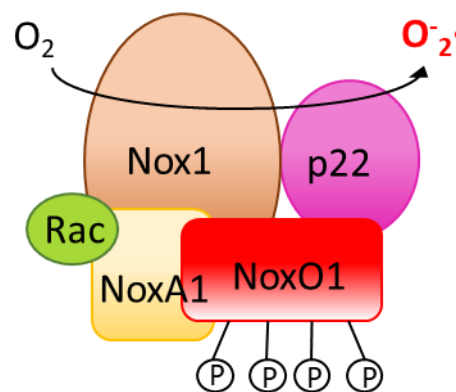


Figure 1. 5 The schematic presentation of the structure of Nox1 when it is activated.

Nox1 is membrane-bound (Cruz-Magalhaes et al., 2018) and is associated with $p22^{phox}$ in the late endoplasmic reticulum, which is necessary during the activation and functioning of Nox1, 2, 4 and 5 (Stasia, 2016). NoxO1 is the organiser and NoxA1 is

the activator during the activation of Nox1. NoxO1 has one phox homology (PX) domain and two Src homology 3 (SH3) domains (Davis, McPhail & Horita, 2011; Davis, McPhail & Horita, 2012; Ueyama, Lekstrom, Tsujibe, Saito & Leto, 2007) and is a homologue of p47^{phox} (Gianni et al., 2009). NoxA1 contains four N-terminal one tetratricopeptide repeats (TPRs), one phox and Bem1 (PB1) and one C-terminal domain SH3 domain (Dutta & Rittinger, 2010; Shrestha et al., 2017) and is a homologue of p67^{phox} (Takeya et al., 2003). On the other hand, different kinetic properties were found with NoxA1 in comparison to p67^{phox} (Kawano et al., 2012).

Various studies have shown that Nox1 is closely linked to cardiovascular pathogenesis. It is enhanced by many vasoactive agonists such as thrombin (Carrim et al., 2015), AngII (Dikalova et al., 2005), as well as growth factors such as epidermal growth factor (EGF), platelet-derived growth factor (Park et al., 2004) and basic fibrosis growth factor. The overexpression of Nox1 upregulated vascular endothelial growth factor (VEGF), which could lead to angiogenesis (Arbiser et al., 2002). Conversely, the growth factor VEGF stimulated Nox1 activation through phosphorylation of Rac by phosphatidylinositol 3-kinase (PI3K). The studies on hypertension by Dikalova et al., 2005, showed that AngII induced vasoconstriction through Nox1. The role of Nox1 in mediating the vasoconstriction suggested that Nox1 is involved in AngII-induced hypertension (Dikalova et al., 2005). When the basic fibrosis growth factor activates Nox1, this process can promote migration of VSMCs, leading to restenosis (Schroder et al., 2007).

1.3.2 Nox2

Nox2 plays a vital role in the development of cardiovascular diseases. Studies using transgenic animal models have been crucial in identifying the role of Nox2 in cardiovascular diseases. For example, Nox2 knockout (KO) mice demonstrated a

significantly reduced level of left ventricular cavity dilatation and dysfunction as compared to wild type mice after myocardial infarction (MI) (Looi et al., 2008). Furthermore, loss of Nox2 was also shown to prevent cardiomyocyte hypertrophy and myocardial fibrosis induced by pressure overload (Parajuli et al., 2014), suggesting a therapeutic potential of targeting Nox2 in the prevention and treatment of heart failure. Additionally, a decrease in the size of myocardial infarct was observed in Nox1 KO, Nox2 KO and Nox1/2 KO mice under the condition of 30 min ischaemia followed by 24 h reperfusion as well as a decrease of post-reperfusion oxidative stress in Nox2 KO mice (Braunersreuther et al., 2013). The structure and activation of Nox2 are illustrated in section 1.4.1.

1.3.3 Nox4

Constructively activated, Nox4 can be found in endothelial cells, cardiomyocytes, fibroblasts, and VSMCs in the cardiovascular system (Zhang et al., 2013). The structure of Nox4 is illustrated in **Figure 1.6**.

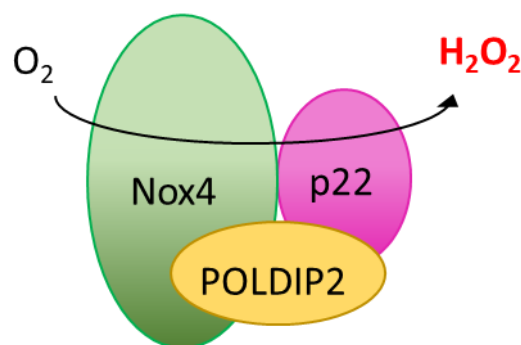


Figure 1. 6 The schematic presentation of the structure of Nox4.

POLDIP2 was found to be a novel regulator of Nox4 by associating with p22^{phox} to activate Nox4 (Lyle et al., 2009). The role that Nox4 plays in vasorelaxation or vasoconstriction is unclear. Nox4 has been shown to promote endothelial cell survival

through downstream extracellular regulated kinase1/2 (ERK1/2) and Akt pathways (Peshavariya et al., 2009). However, when Nox4, as well as its product H_2O_2 , was inhibited, there was a reduction in cell proliferation (Peshavariya et al., 2009). Conversely, Nox4 has also been demonstrated to participate in the IL1- and transforming growth factor β -induced cell senescence by producing H_2O_2 , which leads to DNA damage (Hubackova et al., 2012). Additionally, Nox4 has also shown to create endoplasmic reticulum stress and to promote cell autophagy through Ras-ERK signalling pathway (Wu et al., 2010). Upon pressure overload of murine NADPH oxidase 4 (Nox4) is a significant source of oxidative stress in the failing heart, Nox4 overexpression was observed to exacerbate cardiac dysfunction, hypertrophy, fibrosis and apoptosis, and KO of cardiac Nox4 could attenuate the symptoms (Kuroda et al., 2010). Compared to other Nox homologues, it is suggested that 90% of its Nox4 product is H_2O_2 (and 10% is O_2^-). A high percentage of H_2O_2 from Nox4 is possibly because it only employed one oxygen molecule at a time and that the oxygen was reduced twice sequentially, producing O_2^- and H_2O_2 respectively (Nisimoto et al., 2014). Previous research studies have suggested that H_2O_2 can activate eNOS and promote NO bioactivity through phosphorylation of Ser1177 and dephosphorylation of Thr495 (Thomas, Chen & Keaney, 2002). However, in the long term, the phosphorylation of Ser1179 (a bovine equivalent to human Ser1177) of eNOS would significantly drop due to the inhibited activation of Akt by 5' adenosine monophosphate-activated protein kinase (Hu et al., 2008). Therefore, Nox4 plays a comprehensive role in the development of cardiovascular diseases.

1.3.4 Nox5

The noted regulatory mechanism underlining the pathological features of Nox5 is its sensitivity towards calcium (Ca^{2+}). The ischemic structure of Nox5 is shown in **Figure 1.7**.

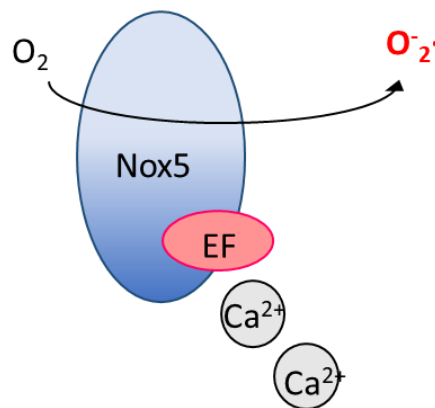


Figure 1. 7 The schematic presentation of the structure of Nox5.

At the N-terminus, Nox5 contains four EF-hand motifs, and their oxidation was linked with a reduced association with calcium and change in the tertiary structure of Nox5 (Petrushanko et al., 2016b).

During atherogenesis, the concentration of Ca^{2+} in vessels is elevated. Therefore, atherosclerosis is linked to the increased activation and misregulation of Nox5. As an example, in human coronary artery disease, it was observed that the Nox5 expression is significantly upregulated in the endothelium (early coronary lesions) and smooth muscle layer (advanced coronary lesions) (Guzik et al., 2008). Table 1.1 summarises different Nox isoforms that were discovered in the human cardiovascular system and their functional mechanisms.

Table 1. 1 Isoforms of NADPH oxidase and their functional mechanisms.

Isoform	Homology to Nox2	Expression	Regulatory Subunits	Subunit	References
Nox1	56	endothelial cells (ECs) and VSMCs	p22 ^{phox} , p47 ^{phox} , Noxo1, p67 ^{phox} , Noxa1 and Rac1	<p>p22^{phox}: stabilisation and maturation;</p> <p>p47^{phox} and its homologue Noxo1: organisers mediating with Noxa1 through tyrosine kinase substrate with four or five SH3 domains (Tks4 or Tks5);</p> <p>Noxa1: activator, mediating with p47^{phox} or Noxo1 through SH3 domain;</p> <p>Rac: interacting with Noxa1</p>	<p>(Gianni et al., 2009; Yu, Zhen & Dinauer, 1997)</p> <p>(Miyano et al., 2006)</p>
Nox2 (gp91)	-	ECs and fibroblasts in adventitia	p22 ^{phox} , p47 ^{phox} , p67 ^{phox} , p40 ^{phox} and Rac1/Rac2	<p>p22^{phox}: stabilisation and maturation;</p> <p>p47^{phox}: binds to the PRR on p22^{phox}; p67^{phox}: activation and this requires the participation of p47^{phox}; Rac: first step of electron transferring i.e. from NADPH to</p>	<p>(Mankelov et al., 2004)</p> <p>(Raad et al., 2009)</p> <p>(el Benna et al., 1994)</p> <p>(Matono et al., 2014)</p>

				Nox2-bound-FAD	
Nox4	39	cardiac myocytes, VSMCs, ECs and fibroblasts in the adventitia	p22 ^{phox} and POLDIP2	p22 ^{phox} : stabilisation and maturation; POLDIP2: p22 ^{phox} binding partner, enhancing the Nox4 activity	(Cheng et al., 2001) (Drummond et al., 2011) (Lyle et al., 2009) (Miller, 2009)
Nox5	27	VSMCs and ECs	-	Four EF-hand motifs: Nox5 activation through the interaction with Ca ²⁺ . Oxidation of cysteine and methionine on EF-hand motifs inhibit Nox5 by reducing the binding of Ca ²⁺ and the formation of the secondary and tertiary structure of Nox5 molecule.	(Banfi et al., 2001) (Petrushanko et al., 2016a)

1.4 Nox2 structure and its activation

Nox2, also known as gp91^{phox}-containing NADPH oxidase, was discovered in phagocytes and is historically the first characterised NADPH oxidase in the Nox family (Bedard & Krause, 2007; Dinauer et al., 1989). As other Nox homologous share certain similarities with Nox2, discussing and studying the regulatory mechanism of Nox2 could facilitate the understanding of the Nox family. Nox2 is a transmembrane protein stabilised by p22^{phox}. Embedded in the cytoplasmic membrane, gp91^{phox} is hydrophobic and has six transmembrane α -helices on which four conserved histidines play a vital role in proton-conducting and heme-binding (Mankelow et al., 2004). When it is

activated, it functions by transferring an electron from NADPH to oxygen and eventually producing O_2^- in cooperation with cytosolic subunits including $p40^{phox}$, $p47^{phox}$ and $p67^{phox}$. It has a flavoprotein domain that has FAD/NADPH binding site on its C terminus and is phosphorylated upon its activation by protein kinase C (PKC), which would increase its diaphorase activity which catalyses the reduction of di- and tri- phosphopyridine nucleotides would occur and a hydrogen ion would be formed (Shimosegawa & Toyota, 1994), and the binding to other functioning compartments including Rac, $p47^{phox}$ and $p67^{phox}$ (Raad et al., 2009). The activation domain on $p67^{phox}$ (amino acid 199-210) is essential during its activation (Han et al., 1998) and this requires the participation of $p47^{phox}$, which binds to the PRR on $p22^{phox}$, and thus $p67^{phox}$ can approach and associate stably to Nox2 (Bey & Cathcart, 1999). Rac, which is important in the first step of electron transfer, i.e. from NADPH to $gp91^{phox}$ -bound-FAD, interacts with $gp91^{phox}$ on the region of residue 419-430 (Matono et al., 2014). **Figure 1.8** illustrates the translocated of $p40^{phox}$, $p47^{phox}$ and $p67^{phox}$ during the activation of Nox2.

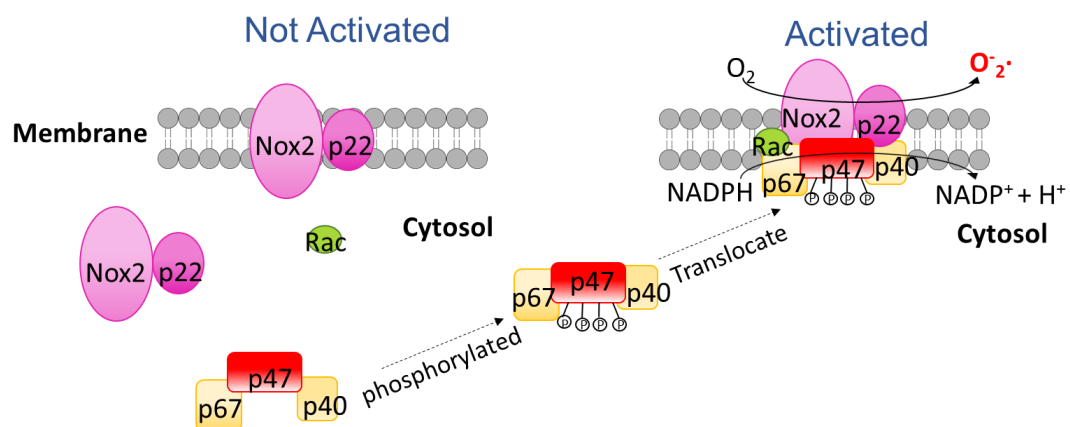


Figure 1. 8 Schematic diagram of the translocation of Nox2 regulatory subunits (p40^{phox}, p47^{phox} and p67^{phox}) during the activation of Nox2.

1.4.1 Nox subunits

Several regulatory subunits involved in the activation of Nox enzymes and targeting the regulatory subunits is one of the effective ways to modulate the function of Nox (Bouin et al., 1998; Bokoch & Diebold, 2002; Li et al., 2002). p47^{phox} is discussed in detail since it is the focus of this study.

1.4.1.1 Rac

Rac1 and Rac2 both belong to the Rho small guanosine triphosphatase (GTPase) family. In Nox homologous, Rac1 has been identified to interact with Nox1, Nox2 and Nox3 while Rac2 was only discovered during the activation of Nox2 (Drummond et al., 2011). During its inactivated state, Rac forms a heterodimeric complex with Rho GDP dissociation inhibitor (GDI). Rac was found to be stabilised through GDI, and upon induction of phosphoinositides, the interaction between Rac and GDI/GDP went through conformational changes thus Rac was able to contact p67^{phox}, the co-effector of Rac (Di-Poi et al., 2001).

1.4.1.2 p22^{phox}

p22^{phox} was discovered to be associated with gp91^{phox} in a 1:1 manner, and together they form a functional transmembrane unit of NAPDH oxidase called flavocytochrome b₅₅₈ (Yu et al., 1999). As studies accumulate, including Nox2, p22^{phox} has also been confirmed to work together with Nox1, Nox3, Nox4, Duox1 and Duox2 (Groemping & Rittinger, 2005). On its N terminus there discovered three transmembrane α -helices, and this locates p22^{phox} on the cell membrane. It has a proline-rich region (PRR) region (residue 151-160) on its C terminus, and it has been

suggested to interact with the two tandem SH3 domains on p47^{phox}. This process has been proved to be essential in the function of NADPH oxidase (Nobuhisa et al., 2006). To achieve the interaction between p22^{phox} and p47^{phox}, phosphorylation of p22^{phox} occurs in two forms. One is through phospholipase D and other through PKC (Regier et al., 2000). Phosphorylation through stimuli has been proved to happen on threonine residues (Thr132 and Thr147) (Groemping & Rittinger, 2005).

1.4.1.3 p40^{phox}

The structure of p40^{phox} is illustrated in **Figure 1.9**.

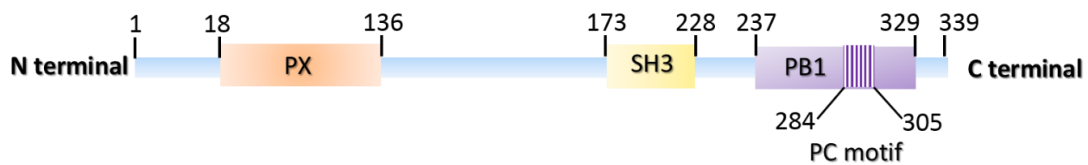


Figure 1. 9 The structure of the functional elements of p40^{phox}.

p40^{phox} consists of 339 amino acids. There is one PX domain (18-136), one SH3 domain (173-228) and one PB1 domain (237-329) which includes a PC motif (284-305).

There is a PX domain (residues 18–136) at its N-terminus, which contains a pocket formed by a lining of basic residues and specifically binds to PtdIns(3)P, a lipid product of PI3Ks (Bravo et al., 2001). In neutrophils, the binding of PI(3)P to PX of p40^{phox} is essential during the assembly of NADPH oxidase complex consisting of cytochrome b₅₅₈ (formed by p22^{phox} and gp91^{phox}) and cytosolic factors (Rac, p40^{phox}, p47^{phox} and p67^{phox}) during the activation of NADPH oxidase and production of ROS (Ellson et al., 2001). Because of this, p40^{phox} has been described as the activator of NADPH oxidase.

However, it also displays the function as an inhibitor through its Src homology 3 (SH3) domain (residues 173-228). Studies showed that SH3 domain of p40^{phox} is

associated with the downregulation of NADPH activity through its binding to PRR on p47^{phox}, the same region that also binds competitively to the SH3 domain of p67^{phox} upon activation (Sathyamoorthy et al., 1997). However, the relationship between these two interactions is not yet clear.

p40^{phox} also has a PB1 domain (residue 237-329) (Groemping & Rittinger, 2005), on which there is a PC motif (residues 284-305) (Lapouge et al., 2002). Since PB1 domain and PC motif form specific dimers through binding sites on the ubiquitous site (Yoshinaga et al., 2003), this motif interacts with the PB1 domain of p67^{phox} ubiquitously, and this might have stabilised p40^{phox} during the resting state of NADPH oxidase since it lacks auto-inhibitory mechanism.

1.4.1.4 p67^{phox}

The structure of p67^{phox} is shown in **Figure 1.10**.

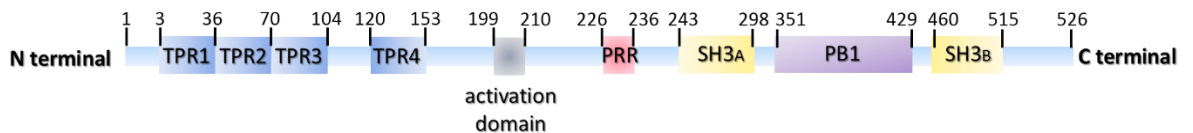


Figure 1. 10 The structure of the functional elements of p67^{phox}.

p67^{phox} consists of 526 amino acids. There are three TPR domains (3-36, 36-70, 70-104 and 120-153), one activation domain (199-210), one PRR (226-236) two SH3 domains (243-298, 460-515) and one PB1 domain (351-429).

At its N terminus, there are four TPRs (residues 3-36, 36-70, 70-104 and 120-153), and they are located within RacI GTP binding region (Ponting, 1996). Specifically, at the presence of GTP, the binding site of Rac was shown to be created by the loop region linking TPR1 and TPR3 at the edge of TPR bundle thus the assembly of cytosolic compartments and Rac could be achieved. Instead, the real TPR groove

was suggested to be in contact with C terminal of the molecule by masking its C terminal phosphorylation site and might have contributed to the auto-inhibition of the molecule when NADPH oxidase is not activated (Lapouge et al., 2000). Interestingly, research also discovered that p67^{phox} has the function of NADPH dehydrogenase activity thus might participate directly in the electron transport chain (Dang, Babior & Smith, 1999).

There also is an activation domain on p67^{phox} (residue 199-210) that has been confirmed to be critical for the function of NADPH oxidase and the production of O₂- in cell-free systems since it directly regulates the electron flow between NADPH and FAD thus controls redox status of flavocytochrome b₅₅₈ (Han et al., 1998; Han & Lee, 2000).

Residue 226-236 is the PRR domain which interacts with the two SH3 domains of p47^{phox}, contributing to the inhibition of p67^{phox} functioning under inactivate status.

Further to its C terminus, there are two SH3 domains (residue 234-298 and residue 460-515). Interestingly, the first SH3 domain is believed by some scientists to increase the affinity with gp91^{phox} but not Nox2 or Nox3, despite their high level of homologues (Maehara, Miyano & Sumimoto, 2009). The second SH3 domain is interacting with the PRR of p47^{phox} directly in two orientations upon the activation of NADPH oxidase (Finan et al., 1996). However, some studies using transfected cells emphasise the importance of the presence of both SH3 domains in terms of the membrane-binding ability and translocation of cytoplasmic components (de Mendez et al., 1994). In between the two SH3 domains, there is a PB1 domain (residue 351-429) that interacts specifically with other PB1 domain on p40^{phox} and stabilise the molecule.

1.4.2 p47^{phox}

p47^{phox} is the organising and coordinating unit of Nox2 enzyme. During the activation of Nox2, it translocates from the cytosol to approach Nox2 through the binding to p22^{phox} thus the cytosolic components, i.e. p40^{phox}-p47^{phox}-p67^{phox} can activate Nox2 (El-Benna et al., 2009). The structure of p47^{phox} and the animal models used for the study of p47^{phox} are reviewed here.

1.4.2.1 Structure of p47^{phox} functional domains

As is shown in **Figure 1.11**, amino acid (AA) sequences of p47^{phox} from many different species share high similarities. For example, p47^{phox} AA sequences from human (*Homo sapiens*) and mouse (*Mus musculus*) have an identity of 81.84%. Here the structure of p47^{phox} discussed is based on human p47^{phox} *in vitro* studies, but it is also able to be extrapolated to most studies discussed here.

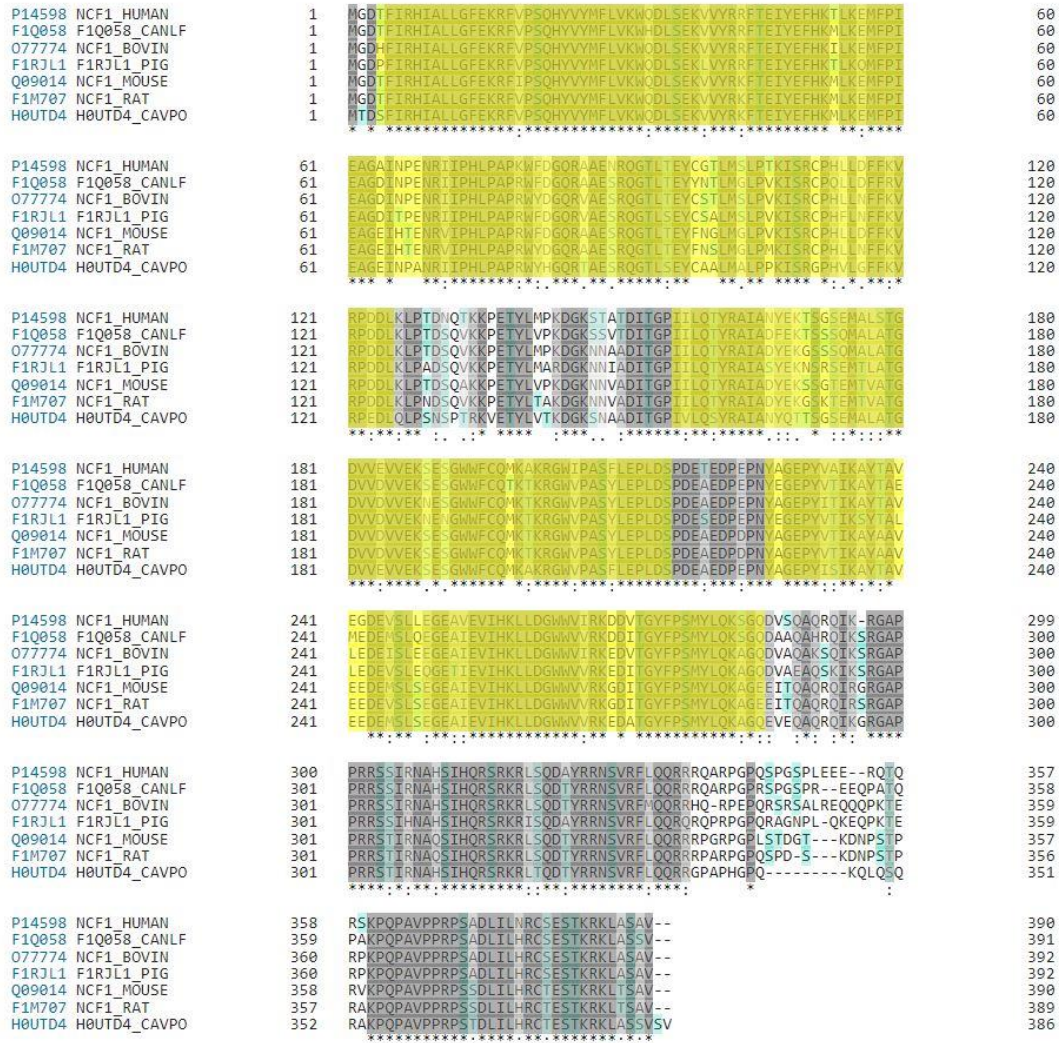


Figure 1. 11 A multiple-sequence alignment in p47^{phox} of different species.

A multiple-sequence alignment in p47^{phox} of different species. Abbreviations and GenBank Accession Numbers: Homo sapiens (Human): P14598; Canis lupus familiaris (Dog): F1Q058; Bos taurus (Bovine): O77774; Sus scrofa (Pig): F1RJL1; Mus musculus (Mouse): Q09014; Rattus norvegicus (Rat): F1M707; Cavia porcellus (Guinea pig): H0UTD4. Functional domains are highlighted in yellow. Serine threonines are highlighted in cyan. Same sequences among all the aligned species are highlighted in grey. The alignment data indicate that the functional domains of p47^{phox} are highly conserved in different species. Sequences aligned from UniProt (UniProt, 2019).

p47^{phox} includes several functional domains, an NH₂ (N)-terminus and carboxyl (C)-terminus, a PX domain, two tandem SH3 domains, one arginine/lysine-rich region

and one PRR (Mizuki et al., 2005). From AA 4-121, it is a PX domain. The two pockets formed by this domain is discovered to be phosphoinositide-binding sites for PtdIns(4)P and PtdIns(3,4)P₂ (Karathanassis et al., 2002). Similarly, p40^{phox} also has a PX domain (AA 18-136), but it binds to PtdIns(3)P. The difference was suggested to be associated with each protein's preference to different types of membranes, i.e. PX domain prefers PtdIns(3)P, locates the protein (in this case, p40^{phox}) to the endosomes while PX domain binding to PtdIns(4)P and PtdIns(3,4)P₂ (on p47^{phox}) tends to direct the protein to the plasma membrane (Ago et al., 2001; Zhou et al., 2003). In addition, PX domain on p47^{phox} could also interact intramolecularly with its C terminal SH3 domain (AA 229-284) to maintain a closed state thus reducing its affinity to the membrane. When p47^{phox} is activated, phosphorylation on Ser (303, 304, 328, 359, 370) Glu facilitates the opening of the molecule (Karathanassis et al., 2002). From AA 159 to 214 and 229 to 284, there are two tandem SH3 domains (here defined as N terminal SH3A and C terminal SH3B). When p47^{phox} is activated, whilst SH3A facilitates the translocation of the cytosolic subunits to the membrane through interaction with a PRR (AA 151-160) on p22^{phox} (deMendez, Homayounpour & Leto, 1997; Huang & Kleinberg, 1999; Nobuhisa et al., 2006), SH3B interacts with PRR on p67^{phox} mediating the translocation of p67^{phox}-p47^{phox}-p40^{phox} complex to the relevant membrane (deMendez et al., 1996; deMendez, Homayounpour & Leto, 1997; Nobuhisa et al., 2006). Under the resting state, the SH3 regions are inhibited by an arginine/lysine-rich region (also known as an auto-inhibitory region (AIR)) from AA 301–320 and 314–335 through GAPPR sequence which holds the intramolecular SH3 domains by recognising reverse sequences (Yuzawa et al., 2004). During the activation of Nox2, C-terminus of p47^{phox} and several AA between two tandem SH3 domains, i.e. Asp-217, Glu-218 and Glu-223 is phosphorylated, resulting in SH3A domain becoming unmasked (Huang &

Kleinberg, 1999; Peng et al., 2003). PRR (AA 363-368) is the other functional and structural region of p47^{phox} which functions by interacting with the c-terminal SH3 domain of p67^{phox} during Nox2 activation (Mizuki et al., 2005). When Nox2 is inactive, this PRR region is occupied by the SH3 domain on p40^{phox} (AA 173-228). Thus, the p67^{phox}-p47^{phox}-p40^{phox} complex is maintained in a stable state in the cytosol (Wilson et al., 1997; Sathyamoorthy et al., 1997). The interactions between SH3 domains and PRR on cytosolic regulatory compartments of Nox2 (p47^{phox}, p40^{phox} and p67^{phox}) are shown in **Figure 1.12**.

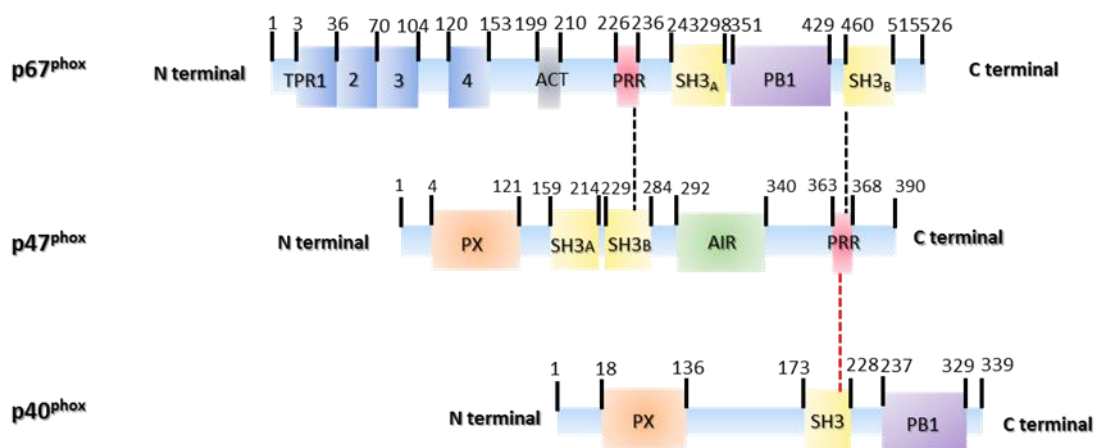


Figure 1. 12 A schematic of interactions between p67^{phox}, p47^{phox}, and p40^{phox}.

A schematic of interactions between p67^{phox}, p47^{phox}, and p40^{phox}. Structural domains and their reported amino acid sites are marked. Reported interactions among these three regulatory subunits of Nox2 are shown in dotted lines. Black: Interactions when Nox2 is activated. Red: Interactions when Nox2 is inactivated.

1.4.2.2 Current p47^{phox} transgenic murine models

Murine models with deficient p47^{phox} are immune-compromised and are associated with a genetic disease in human called CGD. Currently, there are two different ways of targeting p47^{phox} and three p47^{phox}KO transgenic murine models used worldwide and are available from Jackson Laboratory. The model that has been widely

used in cardiovascular studies is called B6N.129S2-Ncf1^{tm1Shl}/J (we define it as p47^{phox}KO 129sv-C57BL/6 in this study). The vector was designed to include a neomycin resistance cassette interrupting amino acid 221 on exon 7 of the neutrophil cytosolic factor 1 (Ncf1, gene name for p47^{phox}) gene. The construct was then electroporated into D3 embryonic system cells with a 129sv background and bred from C57BL/6 female mice (Jackson, Gallin & Holland, 1995). The experimental disease models were typically set up after at least ten generations backcross to C57BL/6J WT. The other model was developed based on an A to C mutation at -2 position at the 5' end of exon 8, and this was able to induce abnormal splicing of Ncf1 transcript. This mutation was reported to arise from B6.BKS(D)-Lepr^{db}/J in the Jackson Laboratory (Huang et al., 2000) and was crossed back to C57BL/6J for three generations before use. We define this model as p47^{phox}KO (Doerries et al., 2007) Cg-C57BL/6 in this study. The other strain with the same mutation is NOD.Cg-Ncf1^{m1J}/MxJ with NOD/SHiLt background. As yet, to the best of personal knowledge, NOD.Cg-Ncf1^{m1J} model has not been used for the investigation of cardiovascular diseases, as is summarised in Table 1.2. Studies using p47^{phox}KO transgenic models relevant to the cardiovascular system discussed in this review are listed in **Table 1.2**.

Table 1. 2 p47^{phox}KO studies on mediating cardiac functioning and redox signalling pathways.

Strain	Disease Model	Signalling	Role of p47 ^{phox}	Reference
129sv-C57BL/6	LAD-CAL	-	increase survival rate (72% in p47 ^{phox} KO versus et al., 48% in WT; P<0.05)	(Doerries 2007)
129sv-C57BL/6	TAC	PO-Ang-ACE2 or PO-Ang-AT1R-p47 ^{phox} -MMP	compensate for ACE2KO	(Bodiga et al., 2011)
129sv-C57BL/6	AngII induced hypertrophy	AngII-p47 ^{phox} -TNF α converting enzyme (TACE)-suppression of ACE2	resistant to AngII-induced TACE phosphorylation	(Patel et al., 2014)
129sv-C57BL/6	Langendorff perfusion	PI3K α (but not PI3K γ) and PKC-GSK3	no different changes in inotropic action	(Liang et al., 2010)

129sv-C57BL/6	TAC	p47 ^{phox} interacting with cortactin and N-cadherin- loss of actin polymerisation and cytoskeletal remodelling	markedly worsen systolic dysfunction	(Patel et al., 2013)
129sv-C57BL/6	SMCs isolated and stimulated with AngII	AngII-AT1R-p47 ^{phox} -Nox2-MMP2	mediate AngII-induced MMP2 expression and activation	(Luchtefeld et al., 2005)
129sv-C57BL/6	CMECs isolated and stimulated with PMA or TNF α	PMA or TNF α -p47 ^{phox} -Nox2	mediate PMA or TNF α stimulated Nox2 activation; KO induce O ₂ ⁻ production	(Li et al., 2002)
129sv-C57BL/6	CMECs isolated and stimulated AngII	AngII-p47 ^{phox} phosphorylation-p47 ^{phox} -p22 ^{phox} formation-Nox2	mediate AngII stimulated Nox2 activation; KO induce O ₂ ⁻ production	(Li & Shah, 2003)
129sv-C57BL/6	CMECs isolated	p40 ^{phox}	p47 ^{phox} KO increases p40 ^{phox} expression and ROS production	(Fan, Teng & Li, 2009)
129sv-C57BL/6	aortae isolated and stimulated AngII	AngII-O ₂ ⁻ production-vasoconstriction and increased MAPK p38/ERK1/2/JNK activity	p47 ^{phox} KO increases ROS production and MAPK p38/ERK1/2/JNK activity, but AngII stimulation in KO was not able to increase the effect	(Li et al., 2004)
Cg-C57BL/6	MA-induced neurotoxicity	ERK-p47 ^{phox} -mitochondria stress-M1 of microglia	protect the signalling induced by MA	(Dang et al., 2016)
Cg-C57BL/6	HFD	increased TFAM and UCP2; reduced PPAR α , CD36, Pref-1	reduce the increase in adiposity	(Ronis et al., 2013)
Cg-C57BL/6	endothelium-denuded aortic rings treated with 100 nM U46619, and 10 μ M PDBu	PKC-p47 ^{phox} -Nox2-reduced NO or PKC-Src-p47 ^{phox} -Nox2-reduced NO or PKC-Rho and CaMIIK-contraction	mediate vasoconstriction response	(Gupte et al., 2009)

Role of p47^{phox} in mediating cardiac functioning and redox signalling pathways studied using p47^{phox}KO murine models. For disease models: LAD-CAL: left anterior descending (LAD) coronary artery ligation. TAC: transverse aortic constriction. MA: methamphetamine. HFD: high-fat diet.

1.5 p47^{phox} signalling in cardiac disorders

1.5.1 p47^{phox} signalling in apoptosis

Many CVDs, including diabetic cardiomyopathy, MI, heart failure and myocardial remodelling and dysfunction, are closely related to cardiomyocyte apoptosis. Various studies have indicated the significant role of ROS generated by p47^{phox}-regulated Nox2 in mediating apoptotic pathways (Pimentel et al., 2001). For example, following experimental MI, p47^{phox} KO mice displayed less severe left ventricle dilation and dysfunction when compared to the WT, although similar

infarction size was observed in both groups. These attenuated symptoms were suggested to have been benefited from the reduced activities of Nox2 and XO, which are known to cause cardiomyocyte hypertrophy and apoptosis (Doerries et al., 2007).

In vivo and *in vitro* studies also investigated in detail p47^{phox} mediated redox-sensitive apoptotic signalling pathways. Under conditions such as hyperglycaemia (Tsai et al., 2012), ischaemia-reperfusion (Kimura et al., 2005b), and during a high level of homocysteine (Sipkens et al., 2011) or AngII, p47^{phox}-mediated O₂⁻ could directly increase and activate various downstream signalling molecules including inhibitor of kappa-light-chain-enhancer of activated B cells, JNK and MAPK pathways (but not Raf/MEK/ERK1/2 pathway). These activated signalling pathways trigger the phosphorylation and nuclear translocation of nuclear factor kappa-light-chain-enhancer of activated B cells (NFκB) and activator protein 1, resulting in the decreased gene expression of the anti-apoptotic Bcl-2 while increased expressions of pro-apoptotic p53 and Bax (Maulik et al., 2000). These would ultimately lead to Caspase-3 cleavage and the apoptosis induction. Additionally, upregulation of other pro-apoptotic factors such as caspase-8 by activated p47^{phox} (or p47^{phox} regulated O₂⁻ in hepatocyte (Reinehr et al., 2005), cytochrome c release from mitochondria through ERK1/2 pathway in microglia (Dang et al., 2016), apoptosis-regulating signal kinase (ASK) 1 and p38MAPK during tuberculosis (TB) infection (Yang et al., 2008), and poly (ADP-ribose) polymerase (PARP) in bronchial epithelial cells (Peng et al., 2017) and GSK3β signalling pathway (Yu et al., 2016) have been observed. However, whether p47^{phox} in cardiac diseases activates similar downstream apoptotic molecules remains unanswered.

Research studies have also demonstrated that during homocysteine (Sipkens et al., 2011) or AngII (Qin et al., 2006)-induced cardiomyocyte apoptosis, there is an

increased level of intracellular oxidative stress generated by p47^{phox} in the nuclear envelope. The elevated level of ROS was correlated with an increased expression of gp91^{phox} and p22^{phox} at the nuclear pore complex (Hahn et al., 2011). This contributed to the inactivation of phospholipids flippase, which could induce membrane flip-flop during apoptosis (Sipkens et al., 2007). Moreover, since activator protein 1 and NFκB are redox-sensitive (Maulik et al., 2000), p47^{phox} mediated O₂⁻ in nuclei rather than O₂⁻ generated in cytosol might play a crucial role in directly activating these transcription factors. Studies have shown that p47^{phox} can also indirectly promote apoptosis. For example, prolonged endoplasmic reticulum stress has been suggested to reduce Bcl-2/Bax ratio leading to apoptosis in an intrinsic pathway where the mitochondria oxidise Ca²⁺/calmodulin-activated kinase II in cardiomyocyte (Roe & Ren, 2013). During this process, there is increased p47^{phox} expression as well as endoplasmic reticulum stress (Donaldson et al., 2009) linked a reduced level of survival due to a defect in the intrinsic apoptotic pathway in p47^{phox}KO mice in the lymphocyte, suggesting a role of p47^{phox} playing in this process. At the same time, some cell deaths are p47^{phox}-independent. One study on industrial ZnO toxicity induced apoptosis to bone marrow-derived macrophages showed no significant change of ZnO uptake or formation of hypodiploid DNA between WT and p47^{phox}KO mice (Wilhelmi et al., 2013). However, the independent role of p47^{phox} in mediating apoptosis in the heart remains to be studied.

1.5.2 p47^{phox} signalling in cardiac pathological hypertrophic growth

Hypertrophic cardiomyopathy is defined as pathological cardiac hypertrophy *in vivo* or a cardiomyocyte hypertrophic growth *in vitro* (Carreno et al., 2006). It is a maladaptive pathological condition of cardiomyocyte which occurs in response to many CVDs including hypertension (Wang et al., 2017), diabetic cardiomyopathy (Eguchi et

al., 2008), recovery from MI or heart failure (Heinzel et al., 2015), and myocardial ischaemia (Dunn & Pringle, 1987), which exert hemodynamic stress to the myocardium. (Frey et al., 2004; Tardiff, 2006) distinguished it from physiological cardiac hypertrophy such as an athlete heart, which is an adaptation of the myocardium to growth signals. Morphologically, pathological hypertrophy tends to display a more severe myocardial wall thickening with collagen accumulation which is accompanied by cardiac fibrosis (Frey et al., 2004). Despite few genes such as atrial myosin light chain 1 increased in both hypertrophic conditions, many genes regulating pathological hypertrophy were found to decrease after endurance exercise training in rats (which could also trigger athlete heart) (Diffie et al., 2003), suggesting the differences between two types of hypertrophy. Here we will focus on pathological cardiac hypertrophy.

There is evidence that p47^{phox}-regulated Nox2 is a major source of O₂⁻ in AngII (Bendall et al., 2002; Polizio et al., 2008) or pressure overload-induced left ventricle hypertrophy. The oxidative stress generated could activate ERK 1/2, ERK5, JNK 1/2 and p38MAPK (Li et al., 2002) that could lead to hypertrophic growth. In diabetic cardiomyopathy, hypertrophic growth was accompanied by enhanced oxidative stress along with elevated expression of p47^{phox} and gp91^{phox} (Yu et al., 2012). Inhibiting Nox2 activity by targeting p47^{phox}, where there was enhanced necrosis was able to attenuate pressure overload-induced cardiac hypertrophy (Cao et al., 2017). Treatment with amlodipine and atorvastatin could reduce cardiac hypertrophy by reducing p47^{phox} expression level and O₂⁻ (Lu et al., 2009). Moreover, p47^{phox}KO mice displayed a reduced level of hypertrophy after experimental MI (Doerries et al., 2007) when compared to WT. Genetic ablation of p47^{phox} is also able to rescue the hypertrophy in AngII converting enzyme 2 (ACE2) KO mice in response to PO (Bodiga et al., 2011). Studies in mice have also suggested that KO of p47^{phox} is able to downregulate the

activity of TNF α converting enzyme (TACE2) induced by two-week AngII infusion, by suppressing ACE2 activity via cleaving and shedding, which reduced the development of cardiac hypertrophy (Patel et al., 2014). However, the downregulation of p47^{phox} expression does not always necessarily result in a reduction of cardiac hypertrophic growth. For instance, when p47^{phox} expression is reduced by COX-2 inhibitors such as acetylsalicylic acid, rofecoxib and nimesulide, only rofecoxib was able to attenuate the development of AngII-induced cardiac hypertrophy (Wu, Laplante & de Champlain, 2005). Therefore, p47^{phox} may participate (either by generating O₂- or alone) in more than one pathological pathway during cardiac hypertrophy. A study conducted by Ronis et al., 2013 showed an increased expression of genes related to hypertrophic cardiomyopathy such as in adipose tissue of p47^{phox}KO mice compared to WT on a high-fat diet. No difference was observed between p47^{phox}KO and WT mice on normal control diet (Ronis et al., 2013).

The redox-sensitive signalling pathways involved with p47^{phox} have also been investigated by many *in vitro* studies. One such pathway involved is Ca²⁺ sensitive calcineurin/nuclear factor of activated T-cell. Calcineurin inhibitors, such as cyclosporine A and FK506, showed different effects on treating cardiomyocyte hypertrophic growth (Leinwand, 2001) and the mechanism in inducing hypertrophy is not yet clear. Studies showed Calcineurin mediated hypertrophy through interaction with muscle atrophy F-box in the z-disk of cardiomyocyte (Li et al., 2004) and via activation of nuclear factor of activated T-cells (NFAT), antagonising against p38MAPK and JNK pathways (Molkentin, 2004). More importantly, the activation of NFAT was demonstrated to be induced through p47^{phox}-regulated Nox2 in response to Ca²⁺ signals. In addition, it could also be inhibited by Nox2 inhibitors and shRNA against p47^{phox} (Gul et al., 2012). Studies have shown that the PI3K/Akt pathway is

involved in preventing cardiac hypertrophy. Amongst its subunits, PI3K α was demonstrated to eliminate AngII-induced adverse inotropic action (Liang et al., 2010). Even though in mice, the activation of NADPH oxidase was downstream of PI3K and that p47^{phox} is phosphorylated by phosphatidylinositol (3,4,5)-trisphosphate (PIP₃) in the microglia (Zhang et al., 2011), p47^{phox} KO did not change the effect of AngII in the cardiomyocytes (Liang et al., 2010).

Another redox-sensitive signalling pathway is mediated through serotonin 5HT_{2B} receptor (5HT-2_BR). Under pathological conditions, lack of 5-HT_{2B}R expression could lead to mitochondria defects and dilated cardiomyopathy, while the over-expression of 5-HT_{2B}R could induce mitochondria hyper-functioning and cardiac hypertrophy (Nebigil & Maroteaux, 2003). While both 5-HT_{2A}R and 5-HT_{2B}R are expressed in cardiac fibroblasts, 5HT-2_BR is more extensively studied as the commercially available antagonists have a higher affinity to this receptor (Jaffre et al., 2004). Interestingly, it has been shown that AngII and isoproterenol-induced cardiac hypertrophy involves the increase in p47^{phox} expression along with the activation of 5-HT_{2B}R. While blocking 5-HT_{2B}R reduced the hypertrophic effect, but it did not change the p47^{phox} expression level. In addition, Nox2 KO also could not inhibit isoprenaline-induced hypertrophy (Monassier et al., 2008). These results suggested that 5-HT_{2B} did not regulate the p47^{phox} expression level and that the hypertrophy induced by 5-HT_{2B}R was p47^{phox} independent.

1.5.3 p47^{phox} signalling in cardiomyocyte survival

As discussed in section 1.5, for a long time, p47^{phox}-regulated Nox2 in the mammalian heart had been intuitively identified as a contributor to pathological cardiac conditions. Based on these, the contribution of p47^{phox} to cardiomyocyte survival when

there was only mild ROS generation has been largely neglected. Although there has not been much research, some signalling pathways are still worth discussing. One such signalling pathway is through CD29 (β 1-integrin). Activation of CD29 increases the oxidative stress level by upregulating Nox2 activity, which improves cardiomyocyte viability through MEK/ERK and PI3K/Akt pathways (Rosc-Schluter et al., 2012). This effect was reduced by loss-of-function of p47^{phox} or genetic ablation of gp91^{phox}.

p47^{phox}-regulated Nox2 also (at least in part) participates in mediating pro-survival pathways in ischemic preconditioning, an adaptive response that promotes cardiomyocyte survival by developing a protective mechanism against ischaemia-reperfusion injury. One example is that Bell et al., 2005 showed a failure of preconditioning protection against 2-cycle I/R in gp91^{phox} KO murine hearts, associated with a lack of Nox2 activity (Bell et al., 2005). The lack of preconditioning protection without gp91^{phox} indicated that Nox2 is required for cardiomyocyte survival after reperfusion injury. Also, the authors showed that during MI, 2-chloro-N⁶-cyclopentyladenosine (CCPA) (a ligand for A_{1A}R, regarded as being able to induce ROS-independent preconditioning) could trigger preconditioning with similar infarction size in WT and gp91^{phox}KO mice without any difference in Nox2 activity between the vehicle and CCPA treated groups (Bell et al., 2005). The ROS-independent preconditioning by CCPA agrees with the result from Ballard-Croft et al., who observed that antioxidant N-2-mercaptopropionyl glycine reduced H₂O₂ activation but not CCPA activated p38 MAPK. Additionally, there was a significant difference in the phosphorylation of p38 in the Triton-insoluble cytosolic membrane activated by H₂O₂ and CCPA (Ballard-Croft et al., 2008). The differences in the activation of MAPK by H₂O₂ and CCPA suggested A_{1A}R as an independent pathway to mediate preconditioning (Ballard-Croft et al., 2008). Studies have also shown A_{2A}R as a

potential mediator for p47^{phox} phosphorylation in response to adenosine (El-Awady et al., 2013). In murine lymph node microvascular endothelial cells (SVEC4–10), by targeting A_{2A}R with A_{2A}R antagonist adenosine deaminase or siRNA, it was able to decrease the upregulation of p47^{phox} phosphorylation induced by AngII stimulation (Thakur et al., 2010).

1.5.4 p47^{phox} signalling in coronary arterial endothelial dysfunction

Endothelial dysfunction is caused by the reduced availability of NO[•] in the endothelium. It has been found in many CVDs such as hypertension (Mita et al., 2005), diabetes (Guzik et al., 2002), MI (Boulanger et al., 2001) and hypercholesterolaemia (Sattler et al., 2006). Under these pathological conditions, endothelial dysfunction can contribute to more damage by causing other vascular problems such as imbalanced inflammation response (Yang, Chang & Wei, 2016), impaired vasoconstriction and vasodilation (Sandoo et al., 2010), dysregulation of anticoagulant properties that could lead to thrombosis (Yau, Teoh & Verma, 2015) atherosclerosis (Patti, Melfi & Di Sciascio, 2005), and abnormal vascular remodelling (De Ciuceis et al., 2005). The overactive Nox2 during pathological stresses such as diabetes (Guzik et al., 2002), atherosclerosis (Guzik et al., 2000), and hyperhomocysteinaemia (Ungvari et al., 2003) is linked with endothelial dysfunction. Under these conditions, the excessive O₂⁻ generated by Nox2 is not scavenged by NO (produced by eNOS) and thus initiates the redox-sensitive pathological pathways leading to development of CVDs.

For example, the use of SOD-mimetic tempol was able to reduce hypertensive-induced vasoconstriction through interaction with O₂⁻ and subsequently increasing the availability of NO without affecting p47^{phox} or eNOS expression under this condition (Christensen et al., 2007). As coronary artery has a high risk of atherosclerosis (Dodge

et al., 1992), here we focus our discussion on endothelial dysfunction-related coronary disorders.

The clinical and *in vivo* studies have demonstrated a close relationship between p47^{phox} and endothelial dysfunction. The vital role of gp91^{phox} and p47^{phox} was demonstrated in patients with stable coronary atherosclerosis by comparing the expression level of gp91^{phox} and p47^{phox} in epicardial adipose tissue (a 3-4 folds increase of p47^{phox} expression as compared to control patients), substernal fat and subcutaneous thoracic adipose tissue (where there were no significant differences in p47^{phox} expression as compared to controls) (Sacks et al., 2011). There is also significantly elevated translocation of p47^{phox} to the membrane and enhanced oxidative stress in human coronary artery endothelial cells (HCAEC) when treated with serum from diabetic patients, which could lead to the expression of E-selectin contributing to endothelial dysfunction (Yun et al., 2006). Studies also showed that the increased expression of p47^{phox} in hypercholesterolaemia was able to be attenuated by a healthy diet which, is in contrast to coronary epicardial vessels, the increased level of p47^{phox} in coronary arterioles could not be reduced by normal post hypercholesterolaemia diet, and thus could lead to enhanced oxidative stress and reduced vascular relaxation in these small vessels (Sattler et al., 2006).

Kobayashi et al. showed that in during early atherosclerosis p47^{phox} and other NADPH oxidase subunits such as gp91^{phox} and p22^{phox} (associated with c-Src and ERK1/2) could induce endothelial dysfunction by increasing the expression of vascular cell adhesion molecule-1. In contrast, through increased expression of eNOS by activating PI3K/Akt signalling pathway could reducing this effect (Kobayashi et al., 2003).

Also, p47^{phox} could activate matrix metalloproteinase-2 (MMP2) through Nox2, which contributes to plaque destabilization when there is an elevated level of AngII in the vessel (Luchtefeld et al., 2005). The enhanced level of p47^{phox} and gp91^{phox} along with reduced eNOS expression was able to be normalised by Rho-kinase inhibitor, Y-27632 (Mita, Kobayashi, Yoshida, Nakano & Matsuoka, 2005). However, it could be easily neglected that p47^{phox} also plays a cytoprotective role in HCAEC by mediating VEGF-stimulated activation of manganese superoxide dismutase (Mn-SOD), which contributes to the reduction of the oxidative stress by reacting with O₂⁻ and producing H₂O and oxygen. p47^{phox} functions through PKC-NFκB and PI3K-Akt-forkhead pathways and ablation of p47^{phox} using antisense oligonucleotides were able to eliminate this effect (Abid et al., 2004). Genetic ablation of p47^{phox} in both coronary microvascular endothelial cells (CMEC) isolated from p47^{phox}KO murine model (with a 129sv background) and CMEC from WT murine model transfected with p47^{phox} antisense can increase O₂⁻ production as compared to WT (Li et al., 2001; Li & Shah, 2003). However, they are not able to respond to stimulations such as phorbol-12-myristate-13-acetate (PMA), TNFα and AngII. Similar results were observed in venous SMCs studies (Chose et al., 2008). This upregulation in ROS production by the p47^{phox}KO CMEC was attributed to the enhanced expression of p40^{phox} as this was almost completely inhibited by p40^{phox} and p47^{phox} double KO (Fan, Teng & Li, 2009). Additionally, this is further partly supported by a study on phagocytes showing recovery of Nox2 activity when there is a fivefold increase in Rac2 and p67^{phox} (Diebold & Bokoch, 2001). Therefore, the enhanced O₂⁻ production in p47^{phox}KO models under basal conditions is also associated with upregulated activation of signalling molecules including ERK1/2, JNK and p38MAPK as shown in a study using p47^{phox}KO murine aortas (Li et al., 2004).

Considering the possibility of the independent role of Nox2 cytosolic subunits discussed above, it seems that there may be vital details missing regarding the mechanism underlining the mild increase of oxidative stress under healthy conditions.

1.5.5 Role of p47^{phox} in contractile dysfunction

Various studies have shown evidence that p47^{phox} is involved in cell contraction. In a study in 2009, the authors Gupte et al. demonstrated a significant role of p47^{phox}-regulated O₂⁻ in smooth muscle cell contraction through c-Src. They observed that gp91^{phox} KO and p47^{phox} KO reduced smooth muscle cell contraction by 50% and 40%, respectively (Gupte et al., 2009). Previously, they demonstrated that the stretch-induced contraction is mediated through c-Src-MEK-ERK but not p38MAPK or JNK pathways, and was attenuated by Nox2 inhibition using apocynin or diphenyleneiodonium (DPI) (Oeckler, Kaminski & Wolin, 2003). In contrast, studies have also demonstrated the SMC contraction by the activated p38MAPK through Nox2-derived ROS (Meloche et al., 2000). One possible reason is that the Nox2 regulatory subunits can also function independently of Nox2 mediated signalling pathways.

For example, it is observed that the p47^{phox} expression level in human vascular endothelial cells is similar to leukocytes. However, the p67^{phox} and gp91^{phox} expression levels are observed to be at reduced levels as compared to leukocytes (2.5% and 1.1% respectively of leukocytes expression levels) (Rueckschloss et al., 2001). Given that the p47^{phox} in phagocytes functions to remove microbes, and in other cell types such as microglia, p47^{phox} has been proven to be involved in the local immune response in the CNS (Wilkinson & Landreth, 2006), this strongly suggested that p47^{phox} (and to a less extent, p67^{phox}) might be playing a role in some other cellular functions in the cardiovascular system.

In 2013, p47^{phox} was demonstrated to play an independent role in interacting with cortactin in a study by (Patel et al., 2013), which showed that the loss-of-function of p47^{phox} could lead to systolic dysfunction during PO-induced biomechanical stress. In this study, it was shown that despite increased N-cadherin level, there was a disruption in the interaction between cortactin and N-cadherin ('mediated' deleted). In addition, there was also decreased focal adhesion kinase activation in p47^{phox}KO hearts subjected to transverse aortic constriction induced by pressure overload. Transverse aortic constriction in p47^{phox}KO mice did not develop adaptive cardiac remodelling and increased heart failure susceptibility because of disrupted actin filaments and cytoskeleton (Patel et al., 2013). Additionally, in this study, the interaction between p47^{phox} and cortactin was suggested to promote the translocation of p67^{phox}-p47^{phox}-p40^{phox} complex to the cell membrane or enhance the on-site activation of Nox2 intracellularly (Touyz et al., 2005).

Here we propose a model for the possible interaction between p47^{phox} and cortactin (**Figure 1.13**) based on the functional groups and interactions among p47^{phox}, p40^{phox} and p67^{phox}. As both cortactin and p47^{phox} can be phosphorylated by c-Src (Touyz, Yao & Schiffrin, 2003; Tehrani et al., 2007), there might be some regulatory mechanism more than just direct binding between p47^{phox} and cortactin through c-Src.

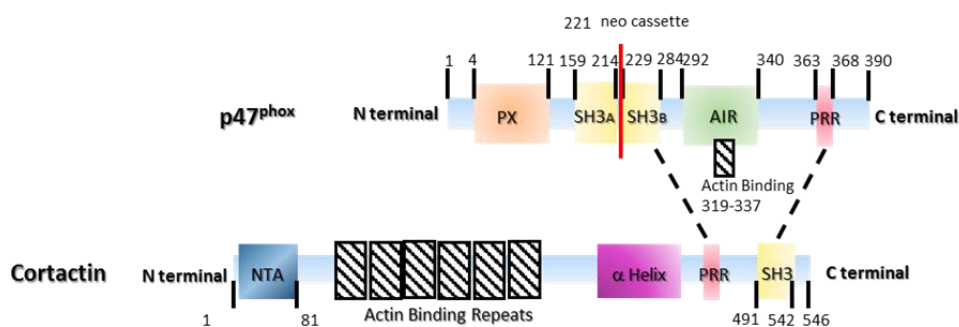


Figure 1. 13 A schematic of interactions between p47^{phox} and cortactin.

Structural domains and their reported amino acid sites are marked. Proposed possible interactions between p47^{phox} and cortactin based on the interaction among p67^{phox} and p47^{phox} are shown in black dotted lines. Genetic modification site in p47^{phox}KO model utilised by Patel et al. is shown in the red line.

c-Src could be activated through ROS generated by NADPH oxidases (Li et al., 2008) and could regulate many other redox-sensitive down-stream molecules such as connexin-43 (Sovari et al., 2011) and endothelin-1 (Manea, Fenyo & Manea, 2016) whose dysregulation contributes to maladaptive cardiac disorders. The regulatory mechanisms of connexin-43 and endothelin-1 by c-Src might be able to fill in the gap mentioned before that ERK, the one regulated by c-Src, but not p38, the one independent form c-Src, is involved in the mediation of SMC contraction. These findings suggested the interaction between p47^{phox} and other molecules and the independent role of p47^{phox} in other cardiac disorders.

p47^{phox} can also bind to other actin-associated proteins directly. Moesin can bind to phosphoprotein 50 (Wientjes et al., 2001), and is important in vascular ROS generation and pathogenesis of many cardiovascular diseases such as cardiac hypertrophy (Al Ghouleh et al., 2016). Coronin isoform 1A (Reeves et al., 2000) was discovered as a biomarker for acute cardiac allograft rejection (Kienzl et al., 2009) and isoform 1B was shown to participate in the development of the heart from the embryo (Hsu et al., 2013), expressing in endocardial cushion and epicardium. Cofilin-2 (Nagaishi et al., 1999) affects muscle contraction by changing the length of actin filaments (Kremneva et al., 2014). Despite the availability of the transgenic models, the effect of KO p47^{phox} in cardiac contractile functioning relating to these actin-filament-regulating proteins has not been studied in detail. To summarise, it is time to review

this long-term doctrine relating to Nox biology possibly by carrying out studies on the independent role of p47^{phox} and other regulatory subunits of Nox in a wide range of pathophysiological studies (not just restricted to cardiac functions).

1.6 Nox inhibitors and antioxidants

1.6.1 Small molecule inhibitors

One type of Nox inhibitors is small molecule inhibitors, and they were usually generated through high throughput screening. Conventional small molecules include DPI and apocynin, which are unspecific (Aldieri et al., 2008). However, DPI was discovered to be the most reliable in reducing O₂⁻ and H₂O₂ production in an *in vitro* study using different small-molecule inhibitors including DPI, apocynin, diapocynin, ebselen, AEBSF and VAS3947 since it could inhibit both oxygen consumption from Nox2 and Nox4 and oxygen generation from Nox2 and Nox5. However, DPI, as a flavoprotein inhibitor, might display unwanted effects such as inhibiting NOS (Stuehr et al., 1991; Szilagyi et al., 2016). In the early 1990s, ebselen was reported as an antioxidant to reduce the lipid peroxidation (Noguchi et al., 1992) in rat brain and liver homogenates and might have an effect in treating the inflammation-associated carcinogenesis (Nakamura et al., 2002). Yet ebselen was also suggested to be an H₂O₂ scavenger (Satheeshkumar & Muges, 2011) and displayed cytotoxicity even at low concentration *in vitro* (Augsburger et al., 2019). Another example is AEBSF, which was shown to inhibit the translocation of p47^{phox} and p67^{phox} (Diatchuk et al., 1997). However, it also inhibits many important endogenous hydrolase enzymes such as esterase, which is crucial in drug metabolism (Powers et al., 2002). The low specificity might be because the homologues of Nox share similar structures and regulatory subunits.

There are also some newly developed molecules, such as VAS2870 and VAS3947, Fulvene-5, Gkt136901, ML171 and Celastrol (Cifuentes-Pagano, Csanyi & Pagano, 2012). Since they were developed not long ago, future studies on their effect, specificity and toxicity are required.

One example that is worth mentioning is ML171, which was found from the endothelium of colon cancer where Nox1 expression was dominant. Its mechanism is not yet clear, and its specificity remained to be decided. ML171 was initially developed as a Nox inhibitor and was shown to inhibit 5-HT and adrenergic receptors (Altenhofer et al., 2015), a family of receptors that belong to GPCR family playing a part in neurotransmission. On the other hand, some studies suggested that its effect was only reversible by Nox1 overexpression, demonstrating its specificity of blocking the activity of Nox1 (Gianni et al., 2010). However, ML171 was also discovered to inhibit serine protease non-selectively (Powers et al., 2002) and was potentially a ROS scavenger (Teixeira et al., 2017). Therefore, future pharmacological studies are needed to determine and elucidate its mechanism and specificity. At the same time, despite the controversial findings at this stage, the potential of targeting Nox1 also needs more justification, based on the discussion from section 1.3 that Nox1, Nox2 and Nox4 share a relatively high level of homology structurally and these Nox homologues were all demonstrated to be involved in the development of different CVDs and that in many systems and organs, Nox1 is not the most expressed compared to Nox2 and Nox4. At the same time, one study looking at ten different molecules of phenothiazine family showed that even with very similar molecular structures, the inhibitory effect of these small molecules could be very much different. The effective inhibitors among these ten candidates are N-substituted phenothiazines such as thioridazine, prochlorperazine and perphenazine (Seredenina et al., 2015).

Treatment with apocynin or AEBSF could reduce the brain O₂⁻ level as detected by DHE fluorescence while treatment with tempol only reduced brain mitochondrial O₂⁻ as detected by DHR123 (Hwang & Kim, 2018).

1.6.2 Peptide-based inhibitors

Peptide-based NADPH oxidase inhibitors are designed for interrupting the protein-protein interaction, i.e. either the assembly of cytosolic components or the association of cytosolic components with the transmembrane subunits of Nox. Compared to small-molecule inhibitors, one advantage of peptide-based inhibitors is that they are able to target a specific Nox isoform. One example, Nox2ds-tat, which inhibits the association between Nox2 and p47^{phox}, by far has been proven to be the most effective and specific both *in vitro* and *in vivo* (Jacobson et al., 2003; Touyz et al., 2002). Its sequence in human Nox2 is [NH₃]-C-S-T-R-V-R-R-Q-L-[CONH₂] and was invented by (Csanyi et al., 2011) and was demonstrated the specificity of just targeting Nox2 but not Nox1 or Nox4. The specificity of Nox2-ds-tat was investigated through a study using COS cells and the Nox2 cell-free system (Csanyi et al., 2011). Other peptides target gp91^{phox} discovered in the 1990s, such as [NH₃]-R-G-V-H-F-I-F-[CONH₂] (Rotrosen et al., 1990), [NH₃]-F-A-V-H-H-D-E-E-K-D-V-I-T-G-[CONH₂], a synthetic peptide mimicking domain 491-504 of gp91^{phox} (Leusen et al., 1994), and peptides corresponding to residues 27–46, 87–100, 282–296, 304–321, 434–455, and 559–565 of gp91^{phox} (Park et al., 1997). Yet they were mainly only tested in the cell-free systems which, although demonstrated the potential of these peptides, did not take into consideration of the complexity of the organisms and failed to show the effect *in vitro*, let alone *in vivo*.

One of the disadvantages of these peptides is low specificity. Specifically, some enzymes in flavoproteins category are responsible for maintaining the normal

function of cells. As an example, NOS plays a vital role in vasodilation and might be directly or indirectly affected (Cifuentes-Pagano, Csanyi & Pagano, 2012) by peptide Nox inhibitors. One evidence is that eNOS and Nox2 are co-regulated by the small GTPase Rac (Selvakumar et al., 2008), and a mechanism targeting the functional regions related to Nox2 Rac functioning might target eNOS as well.

Yet it is well known that peptides, such as insulin, are not available for oral intake since they can be digested through the gastrointestinal system. Therefore, new technologies such as nanoparticles are relied upon for the delivery of these drugs (D'Addio & Prud'homme, 2011), yet these delivery systems might have relatively higher toxicity or cost compared to the small molecules. In addition, it might be challenging for the inhibitors to show a significant effect at the desired site of action owing to the low absorption rate in the gastrointestinal system (Hamman, Enslin & Kotze, 2005). Thus, innovations towards the delivery systems and the efficacy of different delivery systems remained to be investigated.

1.6.3 Antioxidants

In the past several decades, many different antioxidant clinical trials targeting cardiovascular diseases have taken place (Brown et al., 2001; de Waart et al., 2001; Fang et al., 2002; Heart Protection Study Collaborative, 2002; Lonn et al., 2001; Salonen et al., 2000). The major weakness of using antioxidants in the clinical settings is that their use was limited to being supplements, rather than medication (Salonen, 2002), possibly due to their varied pharmacokinetics (PK) characters, low stability and low specificity (Jain, Mehra & Swarnakar, 2015). Antioxidant Supplementation in Atherosclerosis Prevention (ASAP) trial tested vitamin E and C on hypercholesterolemic patients aged 45-69 years for six years (Salonen et al., 2000). During the ASAP trial, another trial using a combination of vitamin E and C to investigate their effect on plaque area during

the coronary atherosclerosis was carried out by Harvard University. The results from this trial suggested their effect in reducing early progression of transplant-associated coronary arteriosclerosis (Fang et al., 2002). As a supplementation, a combination of vitamin E and C was able to reduce the atherosclerotic progression in men by 74%. However, the major limitation in this study is that, the effect of vitamin E and C was only limited to men, with possibly increased risk of higher oxidative stress such as smokers, low endogenous antioxidants or whose diet were lacking antioxidants. On the other hand, one study involving male smokers lacking the detoxification enzyme glutathione S-transferase $\mu 1$ (genotype: GSTM1-0) showed that smokers with GSTM1-0 develop atherosclerosis at a higher rate but no effect from vitamin E was found in the group (de Waart et al., 2001).

Vitamin E was also used alongside ramipril among people with vascular diseases or diabetes in a clinical trial which lasted 4.5 year, but vitamin E was only found a neutral effect (Lonn et al., 2001). Greg Brown et al. also compared the use of Simvastatin plus niacin, and antioxidant vitamins (vitamin E, C, natural beta carotene, and selenium), in combination and alone among patients with coronary diseases, but no effect from antioxidant vitamins was found (Brown et al., 2001). Similar result was found from a 5-year study in which vitamin E, C, and beta carotene were supplied to patients with coronary, vascular diseases or diabetes (Heart Protection Study Collaborative, 2002). These clinical trials last decades, however, did show one advantage of antioxidants, which is its safety.

Despite being proven to be ineffective and challenging, trials on using antioxidants are still going on. One current trial is to use an antioxidant cocktail containing vitamin C, E, and alpha-lipoic acid in middle-aged and aging patients (50 - 85 years old) with cardiovascular diseases. The major cardiovascular measurements in

this study include endothelial function (oxidative stress), arterial stiffness, heart rate variability, leg blood flow, leg muscle oxygenation, and walking ability (Smiljanec et al., 2020). Another antioxidant, cysteamine, which already exists as a drug to treat cystinosis, is being studied and repurposed by the research group of Prof. David Leake for its ability to inhibit lysosomal oxidation by inhibiting production of ceroid and reduce atherosclerotic lesions in the aortic roots in mice (Wen et al., 2019).

1.7 Hypothesis and aim

Cardiovascular diseases are prevalent and are the leading cause of mortality. The left ventricular hypertrophy is a pathological adaptive enlargement of cardiomyocyte that could occur in response to different cardiovascular disorders (Frey, Katus, Olson & Hill, 2004). Cardiac oxidative stress derived from ROS generated under these pathophysiological conditions plays an essential role in cardiac hypertrophic growth.

gp91^{phox}-containing NADPH oxidase (Nox2) is a multi-subunit enzyme consisting of p22^{phox} and gp91^{phox}, and four regulatory subunits including p40^{phox}, p47^{phox}, p67^{phox}, and rac1. Under diseased conditions in the heart, with the phosphorylation of p47^{phox}, different Nox2 regulatory subunits coordinate and by associating with p22^{phox} and gp91^{phox}, are responsible for the production of O₂⁻ (Panday et al., 2015). This process is one of the major sources of oxidative stress in the organs such as the heart (Zi et al., 2019).

In the mammalian heart, p47^{phox} is expressed in the myocardium (Sirker et al., 2016), epicardium and coronary arteries. In cardiomyocytes (Patel et al., 2013), p47^{phox} co-localises with F-actin and associates with cortactin, which was proposed to facilitate the translocation of the p40^{phox}-p47^{phox}-p67^{phox} complex to Nox2 across the plasma

membrane and in the cytosol (including peri-nuclear region) (Tamura et al., 2006). A major role of p47^{phox} linking the oxidative stress and the development of cardiac hypertrophic growth was identified, and extracellular signal-regulated kinase (ERK)1/2, ERK5, c-Jun N-terminal kinase (JNK) 1/2 and p38 mitogen-activated protein kinase (MAPK) was suggested (Cao et al., 2020; Li et al., 2002).

The current antioxidant therapies and Nox inhibitors have potential weaknesses such as low specificity, unclear mechanism or side effects. Therefore, this study aims to investigate the pharmacological properties of a novel small-molecule Nox2 inhibitor previously developed in this lab, LMH001, to target p47^{phox} and understand the role of p47^{phox} in AngII-induced cardiac hypertrophic and p47^{phox} KO murine model. At the same time, developing an effective and specific p47^{phox} inhibitor would be extremely useful in studying the complexity of p47^{phox} functioning in heart.

Based on the background that oxidative stress caused by Nox2 facilitates the development of cardiovascular disorders, my PhD research project hypothesises that the Nox2 regulatory subunit, p47^{phox} is involved in the AngII induced development of cardiac disorders and targeting p47^{phox} by knockout p47^{phox} contributes to retard the pathophysiological conditions. Since LMH001 was developed based on interfering the binding of p47^{phox} to p22^{phox}, we also propose that LMH001 is an effective Nox2 inhibitor. This study first aimed to characterise the pre-clinical PK parameters and the effect of a classic Nox2 inhibitor, apocynin, using WT CD1 male mice with 6-week of age to get a grasp of the PK characterising procedures and the basic chemical properties of the Nox inhibitors. Based on the results from apocynin, the study then set to investigate the PK parameters and chemical properties of LMH001. Role of p47^{phox} and p47^{phox} signalling was also looked at for a better understanding of the effect of LMH001.

Chapter 2

Materials and Methods

2.1 Chemicals and reagents

Otherwise specified, most chemicals of the appropriate grade were purchased from either Sigma-Aldrich or Fisher Scientific. All the reagents used in this study are listed in Appendix I at the end of this chapter. All the antibodies used, including their host species, working dilution and suppliers are listed in Appendix II. The equipment used for different experiments, including sample preparation, high-performance liquid chromatography-tandem mass spectrometry (HPLC-MS/MS), western blot, immunofluorescence and ROS measurement is listed in Appendix III. The suppliers of other consumables such as syringes and HPLC vials were also listed in the text.

2.2 Animals

All animal studies were performed with the approval of the Home Office (PIL: IF25D3465; PPL: 70/8829) following the Animals (Scientific Procedures) Act 1986. CD1 WT mice were initially obtained from Charles River Laboratory (UK), WT and Nox2 KO mice on a C57BL/6 background were originally purchased from Jackson Laboratory (U.S.A). Nox2 KO mice were generated by (Pollock et al., 1995) and were housed at University of Reading Bioresources Unit (BRU) separately in room B29 where barriers were up, and extra necessary measures were taken to keep the mice (such as immune-deficient or weakened) in a clean environment. In B29, irradiated diet and pouched sterile water were used and checked daily, caging and bedding and husbandry consumables were autoclaved before use and cages were cleaned weekly. p47^{phox} KO mice were established previous (Li et al., 2004) in the University of Surrey and originally generated by (Jackson, Gallin & Holland, 1995). p47^{phox} KO mice were

housed under the same condition as Nox2 KO. Male CD1 mice at the age of 12 weeks and C57BL/6 mice at the age of 10-12 months were used for the studies unless specified otherwise.

Upon arrival, all mice were housed either in standard or B29 acclimating room at 18-23 °C and 45-55 % humidity in a 12:12 hour dark cycle with lights on from 7.00 am to 7.00 pm, and water and food available *ad libitum* for at least seven days before fully entering the unit for acclimation. After acclimation, unless specified, housing conditions remained the same as during the acclimation.

2.3 Sample collection and preparation for pharmacokinetics (PK) analysis

The establishment of CD1 murine model for PK is described in section 3.3.2 (apocynin) and 4.3.2 (LMH001).

After iv bolus injection, blood, organs and urine samples were collected at designated time point as described in section 3.3.2 (apocynin) or 4.3.2 (LMH001). Specifically, mice were first sacrificed by overdose sodium pentobarbital (10 × dilutions, 10 µl/g). Approximately 1.2 ml blood each mouse was collected with a 2 ml heparinised (5000 U/ml, LEO Pharma, Ireland) syringe with a 23G needle (BD, UK) and then centrifuged at 2,000 g, 4 °C for 10 min to get plasma. Urine samples were collected during the administration of anaesthetic and from the bladder during the dissection. Tissues including liver, brain, kidney, spleen, pancreas, lung, heart, aorta, muscle and adipose were collected, thoroughly washed in ice-cold PBS and blotted dry with filter paper. The collected tissues were used for PK analysis and ROS measurement.

Each tissue harvested from the PK murine model was cut into two. One half was cut up and accurately weighed (50 mg), homogenised in the diluent, and the other half was preserved using liquid nitrogen. All the samples were stored at -80°C for future analysis.

All the biological samples were processed similarly with minor modifications. The diluent used in the sample processing consisted of methanol: water 1:1 (v/ v). Specifically, for plasma, 100 µl plasma was used as the matrix (for calibration) or analytical samples (for the experiment). It was added with corresponding concentrations of apocynin (phenacetin as internal standard) or LMH001 or the same volume of the diluent (for the experiment) before the protein crash. For different organs such as brain, liver and heart, half of the organ first was cut into pieces in a petri dish, and 45.0 -55.0 mg of the tissue was weighed into an Eppendorf tube using an analytical balance (Kern-ABJ-NM, Germany, min = 10 mg, d = 0.1 mg, e = 1 mg, min = the minimum weight; d = readability, which is the smallest increment of measurement displayed, e = verification scale interval, which is the readability approved). The diluent was then added with the volume equal to five times the tissue weight to form a final tissue concentration of 0.2 mg/µl. The whole process was carried out on the ice to minimise any possible degradation of the target compound. Then tissue in the diluent was homogenised on ice using a homogeniser Polytron PT 1200E (Kinematica, Netherland) and 100 µl was used as a matrix or for analysis. For urine samples, 10 µl of the urine collected and analysed. Since apocynin and LMH001 have different chemical properties, the specific sample processing methods can be found in section 3.2.4 (apocynin) and section 4.2.4 (LMH001).

2.4 HPLC-MS/MS

HPLC used in this study was from Thermo Scientific Accela. HPLC is used to separate different molecules in one sample based on the different hydrophobicity of different molecules (Spiteller, 1985). Used as a reverse phase HPLC, Accela was supplied by a polar, hydrophilic mobile phase (usually an aqueous solution) and a non-polar hydrophobic stationary phase (such as a silica C18 column). As a sample consisting polar and non-polar molecules passes through the column, the non-polar, hydrophobic molecules would absorb or interact with the column (McNaught, Wilkinson & International Union of Pure and Applied Chemistry., 1997), leaving the polar and relatively more hydrophilic molecules to come out of the column first. Reverse-phase HPLC is the more commonly used HPLC method than normal HPLC because of the following two reasons (Hearn, 1980). First, an aqueous mobile phase could be applied to a broader range (around 75 %) of molecules (Robards, Haddad & Jackson, 2004) in terms of reasonable retention time. Second, an aqueous mobile phase could offer scientists with more options on the organic solvent type and pH.

After HPLC separates the molecules based on the different hydrophobicity, each molecule comes out of HPLC at a specific time (retention time), and the molecule of interest with known m/z would be picked up by a mass spectrometer. The mass spectrometer used in this study was LTQ-Orbitrap XL mass spectrometer. After the samples are vaporised, it gets ionised by a beam of electrons to obtain a charge, which in this study, is heated electron spray ionisation. After being accelerated in an electric field, the molecule gains momentum, and at the same time, the deflection happens in a magnetic field which gives the molecule a force proportional to its charge. Therefore, in a mass spectrometer, an individual molecule can produce a path that is proportional to its mass and charge ratio (m/z) (Gross, 2004). This m/z can be recorded and reported

by the computer. LTQ-Orbitrap XL mass spectrometer uses a quadrupole, which consists of four parallel rods arranged around a central axis with static and alternating potentials applied to only allow specific m/z pass through (Yost & Enke, 1978), for a more specific and static selection of the target molecule (m/z) (Chernushevich, Loboda & Thomson, 2001).

2.4.1 Equipment and instrument settings

The development, validation and sample analysis using HPLC-MS/MS method for apocynin and LMH001 PK analysis were performed on a Thermo Scientific Accela HPLC (shown in **Figure 2.1 A**) tandem LTQ-Orbitrap XL mass spectrometer (shown in **Figure 2.1 B** (1) and (2)), storing the data in profile mode. How reversed-phase HPLC-MS/MS works is illustrated by a diagram in **Figure 2.1 (C)**. The column used was a reversed-phase 50 × 2.1 mm ID, 1.9 μm particle, 175 Å pore C₁₈ Hypersil Gold column (Thermo Scientific, USA) with an injection volume of 5 μl for separation of the target compound and internal standard. For quantification, LTQ XL Ion Trap (Thermo Scientific, USA) with heated electrospray ionization (HESI) in negative ion mode using a selected reaction monitoring (SRM) acquisition was used for both apocynin and LMH001 PK analysis.

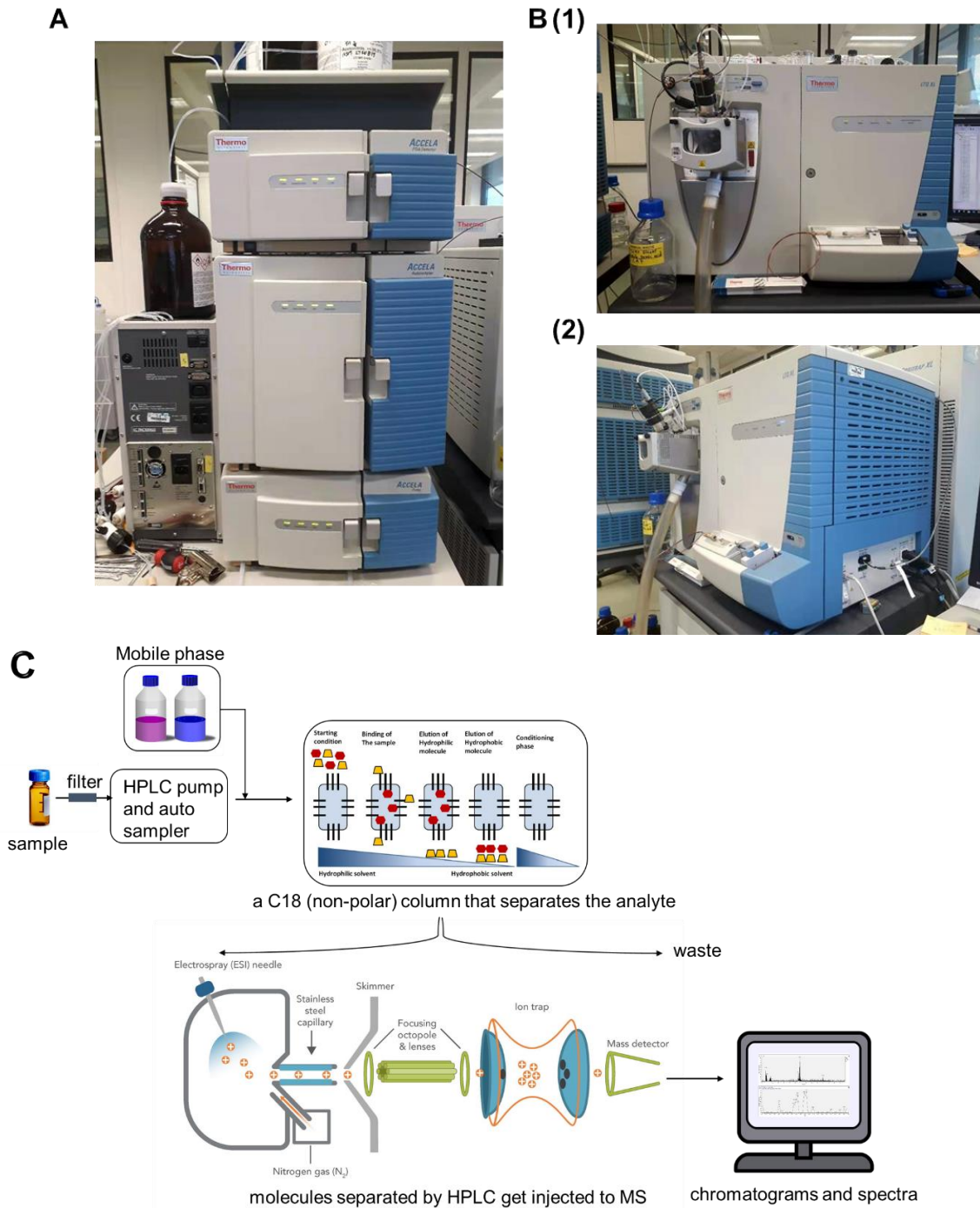


Figure 2. 1 Thermo Scientific Accela HPLC and LTQ-Orbitrap XL mass spectrometer.

A: HPLC from view; B: (1) front view; (2) side view), and C: a diagram of how reversed-phase HPLC-MS/MS generates data from the samples, showing the principles of separation by a non-polar column and MS.

Due to the differences in the chemical properties of apocynin and LMH001, different HPLC-MS/MS running methods, including the chosen mobile phases and selected MS transitions can be found in section 3.2.5 (apocynin) and section 4.2.4 (LMH001).

2.4.2 Quantification

The quantification analysis was carried out using Thermo Xcalibur 3.0 (ThermoFisher, U.S.A.) software. The user peak detection settings are shown in **Figure 2.2** (Identification) and **2.3** (ICIS Integration), with apocynin as an example. The rest of the settings including Detection, ICIS Advanced and Flags were left as default. The quantification result was normalised using the internal standard (500 ng/ml) to minimise the effects of sample manipulation errors.

The screenshot shows the 'User Identification Settings' dialog box with the following configuration:

- Identification Tab:** Name: Apocynin; Plot Type: Mass Range; Scan Filter: ITMS - p ESI SRM ms2 165.10@cid26.00; Mass (m/z): 150.10; Keys: (empty); Retention Time: Expected (min): 5.60, Window (sec): 30.00, View Width (min): 4.00. Use as RT Reference, Adjust Using.
- Detector:** Type: MS
- Peak Detection Algorithm:** ICIS

Buttons at the bottom: OK, Cancel, Apply, Apply To All, Help.

Figure 2. 2 Settings of apocynin Identification in User Peak Detection Settings, Thermo Xcalibur Quan Browser.

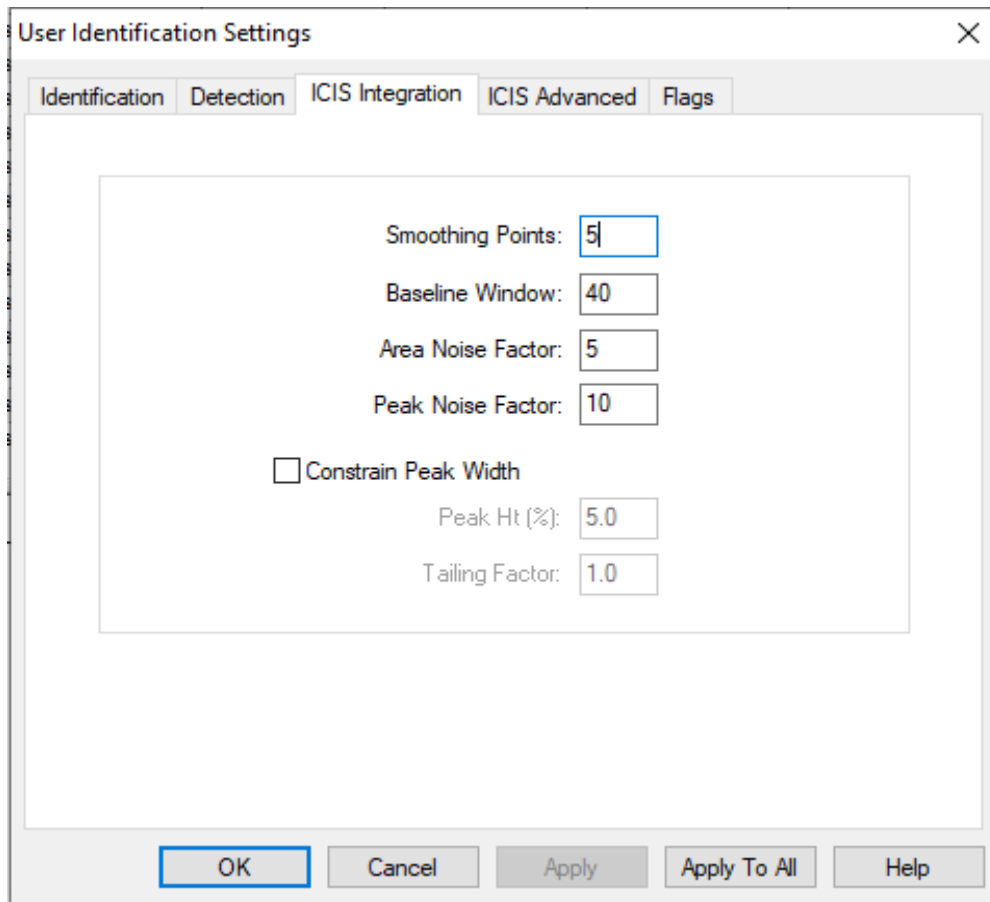


Figure 2. 3 Settings of apocynin ICIS Integration in User Peak Detection Settings, Thermo Xcalibur Quan Browser.

2.5 PK analysis

For PK analysis of the targeted compound, the profiles of plasma concentration changes versus time (average concentration per timepoint calculated by WinNonlin, n=3 per timepoint) were first subjected to a non-compartmental analysis (NCA) in Phoenix WinNonlin 8.1 to understand the overall exposure of the targeted compound to the body, independent from any models or assumptions (Gabrielsson, 2016). After characterising the overall PK parameters, the target compound concentrations in murine plasma versus time were then processed by compartmental analysis using non-linear

mixed effect (NLME) model (n=3 per time-point) to minimise the random effect and learn in-depth the PK characters of the targeted compound (Rotschafer et al., 1983).

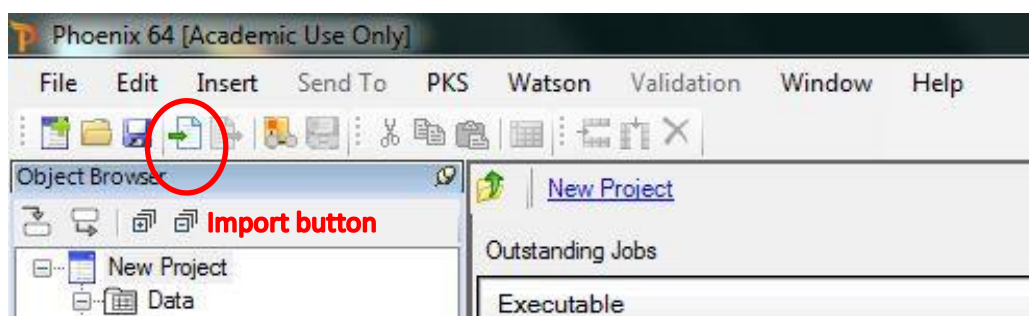
2.5.1 Non-compartmental analysis (NCA)

NCA is used for the estimation of basic PK parameters related to the administration, distribution and elimination following single or repetitive dosing of a drug with a minimum assumption and independent of any model and can provide an empirical description of the correlation between the dosing information and the measured plasma concentration of the targeted compound (Bonate & Howard, 2004). Since this analysing method is carried out in a way to generate the most aspects of the PK parameter of one drug without any model applied or bias, NCA represents an essential PK analysis package during the FDA drug regulatory submissions in the U.S. (Bonate & Howard, 2004; Ross & Kesselheim, 2015). Therefore, in this study, to establish the initial understanding of the PK parameters of the target compound in the CD1 murine model, an NCA was first carried out using Phoenix WinNonlin 8.1 NCA with linear trapezoidal linear interpolation calculation method.

2.5.1.1 organising and importing of the data

For WinNonlin 8.1 to be able to understand and process the data, the concentration of apocynin over time were organised and imported as following **Figure 2.4**. First, data from Excel was imported by the import button, as illustrated in **Figure 2.4.1**. After importing the data, each column was defined as **Table 2.1** and is shown in **Figure 2.4.2**.

2.4.1



2.4.2

The screenshot shows a data table with the following columns: Column1, Time_min (min), Time_h (h), and Conc (ng/ml). The data is organized into rows for different time points (1, 2.5, 5, 15, 30 min) and their corresponding hours (1, 2.5, 5, 15, 30 h). The concentration values are shown in scientific notation.

Column1	Time_min (min)	Time_h (h)	Conc (ng/ml)
1 min_1	1	0.01666667	15240
2 1 min_2	1	0.01666667	14021.667
3 1 min_3	1	0.01666667	14534.667
4 2.5 min_1	2.5	0.04166667	8393
5 2.5 min_2	2.5	0.04166667	8166.3333
6 2.5 min_3	2.5	0.04166667	7641.3333
7 5 min_1	5	0.08333333	3396
8 5 min_2	5	0.08333333	2412.6667
9 5 min_3	5	0.08333333	3210.3333
10 15 min_1	15	0.25	1645
11 15 min_2	15	0.25	193
12 15 min_3	15	0.25	113
13 30 min_1	30	0.5	33.333333
14 30 min_2	30	0.5	37.333333
15 30 min_3	30	0.5	58.333333
*			

Below the table is a 'Columns' dialog box with the following settings:

- Columns: Column1, Time_min, Time_h, Conc
- Data Type: Text (Orange)
- Unit: [none] (Units Builder...)
- Display Format: Custom (G3)
- Required Decimals: 0
- Optional Decimals: 0
- Use Thousands Separator:

Figure 2. 4 The organisation and import of raw data.

2.4.1 How to import concentration of apocynin over time into Phoenix WinNonlin 8.1.

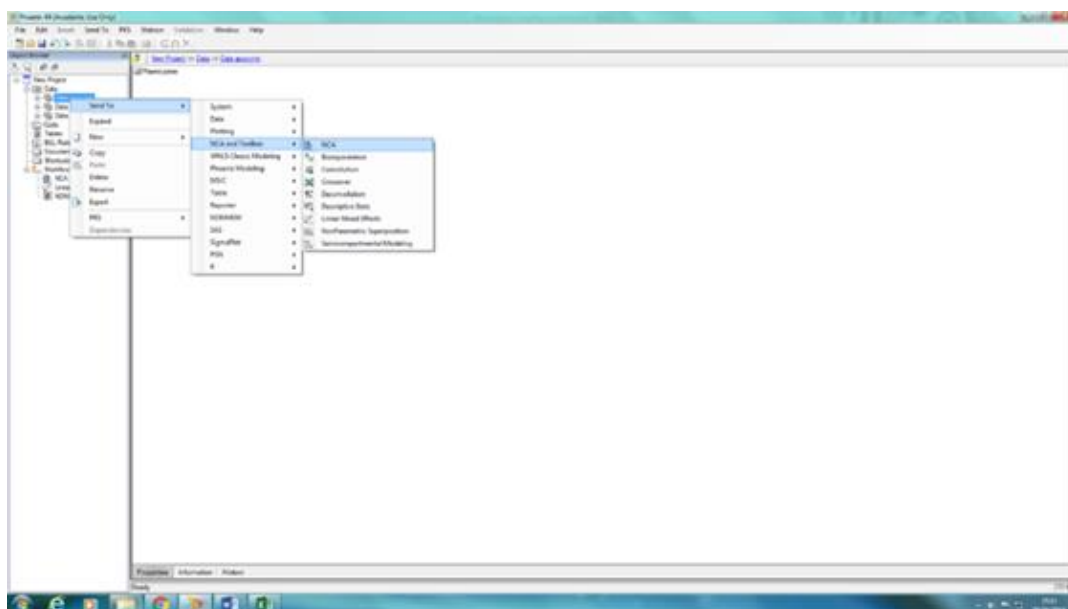
2.4.2 Demonstration of data imported in WinNonlin 8.1.

Table 2. 1 Column defining settings for the data in Phoenix WinNonlin 8.1.

	column 1	column 2	column 3	column 4
Nature	name	time in min	time in hour	apocynin conc.
Type	Text	Numeric	Numeric	Numeric
Unit	none	min	h	ng/ml
Display format	Custom	Custom	Custom	Custom

2.5.1.2 NCA analysis

NCA analysis was carried out by right-clicking the data and choosing Send to → NCA and Toolbox → NCA (as shown in **Figure 2.4.3**).

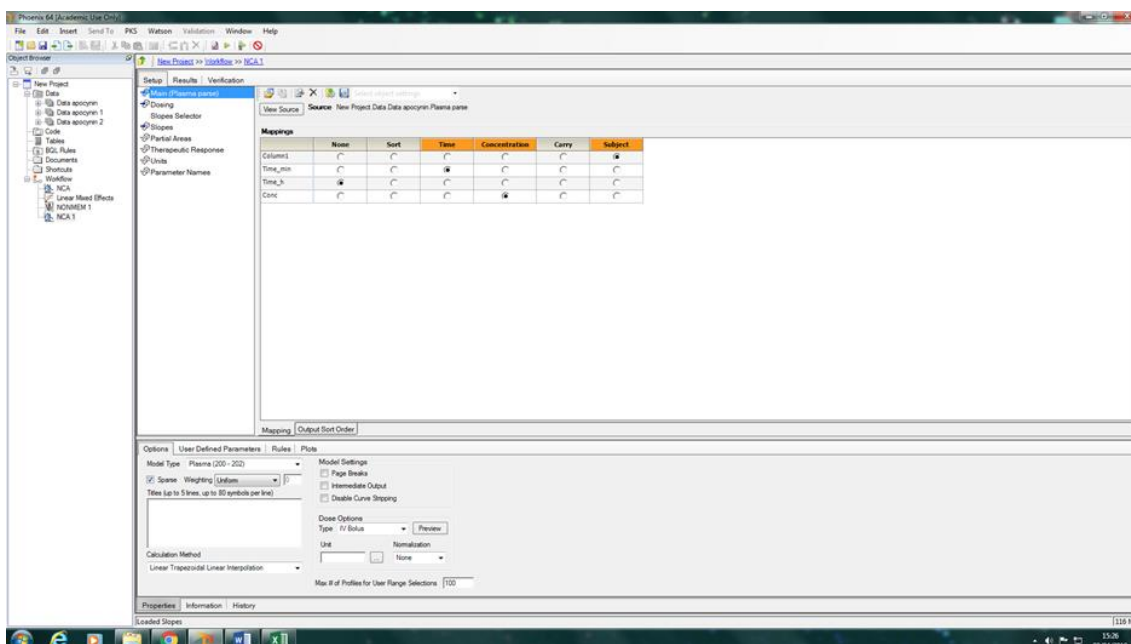


2.4.3 Start of the NCA analysis.

After starting, one window with orange-coloured columns would pop up and required the data to be mapped. In this case, Column 1 was mapped to be the SUBJECT, Time_min to be the TIME and Conc to be the CONCENTRATION.

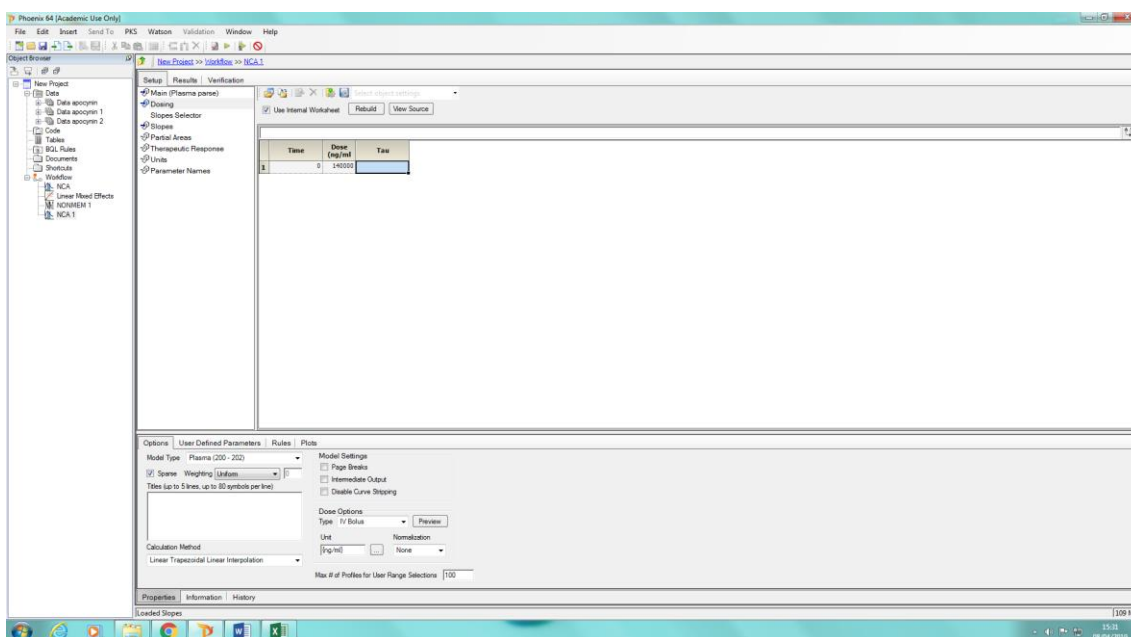
In terms of Options, Plasma (200-202) Model Type was selected, sparse was ticked since this data was collected using sparse terminal sampling, weighting was Uniform, Tile left empty and Linear Trapezoidal Linear Interpolation Calculation

Method was chosen since this is one-off iv bolus. Dose Options was selected as IV Bolus, and others left default as is the screenshot shown in **Figure 2.4.4**.



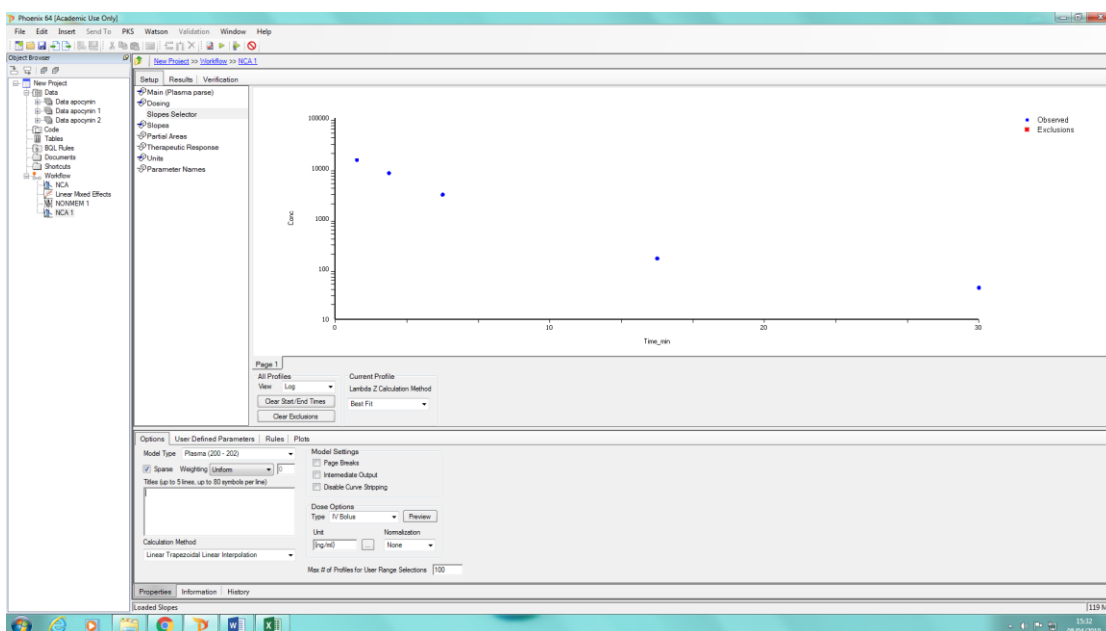
2.4.4 The mapping of the data and the setting for NCA analysis.

Dosing was set up by the initial dose at 5 mg/kg (apocynin) or 10 mg/kg (LMH001) at time 0 min and was based on the average bodyweight of the CD1 mouse used (28 g). The dosing unit was adjusted to ng/ml (**Figure 2.4.5**).



2.4.5 Dosing settings for NCA analysis.

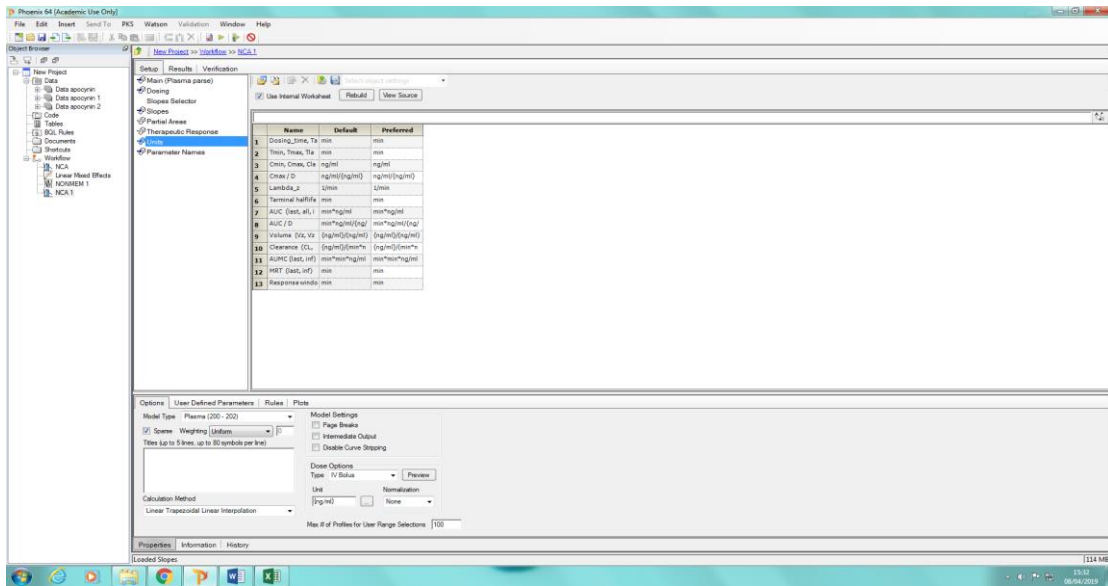
The average concentration of the targeted compound at each time point was then calculated automatically by WinNonlin 8.1 for the slope selector of the NCA PK parameters, as is shown in **Figure 2.4.6**.



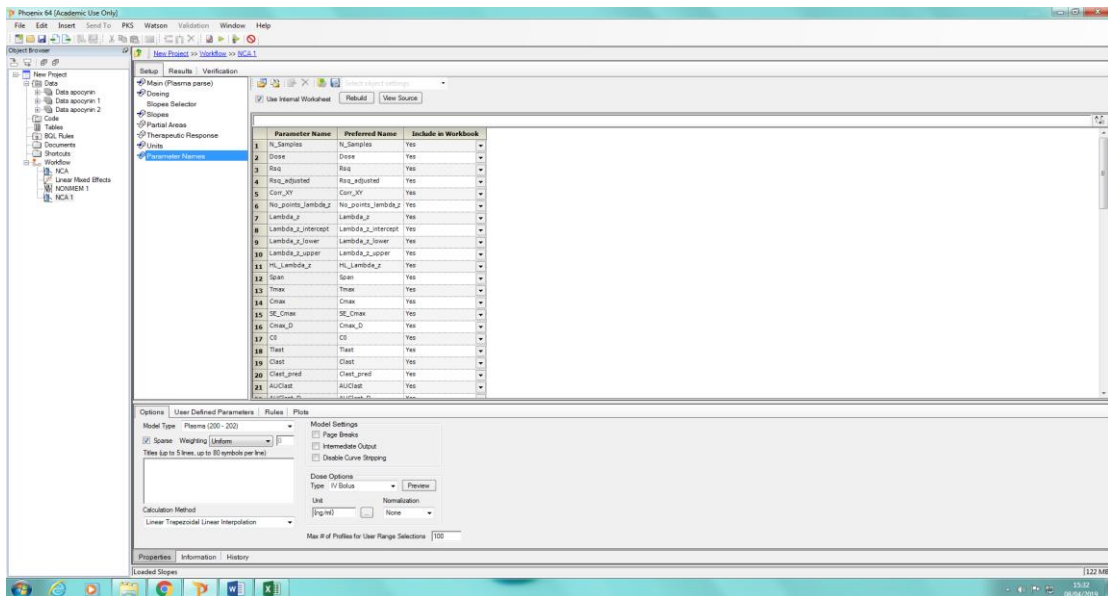
2.4.6 Slope selector of NCA as the average concentration of the targeted compound at each time point was calculated automatically.

The units and parameters in the NCA analysis were left as default (**Figure 2.4.7 (A) (B)**), and the analysis was ready to be executed. The green button on the top was for running the analysis.

(A)



(B)



2.4.7 The units (A) and parameters names (B) in the NCA analysis.

The calculated parameters include C_{\max} , $AUC_{(1-30 \text{ min})}$, k_{el} , $t_{1/2}$, $AUC_{(0-\infty)}$, Clearance (CL), V_i and V_d . These parameters calculated are explained below:

C_{\max} is the maximum concentration that apocynin could reach in the plasma, which, in this study, is read directly from measurement at 1 min.

$AUC_{(1-30 \text{ min})}$ is the area under the plasma concentration vs time curve from 1 min until 30 min. The unit of AUC is the amount of time/volume, e.g. ng·min/ml. In this study, $AUC_{(1-30 \text{ min})}$ was calculated by adding the area of the trapezoids formed between each pair of time points. The formula for calculating the area of a linear trapezoid is:

$$AUC_{(t1-t2)} = [(t2-t1)/2] \cdot (C1+C2) \quad (1)$$

$$AUC_{(t2-t3)} = [(t3-t2)/2] \cdot (C2+C3) \quad (2)$$

And therefore,

$$AUC_{(t1-t3)} = AUC_{(t1-t2)} + AUC_{(t2-t3)} \quad (3)$$

k_{el} (elimination rate constant) represents the fraction of drug eliminated per unit of time. It is observed from a curve (log-linear) and reasonably describes the terminal phase (usually last six points in this study, until 30 min) without a pharmacokinetic program. k_{el} can be used to calculate the terminal half-life, $t_{1/2}$, (i.e. the time taken for the plasma concentration to reduce by half) using the following equation:

$$k_{el} = \log e (2)/t_{1/2} = 0.693/t_{1/2} \quad (4)$$

$AUC_{(0-\infty)}$ is estimated using k_{el} and is the time point corresponding to the last measurable concentration. In this study, since the estimated area from 30 min to infinity is $C_{30\text{min}}/k_{el}$, the area from zero time to infinity is given by:

$$AUC_{\infty} = AUC_{(1-30 \text{ min})} + (C_{30 \text{ min}}/k_{el}) \quad (5)$$

Clearance (CL, specifically refers to total clearance here) is a measure of the overall elimination of a drug from the body and is reported to be a much better indicator of elimination rate than $t_{1/2}$ (Benet & Zia-Amirhosseini, 1995). It is described as a

proportionality constant relating drug concentration to the rate of elimination and is normally calculated from iv bolus data:

$$\text{Rate of elimination} = CL \cdot \text{concentration} \quad (6)$$

In this study, with iv bolus injection, the dose is defined as the total amount of compound injected, which is equal to the total amount of compound eliminated over time zero to infinity. Since AUC_{∞} is the real-time concentration over the same time, if time is considered, equation (6) is equivalent to:

$$\text{Dose} = CL \cdot AUC_{\infty} \quad (7)$$

Therefore,

$$CL = \text{Dose}/AUC_{\infty} \quad (8)$$

As the compound gets metabolised or distributed, the concentration of the compound in one organ changes along with the rate of elimination, but CL remains constant. If it is assumed that the compound enters the body by iv bolus and the plasma concentrations of the drug are measured, CL is defined as the volume of the plasma irreversibly cleared from the compound per unit time. If after giving a dose of drug it was uniformly distributed throughout a certain volume of body fluid, the total CL is the fraction of that total volume that is cleared of drug per time unit. Thus, if this total volume of distribution is defined as V_d and the fraction loss per unit time is k_{el} then:

$$CL = k_{el} \cdot V_d \quad (9)$$

Here V_d represents the distribution volume, which is the notional volume in which the drug must be distributed to yield the observed drug concentration in plasma. It is calculated as:

$$V_d = (\text{Dose}/AUC_{\infty})/k_{el} \quad (10)$$

It is an overestimate of the true volume of distribution, but if the distribution volume is reasonably large ($> 1\text{-}2\text{ L/kg}$ body weight) the error is not clinically important.

However, in reality, the drug distributes into tissues and is eliminated before it thoroughly mixes with plasma. Therefore, the initial distribution volume, V_i after iv dosing is defined as the volume in which the drug is immediately distributed after the bolus iv dose. The calculation is the initial dose divided by the estimated concentration at time zero $C_{(0)}$ is used:

$$V_i = Dose/C_{(0)} \quad (11)$$

The difference between V_i and V_d is that in the calculation of V_d , the $C_{(0)}$ at $t_{(0)}$ is obtained by extrapolation of the terminal phase using AUC_{∞} .

2.5.2 Compartmental analysis using a non-linear mixed effect (NLME) model

Compared to the model-independent NCA, the mechanistic compartmental analysis is model-driven and can be used for understanding in-depth the biological or physiochemical events responsible for the observed effects (Bonate & Howard, 2004). One of the most frequently used models for compartmental analysis is NLME model to incorporate both the fixed and random effect to the non-linear regression, based on the fact that in PK studies, repeated measurements of drug concentration over time from each individual of a population are used, which would introduce random effect in the process of establishing a model (Davidian & Gallant, 1993). It describes a continuous response evolving over one factor (such as time) within individuals from a population of interest (Funatogawa & Funatogawa, 2007). By the approximate representation of the body parts as compartments, NLME model can describe the absorption, distribution and elimination of the drug normally by one-, two-, three- or even more compartmental

analysis. In the NLME model analysis, it is an assumption that the random effect follows a normal distribution, which, may or may not, introduce errors in the model (Drikvandi, 2017)). However, in this study, I would like to point out that since the NLME model has been widely accepted and used till today (Riegelman, Loo & Rowland, 1968). It is beyond my knowledge to discuss in-depth the accuracy of assuming the normal distribution for the random-effect, in this study, the built-in NLME model in Phoenix WinNonlin 8.1 with bolus input and first-order output was used to analyse the pooled drug concentration measured in the plasma versus time to understand the characteristics of the target compound further.

The number of the compartment was selected based on the model fit. NLME can calculate several factors. These include k_a , fractional rate of absorption (1/time), CL, clearance rate (volume/time) and V (volume of distribution). This analysis in PK is critical in developing dosing strategies and guidelines.

2.5.2.1 Organisation and import of data

The data importing method used was the same as NCA analysis, as described in section 2.5.1.1.

2.5.2.2 NLME compartmental analysis

I used one-compartmental analysis as an example to demonstrate the method for carrying out NLME analysis. When starting, the imported and defined data was selected by right-clicking, Send To → Phoenix Modelling → Phoenix Model (as shown in **Figure 2.5.1**) was chosen.

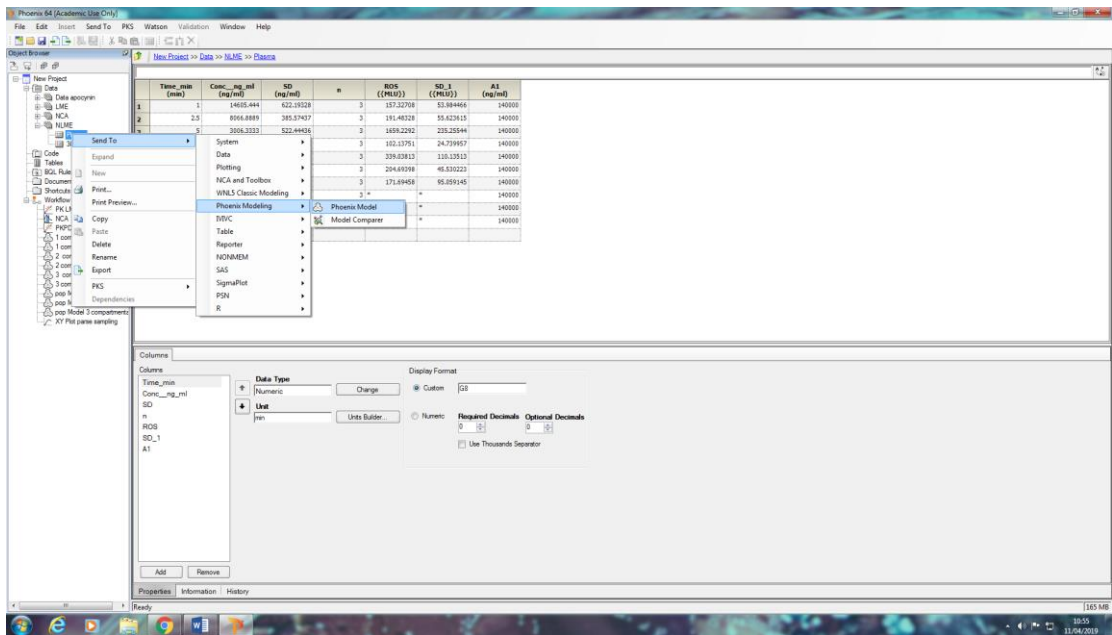


Figure 2. 5.1 The process of one-compartmental analysis by Phoenix WinNonlin 8.1: selecting phoenix model.

Since this study was not populational (population PK could be chosen if the box is ticked, as is shown in **Figure 2.5.2**), the population was unticked. After selecting the Phoenix Model, one window pops up with orange-coloured columns being required to be mapped. In this case, time was mapped to time_min, A1 is the apocynin (LMH001) initial dose used for iv bolus, Cobs is apocynin (LMH001) concentration(conc.) detected in the plasma, as is shown in **Figure 2.5.2**.

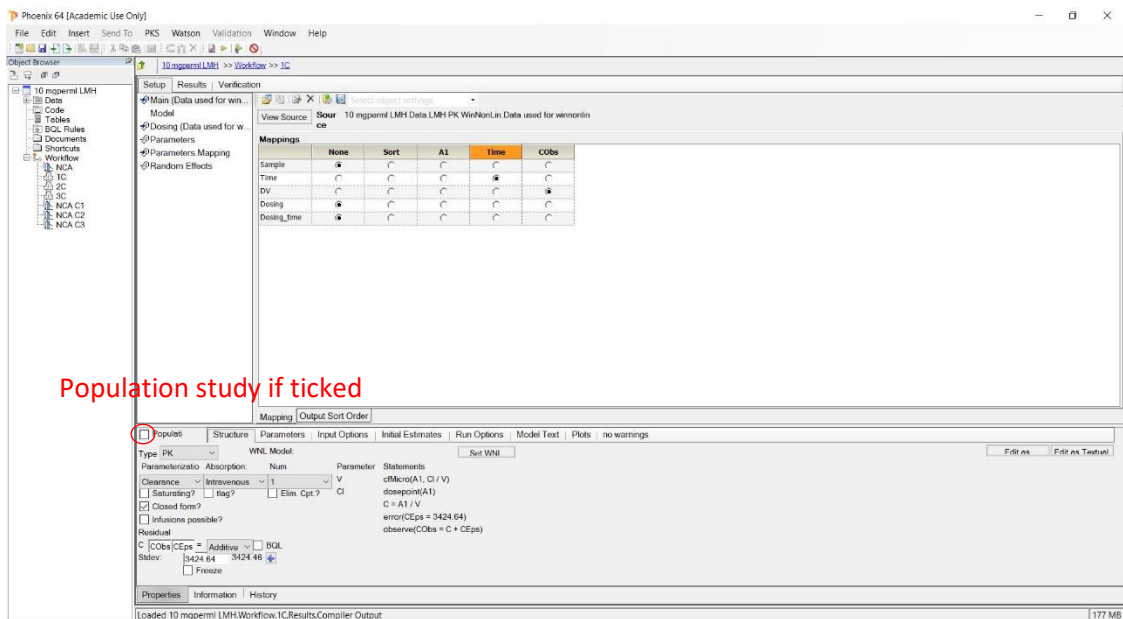


Figure 2.5.2 Parameters selected for NLME analysis (LMH001 analysis as an example).

The initial dosing can be defined under the ‘dosing’ choice. Since the dose used was 5 mg/kg, and the average body weight of the mice used was 28 g, the dose was defined as 140,000 ng (for LMH001, the dose was 10 mg/kg and defined is 280,000 ng). For the fitting model of apocynin/LMH001 PK by iv bolus, Clearance parameterisation was chosen, Absorption by Intravenous and Num Compartments is 1 (up to 3 compartments can be selected, Edit can be used to build in more compartments as Graphical on the right). A closed form meant that there is one absolute V value which would decide the Statement, as is shown in **Figure 2.5.3**.

To explore a rough model first, Initial Estimates was chosen, and the data were fit to the curve as is shown in **Figure 2.5.3**:

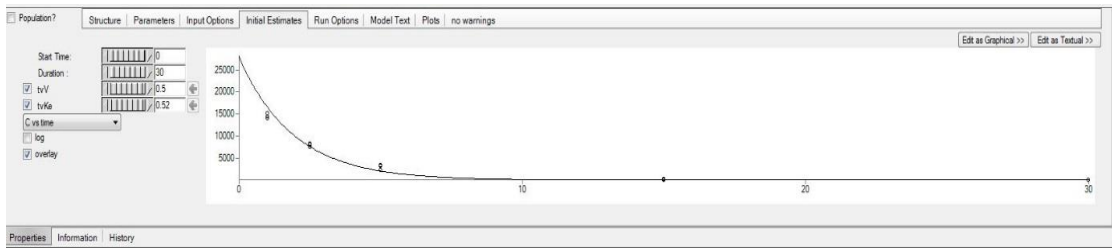


Figure 2.5.3 Initial Estimation of apocynin PK data.

tvV and tvCL were then changed to a level that the observed values can fit in the curve.

After deciding the estimated tvV and tvCL, fixed effects in Parameter was fixed to the estimated values as is shown in **Figure 2.5.4**.



Figure 2.5.4 Initial values fixed for apocynin NLME analysis.

The basic structure of the model defined can be viewed by clicking the Model button (**Figure 2.5.5**).

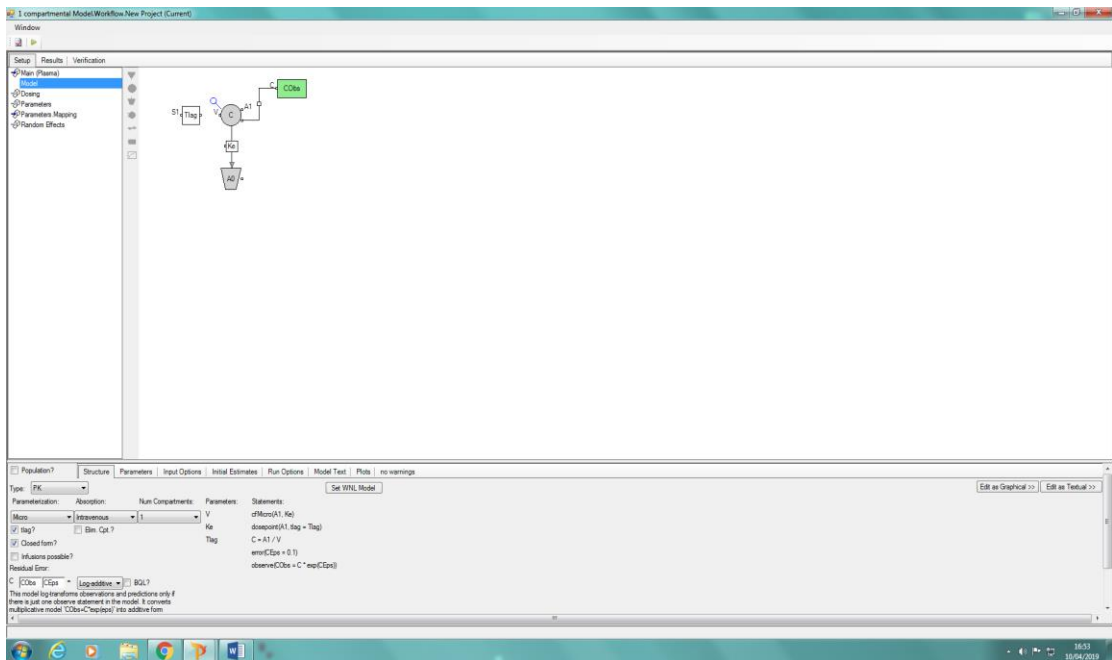


Figure 2.5.5 The defined model in the analysis.

2.5.2.3 Analysis

The green executing button at the top was used for running the analysis. After executing (which might take 1 min or 2), tvV and tvCL was calculated and listed in the result sheet Theta. The evaluation of the model (which includes LogLik and -2LL) was listed in Overall worksheet.

In Phoenix WinNonlin 8.1, model fit including Akaike’s information criterion (AIC), Bayesian information criterion (BIC) and log-likelihood were reported. These estimators for model fit have been traditionally and widely used as standard criteria for selecting the most appropriate model (Olofsen & Dahan, 2013). However, when the sample number n is less than 40, a corrected version of AIC (AICc) which considers the number of observations n and parameters P , is used (Bertrand, Comets & Mentre, 2008). AICc is calculated as follows:

$$AICc = AIC + 2P(P+1)/(n-P-1)$$

in which P is the number of parameters, and n is the total number of observations.

The smallest AICc suggests the best fit for the model (Rajeswaran & Blackstone, 2017).

Therefore, AICc was used for the statistical significance comparison in this study.

Several graphs with more detailed model information are also generated, which are explained in the relevant result chapters.

2.6 Lucigenin chemiluminescence assay

Lucigenin, bis-*N*-methylacridinium nitrate, is a chemiluminogenic probe used for O₂⁻ production detection (Minkenberg & Ferber, 1984). The process of lucigenin getting oxidised by O₂⁻ and releasing one photon contains two main steps. First, lucigenin is reduced to a radical with the appearance of an electron. Then, the reduced radical serves as a reducing agent to react with O₂⁻, resulting in two acridones produced by the decomposition of lucigenin (*N*-methylacridone). Each of the acridones possesses an excited state and its degradation to the ground state involves the emission of a photon (Allen, 1986) (Faulkner & Fridovich, 1993). The advantages of the technique include the high cell-permeability of lucigenin, high level of sensitivity and the rapid reaction time for real-time detection (Fan & Li, 2014). The reported artificial result by xanthine oxidase in the presence of NADH was proved not to exist in mammalian cells (Fan & Li, 2014) and the false signal by lucigenin itself was able to be avoided by using relatively lower concentration (10 µM) (Afanas'ev et al., 2001; Li et al., 1998).

In this study, lucigenin is used in various experiments for the tissue O₂⁻ production. Lucigenin buffer was made up of 80 mM MgCl₂ (stock concentration: 100 mM) and 1.8 mM CaCl₂ (stock concentration: 1 M) in Hanks' balanced salt solution (HBSS) without phenol red, calcium or magnesium (GE Healthcare, USA). First, tissue collected was homogenised in the lucigenin buffer. Then in 135µl lucigenin buffer, 5

μl of the tissue sample homogenates was added to form the final volume of 140 μl . For the analysis, a 96-well white plate with a flat bottom (Evergreen Scientific, USA) was used. $\text{O}_2\text{-}$ was detected using Spectramax L microplate reader (Molecular Devices, USA) with 5 μM lucigenin and 0.1 mM NADPH (to obtain the basal readings without NADPH, NADPH was added after the first ten readings). The specificity of detection of $\text{O}_2\text{-}$ was confirmed by adding tiron (10 mM), a non-enzymatic $\text{O}_2\text{-}$ scavenger. The final $\text{O}_2\text{-}$ production was normalised against protein concentration.

The enzymatic source of the $\text{O}_2\text{-}$ was also examined using lucigenin assay using different inhibitors for ROS-generating enzymes. These include: 1) a NOS inhibitor, N^{G} -Nitro-arginine methyl ester (L-NAME), 100 μM ; 2) a mitochondria electron-transfer chain (complex 1) inhibitor, rotenone, 50 μM ; 3) a xanthine oxidase inhibitor, oxypurinol, 250 μM ; 4) a flavoprotein inhibitor, DPI, 20 μM ; 5) a Nox2 inhibitor, apocynin, 300 μM ; 6) polyethylene glycol-superoxide dismutase (PEG-SOD), 200 U/ml. The experimental procedure was the same as the lucigenin assay described above except that different enzyme inhibitors were added to achieve the working concentration in each well with samples, and the plate was incubated at room temperature in the dark for 15 min before loading to the plate reader for analysis.

2.7 Dihydroethidium (DHE) assay

DHE, dihydroethidium, has been previously used as an *in situ* membrane-permeable $\text{O}_2\text{-}$ indicator in adherent living cells on the chamber slides (Tickner et al., 2011) and fresh tissue cryosections (Du et al., 2013). When added, DHE exhibits blue-fluorescence in the cytosol until oxidised to 2-hydroxyethidium (excitation: 500-530 nm; emission: 590-620 nm) by $\text{O}_2\text{-}$ and ethidium (excitation: 480 nm; emission: 576 nm) by other sources of ROS, where it intercalates with chromosomes of the cells and

stains the nucleus fluorescent red. Due to the possibility of artificial result from the similar wavelengths of 2-hydroxyethidium and ethidium, a low concentration of DHE and control with tiron ($O_2\cdot^-$ scavenger) was used. In addition, this detection was used alongside the lucigenin chemiluminescence for a better interpretation of the result.

In this study, DHE was used as an $O_2\cdot^-$ indicator in fresh tissue cryosections. First, sections of the fresh brain tissues from different designated time points post iv bolus injection (PK analysis), and hearts from AngII-induced p47^{phox} KO model samples were prepared by first embedding the tissue on a cork disk with optimal cutting temperature compound (OCT) and then being cut by a Bright 5040 Cryostat (Bright Instruments, UK) at $-20\text{ }^\circ\text{C}$, with a cutting thickness set to $6\text{ }\mu\text{m}$. Three sections from one sample were set onto one slide.

In situ $O_2\cdot^-$ production by the sections was then detected using $4\text{ }\mu\text{M}$ DHE. Specifically, DHE buffer made up of HBSS with 80 mM MgCl_2 and 1.8 mM CaCl_2 was prepared and pre-warmed in a $37\text{ }^\circ\text{C}$ water bath (Grant Instruments, United Kingdom) and $4\text{ }\mu\text{M}$ DHE in DHE buffer (DHE staining solution) was freshly made and wrapped with aluminium foil. Five microns frozen sections were dried and put in a humidified chamber and applied with DHE buffer and were equilibrated at room temperature for 20 min. After equilibration, controlled sections were treated with 100 mM Tiron (Sigma-Aldrich, United Kingdom) in DHE buffer for 10 min before the application of DHE. The application of $30\text{ }\mu\text{l}$ DHE staining solution ($4\text{ }\mu\text{M}$ DHE) was then carried out, and the slides were immediately put under Nikon Eclipse Ti2-E inverted microscope with a red fluorescent filter (excitation: $530\text{-}560\text{ nm}$; emission: $575\text{-}650\text{ nm}$) for observation and obtaining images. All the images were captured under $20\times$ magnification ($1024\text{ pixels} \times 1024\text{ pixels}$) within the seven minutes of slides being

under the microscope. At least ten images per slide and three sections per mouse sample were taken and quantified using ImageJ 1.50i (NIH, USA) by measuring fluorescent intensity.

2.8 Malondialdehyde (MDA) assay

Another indicator of oxidative stress is lipid peroxidation, mediated by free radicals in the body and resulted in the deterioration of the polyunsaturated lipids (usually the biological membranes) (Rosenblum, Gavaler & Vanthiel, 1989). MDA can be formed during this process as follows. With the presence of a carbon-carbon double bond in the fatty acid, the carbon-hydrogen bond becomes weakened and therefore, gets attacked by free radicals. As a result, peroxy radical can be formed and react with other polyunsaturated fatty acids and form lipid hydroperoxide (Sen, Packer & Hänninen, 2000; Wills et al., 1997). By propagating continually, this chain reaction can produce MDA as one of the products. Therefore, MDA can be an indicator of the free radicals in the detecting system (Folmer et al., 2004; Oter et al., 2005).

In this study, the MDA level in different tissues was detected using its reaction with 2-thiobarbituric acid (TBA) to produce MDA-TBA adduct under low pH. MDA peroxidation assay was carried out using MDA kit (Catalogue No. MAK085, Sigma-Aldrich, UK) according to the manufacturer's instructions. Individually, 8 mg tissue was homogenised on ice in 400 µl MDA lysis buffer containing 4 µL of butylated hydroxytoluene (100×) to prevent auto-oxidation and sodium lauryl sulfate (SDS) for a better lysis effect. 200 µl of the homogenate was then taken out for reacting with 600 µl TBA (one bottle dissolved in 7.5 ml glacial acetic acid and 17.5 ml water) at 95 °C for 1 h. 200 µl MDA-TBA adduct formed was loaded to a transparent 96-well plate and then (Evergreen Scientific, USA) detected using SpectraMax 340PC (Molecular

Devices, USA) at an absorbance of 532 nm (A532). For the standard curve, 10 µl MDA standard solution (4.17 M, supplied in the kit) was first diluted in 407 µl water to prepare a 0.1 M MDA standard stock and then 20 µl of the stock was diluted in 980 µl water to form 2 mM MDA. To a final volume of 200 µl each well, 0, 2, 4, 6, 8, and 10 µl of the 2 mM MDA was added to form a final concentration of 0, 20, 40, 60, 80 and 100 µM of MDA.

2.9 Amplex Red assay

Alongside examination of O₂⁻ production and lipid peroxidation, Amplex Red assay was also used for detecting the level of H₂O₂ production. Amplex Red is a colourless and nonfluorescent chemical. With the appearance of H₂O₂, Amplex Red can be oxidised into resorufin in a 1:1 ratio catalyzed by horseradish peroxidase (HRP). Since resorufin is a fluorochrome with excitation/emission wavelengths at 570 nm/ 585 nm, the signal can then be detected by a fluorescence plate reader with the set filter.

During the assay, 15 µl of heart homogenates and 5 µl HBSS were added to each well of a black, flat-bottom 96-well plate (Evergreen Scientific, USA). H₂O₂ standards were prepared by first 1: 5000 diluting 30% H₂O₂ (Sigma-Aldrich, United Kingdom) in sterilised water, then diluting 1:100 in 0.50 mM potassium phosphate buffer (pH=7.7) to make up 20 µM H₂O₂ solution. 10 µl 0, 0.0625, 0.125, 0.25, 0.5, 1, 2 µM H₂O₂ in duplicates were prepared for standard curve plot, and 50 µl potassium phosphate buffer was added to each standard well. For the measurement wells, 10 µl of PBS was added, and for the control wells, 10 µl of 1000 U/ml of catalase was added. The plate was incubated at 37 C° in darkness for 5 min and at the same time taken to FluoStar OPTIMA (BMG LabTech, United Kingdom) which was set at 37 °C. During the incubation, 4 ml Amplex Red solution containing 25 mmol/L 4-(2-hydroxyethyl)-

1-piperazineethanesulfonic acid (HEPES), pH 7.4, 0.12 mol/L NaCl, 3 mmol/L KCl, 1 mmol/L MgCl₂ was prepared by adding 10 µl Amplex Red (10mM stock solution), 4.8 µl HRP (1U/µl stock solution) and 40 µl glucose 6-phosphate (20 mM stock solution). 2 ml 1 mM NADPH in sterilised water was also prepared. Before the analysis, besides the machine, 50 µl Amplex Red solution was added to each well. The machine was adjusted to read fluorescence at 37 C° with the filter set to excitation: 570 nm/ emission: 585 nm. 25 cycles with 3 min intervals between each reading. 20 µl 1 mM NADPH solution was added to the control and measurement wells before the first reading.

2.10 Western blot

Western blot involves several procedures, including protein mixture separation by SDS–polyacrylamide gel electrophoresis (SDS-PAGE), electro-transferring to appropriate membranes and immunodetection using specific antibodies. It is one of the most commonly used techniques in a research laboratory and has been extensively described previously (Burnette, 1981). This method analyses the proteins of interest using a spatial resolution in which protein mixture is separated according to their different molecular weight and transferred to a suitable membrane on which the protein of interest can serve as an antigen and be recognised by specific antibodies. Since the primary antibodies can be recognised by secondary antibodies which are conjugated with enzymes such as HRP, when the substrate of the HRP is applied on the membrane, chemiluminescence signal could be generated. There are also other available conjugates to the secondary antibodies that generate different signals during the detection, and in this study, HRP conjugated secondary antibodies were used. The general principle of membrane-based western blotting is demonstrated below in **Figure 2.6**.

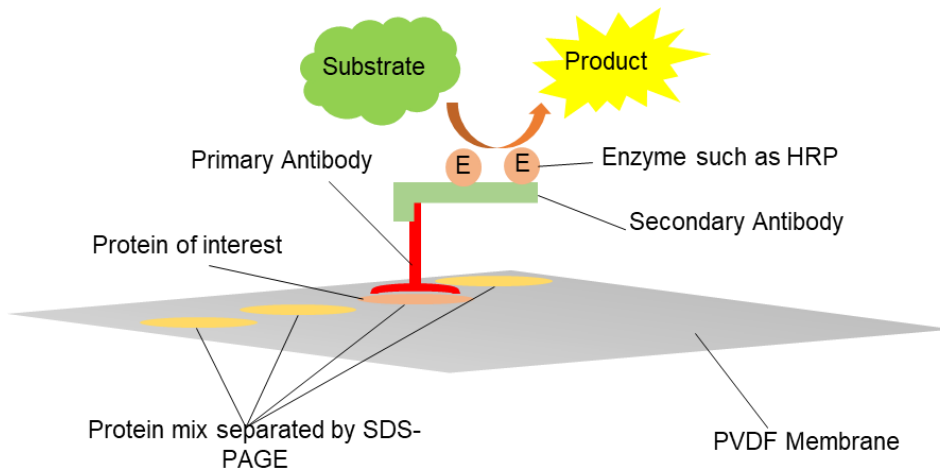


Figure 2. 6 General principles of Western Blot.

2.9.1 Sample preparation

Fresh or frozen tissues were weighed, grinded and homogenised (1 mg/10 μ l) in ice-cold protein lysis buffer containing 50 mM Tris-HCl (pH=7.4), 250 mM NaCl, 5 mM ethylenediaminetetraacetic acid (EDTA, pH=8.0), and 0.3% Triton-X100. In general, 20 mg tissues/per sample was used for protein preparation. For the western sample loading stock, 100 μ l for each sample which contains 33.3 μ l 3x sample loading buffer containing 0.3 M Tris-HCl (pH=6.8), 20 mM SDS, 30 % glycerol, 0.5 mg/ml bromophenol blue and 6 μ l 2-mercaptoethanol, and SIGMAFAST™ protease inhibitor tablets (catalogue No. S8820, Sigma-Aldrich, UK) was used according to manufacturer's instruction. 500 μ g protein diluted in protein lysis buffer (to form the final volume of 100 μ l) were prepared, aliquoted to 20 μ l each and stored at -20 °C for western blot analysis.

2.9.2 Gel preparation

Separating buffer containing 180 mg/ml Tris-base (pH=8.8) and 4 mg/ml SDS and stacking buffer containing 60 mg/ml Tris-base (pH=6.8) and 4 mg/ml SDS was able to be stored at 4 °C for maximum one year. The stock concentration of acrylamide

was 40%, and 10% acrylamide was used for 12-150 kDa protein separation. 0.1 g/ml ammonium persulfate (APS) dissolved in water was used. TEMED is for tetramethyl ethylenediamine. The glass was marked at the 4th well of the 10-well comb for the appropriate size of separating gel. Before the preparation of the SDS gels, the glasses (short plate and spacer plate with 1.0 mm integrated spacers, Bio-Rad, UK) was wiped using 70% (v/v) ethanol until completely clean. The separating gel was first prepared, as shown in **Table 2.2** (for two gels).

Table 2. 2 Reagents for separating gel preparation.

dH ₂ O	10 ml
separating buffer	5 ml
Acrylamide (40%)	5 ml
APS	120 µl
TEMED	12 µl

A small amount of butanol: water 1:1 was added on the top after pouring in the separating gel mix to keep the top of the gel flat and get rid of bubbles. After the gel is completely set (about 40 min), butanol was removed, and the gel was gently washed using water. After preparing the separating gel, stacking gel was then prepared, as shown in **Table 2.3** (for four gels).

Table 2. 3 Reagents needed for stacking gel preparation.

dH ₂ O	7.5 ml
stacking buffer	3 ml
Acrylamide	1.5 ml
APS	160 µl
TEMED	16 µl

As stacking gel was easy to set, the mix was quickly poured in, and the comb was immediately set in.

2.9.3 Sample loading

Two gels with the glasses were assembled on one Mini-PROTEAN® Tetra Electrode (Catalogue No. 1658037, Bio-Rad, UK) and up to four gels could run together on one Mini-PROTEAN® Tetra Vertical Electrophoresis Cell (Bio-Rad, UK). The running buffer (pH=7.4) used was made of 6 mg/ml Tris-base, 29 mg/ml glycine, and 1 mg/ml SDS, and the samples prepared in section 2.9.1 was heated at 95 °C for 3 min before 10 µl was loaded to each well. 4 µl of the protein marker Precision Plus Protein™ Dual Colour Standards (Catalogue No. 1610374, Bio-Rad, UK) was used for each gel (**Figure 2.7**).

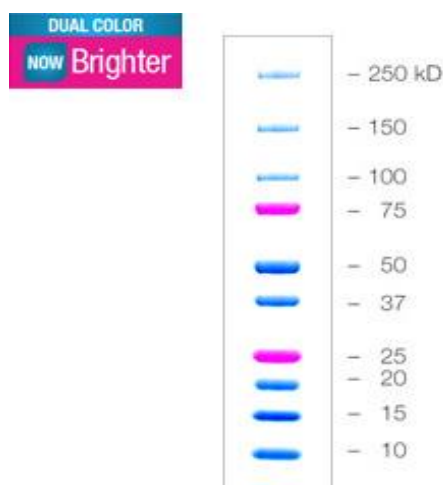


Figure 2. 7 Precision Plus Protein™ Dual Colour Standards for molecular weight estimation of the protein of interest.

2.9.4 Protein separation

For separating the loaded proteins, Mini-PROTEAN® Tetra Vertical Electrophoresis Cell was connected to PowerPac™ Basic Power Supply (Catalogue No. 1658025FC, Bio-Rad, UK), and set at 80 V for approximately 30 min to let the samples pass through the stacking gel. The Electrophoresis Cell was then adjusted to 110 V until the lowest band of the marker reached the bottom of the gel.

2.9.5 Transfer

The semi-dried transfer method was used in the experiments. Polyvinylidene fluoride (PVDF) membrane (Immun-Blot® Membrane, Catalogue No. 1620177, Bio-Rad, UK) was used for the transfer of the separated proteins. The membrane was first cut into 8 cm (length) × 6 cm (width). Before transferring, all membranes were immersed in methanol for 2 min to wash off any traces of contamination. The blot absorbent filter papers (Catalogue No. 1703966, Bio-Rad, UK) were soaked up in 300 ml transfer buffer (3.75 mg/ml Tris-base, 18 mg/ml glycine and 25% methanol) for about 3 min until it was completely wet. Then on a Trans-Blot® SD Semi-Dry Transfer Cell (Catalogue No. 1703940, Bio-Rad, UK), one 'sandwich' for each PVDF membrane containing filter paper, PVDF membrane, the SDS-PAGE gel (with stacking gel cut off) and filter paper (from bottom to the top) was made. The lid was then put on to assemble the cell fully, and the cell was connected to the PowerPac™ Basic Power Supply with the voltage set at 15 V for one hour.

2.9.6 Detection

After transferring, PVDF was then taken out and washed in milk (5 g skimmed milk powder in 50 ml Tris buffered saline-Tween (TBST). Primary antibody (in the milk, dilution referring to manufacturer's recommendation) was then applied to the membrane, placed on an orbital shaker (catalogue No. SSM1, Stuart, UK) and incubated at 4 °C overnight.

The following day, secondary antibodies were prepared according to the host species of the primary antibody (usual dilution is 1:2000 in milk). Before adding the secondary, the membrane was washed with TBST for 10 min, TBS for 10 min and then phosphate-buffered saline (PBS) for 10 min. After washing, the secondary antibody

was added, and the membrane was left on the orbital shaker for one hour at room temperature. After the incubation, the membrane was rewashed using TBST, TBS and then PBS for 10 min each.

The detecting solution was Clarity Max™ western enhanced chemiluminescence (ECL) blotting substrates (catalogue No. 1705062, Bio-Rad, UK) and used according to the manufacturer's instruction. Specifically, for each membrane, 100 µl of Clarity Western ECL substrate and 100 µl of Peroxide Solution & Luminal was mixed and applied for the best effect. The membrane was then visualised by a BioSpectrum AC Imaging System (UVP, UK). Ten images over 20 min were captured using UVP LabWork 4.0 software. The optical density (OD) of each band was then measured using Image J 1.50i (NIH, USA) and the increase/decrease fold of the protein of interest was calculated by normalising to β -Actin or the relevant total proteins.

2.11 Immunofluorescence

Like western blot, antibodies used in immunofluorescence are to detect the expression pattern of the protein of interest by recognising the specific antigens, and the difference is that by visualising the sections under the microscope, the subcellular expression pattern and location (or translocation) of the proteins in the cell (Turner & Shields, 1984). Most used immunofluorescence method in this lab is direct which includes the application of primary antibody recognising the protein of interest on the section, and the application of fluorescent group conjugated (FITC (Riggs, 1978) or Cy3 (Ernst et al., 1989)) secondary antibody which binds to the primary antibody. 4', 6-diamidino-2-phenylindole (DAPI) (Kubista, Akerman & Norden, 1987) was used to visualise the nuclei. The sections were then observed under the Nikon A1R confocal microscope or Nikon Eclipse Ti2-E inverted microscope with a magnification of 20×

or 40×. The intensity of the fluorescent signals given under fluorescent microscope or confocal microscope can then be quantified using Image J 1.50i (NIH, USA).

2.11.1 Section preparation

Since the immunofluorescence was carried out mostly on frozen tissues collected, cryosections were mostly used in this study. Compared to paraffin sections which were also widely used in this lab, cryosections produce substantially less autofluorescence although it did not preserve the cellular structure as well.

For the preparation of the sections, a 3 mm × 3 mm size of the tissue cube from one-third lower part of the left ventricle of the harvested mouse hearts was cut and put on a cork disk (catalogue No. R30001-E, Pyramid Innovation Ltd, UK) which had a small amount of OCT on top. The tissue was then immersed by OCT and quickly dipped in liquid nitrogen pre-cold isobutane to decrease the likelihood of formation of the ice crystals. The sample with OCT was frozen immediately, and the isobutane was wiped using some tissue. The whole process was carried out carefully to avoid any bubbles formed, and the samples were then stored in -80 °C for future use.

Tissue sectioning is performed on a cryostat with Bright 5040 microtome (Bright Instrument, UK). The temperature was set as following: specimen -20 °C and chamber -25 °C, with the cutting thickness of 6 µm. Three sections were set on one slide. The slides were then set out to air dry for at least 10 min and then stacked, wrapped in tinfoil, and stored at -80 °C until needed. Sections can be stored for long periods at -80 °C if they adequately protected.

2.11.2 Fixation

The fixing reagent was made up of methanol: acetone = 1:1, which was pre-chilled at -20 °C for at least 1 hour before use. After taking out the sections from -80 °C, they were dried in front of a fan with the medium speed at room temperature for 15 min.

The slides were fixed by immersing in fixing solution for 9 min 30 s at 20 °C. After fixing, the slides were dried by a fan for 15 min and washed by ice-cold PBS (1×) for 5 min × 3.

2.11.3 Blocking

After the washing, the areas surrounding each section on the slides were dried with a medical wipe. Leaving a gap between each section ensured that each section would be treated individually. Also, when a wax pen was available, an area around each section was drawn to make sure fluid did not flow from section to section. The order of wiping the slide and the areas needed to be dried are demonstrated below in **Figure 2.8**.

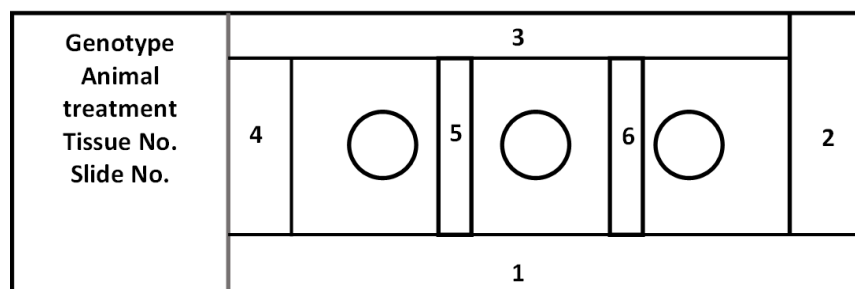


Figure 2. 8 The wiping of the slides. The numbers are used for indicating the order of wiping.

The slides were then blocked using 30 μ l 2% BSA in PBS with 5 μ l of Triton X-100 (Sigma-Aldrich, UK) per section for 1 hour at room temperature inside a humidified chamber.

2.11.4 Application of primary antibody

Slides were then washed using ice-cold PBS for 3 min and dried using the same method described in **Figure 2.8**. Primary antibodies were prepared by being diluted 1:100 in 0.2% BSA in PBS (or according to manufacturer's instruction) and applied 30 μ l each section. The slides were then incubated at room temperature for 1 hour or at 4 °C overnight.

After the incubation, the slides were held horizontally to drain the antibodies onto the tissue paper and were flushed by stiller water to rinse the remaining antibodies. Slides were then washed by ice-cold PBS for 5 min \times 3 and dried in the same way.

2.11.5 Application of secondary antibody

The sections after incubating with the primary antibody were then probed with secondary antibody conjugated with FITC or Cy3 (1:200 diluted in 0.2% BSA) for about an hour in a light-protected humidified chamber at room temperature. Slides were then drained in the same way to rinse off the remaining antibodies, washed 5 min \times 3 using ice-cold PBS and dried the same way as described in section 2.10.4.

If there were triple staining (with another protein of interest), the other primary antibody was only allowed maximum 1 hour before the application of secondary

antibody (1 h incubation time), and the relatively more potent primary antibody was used to minimise the diffusion of the first staining.

2.11.6 Application of 4', 6-diamidino-2-phenylindole (DAPI) to visualise the nuclei

At the end of incubation with the fluorescein isothiocyanate (FITC) - or Cyanine-3 (Cy3) - secondary antibody, 10 μ l 0.5 μ g/ml DAPI was applied to each section for 5 min in the humidified chamber at room temperature for the visualisation of the nuclei. The slides were then immersed in ultrapure water briefly, wiped and dried the same way as described.

2.11.7 Mounting and observation

Mowiol® was used in the mounting reagent due to its properties. It takes hours to solidified, thus forming a permanent bond between the coverslip and the sample and it helps to stabilise the fluorescence at 4 °C. After the samples were washed and dried, antifade solution (0.1% p-phenylenediamine: Mowiol = 1:9) was applied to each section, with a coverslip being put on carefully to avoid bubbles.

A1R confocal microscope (Nikon, Japan) or Eclipse Ti2-E inverted microscope (Nikon, Japan) with a magnification of 20 \times or 40 \times were used to investigate the sections with FITC (excitation/emission: 470-495/510-550nm), Cy3 (excitation/emission: 530-560/575-650nm) and DAPI (excitation/emission: 360-370/420-460nm) filters within 12 hours then stored at 4 °C in a wooden slide box for the record.

2.12 Statistics

Unless specified, all the data presented in this study are presented as Mean \pm standard deviation (SD). It was also assumed that all the results measured and examined using statistical analysis followed a normal distribution. Statistics analysis was carried out using Prism GraphPad 7.0. One-way analysis of variance (ANOVA) is used for determining if there is statistical significance between two independent groups with one measurement variable and one nominal variable (McDonald, 2014), and is an extended version of Student's *t*-test when there are more than two groups (Gauthier and Hawley, 2007). In chapter 3, the statistical significance in the effect of apocynin on O₂-production and lipid peroxidation was examined using one-way ANOVA followed by a Bonferroni *post-hoc* test since there was the iv injection with or without apocynin as nominal viable, and different individual mouse as the measurement variable. *p* values equal to or less than 0.05 were denoted as statistically significant between the two groups. The statistical significance of different inhibitors for ROS production in the HFD brain was analysed using Student's *t*-test since the six parallel HFD brain samples were treated by all the inhibitors at the same time, then measured at the same time. The result of a *t*-test was the same as one-way ANOVA when only two independent groups were compared.

Due to the nature of the study in chapter 6, in which the mice (of the same strain, age and sex) with two different genetic background (WT or p47^{phox} KO) were subjected to two different treatment (saline or AngII infusion), two independent factors (different individual (measurement variable) and different genetic background or treatment (nominal variable)) in the statistical analysis were identified, and one-way ANOVA followed by a Bonferroni *post-hoc* test was used for the unless specified. A *p* value equal to or less than 0.05 was denoted as statistically significant, but *p* values between

0.05 and 0.1 were also stated. For the animal study on the blood pressure, heart weight and body weight, six or seven animals per group were recorded and subjected to statistical analysis; for the experiments of biochemical and molecular assessment of AngII-induced cardiac oxidative stress and signalling pathways, six animals per group were used for the experiments and subjected to statistical analysis.

2.13 Randomisation and blinding

For the setting up of the animal models, three to six mice of the same age, gender, and genotype were randomly caged and picked for different treatments in the study. To minimise the behavioural differences between groups, same housing conditions between different treatment groups were maintained throughout. For the immunofluorescence, DHE assay and DCFH-DA assay where imaging and measurement of fluorescence intensities were involved, the images obtained were labelled with a randomly assigned group number which was able to be traced, to make sure the scientist was blinded to the groups for each image analysed. For other studies, subjective decisions were not involved. Therefore, blinding was not believed to be necessary.

Chapter 3

Pharmacokinetics (PK) Studies and Evaluation of Apocynin in

Reducing Tissue Oxidative Stress in Mice

3.1 Introduction

NADPH oxidase (Nox), initially discovered in phagocytes, is one of the major sources of reactive oxygen species (ROS) generation in most types of mammalian cells (Babior, 1999). gp91^{phox}-containing NADPH oxidase (Nox2) is one of them. Its activation by a wide range of agonists such as AngII (Rajagopalan et al., 1996; Thakur, Du, Hourani, Ledent & Li, 2010) and glucose (Suh et al., 2007) and stress factors such as ageing, could lead to accumulating oxidative stress, which contributes to the development of many health problems such as cardiovascular diseases (Fan et al., 2014; Nabeebaccus, Zhang & Shah, 2011), metabolic disorders (Du et al., 2013; Fan et al., 2017) and neurodegenerative diseases (Cahill-Smith & Li, 2014).

Apocynin (4'-hydroxy-3'methoxyacetophenone) has been used as an effective inhibitor of Nox in the animal models (Du et al., 2013; Saleem, Prasad & Goswami, 2018; Gimenes et al., 2018; Qin et al., 2017; Feng et al., 2017; Kapoor, Sharma, Sandhir & Nehru, 2018; Langley et al., 2017; Rahman et al., 2017). Its mode of action, however, was not entirely understood. The specificity of apocynin was first demonstrated by its a selective inhibiting effect on O₂⁻ production in human polymorphonuclear neutrophils. It reduced the O₂⁻ production without interfering with other cellular defence mechanisms (Stolk et al., 1994). Barbieri *et al.* reported apocynin could reduce the expression and translocation of p47^{phox} during Nox2 activation (Barbieri et al., 2004). One study identified a symmetrical dimer of apocynin, diapocynin as a metabolite of apocynin in endothelial cells (Johnson et al., 2002), which was proven to

have an effect on reducing oxidative stress (Ismail et al., 2014) and therefore it was proposed at the time that diapocynin might be involved in the mode of action of apocynin. In contrast, one study identified apocynin as an antioxidant rather than an inhibitor in the vessels since diapocynin, unlike in leukocytes, was not formed either in vascular endothelial cells or SMCs (Heumuller et al., 2008). Moreover, (Chandasana et al., 2015) did not find diapocynin in apocynin-treated (intravenous (iv) bolus injection and oral dosing) rat plasma samples, so did not identify diapocynin as a metabolite. This result was in line with some other studies which identified apocynin glycoconjugate rather than diapocynin, in the plasma, brain and liver as its metabolite after iv (Okamura et al., 2018) and intraperitoneal (ip) (Wang et al., 2008) injection of apocynin. (Marin et al., 2017) excluded apocynin as a prodrug of diapocynin based on the same dose inducing a similar effect of both molecules on reducing experimental inflammation.

Despite its debatable mechanism, apocynin has been proven to be effective in reducing the oxidative stress in the development of cardiac disorders such as hypertrophy (Saleem, Prasad & Goswami, 2018) and diabetic cardiac remodelling (Gimenes et al., 2018), neurodegenerative diseases such as stroke (Qin et al., 2017), traumatic brain injury (Feng et al., 2017), ischaemia-reperfusion hippocampus injury (Kapoor et al., 2018), Parkinson's disease (Langley et al., 2017) and oxidative stress-mediated liver fibrosis (Rahman et al., 2017). Recently an orally available modified form of apocynin, called mito-apocynin, which specifically targets mitochondria, was synthesized and demonstrated a long-lasting effect of reducing brain oxidative stress in transgenic murine models (Ghosh et al., 2016; Langley et al., 2017). Still, some studies reported apocynin to have little effect on improving cardiac functions despite it being effective in reducing oxidative stress. Specifically, one study found that in diabetic

hypertensive rats, apocynin preserved the antioxidant activity in the heart, yet the myocardial function did not change significantly (Rosa et al., 2016).

On the other hand, apocynin was also reported to have an effect of increasing O₂⁻ production in some studies. It promoted O₂⁻ production, yet downregulated Akt activity in mouse embryonic stem cells, which suggested that apocynin, as a chemical molecule, acted independently from its typical function as a Nox inhibitor in the stem cells (Kucera et al., 2016a). The similar pro-oxidant effect was also found in some organism-free *in vitro* studies, and it was recognised as a toxic side-effect by (Castor, Locatelli & Ximenes, 2010), in which they also pointed out that it was not uncommon for antioxidants to possess pro-oxidant characters.

Pharmacokinetics and pharmacodynamics (PKPD) study link the effects of a drug to its concentration and metabolism in a body compartment (Negus & Banks, 2018), which might be able to provide answers to the contradictory findings on apocynin so far. Even though apocynin has been widely used as a Nox2 inhibitor, studies on its PKPD properties, such as absorption, distribution, metabolism, and excretion (ADME) and efficacy are still limited. Among the studies, one characterised its PK parameter using an in-house developed LC-MS/MS method with a satisfactory level of sensitivity (Chandasana et al., 2015). However, the retention time of apocynin in their method (0.45 – 0.50 min) was short, leaving people questioning if the analyte used in the study was retained and separated enough to achieve a convincing result. Another study characterised its dose-dependent metabolism in the brain using ip injection yet it failed to address to what extent it was able to penetrate the blood-brain barrier, or its absorption rates, systemic distributions, toxicity, and the reason behind its rapid metabolism rate observed in the study (Okamura et al., 2018). In summary, despite the studied inhibitory effects of apocynin and its downstream signalling

pathways as a Nox inhibitor, there is a lack of characterisation of apocynin PK properties as a drug, i.e. its ADME *in vivo*. More importantly, based on the previous studies, the efficacy, selectivity, and oxidative side effects of apocynin needs further exploration.

3.1.1 Aims and objectives

This chapter aims to investigate the *in vivo* PKPD of apocynin in mice. Specifically, there are five objectives in total:

1. To develop an in-house method for apocynin extraction and detection in different tissues using HPLC-MS/MS;
2. To characterise apocynin PK by intravenous administration (iv bolus, 5 mg/kg) to male CD1 mice (12 weeks of age) and analyse the data by NCA and NLME simulation and modelling in Phoenix WinNonlin 8.1;
3. To characterise tissue distribution of apocynin in urine, brain, heart and liver using the established extraction and detection method;
4. To investigate its effect on tissue oxidative stress (the time delay and magnitude of the O₂·⁻ production) using the same tissues collected to build a relationship between the *in vivo* absorption, metabolism of apocynin and its efficacy;
5. To evaluate the therapeutic effect of apocynin on oxidative stress in the brain in dietary-induced middle-aged obesity murine model.

3.2 Materials and methods

3.2.1 Chemicals and reagents

Apocynin with an HPLC purity of 96%, diapocynin with an HPLC purity of 98%, phenacetin (N-(4-ethoxyphenyl) acetamide) with an HPLC purity of 98%, used as internal standard, and ammonium acetate \geq 98% for molecular analysis were obtained from Sigma Aldrich, UK. Methanol, water, acetonitrile of LC-MS grade, and ethanol of HPLC grade were purchased from Fisher Scientific, UK. A more detailed list of reagents used can be found in section 2.1.

3.2.2 Animal Models

3.2.2.1 PK model

Information on the standard housing conditions and detailed procedures are described in section 2.2. For PK analysis, CD1 male mice at 12-week of age were used. Before PK analysis, mice fasted overnight with free access to water.

On the day of the experiment, the injection stock was freshly prepared by dissolving apocynin (50 mg/ml) in ethanol. Injection solution was then prepared by 1:50 (v/v) further diluting the stock in ultrapure water, to form the final apocynin concentration at 1.0 mg/ml. With a non-invasive mouse restraint (**Figure 3.1 A**), 5.0 mg/kg iv bolus injection of apocynin was administered using a 0.5 ml 0.33 mm (29G) \times 12.7 mm Micro-Fine Insulin Syringe (BD, UK) via a lateral tail vein (**Figure 3.1 B**). In parallel, the same volume of diluent used for apocynin (Ethanol: ultrapure water 1:50 (v/v)) as the vehicle was injected to the control group. At least three mice per time-point were used.

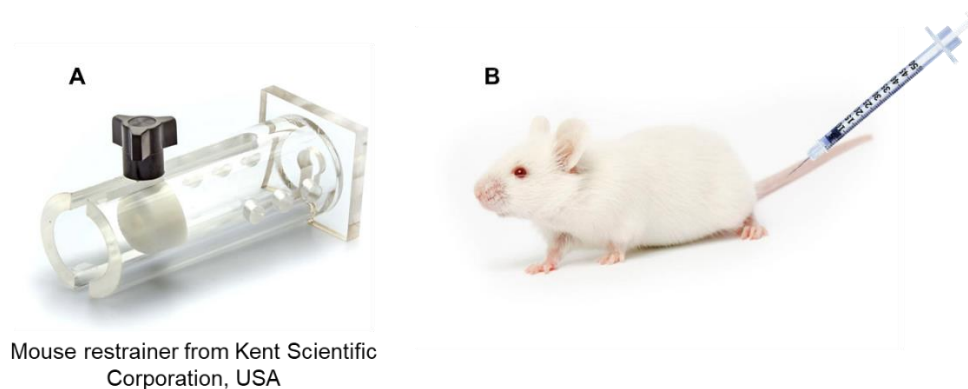


Figure 3. 1 The non-invasive mouse restraint (A) and tail vein injection (B).

After iv bolus injection of apocynin, mice were sacrificed at 1 min, 2.5 min, 5 min, 15 min, 30 min, 60 min, 180 min, 360 min 720 min and 1440 min and the collected tissues were processed as described in section 2.3.1. In summary, the workflow is illustrated in **Figure 3.2**.

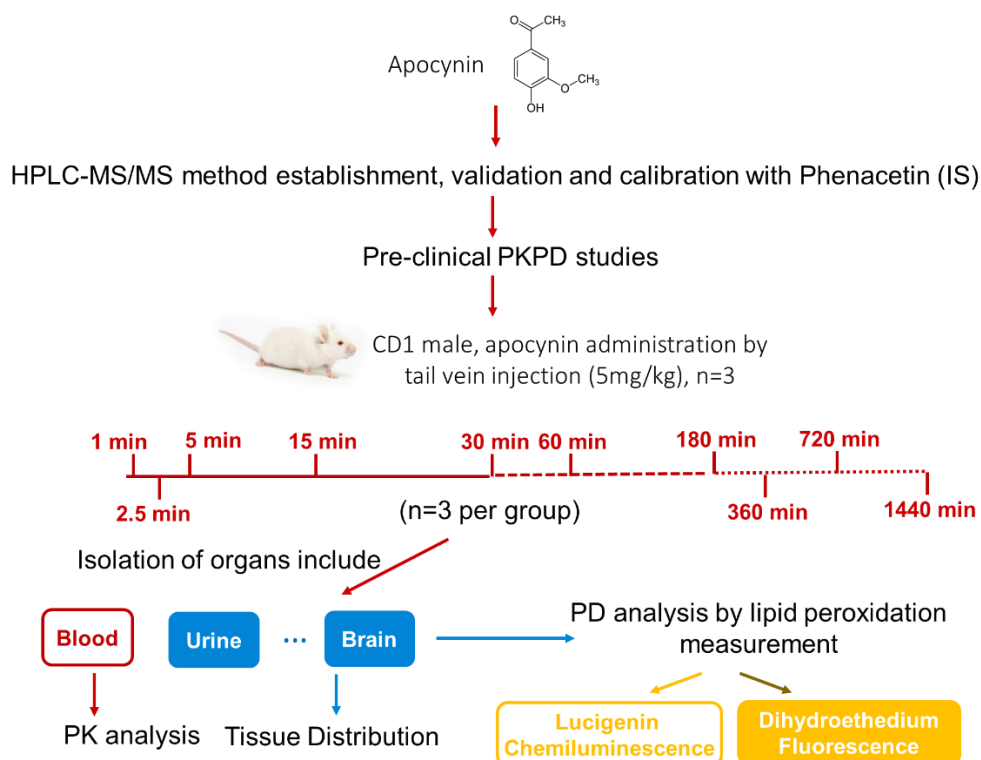


Figure 3. 2 A schematic diagram of the design and workflow of PKPD characterisation of apocynin.

3.2.2.2 Dietary-induced middle-aged obesity murine model

In addition to the standard PKPD study of apocynin, the HFD-induced middle-aged obesity murine model, previously set up by Prof. Li (my supervisor), was also used for a more comprehensive understanding of the therapeutic effect of apocynin.

The murine model was established by feeding an HFD (45% kcal fat) or normal chow diet (NCD, 12% kcal fat) (Special Diets Services, Essex, UK) to male littermates of wild type (WT) and Nox2 KO C57BL/6 mice for four months at the age of 7-month old (n=6 per group). At the same time, apocynin (5 mM supplied in the drinking water) was supplied to one of the WT-HFD groups. The tissues were harvested and preserved in liquid nitrogen and then stored at -80 °C. At the time of analysis, samples were processed by the same method for either HPLC-MS/MS sample analysis or lucigenin chemiluminescence. Here the model set-up along with the analysis is demonstrated in **Figure 3.3**.

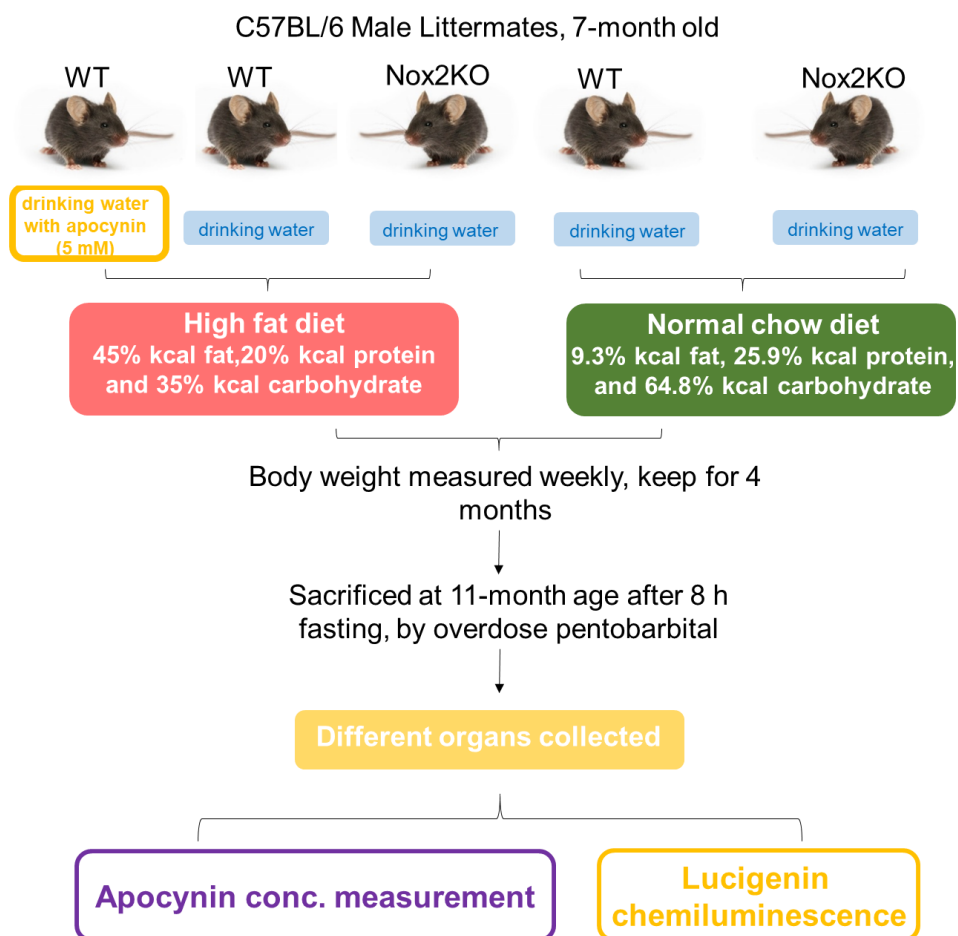


Figure 3. 3 A schematic diagram of the establishment and the analysis of the middle-age diet-induced obesity murine model.

3.2.3 Calibration standards preparation

For the establishment of HPLC-MS/MS detecting method, apocynin and phenacetin stocks were made by dissolving 5.0 mg compound in 0.1 ml of methanol, and further diluted 50 times with water to form a final stock of 1.0 mg/ml. 1 ml of each calibration standard of apocynin was then made by further diluting to different concentrations (1, 5, 10, 50, 100, 500, 1000 and 5,000 ng/ml) with water. A fixed phenacetin concentration (500 ng/ml) in diluent was used. The limit of blank, the limit of detection and the limit of quantification were obtained by running the calibration standards using established HPLC-MS/MS (described in section 3.2.5 and section 2.4).

These standards were also used for the selection of different mobile phases and optimisation of the gradients for HPLC-MS/MS method.

3.2.4 Sample processing

Compared to the time-consuming solid-phase extraction methods of apocynin (Chandasana et al., 2015), we adopted a method using 100 µl acetonitrile and 60 µl methanol for 100 µl biological sample processing, which demonstrated a high recovery rate in all biological samples in this study (Wang et al., 2013). The apocynin calibration standards of plasma, urine and tissues were made by first diluting apocynin stock to different concentrations with the diluent. The stock of phenacetin was made to 7,500 ng/ml with the diluent.

When processing samples, fixed volumes of calibration apocynin with a known concentration (20 µl) and phenacetin (20 µl) were added to the matrix and organic solvent (for protein crash). The final calibration concentrations of apocynin were 1, 5, 10, 50, 100, 500, 1,000, and 5,000 ng/ml with a fixed phenacetin concentration of 500 ng/ml. The details on the sample collection preparation are listed in sections 2.3.1. For apocynin extraction from the collected samples, proteins in the matrix were precipitated by adding 60 µl methanol and 100 µl acetonitrile, vortexing for 1 min and centrifuging at 17,000 g for 20 min at 4 °C. 250 µl supernatant per sample was collected, filtered using 0.20 µm pore size Nylon syringe filter (Sigma-Aldrich, UK), further diluted in mobile phase buffer A (480:20:0.38 water: methanol: ammonium acetate (v: v: w)), and injected into HPLC-MS for analysis. For experiment samples collected at different designated time points after iv bolus, the sample collection and processing were carried out in the same way except for not spiking in apocynin with known concentrations. Instead of apocynin, 20 µl of the diluent was added in parallel with calibration samples

and were processed the same way. Since apocynin is sensitive to light, 2 ml amber HPLC vials (Sigma-Aldrich, UK, catalogue No. 27083-U) were used. The detailed processing steps are illustrated in **Figure 3.4**.

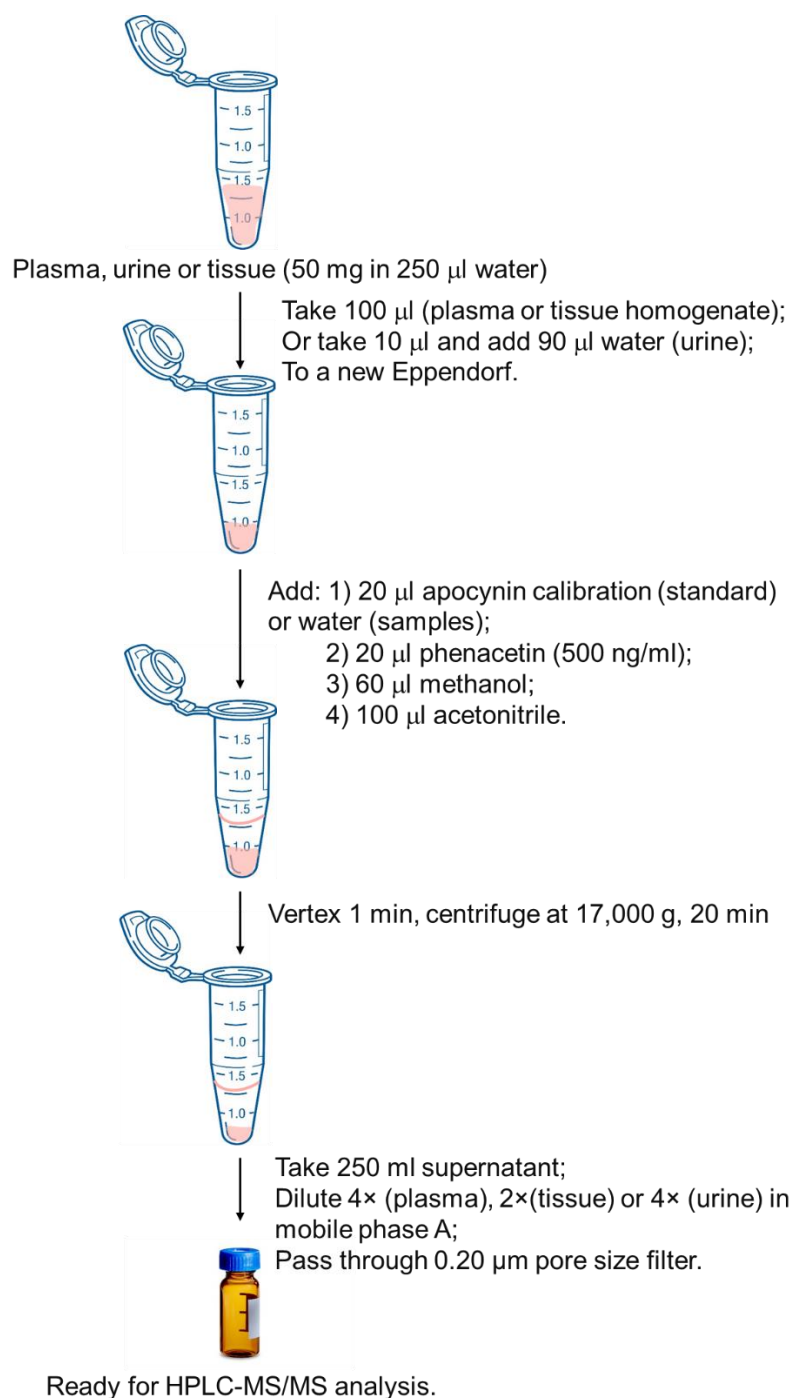


Figure 3. 4 Workflow of apocynin extraction from different biological samples for HPLC-MS/MS analysis.

3.2.5 HPLC-MS/MS method specific to apocynin detection

The details on HPLC-MS/MS instrument and the column used are listed in section 2.4.1. For the separation and detection of apocynin, mobile phase buffers (A) 480:20:0.38 water: methanol: ammonium acetate (v: v: w) and (B) 20:480:0.38 water: methanol: ammonium acetate (v: v: w) with a gradient as follows: held on 5% B for 1 min; between 1 min and 10 min ramped up to 100% B; dropped back down to 5% B over 1 min and held on this for 4 min were employed. The flow rate was 200 μ L/min throughout. The autosampler was maintained at 20° C and the column at 25° C. Before entering the MS, the flow was diverted to waste for the first 4 min, then directed into the MS for 8 min and back to waste for the final 3 min. This method was proven to be able to generate satisfactory peaks for both phenacetin (**Figure 3.5**) and apocynin (**Figure 3.6**) in different organ samples, including plasma, urine, brain, liver and heart.

For quantification, the instrument was operated in negative ionisation mode. Selected transitions for apocynin and phenacetin, at m/z, were: 165.0 \rightarrow 150.0 \pm 5.0 and 178.1 \rightarrow 149.1 \pm 5.0, respectively for better selectivity. Good linearity of apocynin was found in the range of 100 – 100,000 ng/ml in plasma and other tissue organs.

The quantification analysis was carried out using Thermo Xcalibur 3.0 (ThermoFisher, U.S.A.) and the detailed settings on the software are listed in section 2.4.2.

3.2.6 PK analysis of apocynin

The profiles of apocynin concentrations in murine plasma versus time were subjected to NCA (1-30 min) and NLME (1-6 h) model. The detailed methods on the analysis are listed in section 2.5.

3.2.7 Tissue distribution of apocynin

Tissue samples and the corresponding calibrations of different tissues were processed as described in the sample collection and preparation (Section 2.3) and sample processing (3.2.4). The concentration of apocynin in different tissues was determined by the established HPLC-MS/MS method (3.2.5).

3.2.8 Effect of apocynin on tissue ROS production

In order to further understand the real-time effect of apocynin on ROS production, tissues from different designated time points (1 min to 360 min) were processed and the O_2^- was measured by lucigenin chemiluminescence (section 2.6) and DHE assay (section 2.7), and the lipid peroxidation was measured by detecting the level of MDA (section 2.8). The effect of apocynin on reducing the O_2^- level in HFD-induced obesity model was also tested using the lucigenin assay, and the enzymatic source of the O_2^- was investigated using different enzyme inhibitors for ROS production (section 2.6).

3.3 Results

3.3.1 Establishment of HPLC-MS/MS method for apocynin and phenacetin detection

There are different existing HPLC and HPLC-MS/MS methods reported for the determination of apocynin in biological samples, most having some weaknesses such as extremely short retention time (Chandasana et al., 2015) or low level of sensitivity (Wang et al, 2013). To set up a satisfactory detecting method with a good sensitivity, a reasonable retention time and a reasonably symmetrical peak shape for both apocynin and phenacetin (as the internal standard (IS)), we optimised the mobile phase, adjusted the injection volume (reduced from 10 μ l to 5 μ l) and developed the HPLC-MS/MS method as described in section 3.2.5. This HPLC method was proven to be able to generate good separation and satisfactory peaks for both phenacetin (IS) (**Figure 3.5**) and apocynin (**Figure 3.6**) in different organ tissues.

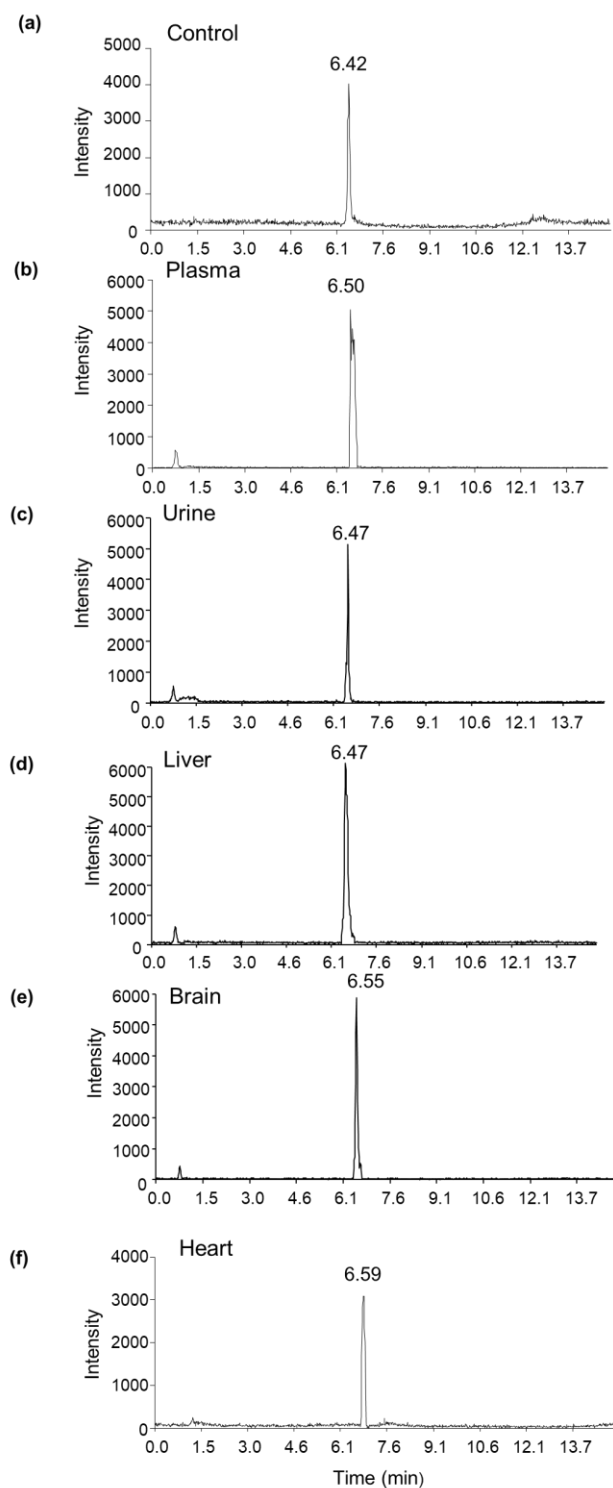


Figure 3. 5 Representative HPLC-MS/MS of phenacetin (IS) in different samples.

Representative selected-reaction-monitoring HPLC-MS/MS chromatograms of phenacetin in (A) the plasma spiked with 500 ng/ml phenacetin (control), (B) plasma, (C) urine, (D) brain, (E) liver and (F) heart.

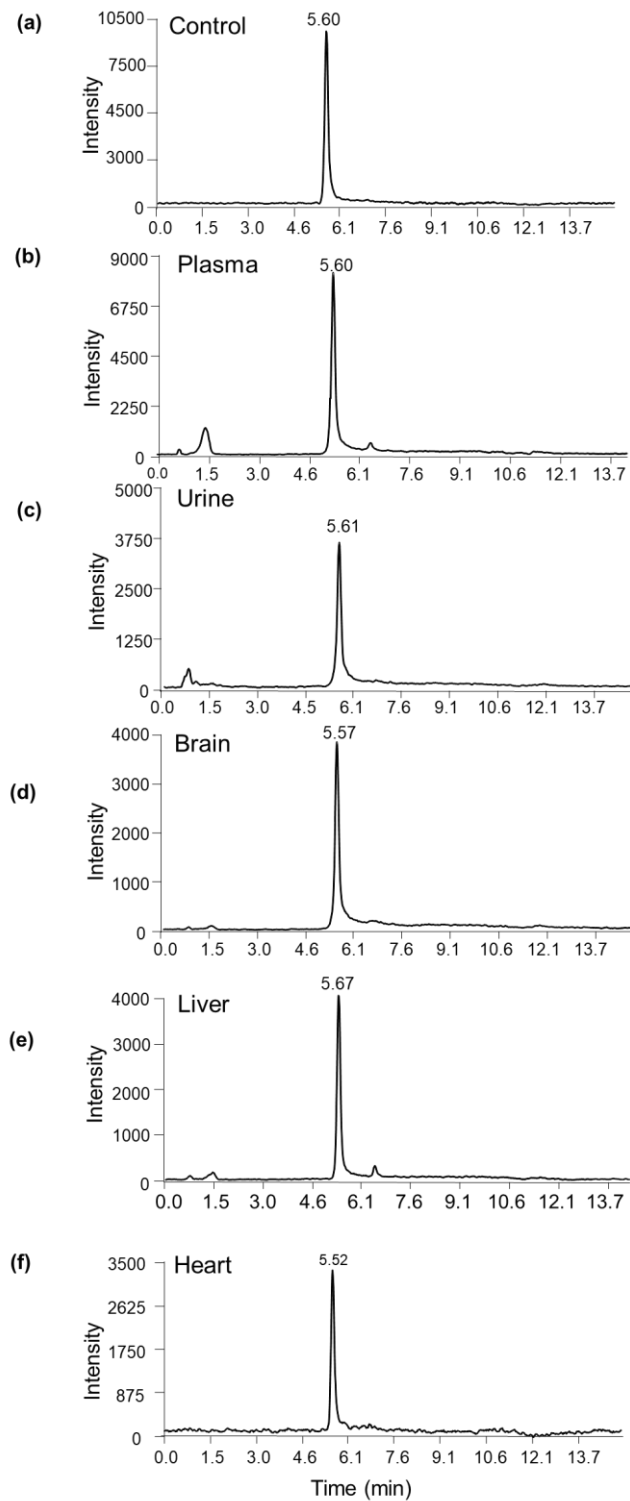


Figure 3. 6 Representative HPLC-MS/MS of apocynin in different samples.

Representative selected-reaction-monitoring HPLC-MS/MS chromatograms of apocynin in (A) the plasma spiked with 500 ng/ml apocynin, (B) plasma, (C) urine, (D) brain, (E) liver and (F) heart.

Full scan and fragmentation optimisation of apocynin was performed by running apocynin (5,000 ng/ml) through the HPLC-MS method with the Orbitrap under the negative HESI mode. The full scan spectrum of apocynin is shown in **Figure 3.7**.

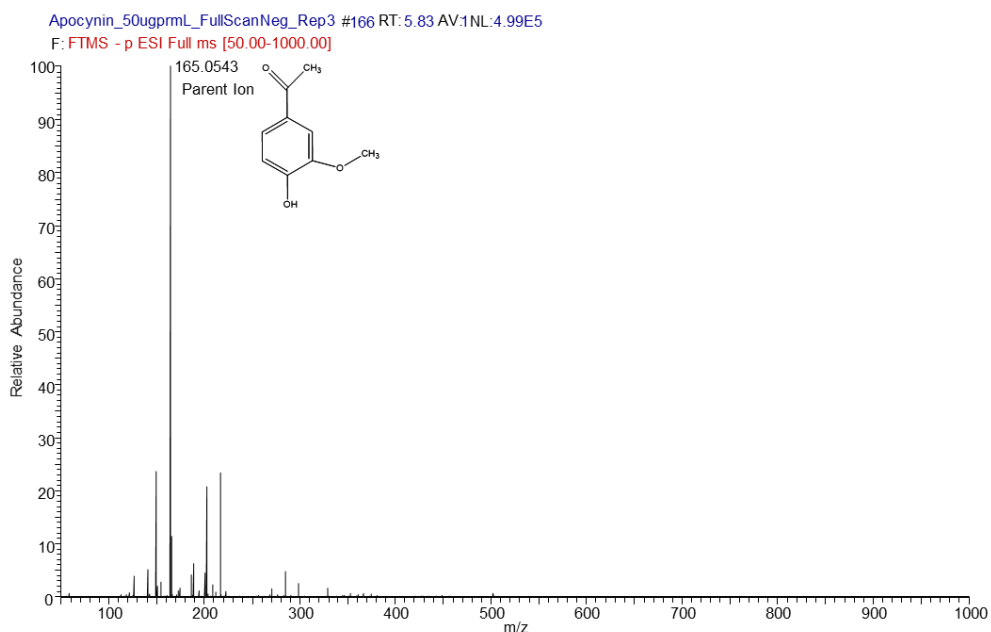


Figure 3. 7 Representative mass spectrum of apocynin.

Spectrum was obtained from calibration standards of apocynin (5,000 ng/ml) in negative HESI mode. Full scan spectrum of apocynin shows prominent parent ion at m/z 165.0543.

Diapocynin (5,000 ng/ml) was also analysed using the established HPLC-MS method for apocynin for further tissue diapocynin measurement. The full scan mass spectrum (**Figure 3.8**) showed that the current HPLC-MS/MS settings for apocynin (section 2.4.1 and section 3.2.5) could also be used for diapocynin detection.

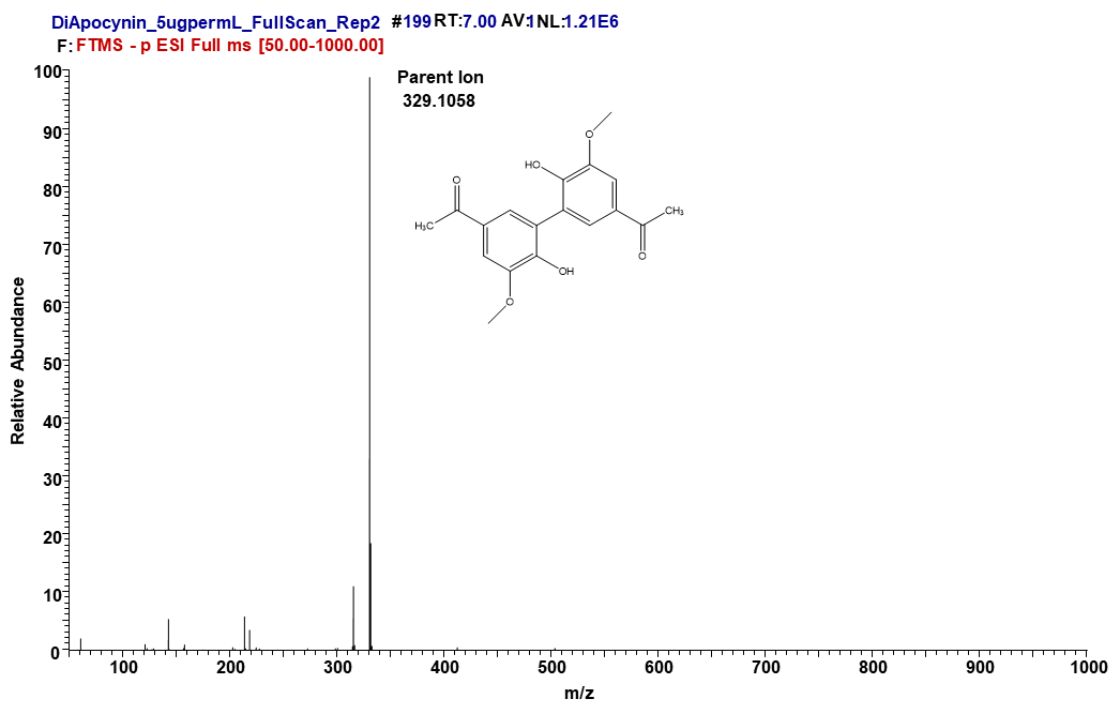


Figure 3. 8 Representative mass spectrum of diapocynin, showing prominent parent ion at m/z 329.1068.

Diapocynin was also detected by the established HPLC-MS/MS method (section 2.4.1) without internal standard. No diapocynin was detected in plasma, brain or liver samples from the same CD1 mice iv bolus injected with apocynin up till 30 min, which agreed with the study from (Okamura et al., 2018) and (Wang et al., 2008).

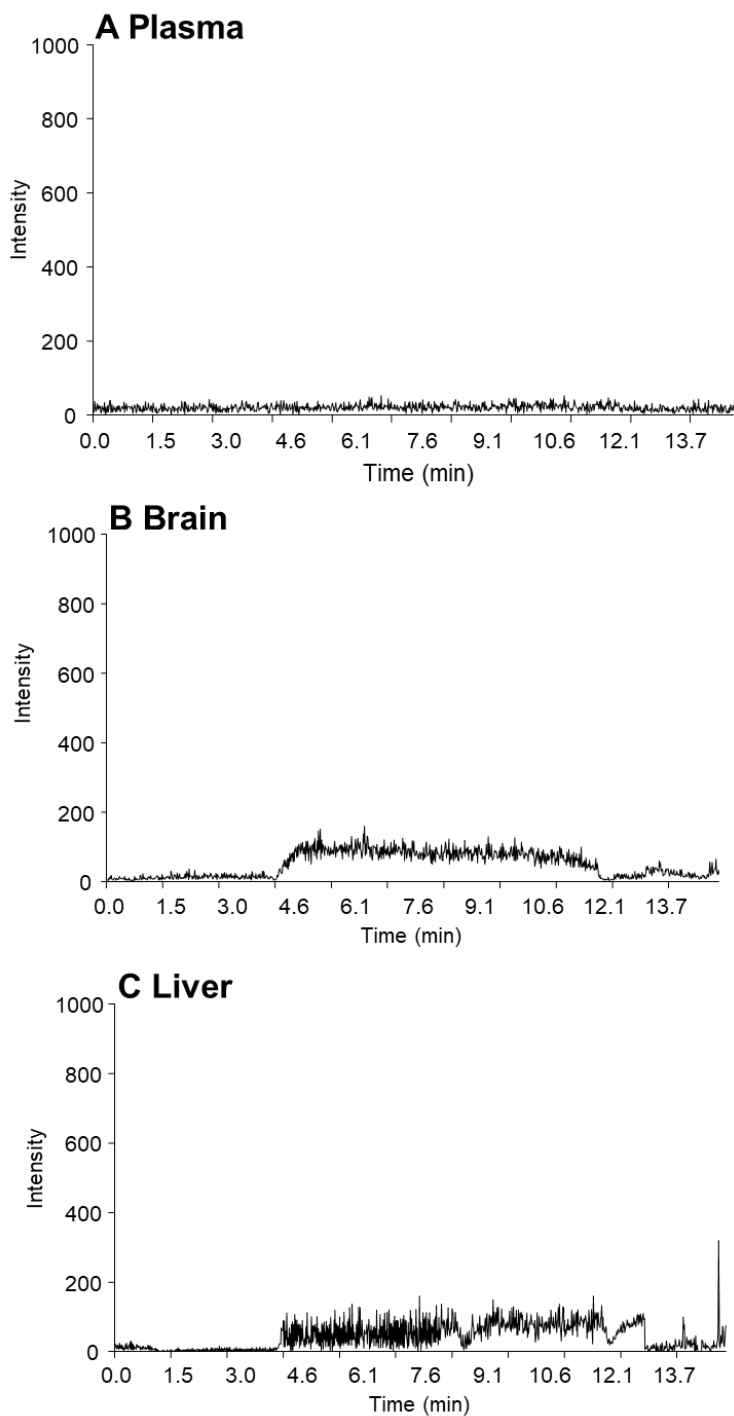


Figure 3. 9 Representative selected-reaction-monitoring HPLC-MS/MS chromatograms of diapocynin detection in (A) plasma, (B) brain and (C) liver from the same CD1 mice PK model.

In this study, Limit of blank (LoB), representing the highest amount of the compound that was detected in the blank, was calculated by the equation $LoB =$

$\text{Mean}_{\text{blank}} + 1.645 \text{ SD}_{\text{blank}}$ (n=3). Limit of detection (LoD), defined as the lowest concentration of the analyte to be reliably distinguished from Limit of Blank, was then calculated by $\text{LoD} = 3.9 \times \text{SD}_{\text{blank}} / \text{slope of standards} = 3.9 \times 25.7 / 76.04 = 1.3$ (n=3) (Armbruster & Pry, 2008). Limit of quantification (LoQ), which is the lowest concentration of the analyte to be reliably detected and quantified, was calculated by $\text{LoQ} = 3 \times \text{LoD}$ (Mascher, 2012) = $3 \times 1.32 = 3.95$. As a local practice, we also used predefined criteria of the coefficient of variation (CV) below 15% from the defined concentration to avoid imprecision, and this was defined using apocynin plasma samples at different concentrations from 1 – 10,000 ng/ml (CV is marked as % in **Figure 3.10**) using the extraction method described in section 3.2.4.

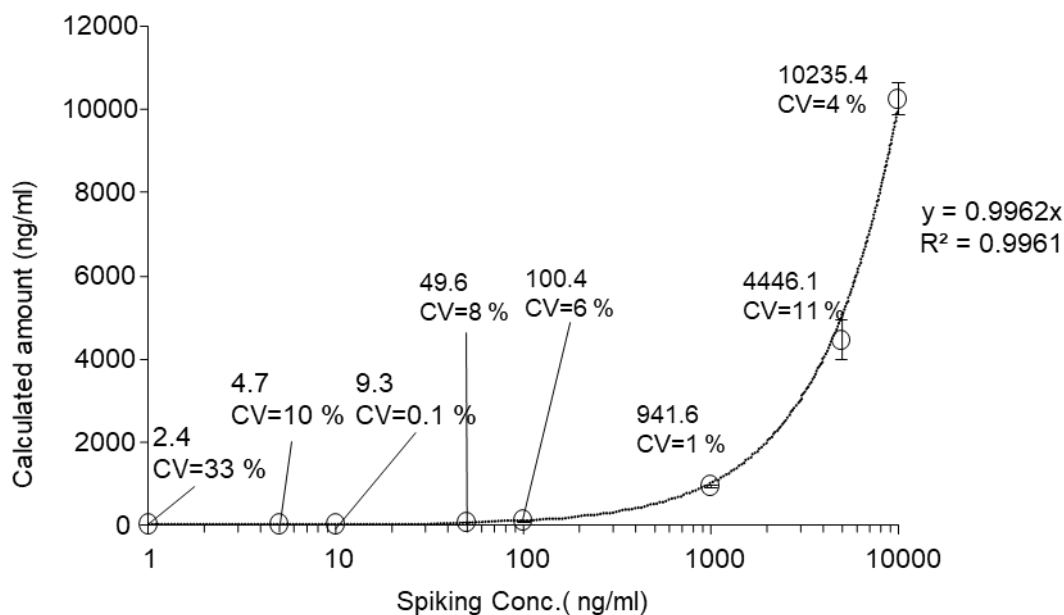


Figure 3. 10 Linearity of apocynin by HPLC-MS/MS.

The curve was constructed using calibration levels of apocynin at 1, 5, 10, 50, 100, 1,000, 5,000 and 10,000 ng/ml in the plasma and was normalised by phenacetin at 500 ng/ml using the extraction and HPLC-MS/MS method described. Each standard and sample were measured in triplicate, and an average of three measurements was used for constructing the curve. CV calculated (%) are presented in below the calculated amount.

3.3.2 Tissue distribution of apocynin in different organs post iv bolus injection

Since the mice used are from the same colony with the same genetic background, age, gender and similar body weight, it was assumed that the mice used in this study have the same absorption, distribution, metabolic and elimination rate. Real-time distributions of apocynin in murine plasma, urine and organ tissues including brain, liver and heart were measured using the established HPLC-MS/MS method to characterise its PK and ADME (**Figure 3.6**). As shown in section 3.3.5 that the limit of quantification of the HPLC-MS/MS method is 5 ng/ml, therefore, concentrations below

5 ng/ml, although still were presented, were interpreted as ‘detectable but not quantifiable’. Since the dilution factor for plasma was 1:10; tissues were 1:10 and urine was 1:100, one criterion of Limit of Quantification in plasma, tissues and urine were 50, 50 and 500 ng/ml, respectively. Parallel calibrations were also used alongside the HPLC-MS/MS analysis, and the limit of quantification was also defined according to the rule of accepting calibration concentration lower than CV=20%. Both criteria were considered during the quantification, and whichever was higher was used as the limit of quantification.

Plasma concentration of apocynin reached $5,494 \pm 400$ ng/ml at 1 min after injection, and gradually declined and maintained above 50 ng/ml until 15 min (55 ± 8 ng/ml) (**Figure 3.11 A**). Apocynin was also detectable from 15 min in urine and peaked at 30 min with a concentration of 20,492 ng/ml and remained above the limit of detection (230 ± 31 ng/ml) until 180 min (**Figure 3.11 B**). Apocynin reached and peaked in brain tissue at 1 min of injection with a concentration of $4,603 \pm 208$ ng/g and was detectable until 30 min (**Figure 3.11 C**). It reached liver at 1 min with a concentration of 429 ± 146 ng/g, peaked at 5 min with a detected concentration of $2,853 \pm 35$ ng/g and was detectable until 15 min (**Figure 3.11 D**). It reached cardiac tissues at 1 min with a concentration of 834 ± 815 ng/g, peaked at 5 min with a concentration of $3,161 \pm 309$ ng/g and remained detectable until 15 min (**Figure 3.11 E**).

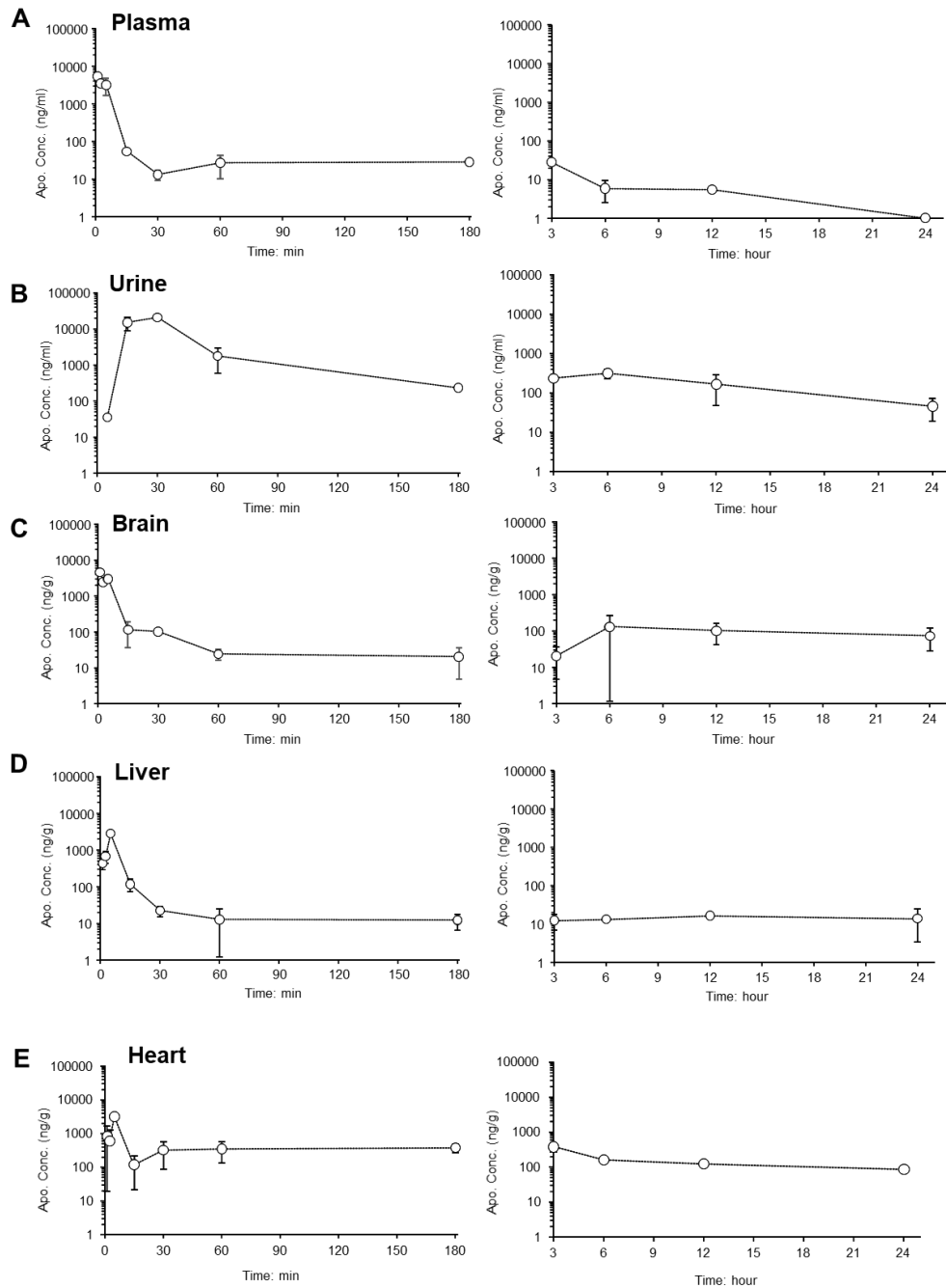


Figure 3. 11 Kinetic change of apocynin concentration in different tissue organs.

Kinetic changes of apocynin from 1 min to 24 h post iv bolus (5 mg/kg) in male CD1 mice (12-week of age, 28-32 g) in (A) plasma, (B) urine, (C) brain, (D) liver, and (E) heart. Three detections per mouse sample were performed, and three mice per group were used. An average concentration of apocynin at one time-point per sample was first calculated, and the error bars were then calculated using different mouse samples at one time-point in one tissue, data presented as Mean \pm SD.

Log BB is an index used for quantitatively defining blood-brain barrier permeability of a drug. It is calculated by the logarithm of the concentration of a drug in the brain divided by its concentration in the plasma (Muehlbacher, Spitzer, Liedl & Kornhuber, 2011). It is generally accepted that if Log BB value is ≥ 0.3 , the drug readily crosses the blood-brain barrier and has access to the CNS if the value is between 0.3 and -1 , the drug can cross blood-brain barrier but has limited access to CNS; and if the value is < -1 , the drug poorly distributes to the brain (Vilar, Chakrabarti & Costanzi, 2010). Log BB of apocynin was calculated at different time points in the first 15 min post iv bolus: 1 min: -0.08 ; 2.5 min: -0.16 ; 5 min: 0.00 ; 15 min: 0.32 and 30 min 0.96 (**Table 3.1**). Therefore, apocynin can penetrate the blood-brain barrier and has access to CNS.

Table 3. 1Log BB of apocynin.

Group	Time	Log BB
1 min	1	-0.08
2.5 min	2.5	-0.16
5 min	5	0.00
15 min	15	0.32
30 min	30	0.96

The designated time point is used for each group. Log BB were calculated by: $\text{Log BB} = \text{Log} (C_{\text{brain}}/C_{\text{plasma}})$. Concentrations of apocynin from 1 – 30 min were used because it remained detectable in the brain until 30 min, $n=3$ per group.

3.3.3 Characterisation of apocynin PK parameters by non-compartmental analysis (NCA) and non-linear mixed-effects (NLME) model

The proposed extraction and HPLC-MS/MS method were successfully applied to the PK study of apocynin in CD1 mice following a single iv administration of 5 mg/kg. For the preliminary understanding of the general exposure of apocynin post

iv bolus, concentrations of apocynin in plasma at different time points was calculated referring to (Gabrielsson, 2016). The calculation was then done using Phoenix WinNonlin 8.1, as described in section 2.5.1. The result from WinNonlin is shown in **Table 3.2** and **Figure 3.12**.

Table 3. 2 Plasma NCA PK profile of apocynin by Phoenix WinNonlin 8.1.

Parameter	Value
C_{max} (ng/mL)	5494.00
$t_{1/2}$ (h)	0.05
k_{el} (/h)	13.65
$AUC_{0-\infty}$ (h·ng/mL)	643.27
CL (L/h/kg)	7.76
V_d (L/kg)	568.74

Abbreviations: C_{max} : measured maximum concentration; $t_{1/2}$: terminal half-life; k_{el} : terminal rate constant; AUC: area under the curve; CL: clearance; V_d : distribution volume.

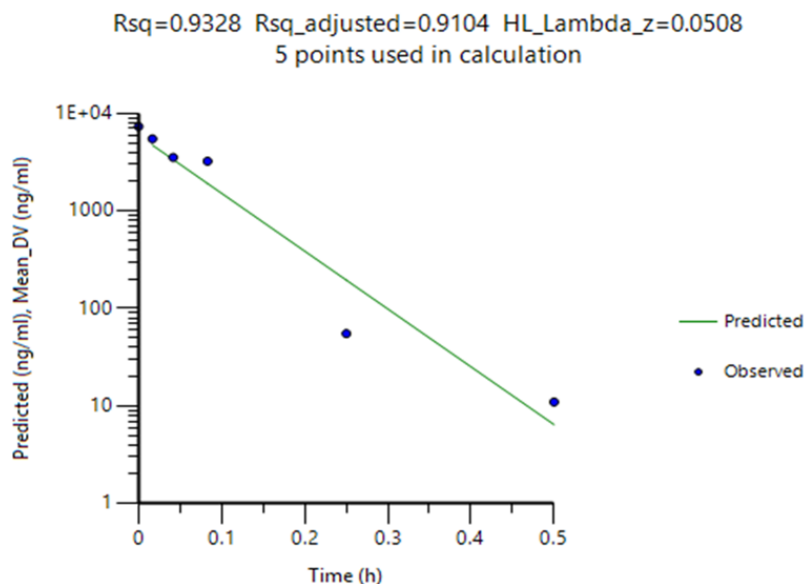


Figure 3. 12 Time-dependent elimination of apocynin in the plasma.

The curve was drawn based on the plasma concentration of apocynin against time (0.017 h to 0.5 h) (an $r^2 = 0.9324$, adjusted $r^2 = 0.9104$), and was used for calculating the NCA parameters.

The compartmental analysis was also carried out using Phoenix WinNonlin 8.1 NLME model, using the data from 1 min to 6 h. Time-dependent concentrations of apocynin measured were fitted into one-, two- and three-compartmental analysis with the setting ‘bolus input and a first-order output, micro-constants as primary parameters’. The criteria for the estimation of the statistical significance of the three models are listed in **Table 3.3**.

Table 3. 3 Model fit of apocynin using compartmental models by WinNonlin 8.1.

Model Compartment	LogLik	-2LL	Likelihood Ratio Test				
			AIC	AICc	nParm	nObs	nSub
1	-186.25	372.50	378.50	379.70	3	24	1
2	-186.25	372.50	382.50	385.84	5	24	1
3	-186.26	372.50	386.50	393.50	7	24	1

Abbreviations: LogLik: Log-likelihood; -2LL: -2 Log likelihood; AIC: Akaike information criterion; AICc: corrected version of AIC, $AICc = AIC + 2 \times nParm / (nObs - nParm - 1)$.

When the sample number versus the number of parameters is small ($n < 40$), the smallest AICc suggests the best fit for the model (Rajeswaran & Blackstone, 2017). Therefore, in this study, the statistical significance comparison of AICc suggested the best-fitted model be one-compartmental with its model parameters (Theta) listed in **Table 3.4** and model diagnostic in **Figure 3.13**. For the observed (DV, ng/ml) versus individual-predicted concentrations (IPRED, ng/ml) (**Figure 3.13 a**), the better the line fits in the dots, the better fit the model is. Values of individual weighted residuals (IWRES) should be approximately $N(0,1)$ and hence concentrated between $y = -2$ and $y = +2$. **Figure 3.13 (c)** and **(d)** show a reasonable distribution of IWRES against concentration and time, with little outliers. Values significantly above 3 or below -3 would be suspected and may indicate a lack of fit and model misspecification. A well-

fitted model typically has few or no outliers (IWRES above $y = +2$ or below $y = -2$) and the blue line being close to $y=0$.

Table 3. 4 NLME model parameters of apocynin one compartmental analysis by Phoenix WinNonlin 8.1.

Parameter	Estimate	Units	Stdev	CV%	2.5% CI	97.5% CI
tvV	530.72	ml	37.94	7.15	451.82	609.62
tvKe	5541.14	ml/h	596.66	10.77	4300.33	6781.95
stdev0	567.66		81.93	14.43	397.27	738.05

The prefix of 'tv' denotes fixed-effect or typical value. V: apparent volume of distribution, Ke: elimination rate constant; stdev: standard deviation.

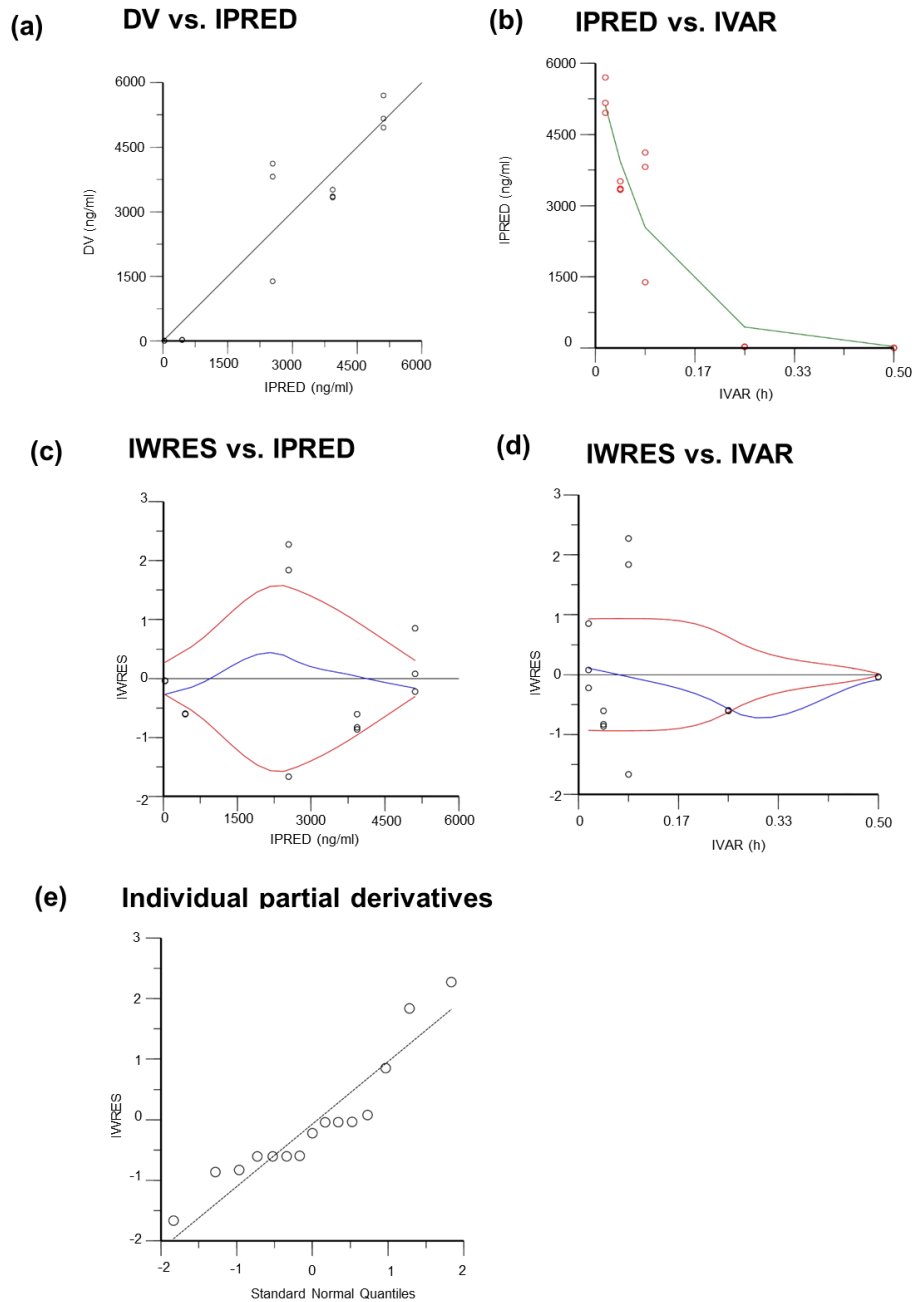


Figure 3. 13 Diagnostic scatter plots of one-compartmental NMLE model fit of apocynin using Phoenix WinNonlin 8.1.

(a) Observed versus individual-predicted concentrations (DV vs IPRED); (b) Individual-predicted concentrations versus time (IPRED vs IVAR); (c) Individual weighted residuals versus individual predictions (IWRES vs IPRED); (d) Individual weighted residuals versus time (IWRES vs IVAR); (e) Quantile-quantile plot of the components of individual weighted residuals.

The NLME result suggests that the body could be regarded as a single and uniform compartment after iv bolus administration, and apocynin distributed and equilibrated instantaneously and rapidly throughout the whole compartment (volume of distribution). Due to the rapid distribution and equilibration, the elimination of apocynin occurs at the same time from the uniform compartment. The interpretation of the model can be used for future predictions of apocynin plasma concentration profiles under different conditions and could benefit future initial dosing regimen to patients.

3.3.4 The effect of apocynin on reducing organ O₂- production

To establish the link between the apocynin PK characters and its effect on Nox2-derived O₂- production, same tissue samples (processed to homogenates as described in section 3.2.8 or cryosections as described in section 3.2.9) from the same mice for the PK studies were analysed by lucigenin-chemiluminescence and DHE assays. Post 1 min iv bolus injection, O₂- production in brain was decreased to 60.4 ± 25.4 % compared to vehicle, with the lowest O₂- production found at 15 min (inhibited to 37.0 ± 5.8 %) and the inhibiting effect lasted until 60 min (**Figure 3.14 B**). Also, it was observed that there was almost no delay in the inhibition taking effect (1 min). DHE fluorescence demonstrated *in situ* O₂- inhibition in a similar pattern (**Figure 3.17**). Compared to the brain, there seemed to have a similar pattern of apocynin taking effect in the liver. Apocynin was able to inhibit liver O₂- production to 60.9 ± 6.8 % post 1 min, and the effect lasted until 30 min, with the lowest at 15 min (41.8 ± 12.8 %) (**Figure 3.15**). In the heart, unlike in the brain or liver, apocynin had a more significant effect (O₂- reduced to 45.1 ± 16.5 % post 1 min iv bolus injection), peaked its effect at 30 min (O₂- reduced to 21.4 ± 15.7 %), and the effect lasted until 6 h (**Figure 3.16**). The O₂- production was NADPH-dependent and could be reduced by tiron (10 mM, an O₂- scavenger) (**Figure 3.14 (A), 3.15 (A) and 3.16 (A)**).

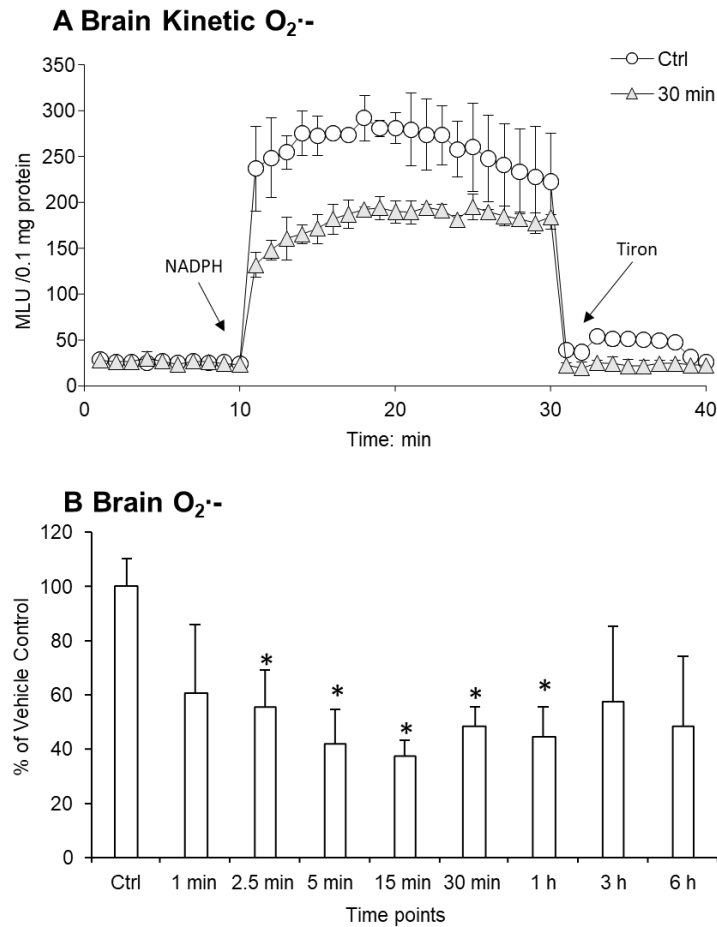


Figure 3. 14 O₂⁻ production in brain homogenates detected by lucigenin chemiluminescence.

(A) Representative kinetic measurement of O₂⁻ production in the brain homogenates detected by lucigenin chemiluminescence. Ctrl: without apocynin; 30 min: 30 min post apocynin iv bolus injection. Signal measured every minute after adding lucigenin (10 μM). NADPH (1 mM) was added at 10 min, and tiron (10 mM) was added at 30 min. (B) O₂⁻ production of CD1 mice brain homogenates from 1 min to 6 h post iv bolus (apocynin, 5 mg/kg). n=3 per group. Data are presented as Mean ± SD. Statistical comparison between the two groups was made using one-way ANOVA. *p <0.05, significantly different from Vehicle Ctrl.

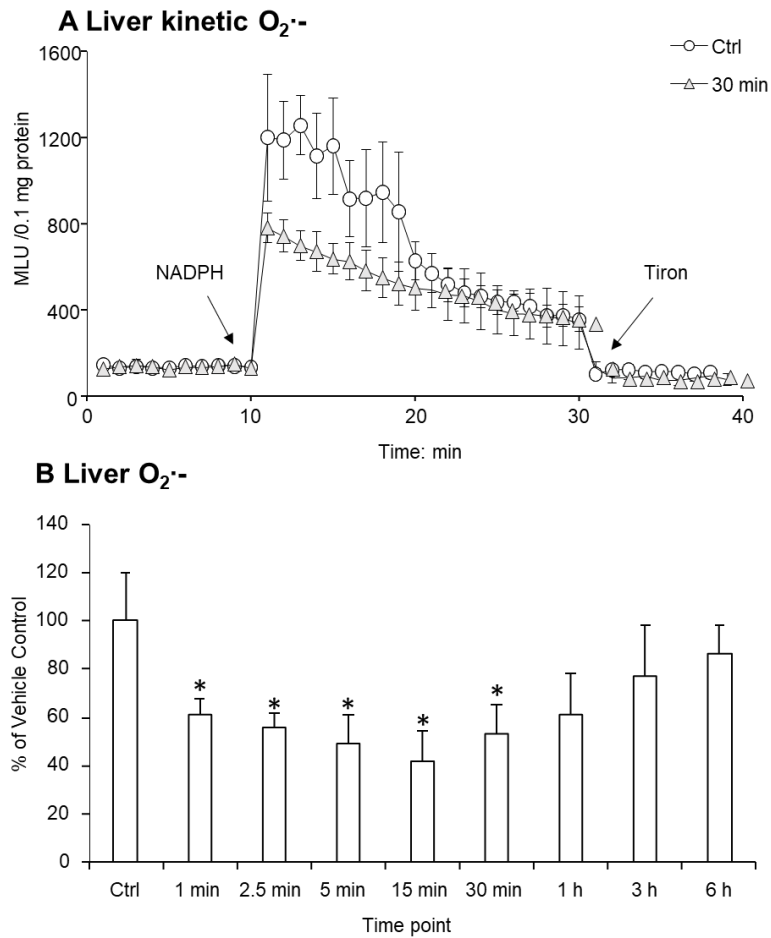


Figure 3.15 O₂⁻ production in the liver homogenates detected by lucigenin chemiluminescence.

(A) Representative kinetic measurement of O₂⁻ production in the liver homogenates detected by lucigenin chemiluminescence. Ctrl: without apocynin; 30 min: 30 min post apocynin iv bolus injection. Signal measured every minute after adding lucigenin (10 μ M). NADPH (1 mM) was added at 10 min, and tiron (10 mM) was added at 30 min.

(B) O₂⁻ production of CD1 mice liver homogenates from 1 min to 6 h post iv bolus (apocynin, 5 mg/kg). n=3 per group. Data are presented as Mean \pm SD. Statistical comparison between the two groups was made using one-way ANOVA. *p <0.05, significantly different from Vehicle Ctrl.

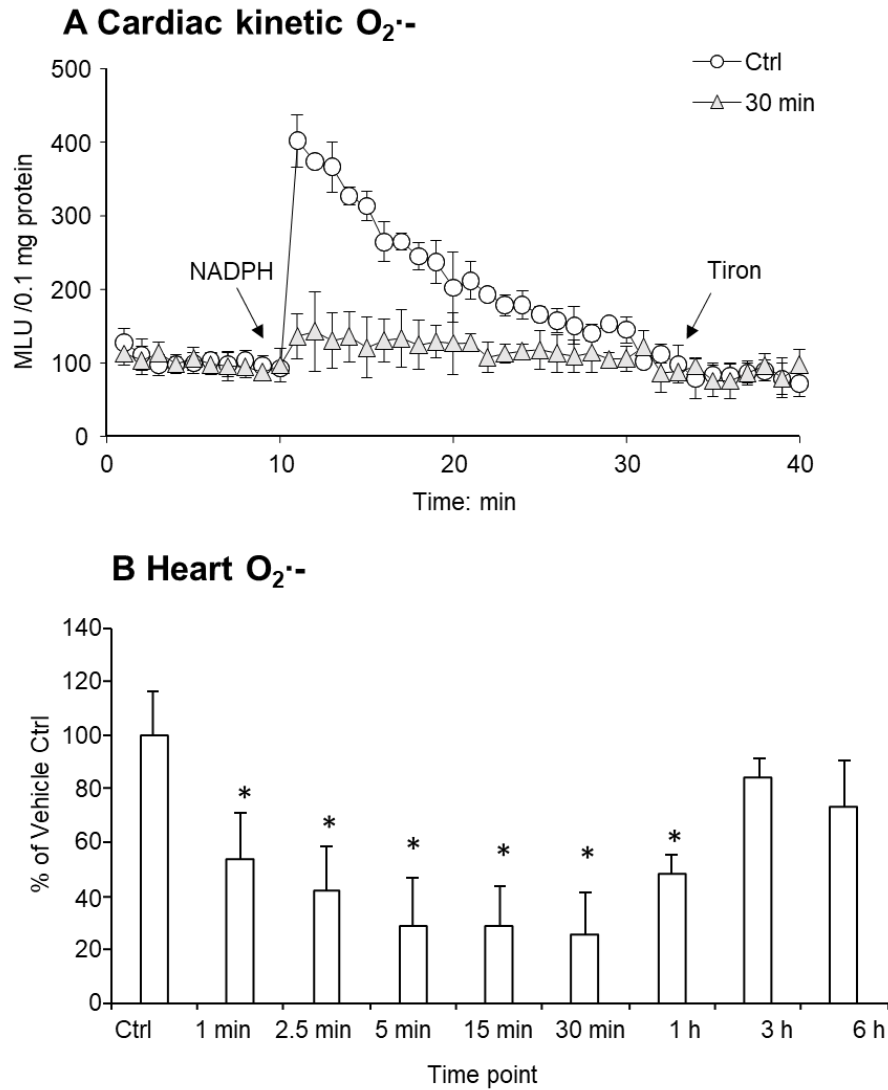


Figure 3. 16 O₂⁻ production in the heart homogenates detected by lucigenin chemiluminescence.

(A) Representative kinetic measurement of O₂⁻ production in the heart homogenates detected by lucigenin chemiluminescence. Ctrl: without apocynin; 30 min: 30 min post apocynin iv bolus injection. Signal measured every minute after adding lucigenin (10 μM). NADPH (1 mM) was added at 10 min, and tiron (10 mM) was added at 30 min. (B) O₂⁻ production of CD1 mice heart homogenates from 1 min to 6 h post iv bolus (apocynin, 5 mg/kg). n=3 per group. Data are presented as Mean ± SD. Statistical comparison between the two groups was made using one-way ANOVA. *p <0.05, significantly different from Vehicle Ctrl.

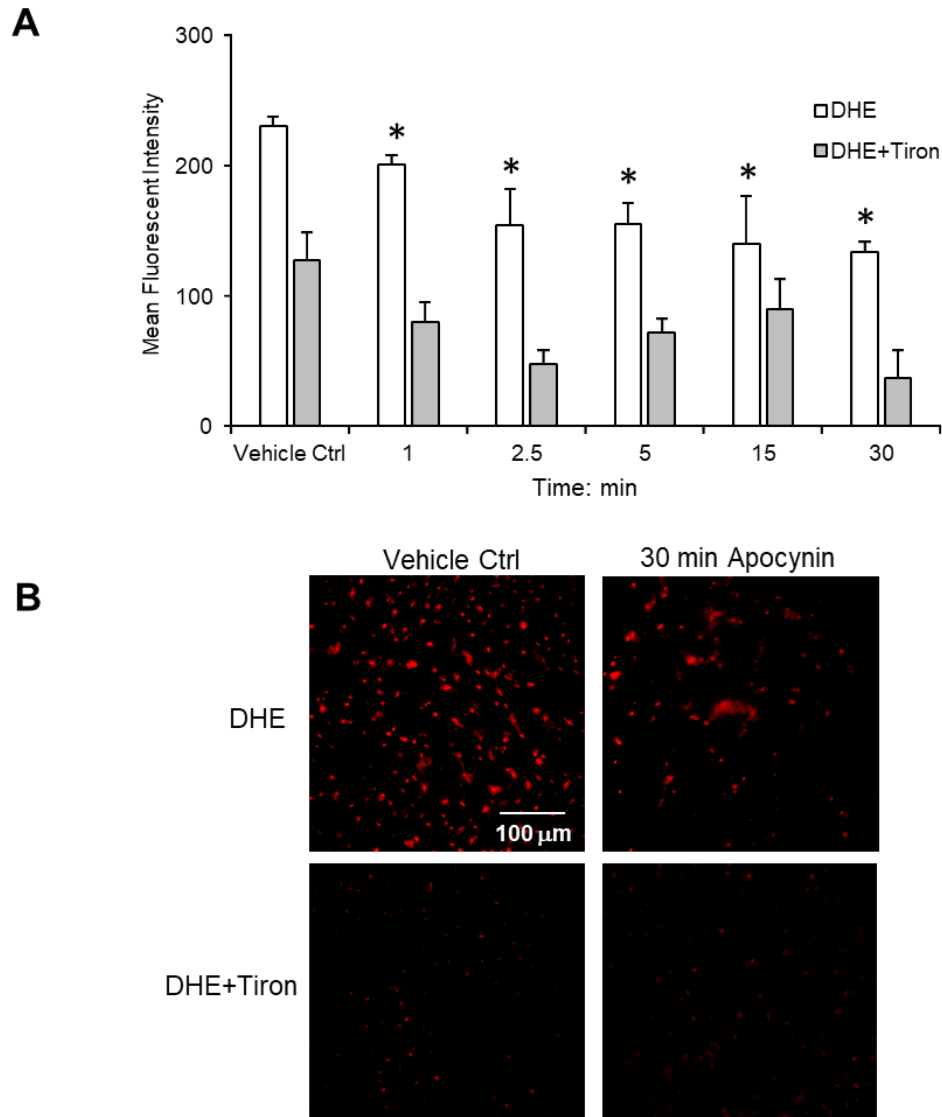


Figure 3. 17 *in-situ* O₂⁻ production in brain sections by detected by DHE.

(A) Quantification of fluorescent intensity of DHE staining with (grey bar) or without (white bar) 10 mM tiron. The fluorescent intensity was calculated by measuring Mean Grey of DHE staining against the background using ImageJ 1.50i. 10-15 images used per section, three sections per mice and n=3 per group. Data are presented as Mean \pm SD. Statistical comparisons between two groups were made using one-way ANOVA. * p < 0.05, significantly different from Vehicle. (B) Representative examples of *in-situ* O₂⁻ production from brain cryosections of CD1 mice with (30 min post iv bolus, 5 mg/kg) or without apocynin. 10 mM tiron was added before DHE as controls. Nuclei stained with DHE are in red. Images were obtained under a Nikon Eclipse Ti2-E inverted microscope with 20 \times magnification.

3.3.5 The effect of apocynin on reducing organ lipid peroxidation

Alongside the effect of apocynin in reducing $O_2\cdot$ - production, its effect on lipid peroxidation was also investigated using MDA assay purchased from Sigma-Aldrich (UK) following the manufacturer's instructions. In the brain, 1 min post iv bolus injection, apocynin was able to reduce lipid peroxidation to 67.4 ± 14.1 %, and the effect lasted until 60 min (74.4 ± 5.1 %) (**Figure 3.18 A**). In the liver, unlike its immediate effect on reducing $O_2\cdot$ - production, a delay was seen in its effect in reducing liver lipid peroxidation. **Figure 3.18 B** shows a reduction of liver lipid peroxidation to 65.4 ± 19.3 % 5 min post iv bolus injection compared to vehicle-only controls, and it maintained lesser until 30 min 63.4 ± 8.3 %. However, in the heart, cardiac lipid peroxidation generation was reduced to 65.3 ± 6.4 % at 5 min compared to the control and the effect lasted until 30 min (78.6 ± 6.8 %) (**Figure 3.18 C**).

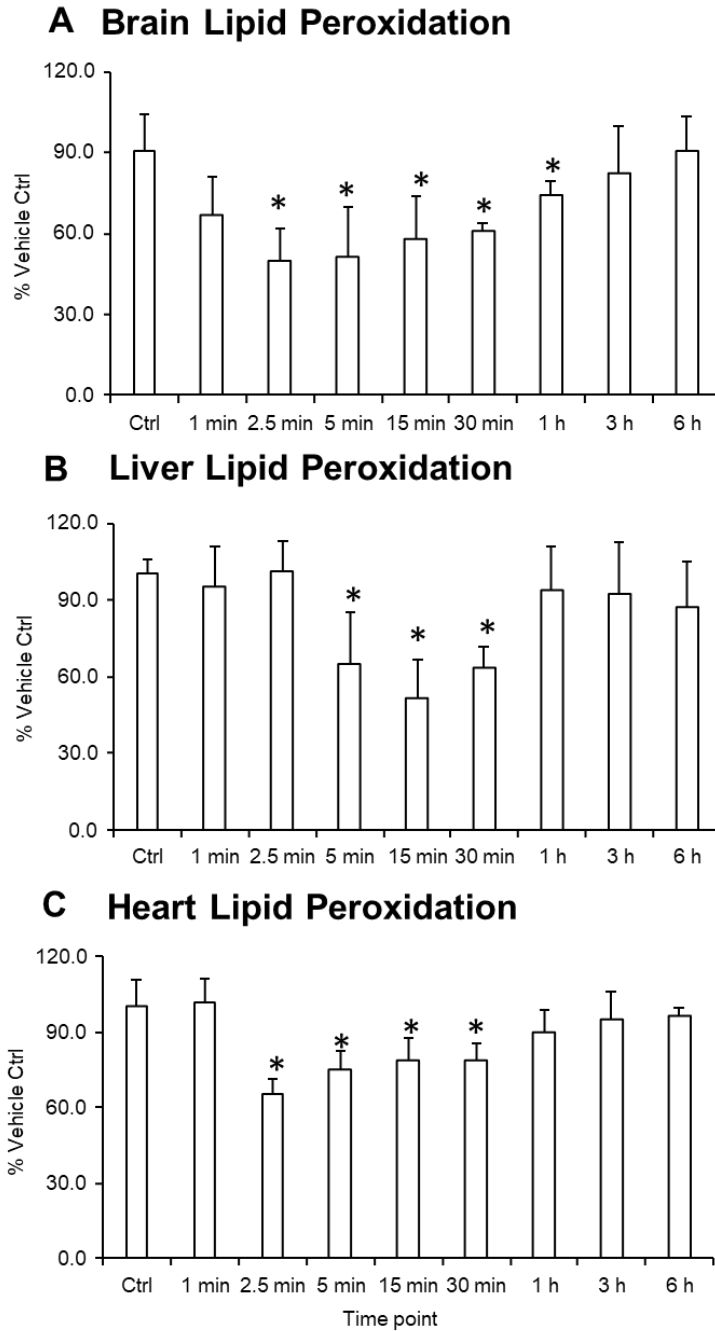


Figure 3. 18 Lipid peroxidation by MDA assay in (A) brain, (B) liver and (C) heart.

Tissue homogenates of CD1 mice were from 1 min to 6 h post iv bolus injection (apocynin, 5 mg/kg). Lipid peroxidation was determined by the reaction of MDA with TBA to form a colourimetric adduct, which is proportional to the MDA. Data are presented as Mean \pm SD. Statistical comparison between the two groups was made using one-way ANOVA. * $p < 0.05$, significantly different from Vehicle Ctrl.

3.3.6 The effect of apocynin on reducing brain O₂⁻ production in dietary-induced middle-aged obesity murine model

The effect of apocynin in reducing organ oxidative stress was tested using an HFD-induced middle-aged obesity murine model, which was previously established (Du, Fan, Mai & Li, 2013). In that previous paper, the effect of diet-induced obesity on vascular Nox2 activity and endothelial dysfunction was examined using the aortas. In this study, I wanted to understand further the absorption and the ability of blood-brain barrier penetration of apocynin and how this would affect the O₂⁻ production in the brain. The model set up method is described in section 3.2.2. The source of O₂⁻ was further investigated using different enzymatic inhibitors. The inhibitors included 250 μM oxypurinol (xanthine oxidase inhibitor), 50 μM rotenone (mitochondrial respiratory chain inhibitor), 100 μM L-NAME (a nitric oxide synthase inhibitor), and 20 μM DPI (a flavoprotein inhibitor). In addition, 200 U/ml PEG-SOD was also used to double-confirm the real level of O₂⁻ instead of background noise.

Using the established HPLC-MS/MS quantification method (section 2.4), the apocynin concentration in the tissues from this middle-aged obesity model was determined. In the apocynin-supplied WT HFD group, apocynin concentration varied in different tissues. For example, in the liver, the maximum concentration detected was 6,217 ng/g while in the brain, it was 7,013 ng/g. In the heart, it was lower than in the liver or brain, with the maximum reaching a level of 1,354 ng/g. Within the group, however, there were also variations. Three mice reached an apocynin liver concentration of 5,000 ng/g with minimum concentration detected 2,822 ng/g. In the brain, the concentration was detected, ranging from 3,823 ng/g to 7,013 ng/g. The detected apocynin tissue concentrations were shown in **Figure 3.19 A**. the O₂⁻ level

detected in the brain in different groups demonstrated that compared to WT, HFD was able to induce a 2.9-fold increase of O_2^- in the brain. While KO or apocynin treatment in drinking water was able to significantly reduce the effect to 26.6 % and 47.2 % of WT-HFD, respectively (**Figure 3.19 B**). The source of O_2^- was also investigated. DPI, the flavoprotein inhibitor, significantly inhibited the production of O_2^- to 18.8 % and SOD was able to catalyse the dismutation of O_2^- to 37.1 % compared to saline-only vehicles with no other significant inhibitory effect from any other inhibitors, which demonstrated the source of the elevated O_2^- to be flavoprotein (which includes Nox2) (**Figure 3.19 C**).

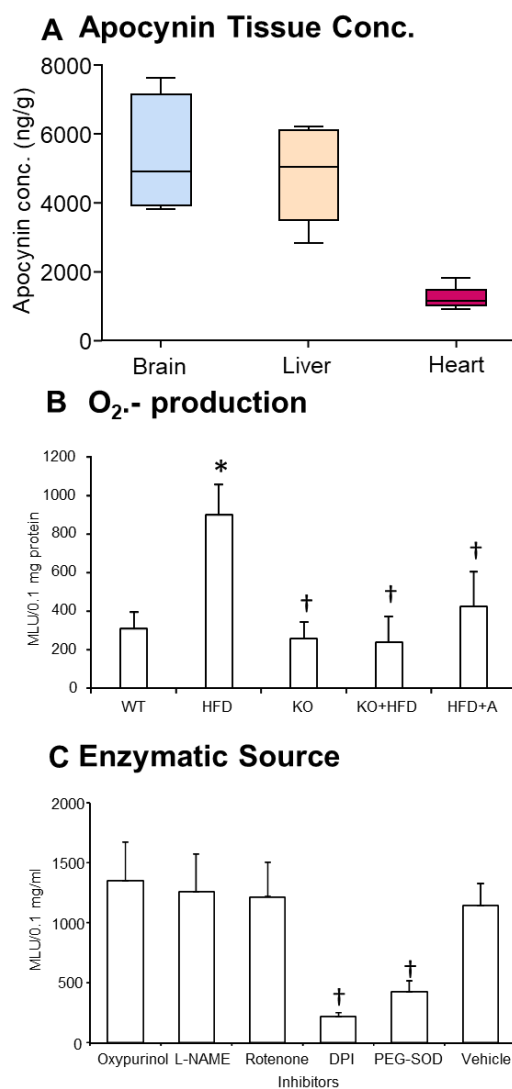


Figure 3. 19 The effect of apocynin in dietary-induced middle-aged obesity murine model.

(A) Apocynin concentration in the brain, heart and liver of WT-HFD, apocynin treated mice (B) O₂.- level in the brain of WT and Nox2 KO-HFD, apocynin treated mice. (C) Effects of different enzyme inhibitors on O₂.- production in the brain of HFD-induced middle-aged obesity murine model. n=6 per group. L-NAME: N^G-nitro-L-arginine methyl ester, DPI, diphenyleneiodonium. PEG-SOD: polyethylene glycol-adsorbed superoxide dismutase, Vehicle: HBSS added as a control. Data are presented as Mean \pm SD. Statistical comparison between the two groups was made using one-way ANOVA. † p < 0.05, significantly different from Vehicle (WT HFD).

3.4 Discussion

In order to thoroughly understand the whole process of small-molecule PK analysis and tissue distribution, this study included the establishment of apocynin detection by HPLC-MS/MS, apocynin dosing regimen design, sample collection at designated time points, sample processing, apocynin concentration detection in different tissues, NCA and NLME modelling and ROS level measurement as an indicator of the effect of apocynin. As a well-established and studied Nox2 inhibitor, apocynin is an ideal compound to start learning the process of PK characterisation of small-molecule Nox2 inhibitors from scratch. For example, in this project, the detection method of apocynin was set up by referring to different methods and developing the one that suits this project the most.

The HPLC-MS/MS method was developed by referring to existing technologies in pieces of literature (Chandasana et al., 2015) (Wang et al., 2013). Phenacetin was chosen to be an internal standard, according to (Chandasana et al., 2015) based on its similarity to apocynin in terms of retention time and derivatisation. However, in that previous paper (Chandasana et al., 2015), they failed to retain apocynin and phenacetin very well (with less than 1 min retention time). Therefore, we developed a better HPLC-MS/MS method by using two different choices of buffers with gradient elution. Choice one was isocratic mode with a mobile phase consisting of acetonitrile: 10 mM ammonium acetate buffer (pH = 4) (80:20) (result not shown here). Choice 2 was gradient mode with A) 480:20:0.38 water: methanol: ammonium acetate (v: v: w) and B) 20:480:0.38 water: methanol: ammonium acetate (v: v: w). It was found that the gradient mode provided good retention and reasonable sensitivity. Compared to some methods that were published, our developed method has the following advantages. 1) a retention time that demonstrated actual interaction with the stationary phase; 2) a neat

and sharp chromatographic peak for quantification; 3) a reasonably high level of sensitivity down to 10 ng/ml.

PK analysis, including the dose (5 mg/kg) and sample collecting point, was also designed by referring to published work. Since the terminal half-life of apocynin in rats was around 4 min (Chandasana et al., 2015), the sampling time points in this study was specially designed. A wider range of time (1 min, 2.5 min, 5 min, 10 min, 15 min, 30 min, 1 h, 3 h, 6 h, 12 h and 24 h) were designed to cover the short half-life following the rule of allocating reasonable spaced time both before and after half-life, unlike the published study which only collected the plasma samples from 5 min time point (later than their calculated half-life) (Chandasana et al., 2015). Sample processing using a protein crash method followed (Wang et al., 2013). However, there are also novelties. In this study, PK parameters of apocynin were characterised by NCA and then further analysed by an NLME regression model to investigate the volume of distribution changed in real-time, which makes it possible to predict the plasma concentration of apocynin at any time point t using $C(t) = f(p, t)$. Additionally, this study characterised the apocynin tissue distribution in mice by measuring apocynin concentrations in brain, heart, liver homogenate and urine for the first time.

Although apocynin has long been studied as a Nox2 inhibitor, or an antioxidant agent as some studies claimed (Rosa et al., 2016), the emphasis has always been put on its effect in reducing oxidative stress in diseased animal models after the drug dosing completes. Real-time impact of apocynin concentration change after dosing or how the metabolism of apocynin affected its efficacy were largely ignored. As an example, in this study, both O_2^- production and lipid peroxidation are reduced instantly after the treatment of apocynin yet the effect only lasted a short time (30 min for lipid peroxidation and 1 h for O_2^-) post iv bolus injection, which could be linked to the

extremely short terminal half-life, or fast metabolism of apocynin. Therefore, it is suggested that when using apocynin, the timing of dosing and experiment should be carefully planned and stated.

However, there are still several other problems. One is that in the chromatograms of apocynin detected in plasma brain and liver, there was a small peak appearing with slightly different retention time, roughly 1 min after apocynin. This peak, by definition, had the same parent ion MS1 (m/z) and daughter ion MS2 (m/z). However, since the difference in retention time (1 min) is big, this peak is identified as unspecific. However, in the blank controls of plasma brain and liver (with saline-injected), it also appeared. Therefore, it can be discounted from analysis and of having any relevance with apocynin treatment.

The other issue is that the terminal half-life of apocynin was calculated to be rather short, i.e. 3.5 min, which is in line with other studies using apocynin iv bolus injection in rats (Chandasana et al., 2015). The short half-life might be attributed to its small molecular weight and simple structure. One problem with the extremely short half-life is that it would be tough to design the dosage regimen clinically. In addition to the PK data obtained, the concentration and effect of apocynin in HFD murine heart were also tested to investigate if a short half-life would have a significant effect. When apocynin was supplied in drinking water, it was discovered that the detected apocynin concentrations in different types of organs varied, which fit in the findings from the tissue distribution in the apocynin PK study. With the same type of organ, there was a difference in the detected apocynin concentration, and this could probably attribute to the short half-life of apocynin. However, the effect in reducing brain O₂.- seemed promising, with a reduced O₂.- generation of (47.2 ± 20.2) % (p = 0.04). The result is in line with the result in section 3.3.4 that apocynin in the brain could last 1 h after iv

bolus injection (supposedly the apocynin effective time does not change with different administrative route). To resolve the problem of having a very short half-life, recently mito-apocynin became available, with a longer half-life and increased mitochondrial permeability due to its triphenylphosphonium moiety. It was discovered to be efficient in reducing oxidative damage in diseased models of neurodegenerative diseases such as Parkinson's (Dranka et al., 2014; Ghosh et al., 2016; Langley et al., 2017).

Intriguingly, both studies on apocynin using the CD1 mice and the HFD-induced model with metabolic disorder showed an accumulation of apocynin concentration in the brain. One limitation of this study is that the BBB permeability and efflux of apocynin were not investigated. One future experiment could involve permeability studies using Madin-Darby canine kidney strain II cells (MDCKII) transfected with multi-drug resistance gene (MDR1) or breast cancer resistance protein (BCRP), in combination with different efflux transport inhibitors to investigate the uptake and/or efflux transporter involved in this procedure. Apocynin also showed a high renal clearance, which is an advantage of apocynin to inhibit renal oxidative stress. During the use of apocynin in the HFD-induced mouse models with metabolic disorders, indexes on the kidney function should be provided. In the case of renal failure and dysfunction, apocynin dose needs to be carefully adjusted to achieve desired PK.

In conclusion, this study characterised the non-compartmental and compartmental PK and the effect of apocynin as a Nox2 inhibitor *in vivo* by designing dosing regimen in mice and established a better method for apocynin extraction and detection in different murine tissue organs. After iv bolus injection, apocynin rapidly distributed to different organs including the brain and had a significant effect on reducing ROS production until 1 h (as detected by lucigenin chemiluminescence, DHE fluorescence for O₂⁻ production and MDA assay for lipid peroxidation). This study

investigated the *in vivo* metabolism of apocynin in real-time, looked at the period the effect could last and provided insights into the dosing regimen and future modification of apocynin.

Chapter 4

Chemical Properties and *in vivo* Pharmacokinetic (PK) Analysis of LMH001 by HPLC-MS/MS

4.1 Introduction

There are two types of Nox inhibitors: small-molecule inhibitors and peptide-based inhibitors, whose functions and limitations are discussed in section 1.6. Current available small-molecule Nox inhibitors include apocynin and its derivatives, DPI, ML171, ebselen, Gkt136901, VAS3947, Fulvene-5, and celastrol. These inhibitors have some disadvantages, including the high potential cytotoxicity (ebselen) (Augsburger et al., 2019), adverse activation of stress-related intracellular signalling pathways (Kucera et al., 2016b), unfavourable inhibition of other enzymes (celastrol and ML171) (Altenhofer et al., 2015) and the possibility to scavenge O₂⁻ (apocynin, ML171, ebselen, and Gkt136901) (Altenhofer et al., 2015; Heumuller et al., 2008) or excessive interactions with another source of ROS (DPI) (O'Donnell et al., 1993; Wind et al., 2010). More importantly, during the initial drug discovery stage, the primary focus for the biomedical and biochemistry labs is usually the mechanism and effect of the target drug *in vitro*, and there is a lack of preclinical pharmacological *in vivo* studies such as pharmacokinetic and pharmacodynamic (PKPD) and pharmacotoxicology (drug safety) investigations on most of these compounds. For instance, the PK or safety profile of Fulvene-5 has never yet been characterised ever since it was proposed as a potential Nox4 inhibitor in 2009 (Altenhofer et al., 2015; Bhandarkar et al., 2009). As a result, many developed Nox inhibitors get stuck in the early discovery stage. Therefore, there are needs for the improvement in Nox-inhibitor discovery processes and the development of more specific Nox inhibitors. The investigations on the PKPD

characterisation of these novel inhibitors would act as a bridge to bring the lab-developed potential inhibitors to the clinical settings.

LMH001 was newly developed by my PhD supervisor Professor Jian-Mei Li and her research team while she was working at the University of Surrey. It is a representative molecule of a group of bi-aromatic and tri-aromatic compounds for Nox2 inhibitors (Patent No. WO 2013/038136 A1). LMH001 was developed based on the first-hand results obtained from the study on the Nox2 activation mechanism. The group (Meijles et al., 2014) discovered that during Nox2 activation, the phosphorylated p47^{phox} was able to bind to the PRR region of p22^{phox} through the exposed SH3 pockets (formed by SH3A and SH3B on p47^{phox}), and LMH001 was able to disrupt this process by competitively binding to the SH3 pockets of p47^{phox}. Theoretically, binding of LMH001 to p47^{phox} would only happen after the activation of p47^{phox}, since the exposure of the binding site requires breakage of the H-bonds linking C-terminus and AIR. This unmasking of the SH3 pocket is only possible after the p47^{phox} phosphorylation at Ser379 (Yuzawa et al., 2004).

In vitro toxicity tests of LMH001 showed no cytotoxicity to different cell types with a dose up to 2901 ng/ml (10 μ M) for 24 h and *in vivo* studies showed no toxicity on bone marrow hematopoietic stem cell (BMHSC) proliferation from 5-month old mice with a dose of 3 mg/kg/day by intraperitoneal (ip) injection lasting for two weeks. However, previous studies focused on *in vitro* toxicity and functions of LMH001, yet did not address its chemical properties or the PK characters. PK evaluation of a drug candidate is a crucial part of drug discovery. Therefore, this study aimed to fill the gap in the development of LMH001 by characterising its chemical and PK properties and propose possible future work that could be done to improve its efficacy during this initial stage of the drug development.

4.1.1 Aims and objectives

This chapter aims to preliminarily characterise the chemical properties and preclinical PK properties of LMH001 as a Nox2-inhibitor. Specifically, there are five objectives in total:

1. To examine the chemical properties of LMH001 using ChemDraw Professional 19.0;
2. Based on the chemical properties, to develop methods for LMH001 extraction, detection and quantification in biological samples using HPLC-MS/MS method;
3. To characterise pre-clinical PK properties of LMH001 by iv administration (bolus, 10 mg/kg) to male CD1 mice (12 weeks of age);
4. To investigate the change of LMH001 under different pH conditions.

4.2 Materials and methods

4.2.1 Chemical properties and fragmentation analysis of LMH001

The chemical properties of LMH001, including boiling point, LogP, tPSA, pKa were analysed by inputting the structure of LMH001 into ChemDraw Professional 19.0 (PerkinElmer, United Kingdom). The possible fragmentation of LMH001 by the mass spectrometry in negative ionisation mode was analysed by Mass Frontier™ 8.0 (ThermoFisher Scientific, USA).

4.2.2 Chemicals and reagents

LMH001 (powder, purity ≥ 99.0) was synthesised by Tocris Biosciences, UK. Unless otherwise specified, most chemicals of the appropriate grade were purchased from either Sigma-Aldrich or Fisher Scientific (HPLC-MS grade for HPLC-MS analysis; gas chromatography-mass spectrometry (GC-MS) or HPLC grade for samples processing and other experiments). All the reagents used in this study are listed in Appendix I. The equipment used for different experiments, including HPLC-MS/MS is listed in Appendix III unless stated explicitly in this chapter (such as GC-MS). The suppliers of other consumables such as syringes and HPLC vials are listed in the text.

4.2.3 Animal model

Information on the standard housing conditions and detailed procedures on the handling of the CD1 mice used for this study are described in section 2.2. For PK analysis, CD1 male mice at 12-week of age were used, and the experimental procedure was the same as apocynin PK analysis with minor changes.

On the day of the experiment, the LMH001 injection solution was freshly prepared by firstly dissolving LMH001 (145 mg/ml) in DMSO, and then further diluting with 1:72.5 dilution factor (v/v) in ultrapure water to achieve a final LMH001

concentration of 2.0 mg/ml. With the same non-invasive mouse restraint (shown in **Figure 3.1 A**), 2.0 mg/kg LMH001 was administered using a 0.5 ml 0.33 mm (29G) × 12.7 mm Micro-Fine Insulin Syringe (BD, UK) via a lateral tail vein (**Figure 3.1 B**). In parallel, the same volume of diluent used for LMH001 as control vehicle was injected to the control group. At least six mice per time-point were used.

After iv bolus injection of LMH001, mice were sacrificed at 1 min, 2.5 min, 5 min, 10 min, 20 min, 30 min, 60 min, 180 min, 360 min, 720 min and 1440 min. The collected tissues were processed, as described in section 2.3.1. In summary, the workflow can be illustrated in **Figure 4.1**.

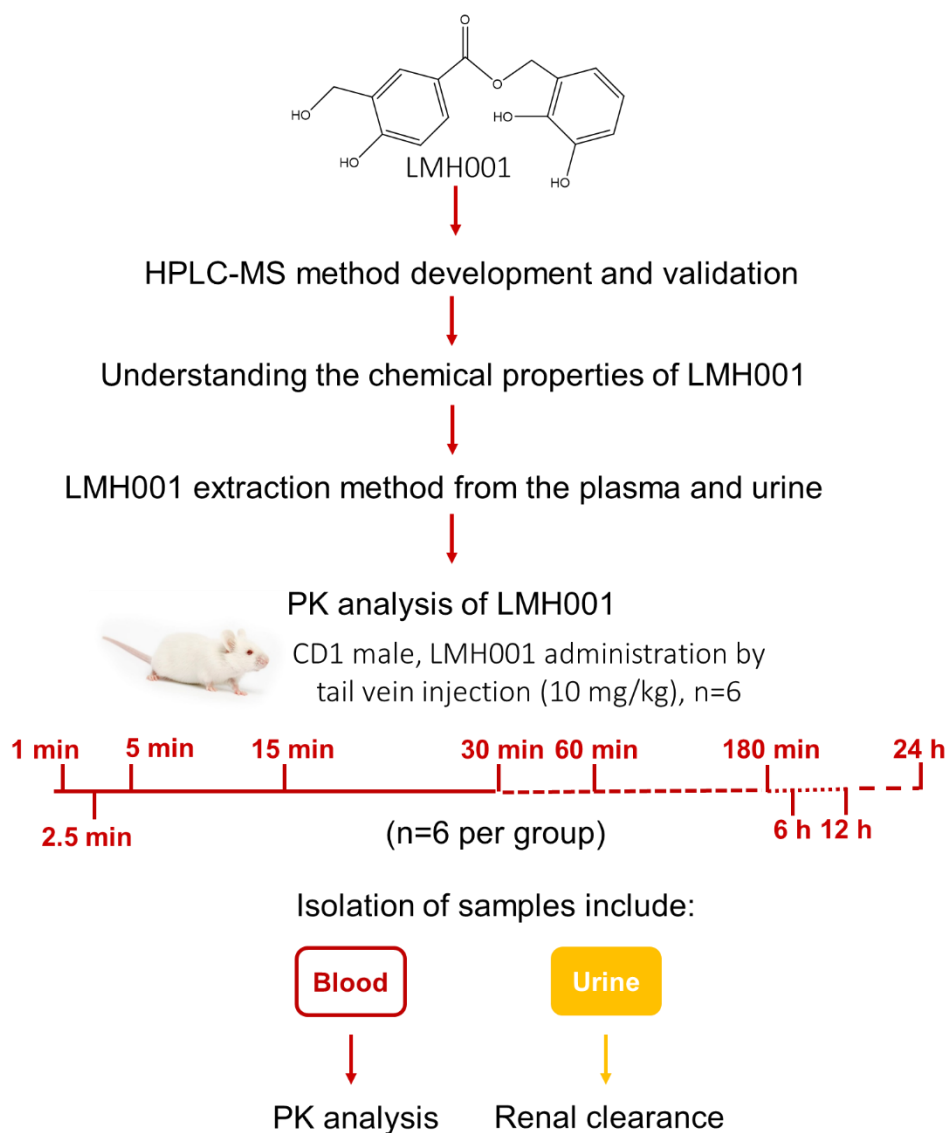


Figure 4. 1 Design and workflow of PK characterisation of LMH001.

4.2.4 Calibration standards preparation

For the HPLC-MS/MS detection and quantification method development, calibration standards of LMH001 were first prepared by dissolving 145 mg compound in DMSO and diluted to 1 mg/ml by the diluent (water, LC-MS grade), and then sub-diluting to 1, 5, 10, 50, 100, 1000, 5000 and 10,000 ng/ml. The calibration standards were used to establish the HPLC-MS/MS detection method, i.e. selecting mobile

phases, running method and column, plasma protein binding, and running along with the samples as external standards.

4.2.5 HPLC-MS/MS methods for detecting LMH001

The HPLC-MS/MS instrument in negative ionisation mode and the column for apocynin detection was also used in the LMH001 study (details listed in section 2.4.1). Mobile buffers were changed to mobile phase buffers (A) 0.1% formic acid in water (v: v) and (B) 0.1% formic acid in acetonitrile (v: v), with a gradient as follows: held on 5% B during the start and between 0 min and 8 min ramped up to 80% B; hold for 1 min and from 9 min to 10 min, dropped back down to 5% B and held on this for 2 min; the flow rate was 200 μ L/min throughout. The autosampler was maintained at 20°C and the column at 25°C. Data were collected between 2 – 12 min. Using this method, LMH001 was able to be detected from plasma and urine processed in this study and produce distinctive single and symmetrical peaks between 4.6 - 4.8 min.

For the quantification of LMH001, selected transition, at m/z, was: 289.0 \rightarrow 167.0 \pm 5.0, for better selectivity and a more reliable result. Good linearity was found in the range of 5 – 10,000 ng/ml in the biological matrices. The quantification method used for LMH001 was similar to apocynin (shown in section 2.4.2) except for opting out the calibration by an internal standard and was calibrated by external standards at 1-10,000 ng/ml calibration samples (pooled plasma or urine). External calibrations were used to minimise the possible interaction between a selected internal standard and LMH001. External standards have been proven to be an acceptable method for quantifying HPLC-MS/MS results (Farthing et al., 1992; Pigini, Cialdella, Faranda & Tranfo, 2006), provided that the individual matrix effect could be ignored.

4.2.6 Method for extracting LMH001 from plasma and urine

Since LMH001 is a novel candidate for Nox2 inhibitors developed by Prof. Jian-Mei Li in this lab, there were no suitable extracting methods that could be adopted directly. By comparing to the extraction method for apocynin and an extensive literature search, it was learnt that LMH001 has a polyphenolic structure, which is similar to naturally occurring polyphenols, stilbenes, found in the plant as secondary metabolites (Quideau et al., 2011). Since stilbenes, such as resveratrol, piceatannol and pinosylvin have been extensively studied as potential anti-cancer (Jang et al., 1997) or oxidative stress drug candidates (Li et al., 2004), the methods for extracting stilbenes in the PK studies were referred to during the set-up of LMH001 extracting method.

By referring to (Zhang et al., 2019) and adapting to local conditions, a method which showed high recovery rate and generated a satisfactory peak of LMH001 in plasma and urine was employed. The method is as follows. First, 5 μl of LMH001 standard (with the appropriate concentration (40 – 400,000 ng/ml), for the calibration), or water, for the samples, was spiked into 100 μl plasma or 20 μl urine diluted in 80 μl water. Then the mixture was vortexed for 30 s. 100 μl HCl (60 mM) followed by 800 μl ethyl acetate was added to extract LMH001 and crash the proteins (extraction buffer pH=1.52, ethyl acetate separated from aqueous layer). The mixture was then vortexed for 3 min before centrifuging at 10,000 rpm for 10 min. The upper organic layer (800 μl) was taken out as much as possible and evaporated to dryness using a stream of nitrogen at room temperature. The residue was reconstituted using 100 μl methanol and 100 μl mobile phase A (0.1% formic acid in water) as the final analyte. The analyte was then put into an insert (Merck, catalogue No. 27400-U) before putting into an amber

glass vial (Supelco, catalogue No. 27087-U). The sample processing procedure is illustrated in **Figure 4.2**.

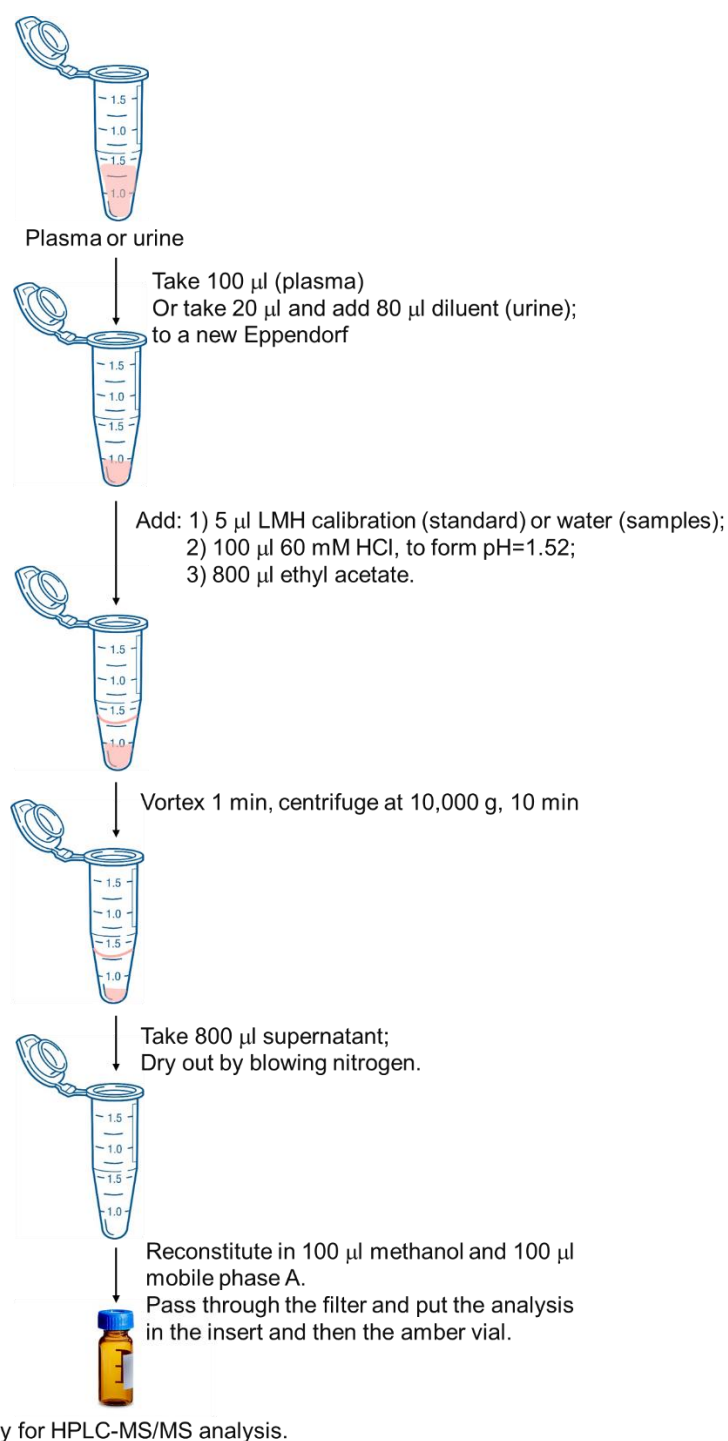


Figure 4. 2 Workflow of LMH001 extraction from different biological samples for HPLC-MS/MS analysis.

4.2.7 Plasma protein binding

Before the PK analysis, the plasma protein binding was determined (Buscher et al., 2014; Lambrinidis, Vallianatou & Tsantili-Kakoulidou, 2015). Plasma from 6 mice was pooled to examine the plasma protein binding of LMH001 at 10, 50 and 1000 ng/ml. The experiment was performed in duplicates. For each replicate, a small volume of 1.0 µg/ml or 10.0 µg/ml LMH001 (less than 5 µl) was used to form a final concentration at 10, 50 and 1000 ng/ml. 200 µl pooled plasma was used as the experimental groups, and 200 µl water was used as controls. After loading the samples, the samples were incubating at 25 °C on an orbital shaker at app. 250 rpm for 1 h before processing 100 µl samples using 100 µl methanol and 60 µl Acetonitrile to precipitate the proteins at pH = 3 and then for analysis by HPLC-MS/MS.

The concentration of apocynin in the plasma was determined by the peak areas (AUC) relative to the water control (LMH001 dissolved 145 mg/ml in DMSO and then sub-diluted to the relative concentration in water). The percentage of apocynin bound was calculated as follows:

$$\%Free = (\text{concentration detected in the plasma chamber}/\text{the water control}) \times 100\%$$

$$\%Bound = 100\% - \%Free$$

4.2.8 The detection of LMH001 in simulated gastric and intestinal fluids

4.2.8.1 Simulated gastric and intestinal fluids

The change of LMH001 concentration was examined in water (LC-MS grade), fasted state simulated intestinal (FaSSIF) and gastric fluids (FaSSGF) by dissolving LMH001 in the relevant solutions to 3,000 ng/ml and incubating at a 37 °C water bath

for 0, 10, 30, 60 and 120 min. The final concentration of LMH001 was detected by the established HPLC-MS/MS method after the incubation. The recipes for fasted state simulated intestinal and gastric fluid are listed in **Table 4.1 A and B** (Klein, 2010). Both intestinal and gastric fluids were stored at 4 °C and used within two weeks.

Table 4. 1 Recipe for the fasted state simulated intestinal (FaSSIF) and the fasted state gastric intestinal (FaSSGF).

(A) FaSSIF

Composition	Concentration
sodium taurocholate (mM)	3
lecithin (mM)	0.2
maleic acid (mM)	19.12
sodium hydroxide (mM)	34.8
sodium chloride (mM)	68.62
pH	6.5

(B) FaSSGF

Composition	Concentration
sodium taurocholate (μM)	80
lecithin (μM)	20
pepsin (mg/mL)	0.1
sodium chloride (mM)	34.2
hydrochloric acid	pH 1.6
pH	1.6

4.2.8.2 Gas chromatography-mass spectrometry (GC-MS) analysis of LMH001

To investigate the possible change of LMH001 in the simulated intestinal fluid, alongside the HPLC-MS/MS, GC-MS was also used for the analysis. GC-MS was carried out at Mass Spectrometry Facility (Waterloo), King's College London with Dr

Francesca Mazzacuva. The analytes were prepared by diluting LMH001 stock in methanol (as control), gastric fluid (pH = 1.6) and intestinal fluid (pH = 6.5) to form a final LMH001 concentration of 1.45 mg/ml. 10 µl analytes (from water, simulated gastric and intestinal fluid) were taken before and after a 60 min incubation at 37 °C for GC-MS analysis.

For the derivatisation of LMH001, N,O-Bis(trimethylsilyl)trifluoroacetamide and trimethylchlorosilane (BSTFA + TMCS, 99:1) (Catalogue No. 33154-U, Sigma-Aldrich, UK) was used as a derivatisation reagent. 10 µl sample was taken before and after the incubation and was dried using Concentrator Plus Complete System (Eppendorf, UK). 50 µl BASFA + TMCS was then added, and the mixture was incubated at 60 °C for 30 min in darkness to allow the silylation to complete. For the analysis, instead of looking at an MW of 290.27 Da, the MW changed to 578.24 Da. **Figure 4.3** shows the structural change of LMH001 before and after the derivatisation.

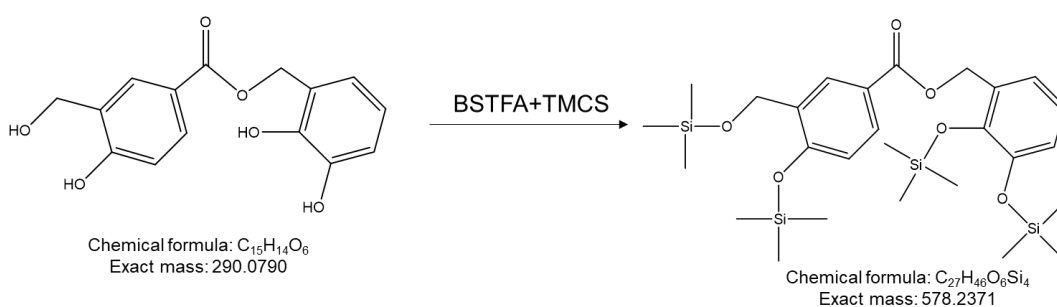


Figure 4. 3 Possible structural change of LMH001 after the derivatisation by BSFTA + TMCS.

BSTFA: N, O-Bis(trimethylsilyl)trifluoroacetamide; TMCS: trimethylchlorosilane; used as derivatisation reagent to increase the volatility and thermal stability of LMH001 for GC-MS study.

GC used was an HP6890 Series GC System Plus⁺ (Agilent Technologies, U.S.), MS used was a 5973 Mass Sensitive Detect (Agilent Technologies, U.S.) and the

autosampler was an Agilent 6890 series injector. The column used was DB-5MS (30 m × 0.250 mm, 0.25 µm film in diameter). The whole unit is shown in **Figure 4.4**. The injection volume was set to 1 µl, splitless mode and the carrier gas used was Helium. The heater was set at 280 °C, the pressure was 7.6 psi, and the total flow was 1.30 ml/min. The oven was set as follows: starting from 50 °C for 1 min, then increasing the temperature to 320 °C at a speed of 10 °C/min (27 min) and after reaching 320 °C, holding for another 10 min. The total run time was 38 min. The solvent delay was set at 5 min, and the acquiring mode was scan. The scan started from 5 min, and the range was set from 33 m/z to 800 m/z. The ionisation method was electron impact ionisation (EI), with the energy of the electron to be 70 eV.



Figure 4. 4 HP (Agilent) 6890-5973 GC-MS System.

4.2.9 PK analysis of LMH001

The profiles of LMH001 concentrations in murine plasma versus time were subjected to NCA (1-30 min) analysis using the simulation software including Comprehensive R Archive Network (R 4.0.1) (RStudio 1.3 as the platform) with a package called PKNCA (Obianom et al., 2020) and Phoenix WinNonlin 8.1. The basic

PK parameters were also calculated according to (Gabrielsson, Weiner & Gabrielsson, 2006).

The plasma concentration of LMH001 from 1 min to 3 h model was also subjected to non-linear mixed-effect model (NLME) for compartmental analysis by Phoenix WinNonlin to incorporate the fixed effect with random effect.

4.3 Results

4.3.1 Chemical properties of LMH001

Chemical properties of LMH001 such as LogP, tPSA, LogS and pKa were predicted using ChemDraw Professional 19.0 (PerkinElmer, United Kingdom) based on its structure. Relevant chemical properties are listed in **Table 4.2**.

Table 4. 2 Chemical properties of LMH001.

Property	Value
Boiling Point	993.4 [K]
Melting Point	761.98 [K]
Critical Temperature	936.89 [K]
Critical Pressure	46.47 [Bar]
Critical Volume	752.5 [cm ³ /mol]
Gibbs Energy	-620.44 [kJ/mol]
Log P	1.84
MR	74.73 [cm ³ /mol]
Henry's Law	20.28
Heat of Formation	-892.78[kJ/mol]
tPSA	107.22
Log S	-3.197
pKa	8.692, 8.913, 14.858, 15.367

According to the definitions (Wells, 1988), the boiling point is the boiling point for the structure, reported in Kelvin (K) at 1 atm. Melting point is the melting point for the structure, reported in Kelvin at 1 atm. Critical temperature indicates the temperature above which the gas form of the structure cannot be liquefied, no matter the applied pressure, reported in Kelvin. Critical pressure is the minimum pressure that must be applied to liquefy the structure at the critical temperature, reported in bars. Critical volume is the volume occupied of a fixed substance at the critical temperature and pressure, reported in cm³/mol. Gibbs Energy is used for the potential of a thermodynamic system, defined by the amount of work that can be done to a system without its expansion.

Log P and tPSA are two parameters that would affect the absorption, distribution, metabolism and elimination (ADME) of a drug. LogP is an indicator for lipophilicity, calculated by ChemDraw 19.0 (Perkin Elmer) in **Table 4.2**, and it shows the level of the unionized compound at an equilibrium between organic and aqueous phase. A drug with Log P > 5 is considered to have high lipophilicity and is associated with fast metabolic rate, low solubility and low rate of oral absorption (Qiu et al., 2017). tPSA is the topological polar surface area and is also related to the accessibility of the molecule to the solvent (Ali et al., 2012). Both Log P and tPSA are also used to calculate the potential of a compound to penetrate the CNS, defined as log BB (Geldenhuys et al., 2015; Pajouhesh & Lenz, 2005). The well-recognised equations for calculating log BB (explained in section 3.3.2) are: 1) Clark's equation: $\log BB = 0.152\log P - 0.0148tPSA + 0.139$ (Clark, 1999) and 2) Rishton's $\log BB = 0.155\log P - 0.01tPSA + 0.164$ (Rishton et al., 2006).

MR is for molar refractivity, which measures the polarisability of one mole of a molecule. Henry's law is the inverse of the logarithm of Henry's law constant (H), $[-\log(H)]$. Henry's law describes that a gas substance could be dissolved in a liquid, and the degree of dissolution is proportional to the partial pressure above the liquid (Chiou, 2002). The heat of formation is used for the structure to indicate a change of enthalpy when one mole of the substance is formed from all its constituent elements (under normal states), reported in kJ/mol at 1 atm and 298.15K.

Like Log P, Log S also demonstrates the partition coefficient. It measures the solubility of a substance in mol/L water. Log S is also a critical parameter in drug development, and 85% of the drugs have a log S between -1 to -5 (Noordik, 2004).

pKa is the negative logarithm of the acid dissociation constant Ka. The lower of a pKa value, the more likely the hydrogen ions of the substance dissociate in water.

Therefore, the lower the pKa value(s) of a substance, a stronger acid a substance is. pKa can affect the extraction method of a compound as a drug candidate from different biological matrices during the preclinical studies and clinical trials (Cranwell, Harwood & Moody, 2017).

The pKa of LMH001 is marked in **Figure 4.5**, with a 3D structure of LMH001 created by Chem3D 19.0 (PerkinElmer, United Kingdom). ChemOffice 19.0 calculates pKa based on the structure of the molecule, and since four potential groups can be ionised, four pKa values, each for one ionisable functional group, were presented. However, by using a traditional titration method, possibly less than four pKa values would be generated. The calculated pKa result indicates that primarily at a low pH, LMH001 would be neutral, and as the pH increases to around pH = 8.5 to 9.0, LMH001 would be ionised due to one of the phenol -OH groups losing H⁺, and a further phenol -OH group would then lose the H⁺ at a slightly higher pH (still around 8.5 – 9.0). However, although the other two ionisable groups are marked with pKa values by ChemOffice 19.0, further ionisations are hard to predict because of the building up electrostatic effects on such a small molecule as LMH001.

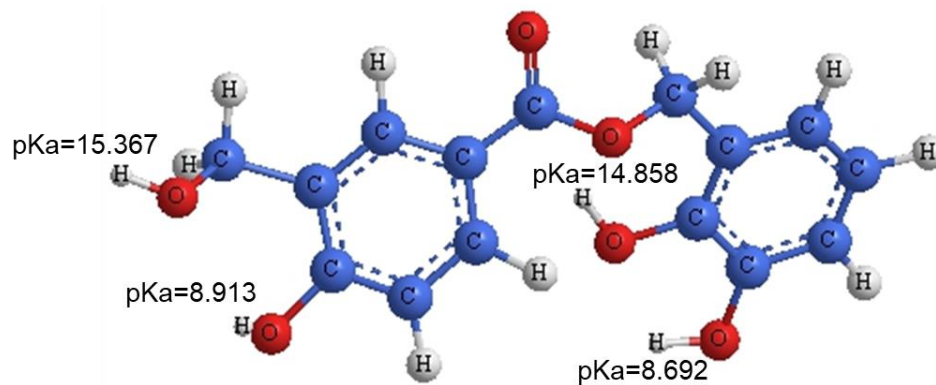


Figure 4. 5 3D structure and the pKa values calculated by ChemOffice 19.0.

Since LMH001 is a polyprotic acid which means more than one H^+ can be ionised, the apparent dissociation of LMH001 in the blood was also calculated. In the blood, $pH = 7.2$ and is not changed after the iv bolus. Therefore, the final pH was 7.2 after 2 mg/ml LMH001 was injected. Since the volume of blood in the mouse is 80 ml/kg, and the initial dose of LMH001 is 10 mg/kg, the initial concentration of LMH001 = (initial dose/volume of blood)/(molecular weight of LMH001) = (10000000 ng/kg) / (80 ml/kg) / 290.076 $\times 10^9$ ng/mol $\times 10^3$ = 505.96 $\times 10^{-6}$ M. Using the definition of pKa (Greco, Rickard, Weiss & Petrucci, 2007), the final apparent pKa of LMH001 in the blood with the current dosage can be calculated as following:



Initial concentration	505.96 $\times 10^{-6}$ M	0	0
Change in concentration	- x	+ x	+ x
Equilibrium concentration	(505.96 $\times 10^{-6}$ - x) M	x	x

According to the definition of pH: $[\text{H}_3\text{O}^+] = 10^{-\text{pH}}$

$$-\text{pH} = \log [\text{H}_3\text{O}^+] = -7.2$$

$$[\text{H}_3\text{O}^+] = 10^{-7.2} = 6.31 \times 10^{-8} = x$$

x represents the disassociation in concentration of LMH001 (unit: M). According to the definition of Ka, $K_a = [\text{H}_3\text{O}^+] [\text{LMH001}^-]/[\text{LMH001}] = x^2 / (505.96 \times 10^{-6} - x) = 3.89$

$\times 10^{-15} / 5.0 \times 10^{-6} = 7.72 \times 10^{-10}$, therefore, the apparent association of LMH001 in the blood is 9.11.

4.3.2 Predicted fragmentation pattern of LMH001

The proposed fragmentation of LMH001 in HPLC-MS/MS in the negative ionisation mode was firstly predicted by Mass Frontier™ 8.0. Analysing the possible fragmentation of LMH001 helped with the understanding of the preliminary HPLC-MS full scan results. The fragmentation analysis was also instructive in establishing HPLC-MS/MS selective-reaction-monitoring (SRM) quantification method. The result of the predicted fragmentation is shown in **Figure 4.6**.

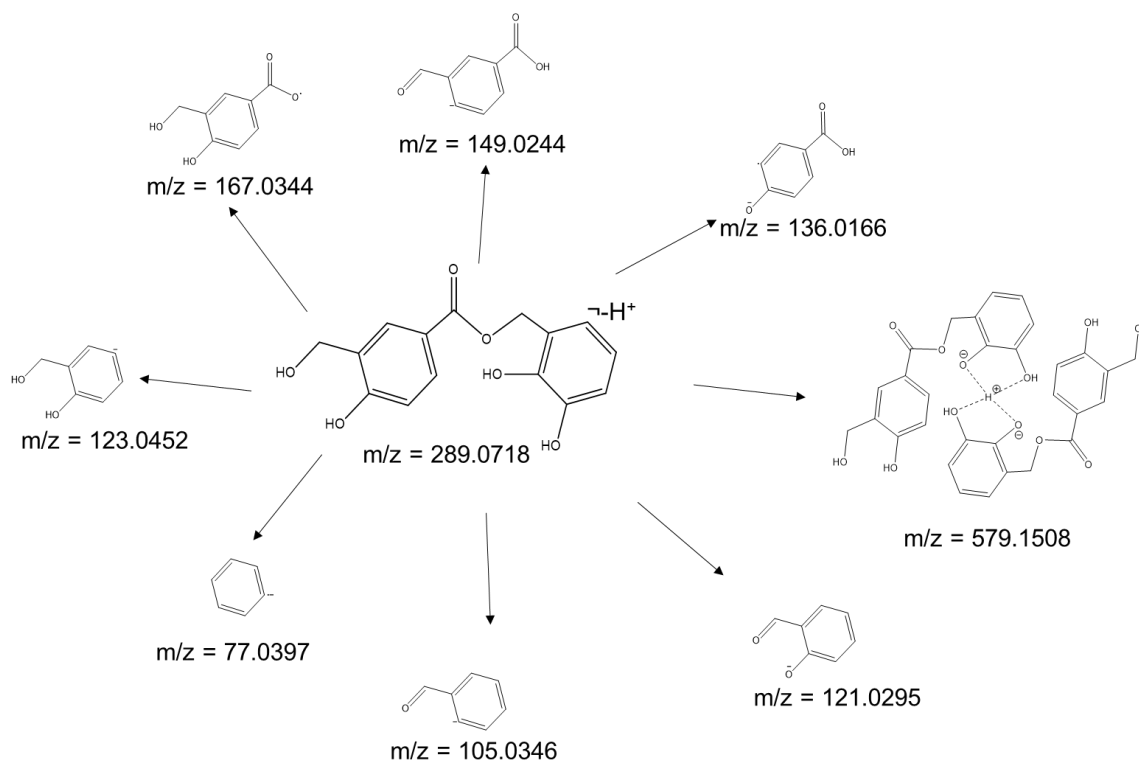


Figure 4. 6 Proposed fragmentation pattern of LMH001 in negative ionisation, result from Mass Frontier™ Spectral Interpretation Software.

4.3.3 Development of HPLC-MS/MS method for LMH001 detection

First, the HPLC-MS method for apocynin, shown in section 2.4 (using the same running buffer, column as apocynin and in negative ionisation mode) was tested, yet no peak was detected in the LMH001 (1,000 ng/ml) calibration samples. After several trials, a method using mobile phases of 0.1% formic acid (v: v) in A) water and B) acetonitrile, the same column (reversed-phase 50 × 2.1 mm ID, 1.9 µm particle, 175 Å pore C18 Hypersil Gold column (Thermo Scientific, USA)) and in negative ionisation mode were found to be appropriate for LMH001 detection. Using the LMH001 extraction method, as discussed in section 4.2.6, along with the detection method, satisfactory peaks of LMH001 in mobile phase A, plasma and urine were able to be generated. **Figure 4.7** shows the representative selected-reaction-monitoring (SRM) HPLC-MS/MS chromatograms of 500 ng/ml LMH001 in (A) mobile phase buffer A (control), (B) plasma, (C) urine.

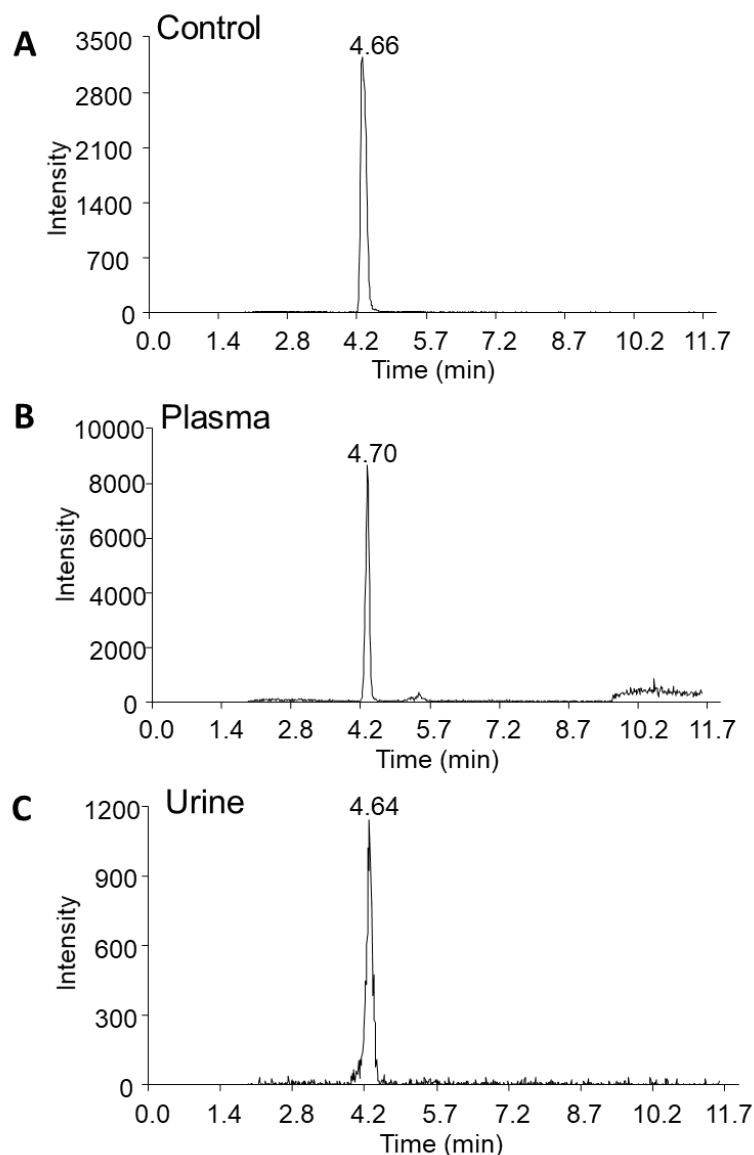


Figure 4. 7 Representative selective-reaction-monitoring HPLC-MS/MS chromatograms of LMH001 in mobile phase A in negative ionisation mode.

The developed method was also used to test the limit of detection (LOD), the limit of quantification (LOQ) and linearity of LMH001 using the new extraction method in the plasma. The same as apocynin, the limit of detection was calculated using the equation: $LOD = 3.9 \times SD_{blank} / \text{Slope of standards}$ and was 2.13 ng/ml and the $LOQ = 3 \times LOD = 6.38$ ng/ml. As a local practice, values whose CV (Coefficient of variation, calculated as the ratio of standard deviation versus the absolute value of mean) above

15 % (marked in % in **Figure 4.8**) were also ruled out for quantification. Good linearity was found between 5-10,000 ng/ml, as is shown in **Figure 4.8**.

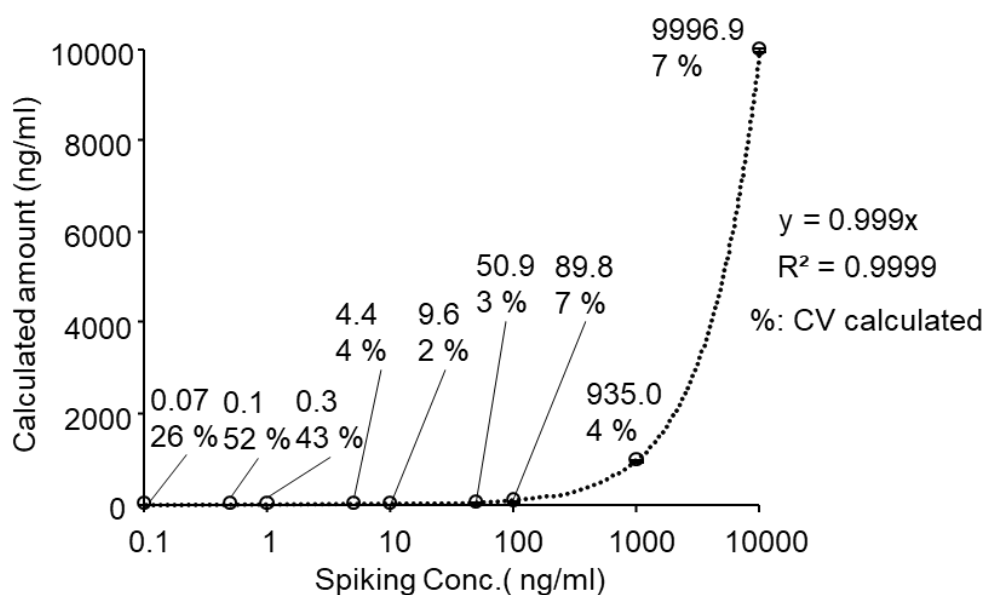


Figure 4. 8 Linearity of LMH001 quantification by HPLC-MS/MS.

The curve was constructed using calibration levels of LMH001 at 0.1, 0.5, 1.0, 5.0, 10.0, 50.0, 100.0, 1,000.0 and 10,000.0 ng/ml in the plasma using the ethyl acetate- HCl extraction method and HPLC-MS/MS described. Each sample was measured in triplicate, and an average of the three measurements was used for constructing the curve. CV marked as (%) is presented below the calculated amount.

4.3.4 Plasma protein binding of LMH001

Plasma protein binding is an indication of an pharmacodynamically effective drug that is unbound and available to circulate and distribute to the sites of effect, and it can also affect the rate of clearance of a drug in the body (Roberts, Pea & Lipman, 2013; Yan & Caldwell, 2004). In murine plasma, measured using the method described in 4.2.7, the plasma protein binding of LMH001 had a %bound of 73.99 ± 5.09 % at 10 ng/ml, 88.75 ± 1.45 % at 50 ng/ml, and 86.05 ± 4.40 % at 1000 ng/ml (**Table 4.3**). These data are instructive in linearity studies of the LMH001 dosage regimen.

Table 4. 3 Plasma protein binding of LMH001 in murine plasma.

LMH Conc. (ng/ml)	% Bound
10	73.99 ± 5.09
50	88.75 ± 1.45
1000	86.05 ± 4.40

4.3.5 The detection of LMH001 in simulated gastric and intestinal fluids

The remaining concentration of 3,000 ng/ml LMH001 in simulated gastric fluid, simulated intestinal fluid and water was measured by HPLC-MS/MS after 0, 10, 30, 60, 90 and 120 min at 37 °C. It was shown in **Figure 4.9** that in the gastric fluid, at 30 min, the concentration of LMH001 dropped to 72.7 ± 0.4 % but maintained relatively stable (ranging from 72.7 ± 0.4 % to 92.7 ± 1.1 % compared to 0 min). However, in the simulated intestinal fluid, the detectable LMH001 dropped quickly to 10.1 ± 0.2 % at 10 min, 1.4 ± 0.1 % at 30 min and eventually reduced to 0.2 ± 0.0 % at 60 min and maintained at 0.2 % level. The concentration of LMH001 in the water was also measured as controls. LMH001 in the water dropped to 59.0 ± 0.7 % at 10 min, and further decreased to 0.9 ± 0.2 % at 60 min and remained at 0.2 ± 0.1 % after that.

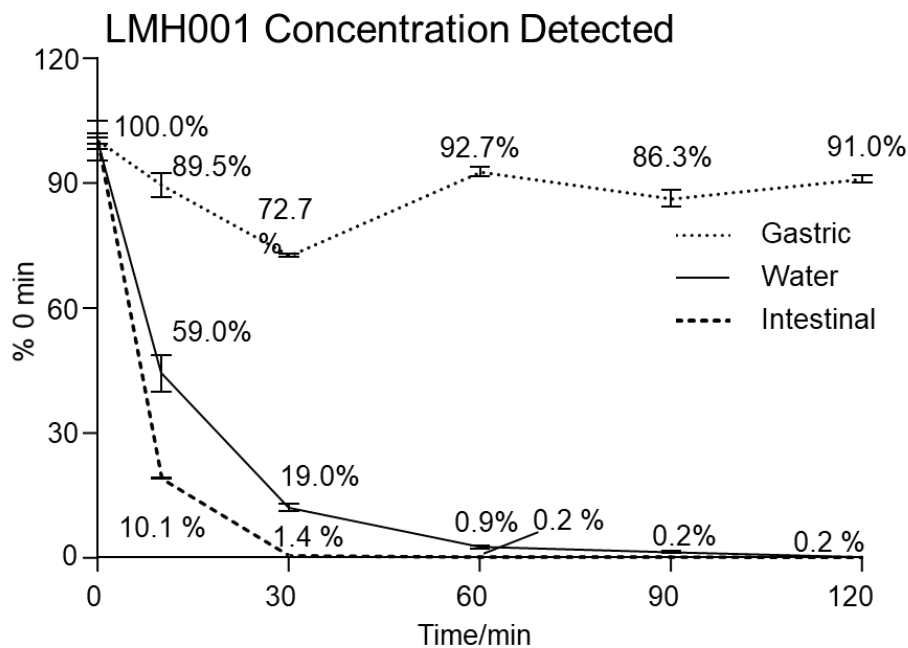


Figure 4. 9 Detected LMH001 in different fluids.

Fluids including simulated gastric fluid (pH = 1.6), simulated intestinal fluid (pH = 6.5) and water (pH = 6.8), detected by HPLC-MS/MS, measured as the percentage remaining after an incubation at 37 °C for 0, 10, 30, 60, 90 and 120 min.

The decrease of LMH001 detection against time at 37 °C was investigated using GC-MS. **Figure 4.10-Figure 4.12** shows the GC results of the LMH001 analysis in simulated intestinal, gastric fluid and methanol (as a control). As is shown in **Figure 4.10 A**, the chromatograms of LMH001 in the simulated intestinal fluid at time 0 of the incubation showed three distinctive peaks with retention times of 11.00 min (denoted as peak 1), 18.43 min (denoted as peak 2) and 26.64 min (denoted as peak 3). **Figure 4.10 B** also showed three distinctive peaks with retention times of 11.05 min (same as peak 1, with similar retention time), 15.63 min (denoted as peak 4) and 18.45 min (denoted as peak 3, as distinguished by retention time). The decreasing abundance of peak 3 and the increasing abundance of peak 4 could be related to the change of LMH001.

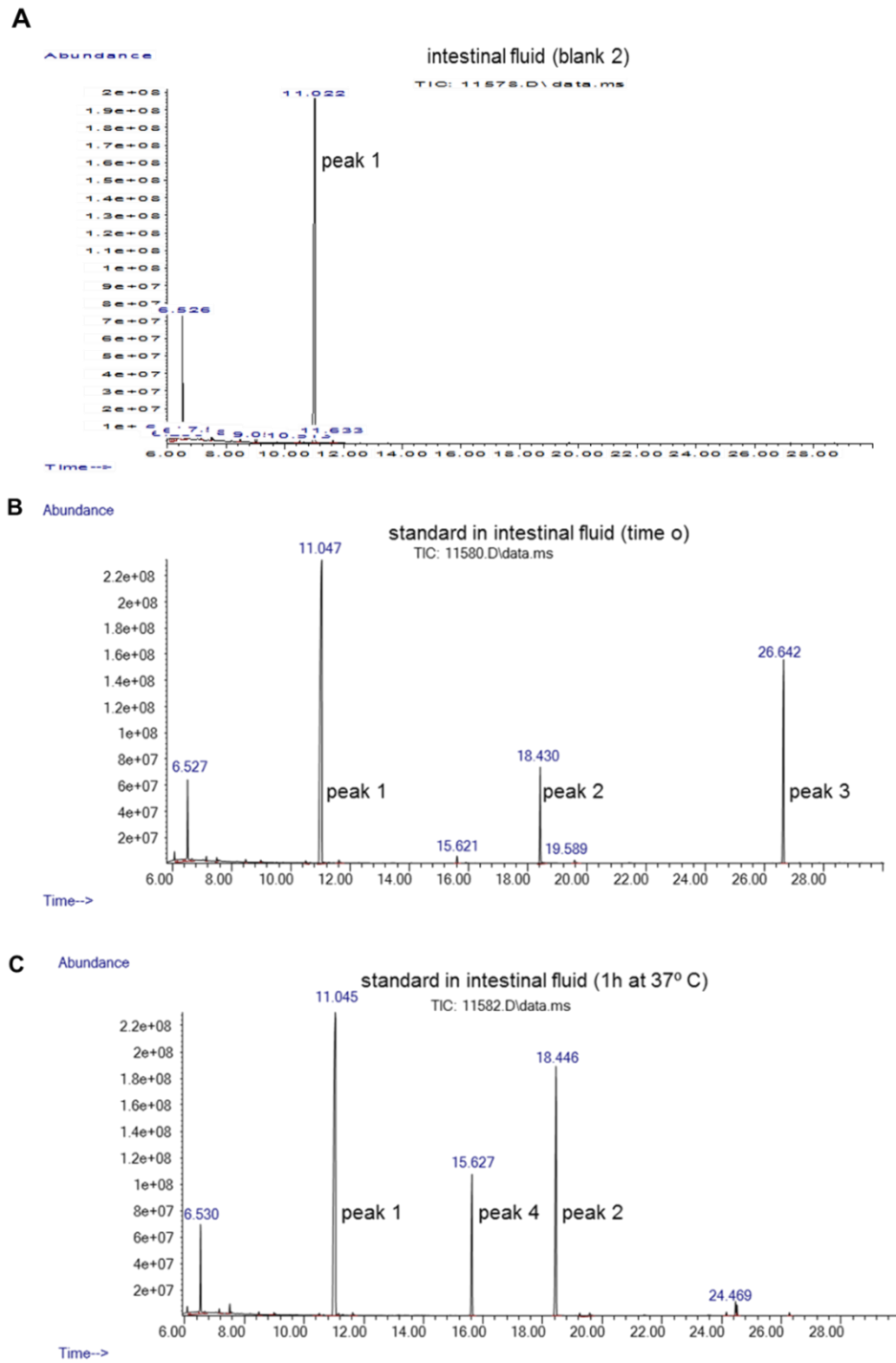


Figure 4. 10 Representative chromatograms of LMH001 in fasted state simulated intestinal fluid (FaSSIF) before and after 60 min.

A. Blank simulated intestinal fluid; B. LMH001 detected at time 0; C. LMH001 detected after 60 min.

Chromatograms from the LMH001 in gastric fluid both before and after 1 h

incubation at 37 °C (**Figure 4.11**) showed two distinctive peaks 1) at 18.43 min and 18.43 min (peak 2) and 2) at 21.64 min and 21.65 min (peak 3), indicating no changes of LMH001 in the gastric fluid, as detected by HPLC-MS/MS.

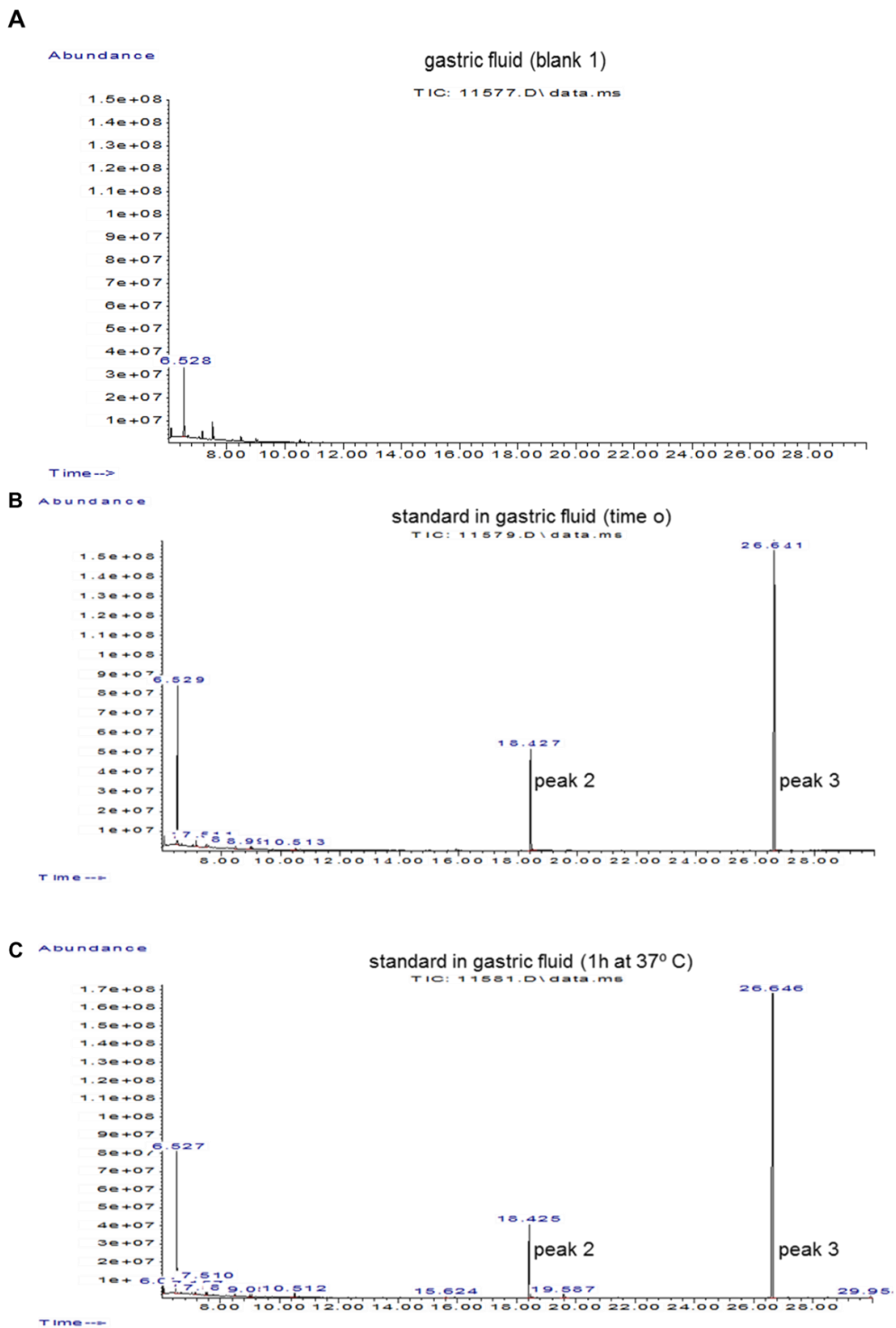


Figure 4. 11 Representative chromatograms of LMH001 in fasted state simulated gastric fluid (FaSSIF) before and after 60 min.

A. Blank simulated gastric fluid; B. LMH001 detected at time 0; C. LMH001 detected after 60 min.

Chromatograms of LMH001 in methanol (as control) were shown in **Figure 4.12**. The same as LMH001 in simulated gastric fluid, peak 2 and peak 3 was detected.

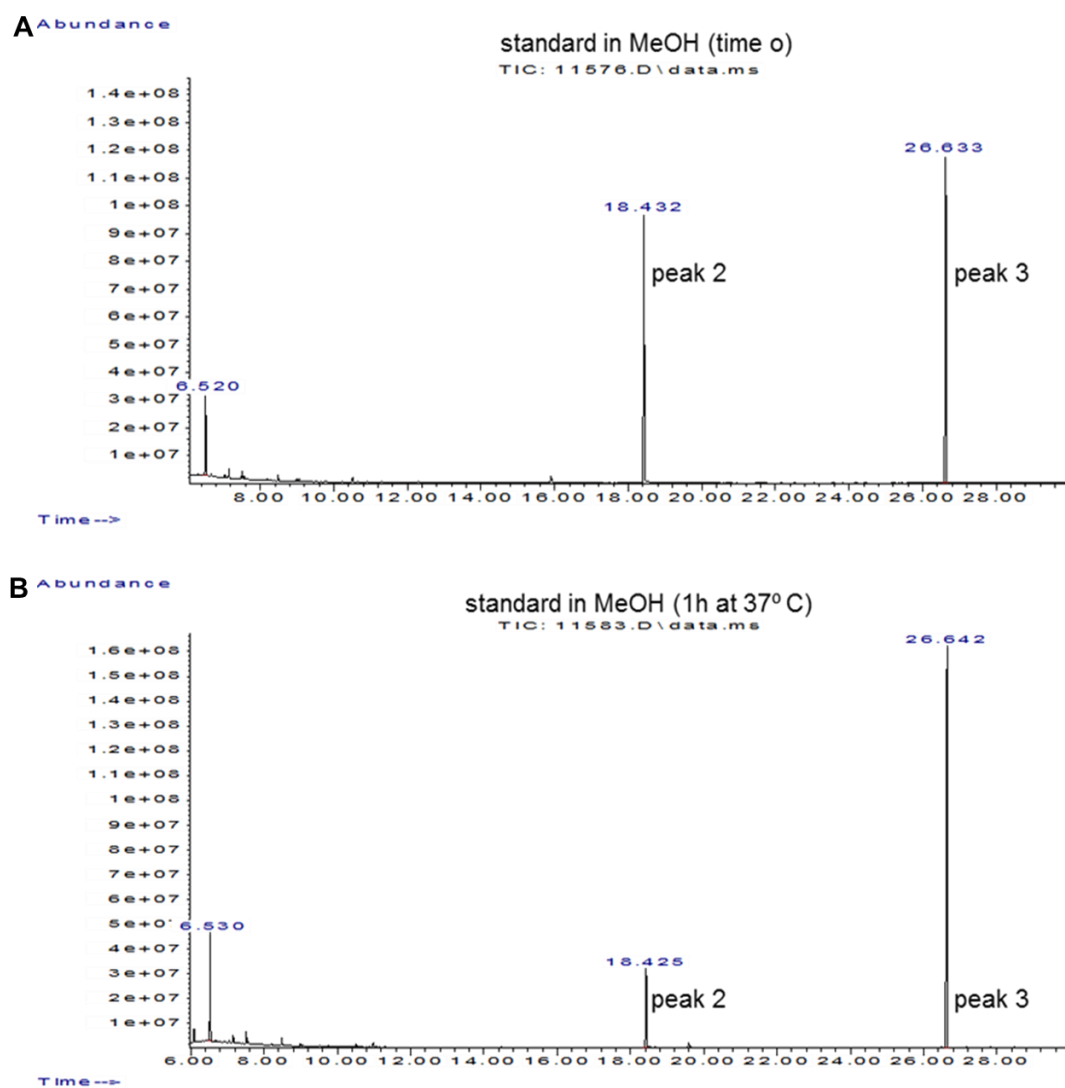


Figure 4. 12 Representative chromatograms of LMH001 in methanol before and after 60 min.

A. LMH001 detected at time 0; B. LMH001 detected after 60 min.

4.3.6 LMH001 distribution in the plasma and urine

As discussed in the apocynin PK study, the same absorption, distribution, metabolic and elimination rate were assumed among these CD1 mice used for LMH001 PK study (section 3.3.2). Using the established HPLC-MS/MS and LMH001 extracting method, concentrations of LMH001 in the plasma and urine of the CD1 mice, collected at designated time points were measured after iv bolus injection at a dose of 10 mg/kg (results are shown in **Figure 4.13**).

Plasma concentration of LMH001 reached $27,271.79 \pm 9,186.93$ ng/ml at 1 min after the iv bolus, and declined to $9,630.83 \pm 3792.06$ ng/ml at 2.5 min; at 10 min it was detected at 780.87 ± 192.55 ng/ml and then decreased to 10.47 ± 4.51 ng/ml at 30 min and 3 h, it was 6.71 ± 4.64 ng/ml. The LOD was 7.054 ng/ml, and the LOQ was 21.16 ng/ml (Uhrovčík, 2014).

The urine was reported after 5 min since it was not detected at the first two time points. The concentration was detected at $1,318.52 \pm 749.43$ ng/ml at 5 min and at 20 min it peaked at $18,213.69 \pm 10,751.33$ ng/ml. It then decreased to 327.31 ± 200.11 ng/ml at 30 min and dropped to 26.02 ± 20.54 ng/ml 3 h after iv injection. The limit of detection was 1.86 ng/ml, and the limit of quantification was 5.58 ng/ml, calculated using the same method as with plasma.

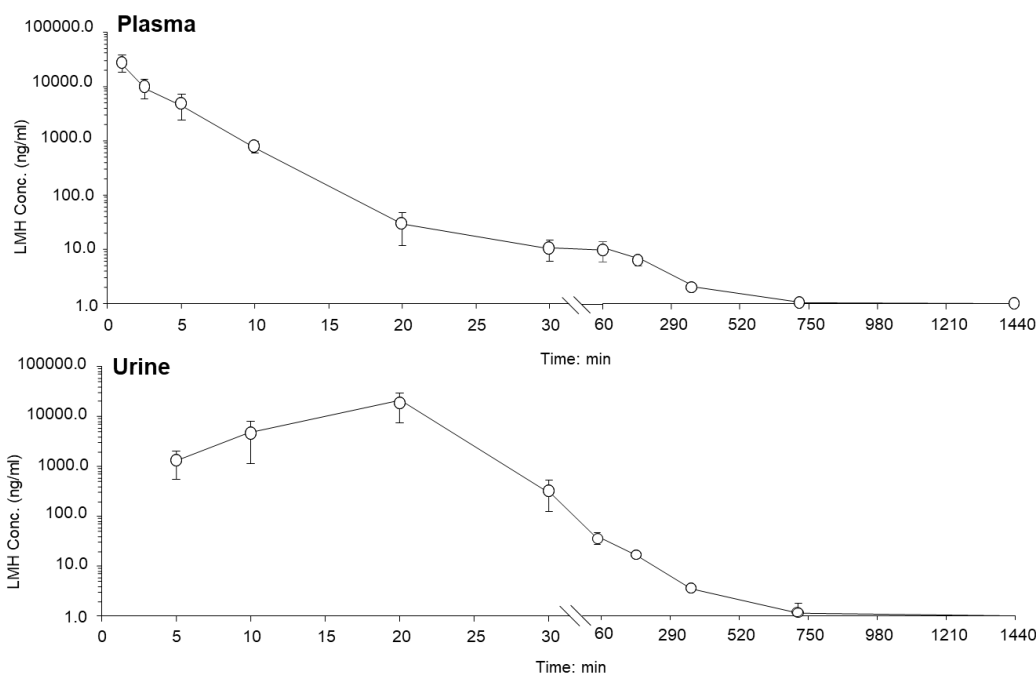


Figure 4.13 Kinetic changes of LMH001 from 1 min to 24 h post iv bolus (10 mg/kg) in male CD1 mice (12-week of age, 26-30 g) in plasma and urine (from 5 min to 24 h).

Three detections per mouse sample were performed, and six mice per group were used. An average concentration of LMH001 at one time-point per sample was first calculated, and the error bars were then calculated using the standard deviation (SD) of different mouse samples at one time-point in one biological fluid. Data presented as Mean \pm SD.

4.3.7 Characterisation of LMH001 PK parameters by non-compartmental analysis (NCA) and non-linear mixed-effects (NLME) model

4.3.7.1 NCA analysis by R 4.0.1

The detected LMH001 concentration in the plasma (1 – 30 min, r^2 defined to be ≥ 0.900 , sparse sampling selected, $n = 6$ per timepoint) were subjected to non-compartmental analysis by R 4.0.1 on the RStudio 1.3 platform with the PKNCA package. **Figure 4.14** shows the R Script details (A) and Console output (B). **Table 4.4** shows the curve fit (r^2 and adjusted r^2 , half-life ($t_{1/2}$) and K_{el}) and parameter calculated

by R, including $AUC_{0-30\text{min}}$, $AUC_{0-\infty}$, and predicted $AUC_{0-\infty}$ ($AUC_{0-\infty(\text{pred})}$). Secondary parameters, including clearance (CL) and volume of distribution (V_d), were calculated based on $AUC_{0-\infty}$ with the following equations:

$$CL = Dose/AUC_{0-\infty}$$

$$V_d = (Dose/AUC_{0-\infty})/k_{el}$$

A. R Script

```

RStudio
File Edit Code View Plots Session Build Debug Profile Tools Help
Go to file/function Addins
AUC-Calculation-with-PKNCAR* x Untitled1* x
1- ## ----check-ggplot, include=requireNamespace("ggplot2"), results="asis"-----
2 cat("ggplot2 is required for this vignette to work correctly. Please install the ggplot2 library and retry building the vignette.")
3
4- ## ----setup-----
5- suppressPackageStartupMessages({
6   library(PKNCAR)
7   library(dplyr)
8   library(cowplot)
9   library(knitr)
10  library(ggplot2)
11 })
12 scale_colour_discrete <- scale_colour_hue
13 scale_fill_discrete <- scale_fill_hue
14
15 my_conc <- data.frame(conc=c(27271.79, 9630.83, 4650.75, 780.87, 29.68, 10.47),
16                      time=c(0.017, 0.042, 0.083, 0.167, 0.333, 0.500),
17                      subject=1)
18 my_conc$BLOQ <- my_conc$conc == 10
19 my_conc$measured <- TRUE
20
21- ## ----setup-visualization, eval=requireNamespace("ggplot2")-----
22 ggplot(my_conc,
23        aes(x=time,
24            y=conc,
25            shape=BLOQ,
26            group=subject)) +
27   geom_line() +
28   geom_point(size=4) +
29   scale_x_continuous(breaks=my_conc$time) +
30   theme(legend.position=c(0.8, 0.8))
31
32- ## ----load dose data-----
33 my_dose <- data.frame(dose=c(1000000),
34                     time=c(0),
35                     subject=1)
36
37- ## ----calc_nca-----
38
39 conc_obj <- PKNCARconc(my_conc, conc~time|subject)
40 dose_obj <- PKNCARdose(my_dose, dose~time|subject)
41 data_obj <- PKNCARdata(data.conc=conc_obj, data.dose = dose_obj,
42                      intervals=data.frame(start=0.017,
43                                          end=0.500,
44                                          auc1=TRUE,
45                                          auc1ast=TRUE,
46                                          aucinf.pred=TRUE,
47                                          aucinf.obs=TRUE))
48
49 results_obj <- pk.nca(data_obj)
50 kable(as.data.frame(results_obj))
51 pk.calc.c0(conc=c(27271.79, 9630.83, 4650.75, 780.87, 29.68, 10.47),
52          time=c(0.017, 0.042, 0.083, 0.167, 0.333, 0.500), time.dose = 0, check = TRUE)

```

B. R Console Output

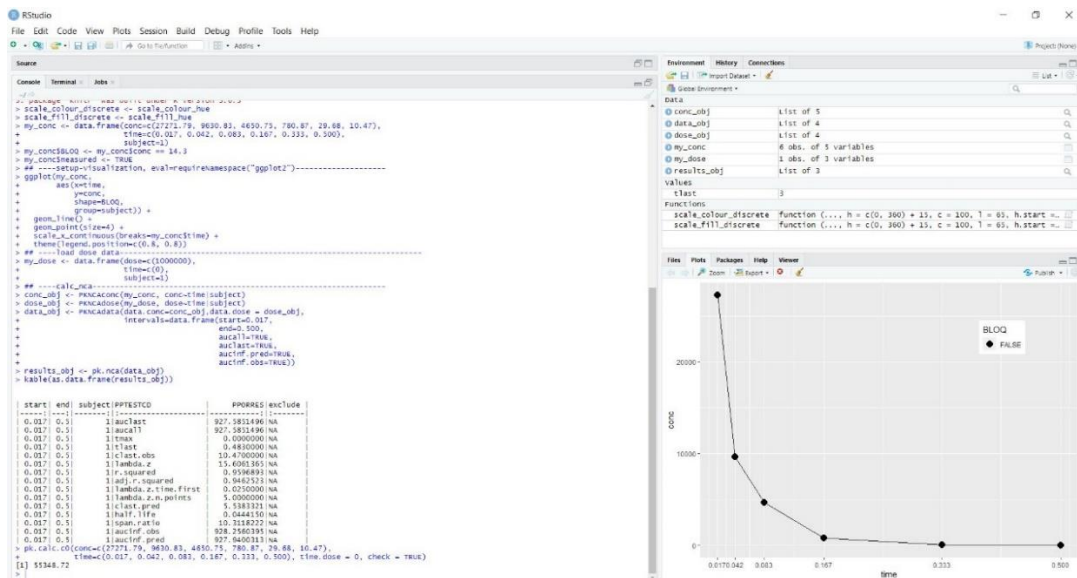


Figure 4. 14 NCA analysis by R 4.0.1, including the R Script (A) and Console (B).

Table 4. 4 Curve fit and NCA PK calculation of LMH001 by R 4.0.1, with PKNCA package.

Pharmacokinetic parameters	Units	NCA
C_0	ng/mL	55348.72
C_{max}	ng/mL	27271.79
r^2	-	0.96
r^2 , adjusted	-	0.95
$AUC_{0-30min}$	h·ng/mL	927.59
$C_{last(obs)}$	ng/mL	10.47
$AUC_{0-\infty}$	h·ng/mL	928.26
$C_{last(pred)}$	ng/mL	5.54
$AUC_{0-\infty(pred)}$	h·ng/mL	927.94
$t_{1/2}$	h	0.044
K_{el} (lambda z)	1/h	15.61
$CL_{(obs)}$	mL/h/kg	10772.89
$V_{d(obs)}$	mL/kg	690.30
$CL_{(pred)}$	mL/h/kg	10776.56
$V_{d(pred)}$	mL/kg	690.54

C_0 : extrapolated plasma concentration at time 0; C_{max} : maximum (or peak) plasma concentration; $AUC_{0-30min}$: Area under the curve from 0 to 30 min; $AUC_{0-\infty}$: Area under the curve from time 0 extrapolated to infinite; $t_{1/2}$: terminal half-life; K_{el} : elimination rate constant; CL: clearance; V_d : volume of distribution. Obs: observed; Pred: predicted.

r^2 adjusted is the adjusted r-squared value when r^2 and the number of points were taken into account. The AUC calculation method used in the package was the linear-log trapezoidal rule (linear-up/log-down), where during the rising of the curve, a linear rule is applied, while the logarithm rule is applied during the declining of the curve (Jawien, 2014). In this package, $AUC_{0-\infty}$ was calculated by a continuous curve for the AUC integration, and $AUC_{0-\infty(pred)}$ was calculated by the $C_{last(pred)}$ (a jump from $C_{last(obs)}$ to $C_{last(pred)}$) with the fitted curve (lambda z). In this case, both $AUC_{0-\infty(obs)}$ and $AUC_{0-\infty(pred)}$ were selected for the calculation of CL and V_d . The compiled report exported from R is included in Appendix IV.

4.3.7.2 NCA analysis by Phoenix WinNonlin 8.1

At the same time, the LMH001 plasma concentrations were also subjected to NCA in Phoenix WinNonlin 8.1, with the same conditions defined as in R. The AUC calculation method used in WinNonlin was linear trapezoidal linear interpolation rule with a sparse sampling method. $AUC_{(t_2-t_1)}$ and the specific concentration predicted (C^*) at the time (t^*) are calculated by the following equations:

$$AUC(t_2 - t_1) = \frac{(t_2 - t_1)(C_1 + C_2)}{2}$$

$$C^* = C_1 + \frac{(t^* - t_1)}{t_2 - t_1} (C_2 - C_1)$$

Figure 4.15 shows the time-dependent elimination of LMH001 by WinNonlin and the curve fitted ($r^2 = 0.9575$, r^2 , adjusted = 0.9468) was used for calculating the NCA parameters of LMH001. **Table 4.5** summarises the parameters calculated by WinNonlin. the following formula calculated r^2 adjusted in WinNonlin, and λ_z (K_{el}) was estimated using the largest adjusted r^2 :

$$Adjusted\ r^2 = 1 - \frac{(n - 1)(1 - r^2)}{n - 2}$$

Time-dependent elimination of LMH001 in the plasma

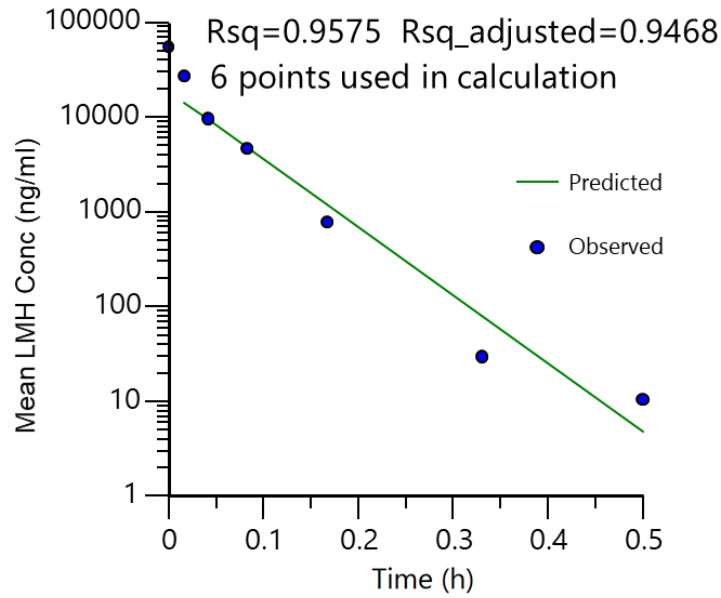


Figure 4. 15 Curve fit of LMH001 plasma concentration against time (0.017 h to 0.5 h) generated by Phoenix WinNonlin 8.1.

Table 4. 5 Curve fit and NCA PK calculation of LMH001 by Phoenix WinNonlin 8.1.

Pharmacokinetic parameters	Units	NCA
C_0	ng/mL	54593.44
C_{max}	ng/mL	27271.79
r^2	-	0.96
r^2 , adjusted	-	0.95
$AUC_{0-30min}$	h·ng/mL	1759.34
$AUC_{0-\infty}$	h·ng/mL	1759.75
$AUC_{0-\infty(pred)}$	h·ng/mL	1759.34
$t_{1/2}$	h	0.042
k_{el} (lambda z)	1/h	16.55
$CL_{(obs)}$	mL/h/kg	5682.63
$V_{d(obs)}$	mL/kg	343.43
$CL_{(pred)}$	mL/h/kg	5683.93
$V_{d(pred)}$	mL/kg	343.43

4.3.6.3 NCA analysis using non-linear regression in Excel

The PK parameters, including K_{el} , $t_{1/2}$, $AUC_{0-30min}$, $AUC_{0-\infty}$, CL and V_d were also calculated by fitting a non-linear regression curve in the Excel. **Figure 4.11** is the curve fit by Excel to calculate the LMH001 PK parameters. **Table 4.6** summarises the final PK parameters of LMH001 calculated by hand, with r^2 being 0.9595, calculated by Excel, and AUC is calculated using the linear trapezoidal method:

$$AUC(t_2 - t_1) = \frac{(t_2 - t_1)(C_1 + C_2)}{2}$$

$$AUC(0 - \infty) = AUC(0 - 30min) + \frac{C_{30min}}{K_{el}}$$

The secondary PK parameters, including CL and V_d , were calculated using the same equations used in the R calculation (section 4.3.5.1).

Time-dependent elimination of LMH001 in the plasma

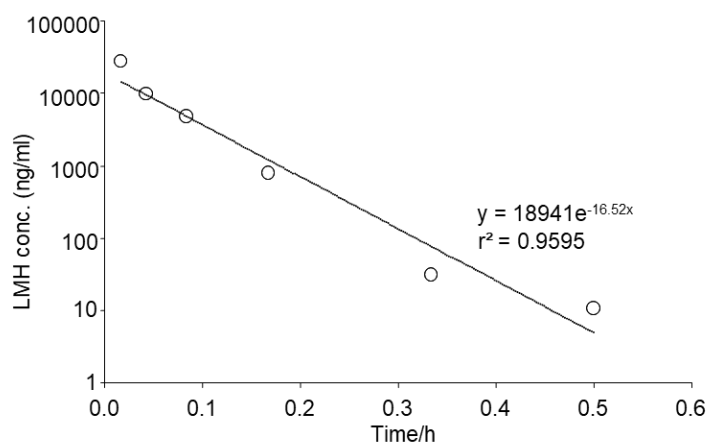


Figure 4. 16 The non-compartmental analysis of LMH001 by Excel and hand calculation.

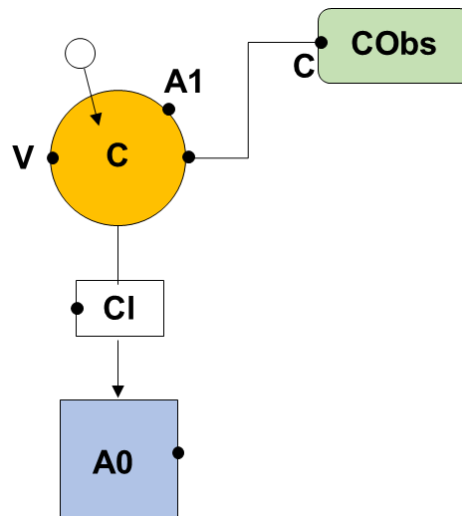
Table 4. 6 Curve fit by Excel and NCA PK calculation of LMH001 by hand.

Pharmacokinetic parameters	Units	NCA
C_0	ng/mL	18941.00
C_{max}	ng/mL	27271.79
r^2	-	0.96
$AUC_{0-30min}$	h·ng/mL	1056.02
$AUC_{0-\infty}$	h·ng/mL	1056.53
$t_{1/2}$	h	0.042
K_{el}	1/h	16.52
CL	mL/h/kg	9464.97
V_d	mL/kg	572.94

4.3.7.4 NLME modelling by Phoenix WinNonlin 8.1

The compartmental analysis of LMH001 was also carried out using Phoenix WinNonlin 8.1 NLME model, with the model expressed as $Y = f(\theta, \text{Time})$, where θ was the PK parameters. Time-dependent change of LMH001 concentration (n=6 per timepoint, from 1 min to 3 h) were fitted into one-, two- and three-compartmental analysis with the following setting: bolus input and a first-order output, Clearance as primary parameters. The statements for one, two and three compartmental analysis, along with the model illustrations are as following (model illustrations in **Figure 4.17.1, 2 and 3**):

4.17.1 Schematic diagram of one compartmental model.



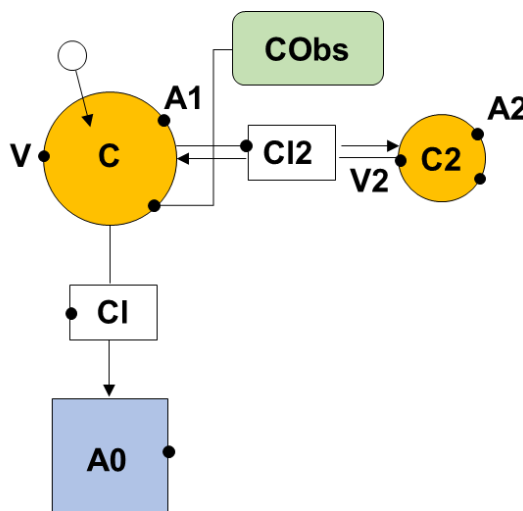
Statements for one compartmental analysis:

$$\text{cfMicro (A1, Cl/V)}$$

$$\text{dosepoint (A1)}$$

$$C = A1/V$$

4.17.2 Schematic diagram of two compartmental model.



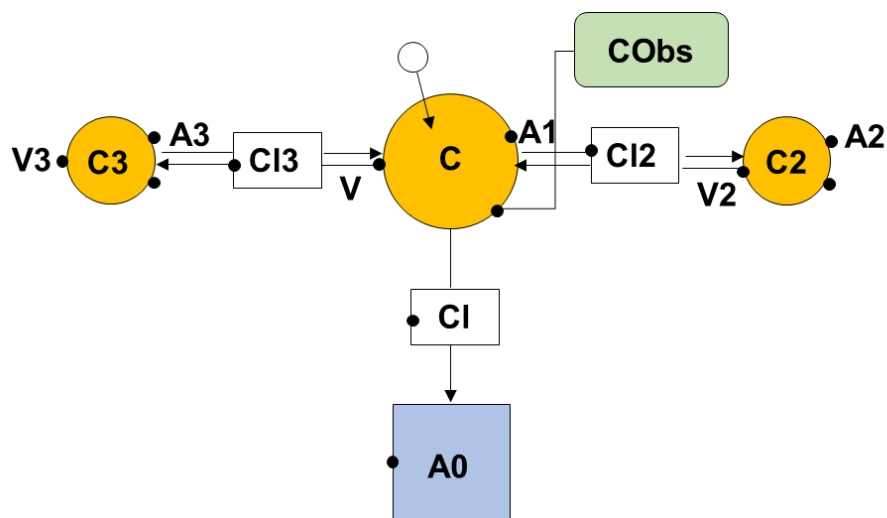
For two compartmental analysis:

$$\text{cfMicro (A1, Cl/V, Cl2/V, Cl2/V2)}$$

$$\text{dosepoint (A1)}$$

$$C = A1/V$$

4.17.3 Schematic diagram of three compartmental model.



For three compartmental analysis:

$$\text{cfMicro (A1, CI/V, CI2/V2, CI3/V, CI3/V3)}$$

$$\text{dosepoint (A1)}$$

$$C = A1/V$$

Figure 4. 17 Schematic illustrations of one, two and three compartmental models.

The overall result of the PK parameters (θ) calculated is listed in **Table 4.7**.

Table 4. 7 Compartmental analysis of LMH001 by WinNonlin 8.1.

Pharmacokinetic parameters	Units	time point: 0 - 3 h		
		1-C	2-C	3-C
AUC _{0-∞}	h·ng/mL	1504.45	1506.49	1782.15
tvCL	mL/h	9849.00	9767.67	4054.89
tvCL2	mL/h	-	81.55	1682.53
tvCL3	mL/h	-	-	74.23
tvV	mL	274.37	274.37	27.58
tvV2	mL	-	1200.08	62.76
tvV3	mL	-	-	339.76

1-CA, 2-CA or 3-CA: one, two or three compartmental analysis, data used are from 1 min – 3 h; AUC_{0-∞}: Area under the curve from time 0 extrapolated to infinite time; CL: clearance; CL2 or CL3: second or third compartment clearance, the prefix of 'tv' denotes fixed-effect or typical value; Vd: volume of distribution; V1, V2 or V3: first, second or third compartment volume of distribution, the prefix of 'tv' denotes fixed-effect or typical value.

The model diagnostic parameters, including Log-Likelihood (LogLik), -2 Log Likelihood (-2LL), Akaike information criterion (AIC), Bayesian information criterion (BIC), and the corrected AIC (AICc) are listed in **Table 4.8**. In these three models, the residual (ϵ) calculation method chosen was Additive, which incorporated the observation with standard deviation using the following formula:

$$Y = f(\theta, \text{Time}) + \epsilon$$

In WinNonlin, it was expressed as:

Error (CEps = estimated standard deviation)

Observe (Cobs = C + CEps)

Table 4. 8 Model diagnostic parameters of LMH001 compartmental analysis, fitted with NLME model.

Model Fit	1-C	2-C	3-C
-2LL	917.54	917.53	913.83
AIC	923.54	927.53	927.83
AICc	924.08	928.96	930.63
BIC	929.15	936.89	940.93
nParm	3	5	7
nObs	48	48	48

LogLik: log likelihood; AIC: Akaike information criterion; AICc: the corrected AIC, $AICc = AIC + 2 \times nParm (nParm+1)/(nObs-nParm-1)$, used when $nObs/nParm < 40$ (Bertrand, Comets & Mentre, 2008); BIC: Bayesian information criterion; nParm: number of PK parameters; nObs: number of observations.

The compartmental analysis with the smallest AICc (one-compartmental analysis) was accepted, and **Figure 4.18** shows the model diagnosis of LMH001 one compartmental model.

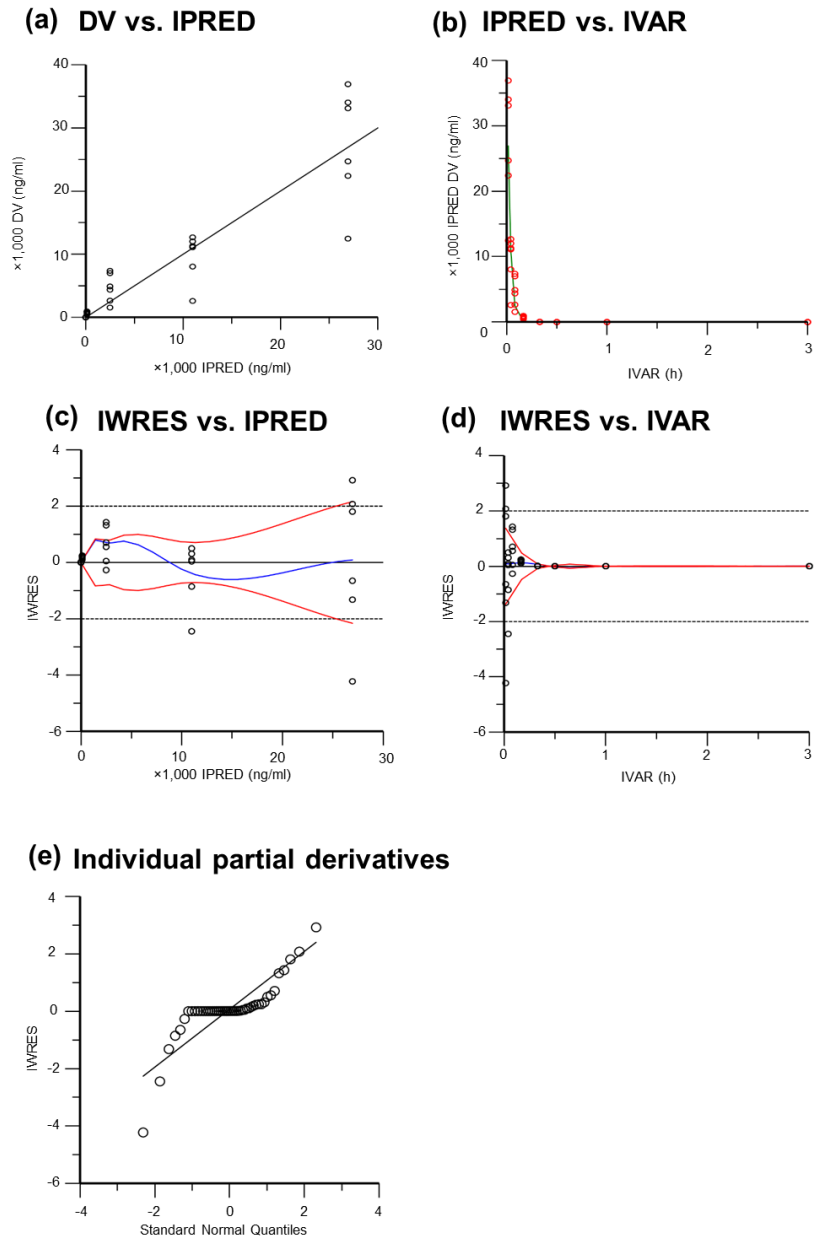


Figure 4. 18 One-compartmental NLME model fit of LMH001 using Phoenix WinNonlin 8.1.

Diagnostic scatter plots of the one-compartmental NLME model. (a) Observed versus individual-predicted concentrations (DV vs IPRED); (b) Individual-predicted concentrations versus time (IPRED vs IVAR); (c) Individual weighted residuals versus individual predictions (IWRES vs IPRED); (d) Individual weighted residuals versus time (IWRES vs IVAR); (e) Quantile-quantile plot of the components of individual weighted residuals.

4.4 Discussion

LMH001 is one of the simplest bi-aromatic and tri-aromatic compounds developed by Professor Jian-Mei Li's research as one of the 36 Nox2 inhibitors. It is effective in reducing ROS production among different cell types including murine lymph node microvascular endothelial cell line SVEC4-10, murine embryonic fibroblast cell line NIH-3T3 fibroblasts, human promyelocyte leukaemia cell line HL-60, human foetal lung fibroblast cell line IMR90, human hepatocytic cell line HPMEC, and human lung adenocarcinoma epithelial cell line A549 after the appropriate stimulation with either TNF α (100 U/ml), AngII (200 nM) or EGF (10 ng/ml). At the same time, LMH001 was found to have no cytotoxicity up to 10 μ M and is therefore believed to have greater potential in treating oxidative-stress related diseases. In this study, the chemical and PK properties of LMH001 were characterised for the first time. By looking at the PK parameters and the metabolism of LMH001 *in vivo*, we can understand the ADME of LMH001, as a representative Nox2 inhibitor for the bi- and tri- aromatic compounds developed in this lab, and make sensible choices for the dosing route and regimen in the future preclinical and clinical studies.

The PK study of LMH001 was designed based on results from apocynin (chapter 3) and the *in vitro* studies of LMH001 (chapter 5). For example, since both LMH001 and apocynin are small molecules (< 900 Dalton) (LMH001: 290.08 Da; apocynin: 166.17 Da), structure, pKa (strongest acidic pKa of apocynin = 8.27, from drugbank.ca/drugs/DB12618) and hydrophilicity, time points of LMH001 post iv bolus were designed to be 1 min, 2.5 min, 5 min, 10 min, 20 min, 30 min, 1 h, 3 h, 6 h, 12 h and 24 h, based on the short half-life of apocynin (0.05 h) and its rapid distribution to different organs. The dosing regimen of 10 mg/kg was also designed according to apocynin studies. Since 5 mg/kg apocynin in the PK study displayed noticeable and

promising results in different organs, with the difference of molecular weight between apocynin and LMH001 in mind, LMH001 dosage was therefore increased to 10 mg/kg. The dosage of LMH001 was not designed to achieve the same concentration as apocynin because it was taken into account that LMH001 was a new compound whose PK parameters had never been looked at before, and a stronger signal from a higher dosage within the toxicity limit would be able to give a more promising and convincing result. In addition, it is worth pointing out that for one certain compound, its metabolism is not affected by the dosing regimen (Kufe, Holland, Frei & American Cancer Society., 2003) and therefore, the change of the dose in this study in comparison to apocynin study, would not affect the PK properties such as clearance and half-life of LMH001 and the results are still able to be compared to apocynin.

During the development of HPLC-MS/MS method for LMH001 detection, based on the chemical structure and properties of LMH001, two sets of gradient buffers: set One: A) 480:20:0.38 water: methanol: ammonium acetate (v: v: w) and B) 20:480:0.38 water: methanol: ammonium acetate (v: v: w); set Two: (A) 0.1% formic acid in water (v: v) and (B) 0.1% formic acid in acetonitrile (v: v) were tested. The results showed that only set B was able to give a satisfactory result with reasonable sensitivity (LOD = 2.13 ng/ml) and good linearity between 5 – 10,000 ng/ml LMH001 ($r^2 = 0.9999$). The extraction method for LMH001 was established by first trying out the extraction method for apocynin. However, alongside the result shown in section 4.3.1, it was also discovered that the filter used for apocynin (Whatman, 13 mm, Nylon filter media with polypropylene housing, pore size 0.2 μ m, 6789-1302) caused a significant loss (recovery rate = 2.4 %). Therefore, after consulting Sigma-Aldrich technical supports, the filter was changed to IC Millex LG (hydrophilic polytetrafluoroethylene membrane, 0.2 μ m, 13 mm diameter, housing high-density

polyethylene, catalogue No. SLLG013SL) and it could maintain a recovery rate at (90 ± 5) %.

Using the HPLC-MS/MS, LMH001 was not detectable in the simulated intestinal fluid after 1 h. LMH001 (different peaks) were able to be detected by GC-MS with a stronger ionisation. The result suggested a change in the ionisation, solubility or the structure of LMH001 in higher pH aqueous solutions. This change might have contributed or be related to the rather short terminal half-life of LMH001, and could be due to the hydrolysis of the ester summarised as **Figure 4.19**. However, the mechanism proposed here are mere speculations based on the results, and one of the more accurate ways to track and confirm the changes of a drug molecule is to use radioactive tracers such as ^{14}C (Guengerich, 2012; Isin et al., 2012).

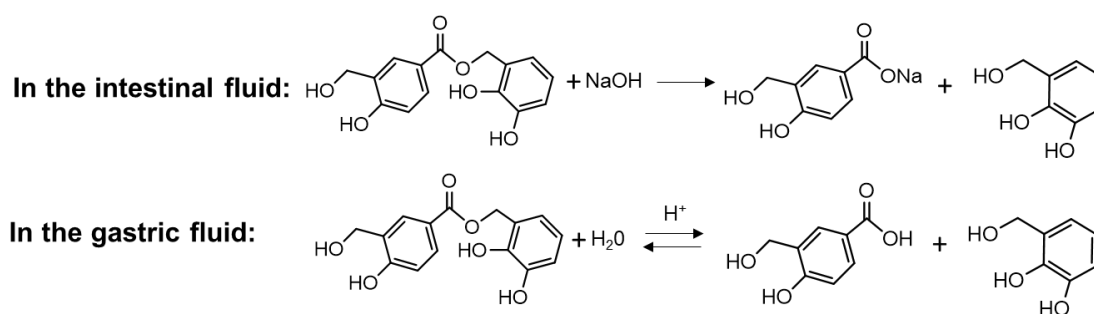


Figure 4. 19 The predicted hydrolysis of LMH001 in simulated intestinal and gastric fluid.

The process was the hydrolysis of ester, and it started with the autoionization of water, followed by the protonation of the ester group in the compound (Gunaydin & Houk, 2008). For esters activated in the ethyl portion with a leaving group in the range of $\text{pK}_a = 12.0 - 16.0$ (such as LMH001), the second part of the process would involve a second water molecule (acting as a base) donating the hydroxide ion as an attacker to the leaving group and the hydrolysis was dependent on the reactivity of the attacking reagent and its ability to aid the expulsion of the leaving group (Fersht & Kirby, 1967;

Li & Bugg, 2007). The hydrolysis of ester should be considered in all aqueous solutions (da Silva, Guimaraes & Pliego, 2013) and is indeed prevalent in the drug development settings (Waterman et al., 2002). There are two types of carboxylesterases (human carboxylesterase 1 and 2) distributed throughout the human body which can catalyse the hydrolysis of amides, carbamates esters, and thioesters (Williams, 1985; Laizure et al., 2013). While it was in mice and rats that the carboxylesterase activity seemed to dominate compared to humans, cholinesterase activity was significant in human (Rudakova, Boltneva & Makhaeva, 2011).

This could also be due to metal ion contamination. This is because Cu (II) and Fe (III) ions could act as catalysts during the oxidation happening in the air. In fact, ascorbic acid was found to have a much faster rate of being oxidised under a low pH (ranging from 2-5.5) (Khan & Martell, 1967).

There are several ways to overcome this limitation. For example, the addition of caffeine was shown to be effective in preserving the hydrolysis of benzocaine (Higuchi & Lachman, 1955), procaine (Higuchi & Lachman, 1955) and tetracaine (Lachman & Higuchi, 1957). Methylphenidate relies on modified-release formations as a commercially available once-daily self-administered medicine (Coghill et al., 2013; Coghill et al., 2015; Cortese et al., 2017). Another way to prevent the hydrolysis is to modify the compound structure in the early drug development stage, provided that the hydrolysis is discovered early enough and well-recognised. The standard methods include adding steric shields (such as by adding an alkyl group), utilising the electronic effects of bioisosteres (such as by replacing the ester group by amine group) or undergoing stereo electronic modification (Karaman, 2013). Therefore, in future

studies, these methods can be utilised to improve the efficacy of LMH001 and even the whole group of bi-aromatic and tri-aromatic compounds developed in this lab.

In this study, however, the focus of this thesis is the PK characterisation of LMH001, the data generated *in vivo* are based on the experiment designs, with proper controls. The LMH001 concentration measured in the plasma and urine still reflect its PK in mice and can be used for PK interpretation. Also, the hydrolysis that was suspected of having happened in the simulated intestinal and gastric fluid did not necessarily reflect the *in vivo* situation, since LMH001 was novel and might have some other undiscovered chemical properties that could affect its state. For example, it was suggested to be light-sensitive by TOCRIS Bioscience (United Kingdom) when it was synthesised. Moreover, the result from section 4.3.4 suggested significant amount of LMH001 still excreted from urine after 30 min. Another aspect that should not be neglected is its effect. The effect of LMH001 on the ROS production in the rat cardiomyocyte cell line H9C2 cells was also investigated, which is further discussed in chapter 5.

A short half-life could also be attributed to the small size of the molecule (as apocynin). Having a short half-life means that to reach a steady-state preferred level of drug concentration and exposure, multiple dosing in one day or even more complicated dosing regimen would be required. To solve this problem, chemists and engineers have come up with multiple solutions (Smith et al., 2018). Apart from the approaches mentioned above about preventing the hydrolysis of ester in the body, one way to prolong the half-life of a drug is to use a modified-release formulation (extended-release rather than immediate-release), such as tofacitinib (Lamba et al., 2017; Lamba et al., 2016). Another way is to explore the opportunities with the derivatives of the

current drug, such as apocynin, whose derivatives were effective in reducing the cancer cell migration (Klees et al., 2006), and whose derivative, mito-apocynin (Patent No. US 8,962,600 B2) was able to reduce the ROS production in microglia (Sarkar et al., 2017) and promote the locomotor function (Dranka et al., 2014). Since the development of LMH001 and this group of bi-aromatic and tri-aromatic Nox2 inhibitors are still in an early development stage, many methods could be adopted to improve its efficacy.

The PK non-compartmental analysis methods used in this study include PK NCA package in R, Phoenix WinNonlin and curve fit by Excel. Since there were differences in the trapezoidal rule, different PK values (especially CL and V_d , derived from the difference in $AUC_{0-\infty}$) were reported. For example, $AUC_{0-\infty}$ observed in R was 928.26 while in WinNonlin observed $AUC_{0-\infty}$ was 1759.75. **Figure 4.20** demonstrates this difference. The differences came from the linear trapezoidal method and the logarithmic trapezoidal method. Since the elimination phase of LMH001 fitted in with a non-linear regression (mono-exponential decline), the trapezoidal methods by linear estimation would result in an over-estimation.

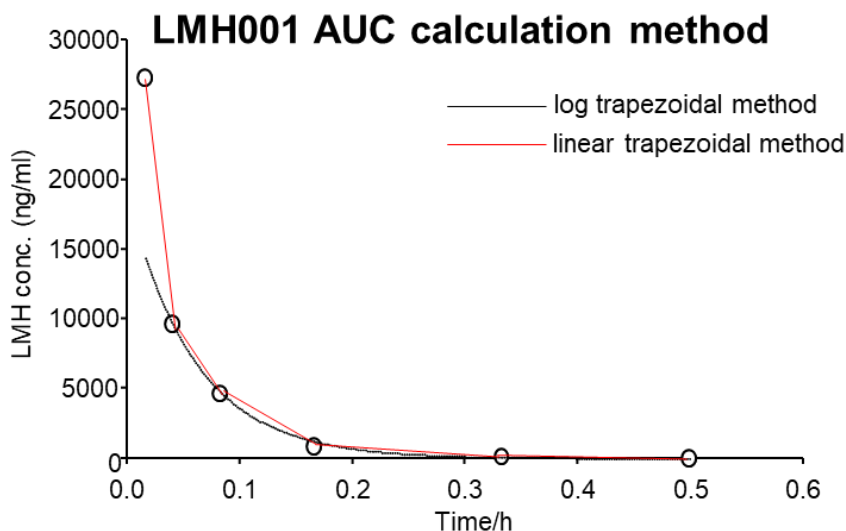


Figure 4. 20 The comparison between the logarithmic (black) and linear (red) trapezoidal method in calculating AUC.

The black line represents a mono-exponential decline of LMH001, and the curve was the LMH001 plasma concentration change from 1 min to 30 min (without error bars). The red line is higher between every two points in comparison to black lines, suggesting an over-estimation by the linear trapezoidal method. At the same time, during the absorption stage, the logarithmic trapezoidal method can underestimate the exposure with ascending curves (Shargel & Yu, 2016).

The tissue concentration of LMH001 was not measured, and this is one of the major limitations of this study. As a result, the effect of LMH001 on organ oxidative stress was still poorly understood at this stage. As a preliminary study, dependent on the objectives of the study, many different experiments such as LMH001 microsome stability, hepatocyte stability, tissue distribution, BBB permeability using MDCKII cell models, and PD studies are still needed.

In conclusion, this study successfully developed the extraction and detection method for LMH001, which were then used to characterise its PK parameters in mice via iv injection. As a novel representative compound for Nox2 inhibitors, LMH001 showed some advantages such as rapid distribution to the body and quick metabolism.

However, future studies on its PK parameters, such as PK by oral intake and iv infusion, and more importantly, the modification on the structure or the design for the formulation are still required.

Chapter 5

Evaluation of LMH001 in Reducing Oxidative Stress Angiotensin

II (AngII)-stimulated H9C2 cells

5.1 Introduction

A PD study characterises molecular and physiological effects of a drug, such as the binding to the target and downstream biochemical effect initiated by the drug-target interaction (Rang, 2006). Since the binding of LMH001 to p47^{phox} was previously measured, the biochemical effect of LMH001 was examined by the O₂⁻ production using lucigenin chemiluminescence.

Oxidative stress in the cardiovascular system is closely related to the development of cardiovascular disorders such as long-term hypertension due to the impairment of NO availability and vasoconstriction, the development of atherosclerosis and cardiac remodelling (Maulik & Kumar, 2012; Senoner & Dichtl, 2019). This study used a myoblast cell line H9C2 with an AngII-stimulation to initiate the oxidative stress in the heart and to mimic the development of cardiac hypertrophy as a maladaptive response to the high blood pressure.

Some Nox inhibitors have been used before in the investigations of oxidative stress-related Nox activities and redox signalling in H9C2 cells. For instance, apocynin, as a Nox2 inhibitor, was discovered to reduce the Nox activities (as measured by the O₂⁻ production), p47^{phox} expression, the MAPK signalling and apoptosis in AngII-stimulated H9C2 cells (Qin et al., 2006). DPI could reduce the oxidative stress (measured by DCFH-DA and lucigenin), p47^{phox} expression and lipid peroxidation in H9C2 cell with the oxidative stress generated by simulated ischaemia (Borchi et al.,

2009). Therefore, with these previous studies, H9C2 cells with AngII stimulation would act as a suitable cell model to study the PD and pharmacological effect of LMH001 and act as a bridge between its mechanism and effect in oxidative stress-related diseases *in vivo*.

5.1.1 Aims and objectives

This chapter aims to evaluate the effect of LMH001, as a Nox2 inhibitor, in reducing oxidative stress *in vitro*, in the echo to the chemical property and PK characterisation of LMH001 in Chapter 4. Specifically, there are two objectives in total:

1. To characterise the PD of LMH001 on the AngII-induced oxidative stress *in vitro*, using the rat myoblast cell line H9C2;
2. To examine the effect of LMH001 on the p47^{phox} and Nox expression and the activation of MAPK/ERK signalling pathway upon AngII stimulation, i.e. phosphorylation of p38 MAPK and ERK1/2 *in vitro*.

5.2 Materials and Methods

5.2.1 Cell culture

5.2.1.1 Culture conditions, retrieve, counting, viability and cryopreservation

A rat cardiomyocyte cell line, H9C2(2-1) from embryonic BD1X rat heart tissue (Kimes & Brandt, 1976) was a kind gift from Dr Andrew Snabaitis. The medium used was Dulbecco's modified Eagle's medium (DMEM), adjusted to contain 4 mM L-glutamine, 1000 mg/L glucose, 1.5 g/L sodium bicarbonate, 100 U/ml ampicillin, 100 µg/ml streptomycin and supplemented with 10% fetal bovine serum (FBS). H9C2 cells were cultured in non-coated flasks at 37.0 °C, with 95% air and 5 % carbon dioxide. As suggested by American Type Culture Collection (ATCC), since the myoblastic cells deplete rapidly after confluency, H9C2 cells were sub-cultured when reaching 80% of the confluency with a sub-cultivation ratio at 1:2. Cell culture was performed in a sterile Class II laminar flow hood until harvesting (ThermoFisher, UK).

The cell retrieving first started by first removing from the liquid nitrogen storage straw and immediately put in the 37.0 °C water bath. Right before the completion of thawing the vial, it was taken out, and 1 ml of the cell suspension (1×10^6) was mixed with 4 ml of the DMEM (alone) in a 15 ml Falcon tube and centrifuged at 800 rpm for 10 min. The pellet was then collected and resuspended in 1 ml complete medium. 1 ml cell suspension was then seeded to a T25 flask with 3 ml of complete medium and kept in a 37 °C incubator with the conditions described. The media renewal was every three days.

The cells were passaged after it reached 80% confluency, and the number of cells and their viability were checked during every cell passaging. When the cells

reached 80% confluency, the medium was first removed and discarded. The cells were briefly rinsed with PBS to remove all traces of serum which would interrupt the functioning of trypsin. 2 ml of 0.25% (w/v) Trypsin-0.53 mM EDTA solution was then added to the T75 flask (0.5 ml Trypsin-EDTA solution was used for T25) and the cells were observed under an inverted microscope until cell layer was dispersed (usually within 5 min). Eight millilitres complete medium (3 ml if T25) was then added to stop the trypsinisation. The cells were aspirated before being put into a 15 ml Falcon tube and centrifuged at 800 rpm for 10 min. After the centrifuging, cells were resuspended in 1 ml complete medium.

The number of the cells were then counted using 10 μ l of the cell suspension, mixed with 10 μ l Trypan Blue, and 20 μ l PBS under a haemocytometer. 20 μ l of the mixture was then loaded onto the haemocytometer with the coverslip. The unstained cells (white) suggested good membrane integrity and therefore were alive. With phase-contrast, both the live (white) and dead (dark blue or blue) cells in the four large corner squares and the centre square with the right-hand and lower boundary were counted. The cell number was then calculated as the following equation:

$$\text{Number of cells} = \frac{\text{number of cells} \times 10,000}{\text{number of square counted}} \times \text{Dilution factor} (4)$$

The cell viability was then calculated using the equation:

$$\text{Cell viability} = \frac{\text{number of live cells}}{\text{number of live cells} + \text{number of dead cells}}$$

After counting, the cells were then seeded or stored long term by being frozen and kept in the liquid nitrogen vapour phase.

To cryo-preserve, the cells, complete growth medium supplemented with 5% (v/v) DMSO (final) was used. Precisely, after counting the cells, a volume of cell suspension with 1×10^6 cells was taken out, and complete media was added to achieve a final volume of 0.5 ml. On the ice, the pre-cooled complete growth medium supplemented with 10% (v/v) DMSO was added to the 0.5 ml cell suspension drop-by-drop and placed in Mr Frosty™ Freezing Container (Thermo Scientific, Catalogue No. 5100-0001), filled with isopropanol. Mr Frosty™ was then quickly put in $-80\text{ }^{\circ}\text{C}$ freezer overnight before transferring to the liquid nitrogen cell storage for preservation.

5.2.1.2 Stimulation of H9C2 cells using AngII and the effect of LMH001

Research has discovered that AngII can be generated locally in the heart (Kumar, Singh & Baker, 2009; Kurdi, De Mello & Booz, 2005), and an elevated amount of AngII is closely linked to cardiomyocyte hypertrophic growth (Watkins, Borthwick, Oakenfull, Robson & Arthur, 2012). In this study, different concentrations (0, 10, 25, 50, 100 nM) of AngII (Sigma-Aldrich, United Kingdom, antibody adsorbent: Asp-Arg-Val-Tyr-Ile-His-Pro-Phe-OH · $2\text{CH}_3\text{COOH} \cdot \text{H}_2\text{O}$, 1.2-10.4% acetate) was first used to stimulate the H9C2 cells. AngII was first dissolved in sterilised $1 \times \text{PBS}$ to form a stock concentration of 5 mM, following the instructions by Sigma, and stored at $-80\text{ }^{\circ}\text{C}$. When it reached 75% confluency in the T25 flask or 24 well-plate, H9C2 cells were first cultured in the serum-free media for 24 h to eliminate the effect of serum, before adding the AngII of the appropriate concentration for 24 h under the standard culturing conditions. After 24 h, cells were then washed, harvested, snap-frozen in the liquid nitrogen, stored at $-20\text{ }^{\circ}\text{C}$ and used for future analysis.

By examining the ROS ($O_2^{\cdot-}$ and H_2O_2) production, 100 nM AngII stimulation was then used to investigate the effect of LMH001. LMH001 was dissolved in dimethyl sulfoxide (DMSO) (Sigma-Aldrich, United Kingdom) at a stock concentration of 0.5 M and stored at $-80\text{ }^\circ\text{C}$ for the analysis. For the characterisation of LMH001 PD on the $O_2^{\cdot-}$ production, H9C2 cells were stimulated with 24 h 100 nM AngII or saline (as a basal condition) and then treated with 0.29, 2.90, 7.25, 29.01, 145.04, 290.07, 1450.35, and 2900.71 ng/ml (0.001, 0.01, 0.025, 0.10, 0.50, 1.00, 5.00 and 10.00 μM) LMH001 in a 24-well plate for 30 min under the standard culturing conditions, according to previous protocols. The cells were then washed, harvested, snap-frozen in the liquid nitrogen, stored at $-20\text{ }^\circ\text{C}$ and used for future analysis. The effect of AngII stimulation and LMH001 on the p47^{phox} and Nox expression and MAPK activation was examined using 100 nM AngII stimulation and 2900.71 ng/ml (10 μM) LMH001 treatment. In parallel, 30 min treatment of apocynin (10 μM , a Nox2 inhibitor), DPI (10 μM , a flavoprotein inhibitor), and Nox2-tat (10 μM) ([H]-RKKRRQRRRCSTRVRRQL-[NH₂], PeptideSynthetics, Peptide Protein Research Ltd.) were also used during the measurement of $O_2^{\cdot-}$ production for comparisons against LMH001, and tiron (10 mM) was used as an $O_2^{\cdot-}$ scavenger.

5.2.2 Protein concentration measurement

The experiment results (ROS measurement and western blot) were normalised by protein concentrations. The standards were prepared by dissolving 0, 2.5, 5, 12.5, 25, 50 mg/ml BSA in HBSS and 5 μl was loaded onto a transparent flat-bottom 96 well plate (Evergreen Scientific, USA) in duplicates. In parallel, 5 μl sample was loaded. 145 μl Bradford Reagent (Sigma-Aldrich, United Kingdom) per well was used for the analysis. The absorbance at 550 nm was measured using a plate reader, SpectraMax

340PC (Molecular Devices, USA) and protein concentration were calculated and adjusted according to the standard curve.

5.2.3 Effect of LMH001 on ROS production *in vitro*

5.2.3.1 PD analysis on O₂⁻ production

To investigate the PD of LMH001 in relation to the NADPH-dependent O₂⁻ production in AngII-stimulated H9C2 cells, lucigenin chemiluminescence was used, and the method was detailed in sections 2.6. LMH001 concentration-dependent AngII-stimulated O₂⁻ production was subjected to four different PD models with inhibitory effects by Phoenix WinNonlin 8.1. The basal values were generated before adding NADPH. In the model analysis, the LMH001 concentration was defined as X and the detected O₂⁻ production as Y. **Table 5.1** summarises the information on the four models used, and the model with the minimum AICc was selected as the favoured model. AICc was calculated as $AICc = AIC + 2 \times n_{\text{Parm}} (n_{\text{Parm}} + 1) / (n_{\text{Obs}} - n_{\text{Parm}} - 1)$, in which nParm is the number of parameters and nObs is the number of observations.

Table 5. 1 Model details for the PD analysis of LMH001 in AngII-stimulated H9C2 cells.

Model description	Y at C=0	Y at C=infinity	Notation
Inhibitory Effect E0	E0	0	$E = E0 \times [1 - (C / (C + IC50))]$
Inhibitory Effect Imax	E0	E0-Imax	$E = E0 - Imax \times [C / (C + IC50)]$
Inhibitory Effect Sigmoid E0	E0	0	$E = E0 \times [1 - C^\gamma / (C^\gamma + IC^\gamma 50)]$
Inhibitory Effect Sigmoid Imax	E0	E0-Imax	$E = Imax(E0 - Imax) \times [C^\gamma / (C^\gamma + IC^\gamma 50)]$

E0: Y value when the drug has the baseline effect; Imax: Y value reduced when the drug achieves the maximum effect; γ : shape parameter; IC50: drug concentration required to produce 50% of the maximal effect (E0-Imax).

5.2.3.2 Other sources of ROS

Alongside the $O_2^{\cdot-}$ production, the H_2O_2 level in the cell homogenates were also examined using Amplex red assay (section 2.9). General ROS production in the cells was also visualised using 2',7'-dichlorofluorescein diacetate (DCFH-DA).

DCFH-DA has been widely used for the detection of intracellular H_2O_2 and oxidative stress, usually with other supplementary methods for a valid result (Chwa et al., 2006; Kalyanaraman et al., 2012; Kitajima et al., 2016; Kotamraju et al., 2003; Lee et al., 2009; Tampo et al., 2003). DCFH-DA, with the functional group being DCFH, is non-fluorescent and cell-permeable. Once the DCFH enters the cell, it is hydrolysed to the DCFH carboxylate anion. The hydrolysis could keep DCFH retained and ready to be oxidised by two electrons and form the fluorescent DCF, whose signal can then get picked up by a fluorescent microscope or a flow cytometer (Kalyanaraman et al., 2012). In this study, 1×10^4 H2C9 cells per well were seeded into a black 96 well plate (Sigma-Aldrich, Catalogue No. CLS3603) (replicate number: n=6 per group) and cultured overnight. The next day, H9C2 cells were treated with (1) PBS, (2) AngII (100 nM) or (3) AngII (100 nM) with 30 min LMH001 (2900.7 ng/ml, 10 μ M) treatment for 24 h, and then were gently washed with PBS. The phase-contrast images were then taken using the EVOS M5000 Imaging System (ThermoFisher Scientific, UK). To detect the oxidative stress level among these three treatments: PBS (saline), AngII or AngII+LMH001, 5 mM DCFH-DA was added and incubated in the dark for 30 min before getting visualised under Nikon Eclipse Ti2-E inverted microscope under 20 \times magnification with a green fluorescent filter at an excitation/emission at 485 nm / 535 nm. At least seven images were taken per well, and the fluorescent intensity was quantified using ImageJ 1.50i against the background (DCFH-DA only).

5.2.4 Effect of LMH001 on p47^{phox} and Nox expression, and the activation of the MAPK signalling pathway

Western blot was used to examine the expression of p47^{phox}, Nox1, Nox2 and Nox4 in the saline, AngII-stimulated and AngII-stimulated, LMH001-treated H9C2 cells. The effect of LMH001 treatment on the AngII-stimulated activation of MAPK signalling pathway was also investigated using western blot by the phosphorylation levels of p38 MAPK and ERK1/2 against their corresponding total protein levels.

In summary, the analysis of the effect of LMH001 was outlined in **Figure 5.1**.

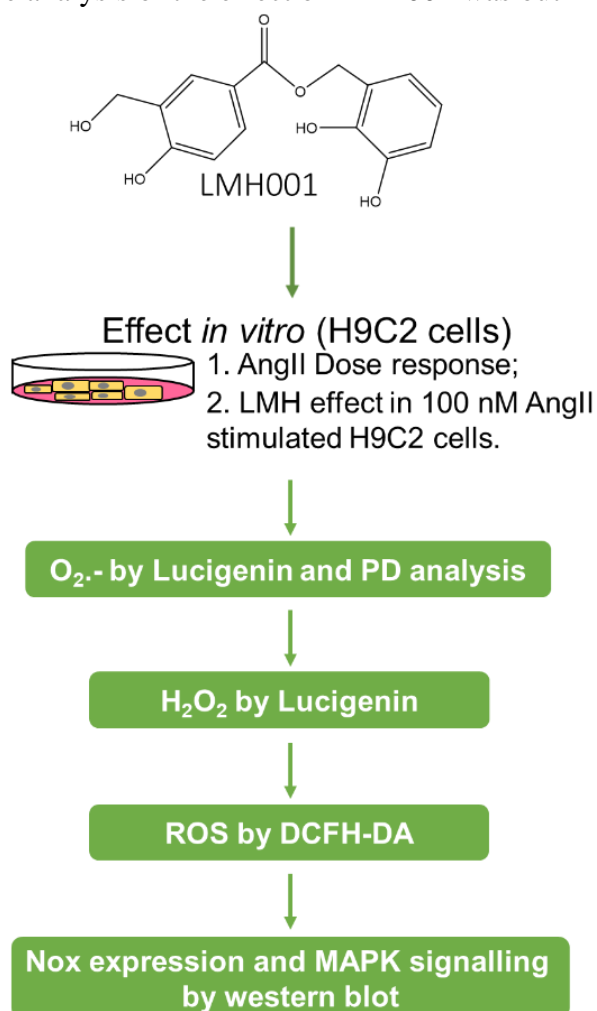


Figure 5. 1 Outline of the experiments carried out to study the effect of LMH001 *in vivo* and *in vitro*.

5.3 Results

5.3.1 Effect of LMH001 on O₂⁻ production in AngII-stimulated H9C2 cells, examined by lucigenin chemiluminescence

To investigate the O₂⁻ production in H9C2 cells in response to AngII, and to decide an appropriate dose for activating Nox2 in H9C2 cells (characterised by an increased O₂⁻ production), different concentrations of AngII were used to stimulate H9C2 cells and NADPH-dependent O₂⁻ production was measured (**Figure 5.2 A**). AngII at a dose of 50 nM was able to induce a 2.51 ± 0.79 fold increase in NADPH-dependent O₂⁻ production compared to the controls (saline only), and 100 nM AngII could induce 3.24 ± 0.90 fold increase of O₂⁻ production, both significantly different from the controls ($p < 0.05$). **Figure 5.2 B** summarised the effect of 2900.7 ng/ml (10 μ M) LMH001 on reducing 100 nM AngII-stimulated O₂⁻ production in H9C2 cells. 10 mM LMH001 was able to reduce the O₂⁻ production to 0.41 fold in comparison to the control (DMSO only), more effective than 10 μ M Nox2tat (a peptide-based Nox2 inhibitor) but less potent than DPI (a flavoprotein inhibitor) ($p < 0.05$), and tiron (O₂⁻-scavenger) was able to scavenge the O₂⁻ (**Figure 5.2 C**).

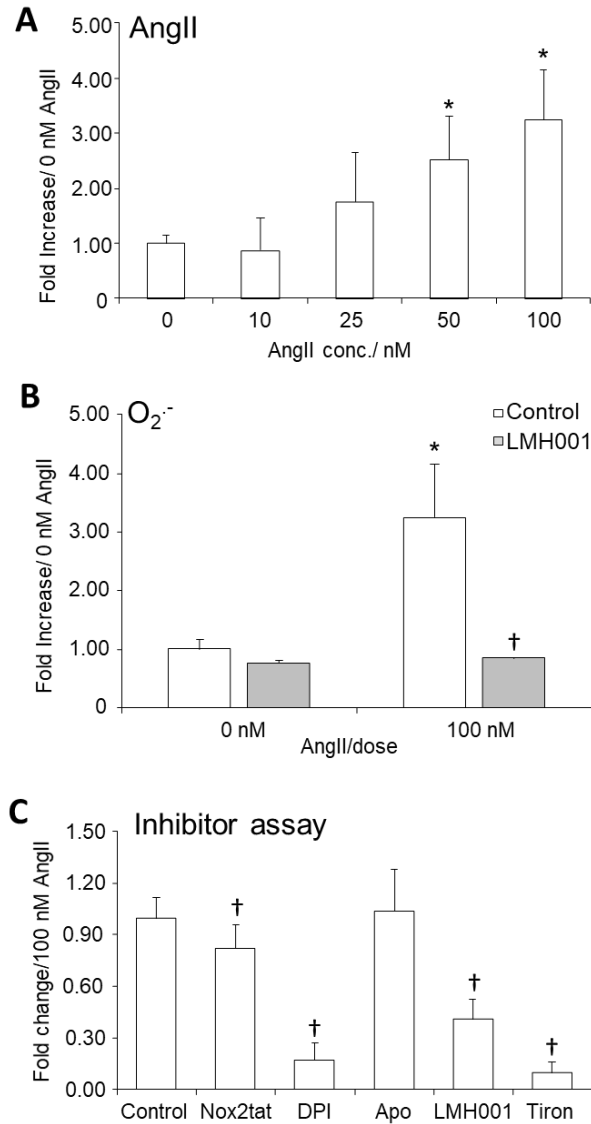


Figure 5. 2 O₂^{·-} production in saline and AngII treated H9C2 cells.

A. AngII dose-response expressed in NADPH-dependent O₂^{·-} production fold increase compared to 0 nM AngII saline controls (1.00-fold increase). **B.** O₂^{·-} production in 100 nM AngII- or saline (0 nM AngII)-stimulated H9C2 cells, in fold increase compared to 0 nM AngII without LMH001. **C.** O₂^{·-} production in 100 nM AngII stimulated H9C2 cells, treated with different inhibitors including Nox2tat, DPI, apocynin (apo), LMH001 and O₂^{·-} scavenger tiron at a consistent concentration of 10 mM, fold change compared to 100 nM AngII vehicle (1.00-fold). Data were presented as Mean ± SD and n = 3 per group. Statistical comparison between the two groups was made using one-way ANOVA. * p<0.05, significantly different from 0 nM AngII-stimulated H9C2 cell; † p <0.05, significantly different from 100 nM AngII-stimulated H9C2 cell.

5.3.2 PD analysis and modelling of LMH001 in AngII-stimulated H9C2 cells

The effect of LMH001 was examined by using LMH001 at different concentrations to treat AngII-stimulated H9C2 cells and measuring the response ($O_2^{\cdot-}$ production by lucigenin assay, the result shown in **Figure 5.3**). The half-maximal inhibitory concentration (IC₅₀) and Hill slope were first calculated by subjecting the response ($O_2^{\cdot-}$ production) versus LMH001 concentration to a non-linear regression with [Inhibitor] vs response, variable slope (four parameters) in Prism GraphPad 7.0, n=3 per group. The IC₅₀ of LMH001 in reducing AngII-stimulated $O_2^{\cdot-}$ production was 142.4 ng/ml, calculated by fitting a non-linear regression curve with a Hill slope of 0.543 (best-fit).

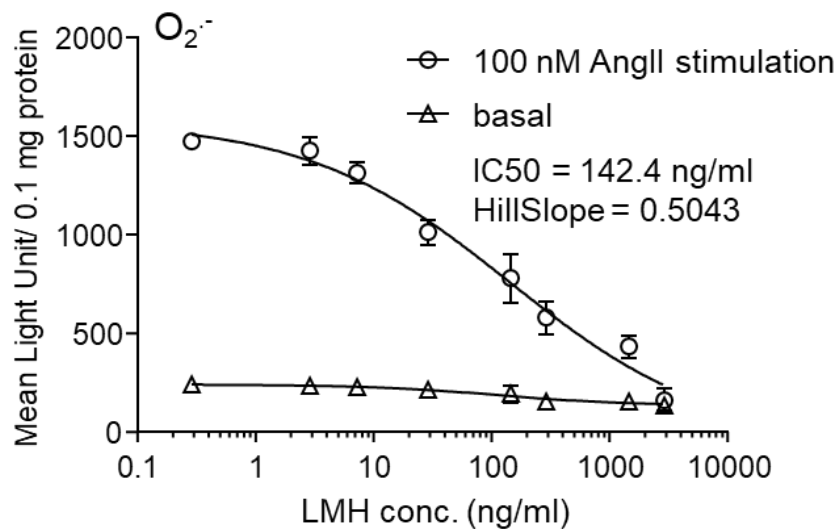


Figure 5. 3 Non-linear regression analysis of LMH001 in reducing 100 nM AngII-stimulated H9C2 cells.

The in-depth PD analysis was carried out by subjecting the detected O₂⁻ production (MLU, mean light unit value for each group, n = 3, nObs = 8) to Phoenix WinNonlin 8.1 PD inhibition models. **Table 5.2** summarises the PD parameters calculated by fitting the models.

Table 5. 2 Calculated PD parameters of LMH001 in reducing O₂⁻ production in AngII-stimulated H9C2 cells.

PD Parameters	Unit	PD Models			
		Inhibitory Effect E0	Inhibitory Effect I _{max}	Inhibitory Effect Sigmoid E0	Inhibitory Effect Sigmoid I _{max}
E0	MLU	1367.37 ± 81.82	1424.80 ± 68.02	1564.12 ± 91.36	1632.56 ± 468.49
IC50	ng/ml	219.08 ± 70.68	89.72 ± 35.97	124.00 ± 42.67	141.74 ± 119.98
I _{max}	MLU	-	1159.57 ± 99.05	-	1576.62 ± 146.88
γ	-	-	-	0.53 ± 0.077	0.50 ± 0.21
AIC	-	97.96	93.45	87.09	89.03
AICc	-	100.36	99.45	93.09	102.36
BIC	-	98.12	93.69	87.32	89.35

E0: Y value when the drug achieves the minimum (baseline) inhibitory effect value; IC50: drug concentration required to produce 50% of the maximal effect (E0-I_{max}); I_{max}: Y value reduced when the drug achieves the maximum inhibitory effect; γ: shape parameter; AIC: Akaike information criterion; AICc: corrected Akaike information criterion; BIC: Bayesian information criterion.

The model with the smallest AICc was selected. Therefore, with an assumption that theoretically, when C=infinity, the I_{max} of the drug would be able to reduce the effect to 0 (I_{max} = E0), the PD of LMH001 in reducing *in vitro* AngII-stimulated O₂⁻ production in H9C2 cells were best fitted into the Inhibitory Effect Sigmoid E0 PD model, with an E0 = (1564.12 ± 91.36) MLU, an IC50 = 124.00 ± 42.67 ng/ml and

$\gamma = 0.53 \pm 0.077$. The predicted model and the residue distribution are shown in **Figure 5.4.**

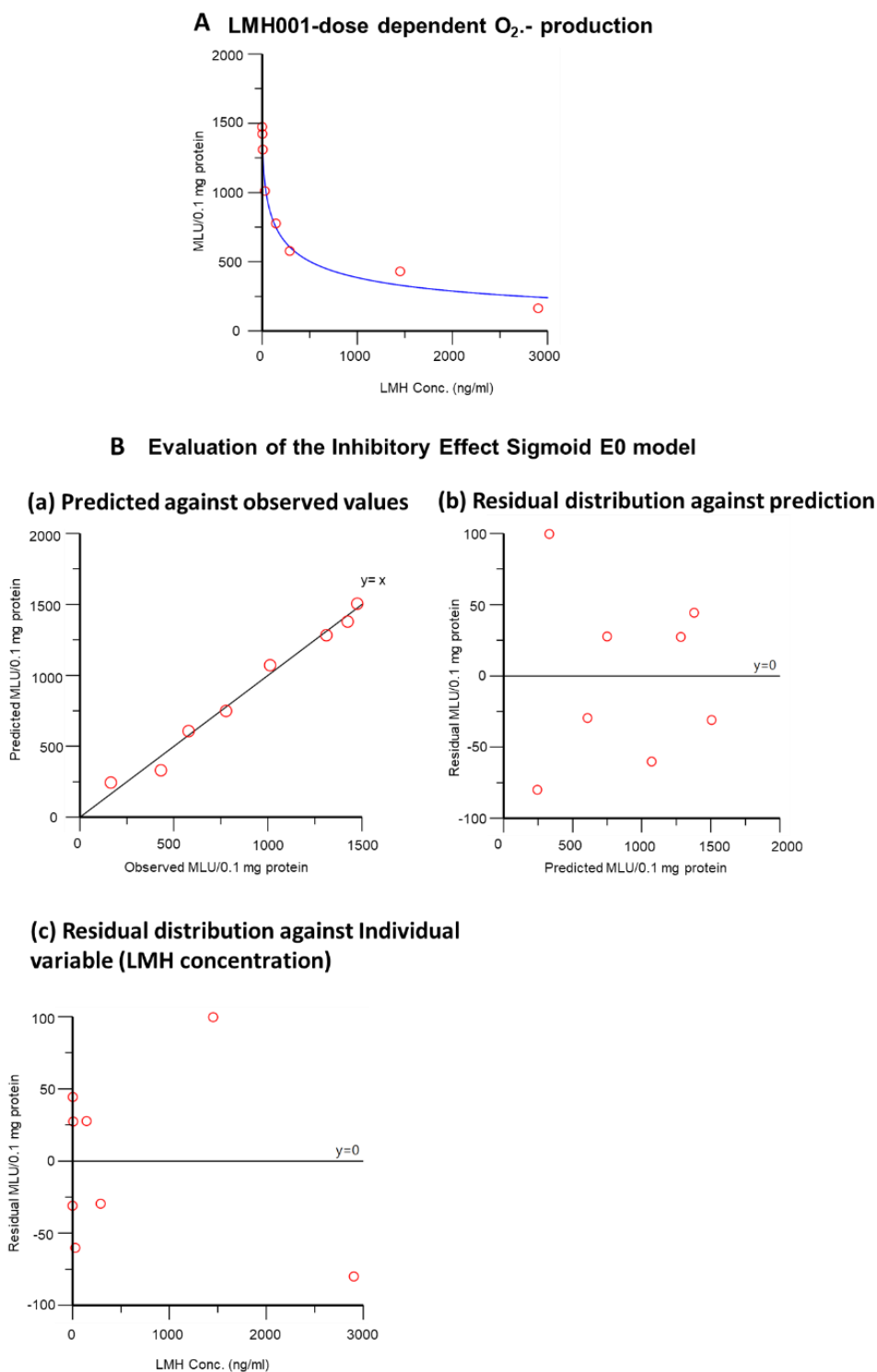


Figure 5. 4 PD analysis and residue distribution of LMH001 on the inhibition of O₂- production in 100 nM-stimulated H9C2 cells.

A. Curve ($E = E_0 \times [1 - C^y / (C^y + IC_{50}^y)]$) fit for the LMH001 dose-dependent O_2^- production; **B.** (a) the measured O_2^- against predicted O_2^- production, a distribution close to and equally alongside $y = x$ indicates a reasonable prediction; (b) the residue distribution against the predicted O_2^- production, a random distribution of the residues around $y = 0$ residue indicates a good model fit; (c) the calculated residue distribution against the LMH001 concentration, a random distribution of the residues around $y = 0$ residue indicates a good model fit.

5.3.3 Effect of LMH001 on ROS production in AngII-stimulated H9C2 cells, examined by Amplex red and DCFH-DA

Alongside the NADPH-dependent O_2^- production by lucigenin chemiluminescence, H_2O_2 production in response to AngII and the effect of LMH001 in reducing H_2O_2 production in AngII-stimulated H9C2 cells were also examined by Amplex red fluorescence. **Figure 5.5** shows that AngII at a dose ≥ 25 nM was able to increase H_2O_2 production in H9C2 cells significantly ($p < 0.05$), and 10 μ M LMH001 mildly reduced the H_2O_2 level in comparison to 100 nM AngII stimulated controls (without LMH001) ($p = 0.08$).

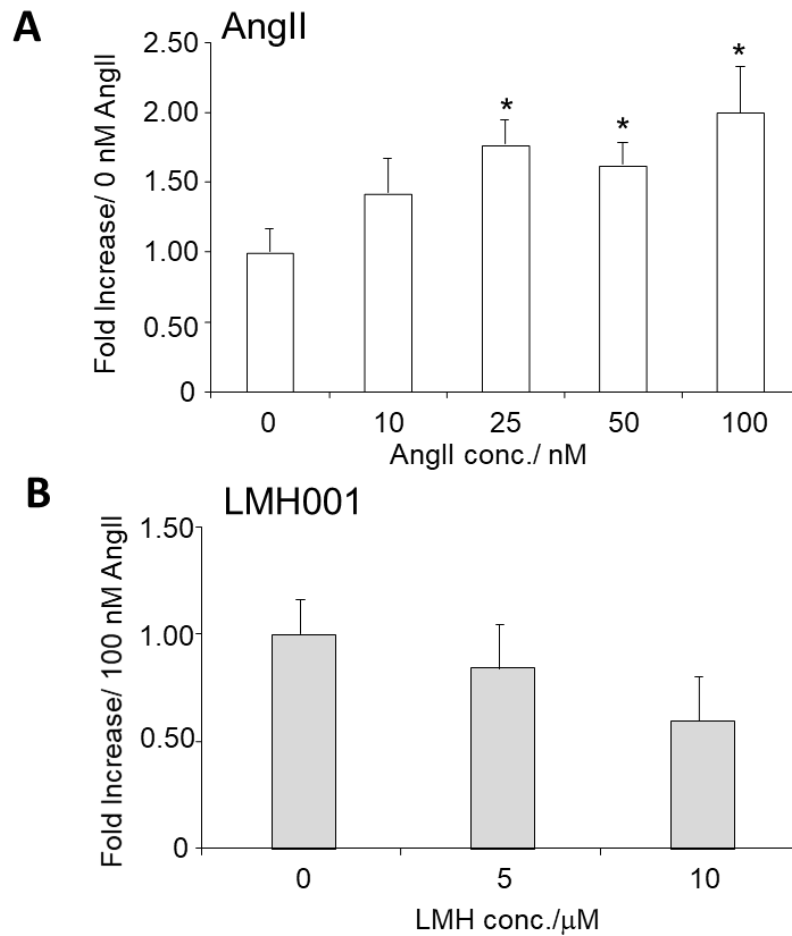


Figure 5. H_2O_2 production in H9C2 cells in response to AngII examined by Amplex red fluorescence.

A: H_2O_2 in response to an increasing concentration of AngII, expressed in fold increase compared to 0 nM AngII saline controls (1.00-fold increase) ($n=3$ per group). **B:** H_2O_2 production in 100 nM AngII-stimulated H9C2 cells with the treatment of 0, 1450.36 or 2900.71 ng/ml (0, 5 or 10 μM) LMH001, calculated by fold increase in comparison to 100 nM AngII-stimulated, 0 μM LMH001 treated H9C2 cells. Data were presented as Mean \pm SD. Statistical comparison between the two groups was made using one-way ANOVA. * $p<0.05$, significantly different from 0 nM AngII-stimulated H9C2 cell.

The overall oxidative stress in the AngII-stimulated H9C2 cells and the effect of LMH001 were also illustrated using DCFH-DA fluorescence in **Figure 5.6**. The green colour indicates DCF in the cytosol, and the result demonstrates an increased

level of ROS in AngII-stimulated H9C2 cells, and LMH001 was able to reduce the ROS level ($p < 0.05$) significantly. The bright field phase-contrast images of 0 and 100 nM AngII stimulated, and LMH001-treated cells are included in Appendix V.

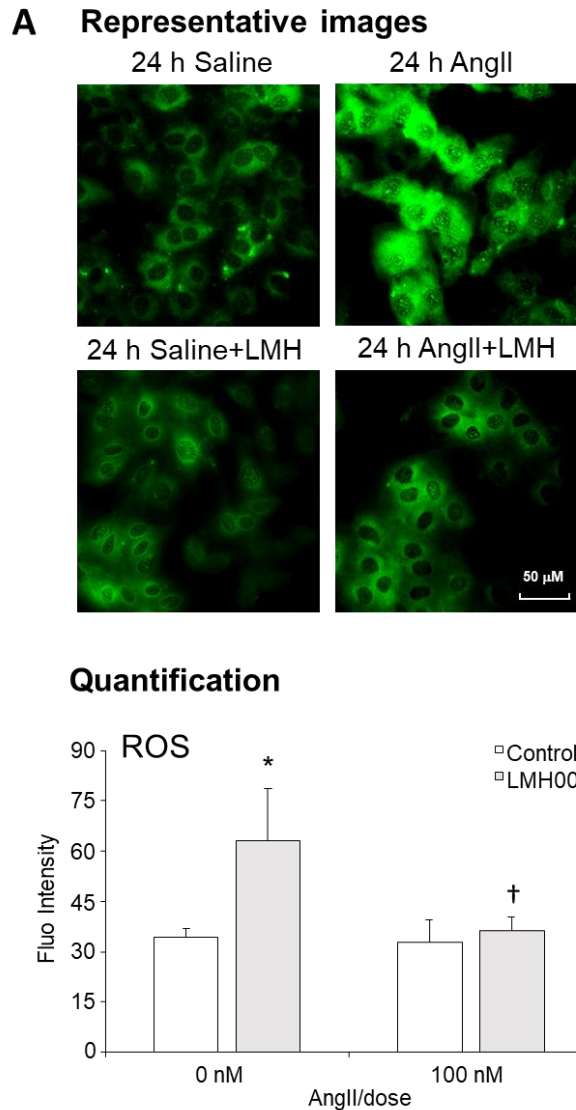


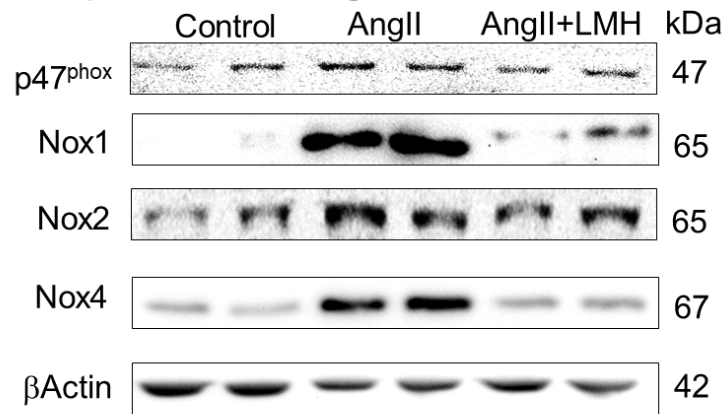
Figure 5. 6 The effect of LMH001 in reducing AngII-stimulated oxidative stress, examined by DCFH-DA fluorescence.

A: representative images of DCF fluorescence in the 100 nM AngII or saline stimulated, LMH001 treated H9C2 cells. DCF is in the cytosol and green. Images were obtained under Nikon Eclipse Ti2-E inverted microscope with a green fluorescent filter, 20× magnification. **B:** quantification of fluorescent intensity of DCF. The fluorescent intensity was calculated by measuring Mean Grey of DCF against the background using ImageJ 1.50i. 10-15 images used per well were used, n = 3 per group. Data were presented as Mean ± SD. Statistical comparison between the two groups was made using one-way ANOVA. *p<0.05, significantly different from 0 nM AngII-stimulated H9C2 cell; † p <0.05, significantly different from 100 nM AngII-stimulated H9C2 cell.

5.3.4 Effect of LMH001 on the expression of p47^{phox} and Noxes in AngII-stimulated H9C2 cells, examined by western blot

A long-term (24 h) 100 nM AngII stimulation increased the expression level of p47^{phox}, Nox1, Nox2 and Nox4 significantly ($p < 0.05$), while treatment with LMH001 at 10 μ M for 30 min could reduce the expression levels of Nox1, Nox2 and Nox4 ($p < 0.05$, one-way ANOVA). **Figure 5.7** shows that LMH001 treatment did not reduce AngII-induced p47^{phox} expression (3.3 ± 0.9 fold increase in AngII-stimulated cells and 2.7 ± 0.5 fold increase in LMH001-treated cells, in comparison to 0 nM AngII controls (1.0 ± 0.5 fold); Nox1 was reduced by LMH001 from 2.4 ± 0.3 fold in AngII-stimulated cells to 1.7 ± 0.2 fold (1.0 ± 0.2 fold in controls); Nox2 from 2.4 ± 0.3 fold to 1.5 ± 0.4 fold (1.0 ± 0.4 fold in controls); and Nox4 from 2.6 ± 0.3 fold to 1.7 ± 0.2 fold (1.0 ± 0.0 fold in controls). The calculated molecular weight for Nox4 is 67 kDa, and Nox1 is 65 kDa. The Nox2 detected was the non-glycosylated gp91^{phox} with a molecular weight of 65 kDa (Banerjee & Henderson, 2012). Full-gel images for the representatives are included in Appendix VI at the end of this chapter.

A Representative images



B Quantification

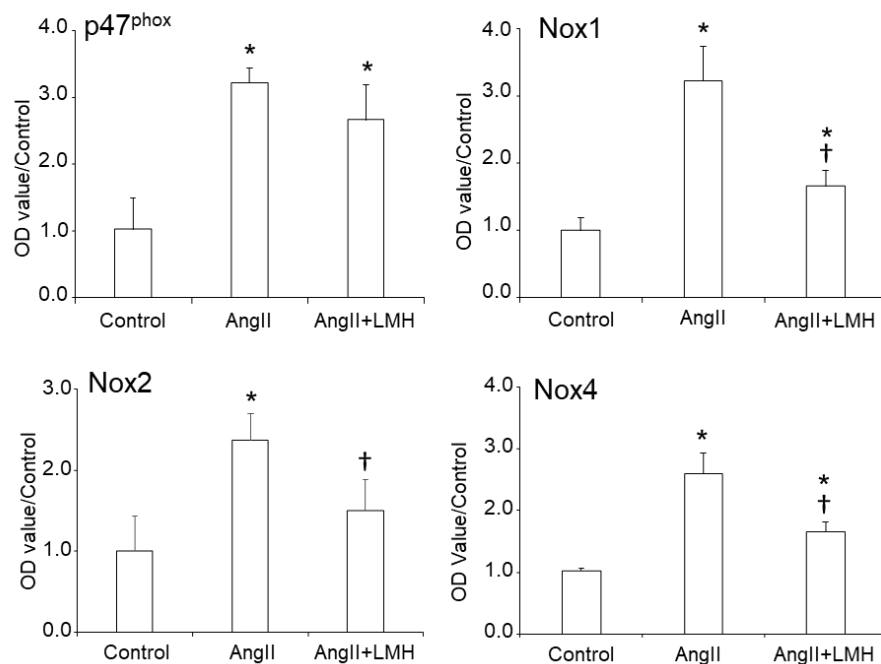


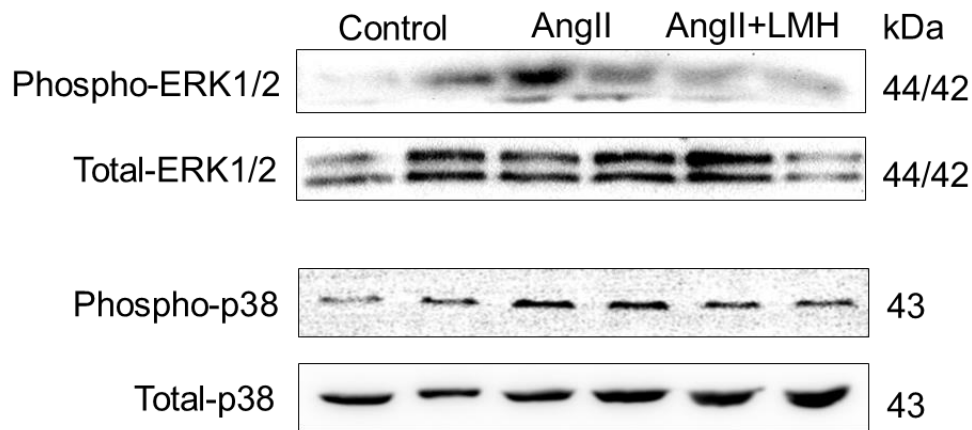
Figure 5. 7 The p47^{phox}, and Nox expression in 24 h control, AngII-stimulated and LMH001-treated H9C2 cells.

βActin detected in the same samples were used as loading controls. **A:** representative western blot images of p47^{phox}, Nox1, Nox2, Nox4 and βActin. **B:** Quantification of the optical density (OD) of p47^{phox}, Nox1, Nox2 and Nox4 bands using ImageJ 1.50i, with normalisation to the βActin levels and 0 nM AngII-stimulated, none LMH001-treated H9C2 (controls) to one-fold. Data were presented as Mean ± SD. Statistical comparisons between two groups were made using one-way ANOVA. * p <0.05, significantly different from 0 nM AngII, without LMH001 treatment; † p <0.05, significantly different from 100 nM AngII, without LMH001 treatment.

5.3.5 Effect of LMH001 on the activation of MAPK/ERK signalling pathway in AngII-stimulated H9C2 cells, examined by western blot

The activation of the MAPK signalling pathway is associated with the AngII-induced oxidative stress in H9C2 cells (Liu et al., 2011). In this study, the phosphorylation of p38 MAPK (at Thr180/Tyr182) and ERK1/2 (at Thr202/Tyr204) were analysed by western blot. The result is shown in **Figure 5.8**. 24 h 100 nM AngII stimulation induced the phosphorylation of p38 MAPK and ERK1/2 ($p < 0.05$, one-way ANOVA), and 2900.71 ng/ml (10 μ M) LMH001 was able to reduce the phosphorylation of p38 from 1.9 ± 0.5 to 1.2 ± 0.4 fold increase, in comparison to 0 ng/ml LMH001 100 nM AngII controls ($p < 0.05$, one-way ANOVA), but only mild phosphorylation of ERK1/2 ($p = 0.06$, one-way ANOVA). The full-gel images for the representatives are also included in Appendix V.

A Representative images



B Quantification

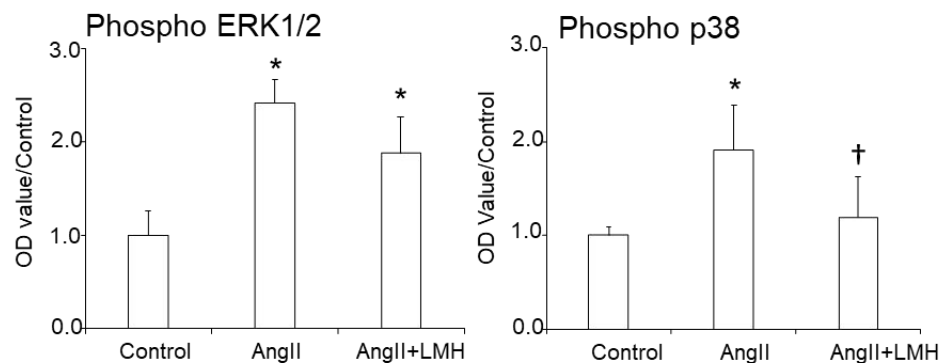


Figure 5. 8 The ERK1/2 and p38 MAPK phosphorylation in 24 h control, AngII-stimulated and LMH001-treated H9C2 cells.

The corresponding total protein detected in the same samples was used as loading controls (total ERK1/2 (H-72) and total p38 MAPK (C-20)). **Upper panel:** representative western blot images of phosphorylated and total ERK1/2 and p38 MAPKP. **Lower panel: B** Quantification of the OD of phosphorylated ERK1/2 and p38 MAPK using ImageJ 1.50i, with normalisation to the total protein levels and 0 nM AngII-stimulated, no LMH001-treated H9C2 (controls). Data were presented as Mean \pm SD. Statistical comparisons between two groups were made using one-way ANOVA. * $p < 0.05$, significantly different from 0 nM AngII, without LMH001 treatment; † $p < 0.05$, significantly different from 100 nM AngII, without LMH001 treatment.

5.4 Discussion

Oxidative stress has been identified in many cardiovascular diseases including hypertension and cardiac hypertrophy (Hingtgen et al., 2006), and cardiomyocyte Nox2 (not Nox2 in endothelium) has been discovered to be responsible for the oxidative stress generated during the development of hypertrophy after MI (Sirker et al., 2016). In this study, to elucidate the effect of LMH001 under a pathophysiological condition (in this case, to mimic the AngII-induced cardiac hypertrophy) in-depth, a cardiomyoblast model using 100 nM 24 h AngII stimulation in H9C2 cells was employed.

In the experiment of measuring LMH001 reduced NADPH-dependent O₂- production in AngII-stimulated H9C2 cells, an IC₅₀ of 142.4 ng/ml was calculated by fitting a non-linear regression curve using Prism GraphPad 7.0. Since the PD model is not detailed in the Prism Graph, a detailed PD analysis using Phoenix WinNonlin 8.1 was also employed in this study. The data (minus basal) were subjected to four classic inhibitory PD models and was fitted best to a sigmoid E₀ model, with an IC₅₀ = 393.0 ± 172.1 ng/ml. Both the IC₅₀ values are higher than in the isolated cardiac microvascular endothelial cells (CMECs) from C57BL/6 (IC₅₀ below 100 ng/ml, not published). Although cardiac LMH001 concentration was not measured yet, the PK study of apocynin in Chapter 3 showed that at a dose of 5 mg/kg, CD1 mice with an average bodyweight of 28 g could achieve a cardiac apocynin concentration of 834 ng/g. Although this is not a direct comparison, with similar physical-chemical properties such as pK_a, Log P and tPSA, 10 mg/kg by iv LMH001 would be expected to reach beyond the concentration of 393.0 ± 172.1 ng/g in the cardiac tissue, and therefore should affect the cardiac ROS generation in the diseased models. In addition, parenteral dosing method (iv injection) were used for the preliminary PK study and iv or ip injections should continue to be used for treatment of AngII-induced hypertensive diseased *in vivo*

models (currently being carried out, but considered as future study when the thesis was drafted) to achieve the desirable dosage, avoiding first-pass metabolism and a better bioavailability.

There are different stimuli found being involved in the ROS production and redox signalling: neurotransmitters such as oxytocin (Jankowski, Broderick & Gutkowska, 2020), hormones such as AngII, and mechanical stimuli such as excitation-contraction coupling in heart by stretching via MyoTak-coated micro-rods (Prosser et al., 2013). In this study, AngII was chosen because Nox2 mediates many known pathophysiological effects of AngII in the cardiovascular system through ROS generation (Forrester et al., 2018; Kawai et al., 2017; Munzel et al., 2015), therefore is suitable for studying a novel molecule as a potential Nox2 inhibitor. Morphologically, preliminary data of the phase-contrast images taken during the experiment showed enlarged cells in the AngII-treated group (1.69 ± 0.33 -fold increase, $p = 0.09$, Student's *t*-test, analysed using ImageJ 1.50i, $n = 3$, Appendix V). This is in line with the result *in vivo* (chapter 6) and (Yang et al., 2017), in which AngII significantly increased the cell surface areas of H9C2 cells as well as the cross-sectional areas of the cardiomyocytes in rats. In combination with the ROS production results obtained, it was suggested that the H9C2 *in vitro* PD model used in this study serves as a link to the *in vivo* investigation on the effects of LMH001, and is meaningful in predicting the formulation and efficacy of LMH001 *in vivo* PK analysis and in the cardiac hypertrophic models.

Ever since the first discovery of Nox2 in murine and human cardiomyocytes (Heymes et al., 2003; Li et al., 2002), different studies have examined its role on the generation of cardiac oxidative stress and remodelling (Joseph et al., 2017; Krijnen et al., 2003; Sirker et al., 2016; Zhang et al., 2015). It is worth mentioning that a co-

localisation of the capillaries and the cardiomyocytes was discovered in the mammalian hearts, and bi-directional crosstalk between the ECs and cardiomyocytes suggested a role of ECs to direct cardiomyocytes through various local protective signals, while cardiomyocytes reciprocally secrete the signalling factors. (Chen et al., 2010; Colliva et al., 2019; Condorelli et al., 2001; Hsieh et al., 2006). The ROS signalling from the mitochondrial electron-transport chain, XO, uncoupled NO synthases (NOS), and Nox between different cardiac cell types can be mediated by 1) diffusion; 2) influencing the extracellular matrix (ECM composition); 3) ROS-dependent alteration of paracrine factors, and could affect the contractile function, hypertrophic growth, and cardiac remodelling in the heart (Zhang & Shah, 2014). Therefore, the effect of LMH001 (IC50) might be affected by the differences in the roles and functions of the ECs and cardiomyocytes in the heart, and the PD modelling of LMH001 in different cardiac cell types would provide insights into the crosstalk between different cell types in the heart.

Pathophysiological effects of Noxes are isoform-specific, cell-specific and context-specific. LMH001 was developed based on the activation mechanism of autoinhibitory mechanism of the tandem SH3 domains on p47^{phox} and its phosphorylation (explained in chapter 4). The treatment of 2900.7 ng/ml LMH001 for 30 min could 1) significantly reduce the AngII induced ROS production and reduced the Nox1, Nox2 and Nox4 expression. These effects of LMH001 are closely linked to its targets and functions as a Nox2 inhibitor (Keiser et al., 2009; Kuhn et al., 2008). The reduction in the O₂⁻ production and the Nox2 expression could be directly attributed to the reduced p47^{phox} activity based on the proposed mechanism of LMH001. On the other hand, a reduced Nox4 expression after the LMH001 could be an indirect effect of LMH001 from the reduced activity of Nox2 and oxidative stress in general (Byrne et al., 2003). However, the altered Nox1 expression could be due to different factors. One

could be its response to the reduced ROS level in H9C2 cells in general. Still, another could stem from a reduced/inhibited activity of NOXO1, which is a Nox1 organiser, a homologue of p47^{phox} and has tandem SH3 domains isoform (discussed in section 1.3.1). Since LMH001 targets the tandem SH3 domains on the p47^{phox}, more evidence on its specificity and binding affinity are needed. Bearing this complexity in mind is vital in developing specific therapeutic approaches that target the detrimental effects of Noxs in the heart (Zhang et al., 2013). The complexity also made it hard to understand the downstream signalling such as p38 MAPK and ERK1/2 activation.

As discussed above, this highlights one of the major limitations of this study, which is the lack of data on the LMH001 binding affinity, K_d. By using different binding assays such as isothermal titration calorimetry (ITC), surface plasmon resonance (SPR) or bio-layer interferometry (BLI) assay, its binding affinity could be determined. Although the binding model was predicted, the proposed interactions between the LMH001 and the protein need further validation for its specificity, such as by using mutant(s) of the p47^{phox} tandem SH3 domain in an *in vitro* model or synthesizing and testing an analogue which is chemically modified to lose the essential interactions with the p47^{phox} tandem SH3 domain. At the same time, effects of LMH001 on morphological changes of the H9C2 cells (such as cell surface area, contraction etc.) had been overlooked and are worth investigating.

In conclusion, this chapter explored the effect LMH001 as a Nox2 inhibitor on the NADPH-dependent O₂⁻ production *in vivo*, and its concentration-dependent PD in an AngII-stimulated H9C2 cell model *in vitro*. LMH001 is effective in reducing the AngII-induced oxidative stress levels, accompanied by a decrease in Nox2 and Nox4 expression, and reduced activation of p38 MAPK. However, the activation of ERK1/2

does not seem to change significantly. Understanding the role of the target of LMH001, p47^{phox}, might provide insights into its effects.

Chapter 6

The Role of p47^{phox} in Angiotensin II (AngII)-induced Cardiac Hypertrophy in Mice

6.1 Introduction

Nox2 is a multi-subunit enzyme responsible for the production of O₂⁻ in many different types of cells in the cardiovascular system (Cave et al., 2006). This study has characterised the PKPD of a novel Nox2 inhibitor, LMH001, and examined its effect on inhibiting ROS production in AngII-stimulated H9C2 cells. However, the effect and the mechanism of p47^{phox} inhibition in the heart under pathophysiological conditions were not elucidated. Evidence has suggested the existence of gp91^{phox}-containing NADPH oxidase (Nox2) and its regulatory subunits such as p47^{phox} in mammalian myocardium (Sirker et al., 2016), epicardial adipose tissue (Sacks et al., 2011) and coronary arteries (Sattler et al., 2006). Overproduction of ROS by Nox2 has been implicated in the development of numerous cardiovascular diseases including hypertension (Forte et al., 2016), atherosclerosis (Judkins et al., 2010) and atherothrombosis (Violi et al., 2017). For example, infusion of a vasoconstrictor, AngII, could generate higher blood pressure and result in compromised vasorelaxation by acetylcholine in the Nox2-overexpressed mice compared to WT (Murdoch et al., 2011), while AngII did not have a significant effect on the blood pressure in Nox2 KO mice (Chan & Baumbach, 2013). Research has demonstrated a close relationship between the activation of Nox and AngII-induced activation of MAPK signalling pathways (Cruzado et al., 2002; Ebrahimian et al., 2011; Knock & Ward, 2011) and inhibiting Nox by inhibitors or reducing the level of ROS by antioxidants could reduce the effect of AngII in the cardiomyocytes (Hingtgen et al., 2006).

Many studies have revealed a vital role of the p47^{phox} subunit in regulating the activation of Nox (Fan, Teng & Li, 2009; Li et al., 2005; Li et al., 2002; Li & Shah, 2003; Li et al., 2004; Meijles et al., 2014). As the main regulatory subunit of Nox2, p47^{phox} is intuitively and traditionally considered to be involved in the development of many oxidative-stress related cardiac disorders such as myocardial dysfunction and remodelling after MI (Doerries et al., 2007; Leiding et al., 2013; Li et al., 2015), hypertrophic cardiomyopathy (Grote et al., 2006), dilated cardiomyopathy (Leiding et al., 2013), diabetic cardiomyopathy (Sharma et al., 2016), congestive or end-stage heart failure (Patel et al., 2013), coronary artery disease (Barry-Lane et al., 2001) and ischaemia/reperfusion (I/R) injury (Loukogeorgakis et al., 2010). This study focuses on the role of p47^{phox} and oxidative stress in cardiac hypertrophic growth and consequently, cardiac remodelling. The entire process of cardiac remodelling is not yet clear, but it was suggested to occur following myocardial infarction, coronary artery disease, or in response to a long-term hypertension (Rababa'h et al., 2018). Cardiac maladaptive hypertrophic growth normally would happen first, which involves the stretch of the myocyte. In response, neurohormones such AngII would then increase locally, and result in ROS production and activation of different signalling pathways (Dahlof, 1995; Fyhrquist, Metsarinne & Tikkanen, 1995; Horton et al., 2016; Wray et al., 2008). In turn, further deterioration of cardiac functioning follows, which then generates cardiac oxidative stress and an overwhelming neurohormones rush. This vicious cycle involving ROS plays an important role in cardiac fibrosis and remodelling (Cohn, Ferrari & Sharpe, 2000). p47^{phox} serves as a mediator for the activation of Nox2 in generating oxidative stress and activating reduction-oxidation reaction (redox) signalling which could induce the activities of different cytokines and aldosterone.

Unlike in neutrophils, in the cardiovascular system, p40^{phox}, p47^{phox} and p67^{phox} exist as a preassembled complex and co-localise with gp91^{phox} and p22^{phox} in cytoskeletal fractions with a peri-nuclear distribution in vascular endothelial cell lines under basal conditions (Li & Shah, 2002), suggesting different locations (i.e. intracellularly comparing to in the plasma membrane in neutrophils) and distinctive functions (i.e. generating O₂⁻ intracellularly as signalling molecules rather than assisting with microbial killing in neutrophils) of Nox2 in non-phagocytic cells. In VSMCs (Touyz et al., 2005) and cardiomyocytes (Patel et al., 2013), however, p47^{phox} has been found to co-localise with F-actin and associate with cortactin, which was proposed to facilitate the translocation of the p40^{phox}-p47^{phox}-p67^{phox} complex to Nox2 which locates both on the plasma membrane and the cytosol (including peri-nuclear region) (Krijnen et al., 2003). It was also shown in lung endothelial cells stimulated with hyperoxia that the p47^{phox} subunit associates with the actin cytoskeleton and p47^{phox} mobilisation occur upon stimulation with AngII (Usatyuk et al., 2007). It was discovered that with TNF α stimulation, p47^{phox} in the endothelial cells was able to interact with TNF receptor-associated factor 4 (TRAF4) thus getting phosphorylated, which could serve as a mechanism to localise the activated oxidase and its products to the targeted downstream kinases of induced ROS production such as ERK1/2 and p38 MAPK via interactions of TRAF4 with the cytoskeleton (Li et al., 2005). Disruption of this interaction by knocking down TRAF4 or using a ROS scavenger tiron could prevent the ERK1/2 phosphorylation, which demonstrated the role of the O₂⁻ in the downstream signalling pathways. At the same time, phosphorylated p47^{phox} was also discovered to interact with scaffold proteins such as Wiskott–Aldrich syndrome verprolin-homologous protein complex 1 and the actin cytoskeleton to direct the intracellular localisation of the active Nox (Tamura et al., 2006; Wu et al., 2003).

Phosphorylation of conserved serine residues in the c-terminal region of p47^{phox} was identified as being a key mediator of the signalling ligands secreted under pathophysiological conditions and the activation of p47^{phox} downstream signalling pathways (Didichenko et al., 1996; Fontayne et al., 2002; Meijles et al., 2014).

However, the complex role of p47^{phox} and the p47^{phox} signalling under pathophysiological conditions remain to be investigated. This study set out to look at the p47^{phox} signalling and the effect of targeting p47^{phox} on AngII-induced cardiac oxidative stress and hypertrophy.

6.1.1 Aims and objectives

Despite the studies on activation and regulatory mechanisms of Nox2 in the cardiovascular system, the role of p47^{phox} in AngII-induced cardiac hypertrophy had not been characterised. In this study, we first proposed that p47^{phox} signalling pathways might be involved in the AngII induced development of cardiac hypertrophy and targeting p47^{phox} by knockout or inhibition its function could prevent or reduce the levels of cardiac hypertrophy. Previously research discovered that *ex vivo* incubation with AngII (200 nM, 30 minutes) did not induce the O₂^{·-} production, and the aortic relaxation in p47^{phox} KO mice was preserved (Li et al., 2004). Therefore, we propose that targeting p47^{phox} by global KO would protect the heart from AngII-induced oxidative stress and thus retard the development of AngII-induced hypertrophy in the heart. Specifically, the objectives of this chapter are as following:

1. To assess the effect of p47^{phox} KO on AngII-infusion induced high blood pressure and cardiac hypertrophy;

2. To look at the effect of KO p47^{phox} on the AngII-induced cardiac oxidative stress. This includes the O₂^{·-} and H₂O₂ productions, and the expression patterns of Nox homologues including Nox1, Nox2 and Nox4;

3. To investigate the role of p47^{phox} in the activation of AngII-induced MAPK signalling pathway and DNA damage by the phosphorylation of H2A histone family member X (H2AX) and ASK1 in the heart.

6.2 Materials and Methods

6.2.1 Chemicals and reagents

Reagents of the appropriate grade, instruments and antibodies used in this study are listed in Appendix I, II and III, if not specified.

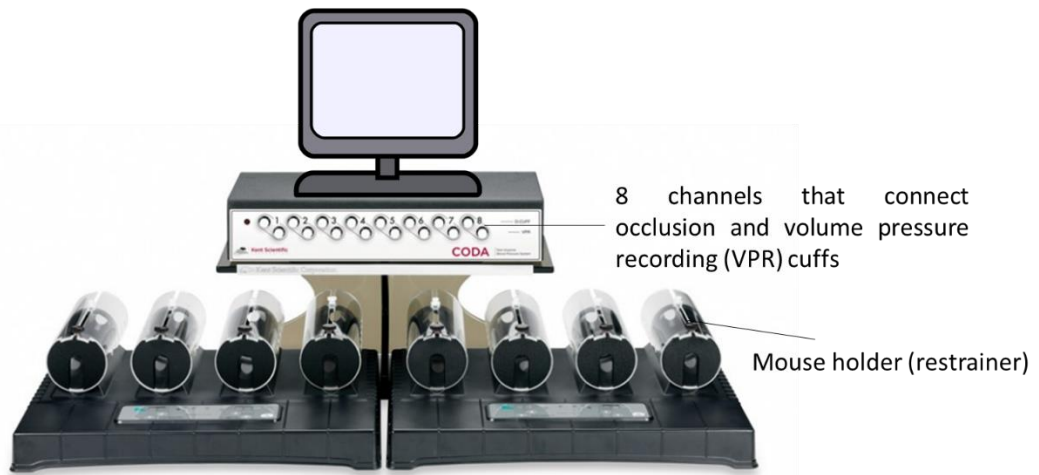
6.2.2 AngII-induced cardiac hypertrophy and cardiac samples from wild-type and p47^{phox} KO mice

The *in vivo* experiments were done by Prof. Li (my supervisor) group, as described previously (Fan et al., 2014). I was trained to measure blood pressure and harvest organs from mice. However, I did not do the implantation of mini pumps. Briefly, AngII at 800 ng/kg/min was delivered through osmotic minipumps (ALZET Osmotic Pumps, DURECT Corporation, U.S.A), and control mice received saline delivering for 14 days at the age of 10~12 months. Systolic and diastolic blood pressure was measured using computerised tail-cuff system (CODA, Kent Scientific, UK) (**Figure 6.1 A and B**) (Thatcher, 2017) on conscious mice following one week of the training period (Du et al., 2013). The CODA blood-pressure measurement is non-invasive and utilises a tail occlusion cuff (OCuff in **Figure 6.1(C)**) and a tail cuff with VPR (volume pressure recording) sensor. The VPR sensor measures the systolic and diastolic blood pressure based on the blood flow changing during the occlusion cuff is being deflated. **Figure 6.1 (C)** channel 1 shows an example of the blood pressure measurement, in comparison to channel 3 being empty.

Bodyweight and heart weight were measured, and the tissues were harvested and stored in -80 °C freezer. I used cardiac tissues of both WT and p47^{phox}KO mice; control (saline-infused) group versus AngII-infused group (n=9/group) for *ex vivo* experiments. All the subsequent experiments of biochemical and molecular assessment

of AngII-induced cardiac oxidative stress and signalling pathways were done by myself. A diagram (**Figure 6.2**) demonstrates the model establishment and the subsequent experiments that have been carried out in this study.

(A) CODA non-invasive blood pressure measurement system.



(B) The application of occlusion and VPR cuffs, mouse restrained by a mouse holder.

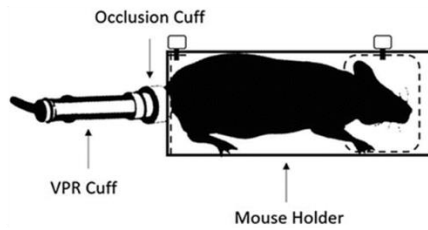


Image adapted from (Thatcher, 2017).

(C) A representative blood pressure trace by CODA.



Figure 6. 1 CODA non-invasive murine blood-pressure measurement system, its application on conscious mice, and the representative blood pressure trace.

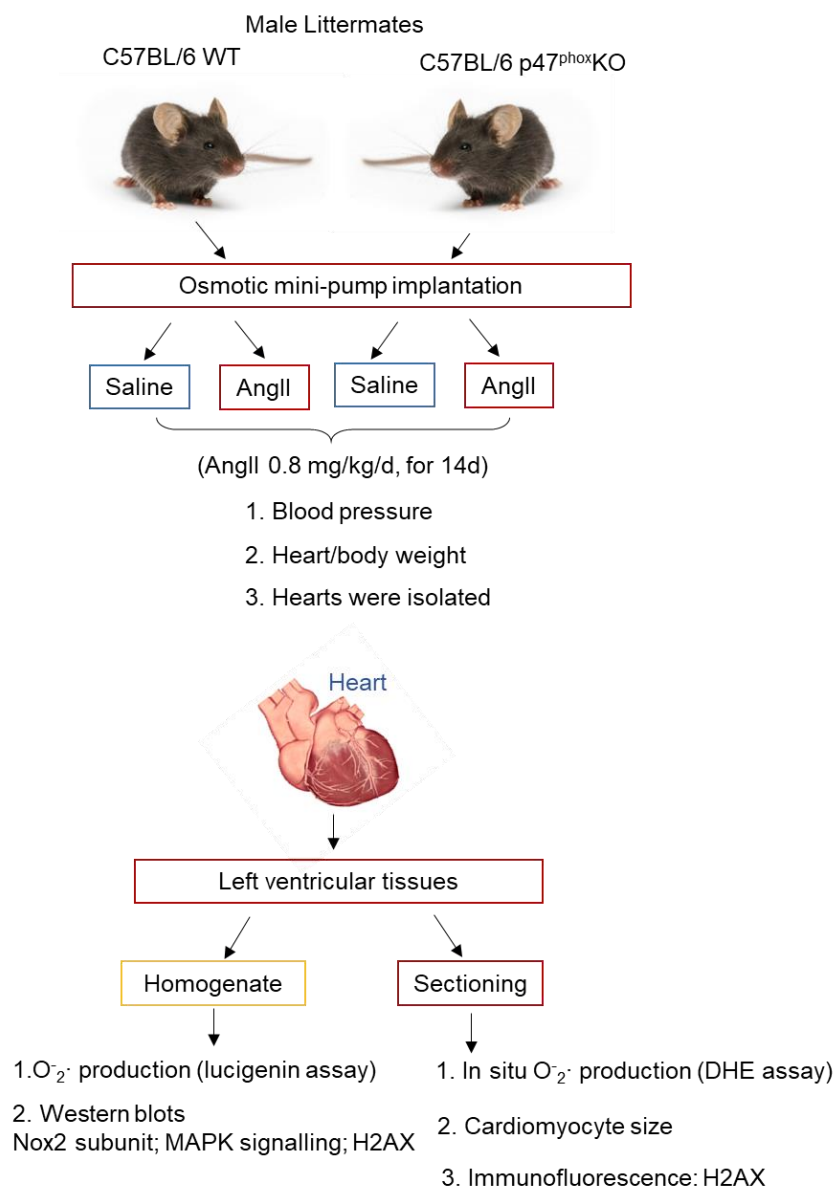


Figure 6. 2 Set-up of 2-week AngII-infused middle-age WT and p47^{phox} KO murine model and the biochemical and molecular experiments for the assessment.

6.2.3 Measurement of cardiac hypertrophy by cross-sectional cardiomyocyte size

To determine the level cardiac hypertrophy, alongside the heart/body weight, which was recorded at the time of cull, I measured the cross-sectional area of the cardiomyocytes under microscopy for each treatment group, since one of the indicators

of a hypertrophied cardiomyocyte is its enlargement cross-sectionally (Bensley et al., 2016). In the past, researchers found wheat germ agglutinin (WGA) staining was pericellular (Ohno, Tajima & Utsumi, 1986) and therefore have used it to measure the cross-sectional area of the myocyte (Del Re et al., 2013). WGA can bind to N-acetyl- β -D-glucosaminyl residues and N-acetyl- β -D-glucosamine oligomers, the necessary and abundant component of hyaluronic acid and keratin sulphate on the cell membrane (Chen, Shen & Liu, 2010). Therefore, in this study, to measure the cross-sectional area of the cardiomyocyte, a commercially available WGA (FITC conjugated, Sigma-Aldrich, UK) was used on cardiac cryosections from WT and p47^{phox} KO mice infused with AngII. Specifically, 5 mg of the WGA-FITC was dissolved in 5 ml PBS (final conc. 1 mg/ml) and stored at -20°C . The working solution used was 1 $\mu\text{g}/\text{ml}$ (1 μl stock in 1000 μl PBS) directly applied to the section and incubated for 30 min at room temperature, avoiding light. At the end of the incubation, 10 μl 0.5 $\mu\text{g}/\text{ml}$ DAPI was applied to each section for 5 min and washed by ultrapure water, as described in section 2.10.6. After being air-dried thoroughly avoiding light, the sections were mounted as described in 2.10.7 and observed by A1R confocal microscope (Nikon, Japan) (20 \times magnification). Images were taken (1024 pixel \times 1024 pixel) and the cross-sectional area of the cardiomyocytes was measured by ImageJ 1.50i (NIH, USA).

6.2.4 Sample preparation

For lucigenin, Amplex red and western blot, the left ventricular part of the isolated hearts (stored in -80°C) were first ground into powder using mortar and pestle in liquid nitrogen at -70°C on dry ice. Then approximately 2 mg (for lucigenin or Amplex red assays) or 20 mg (for western blot) of the tissue powder was added to 200 μl HBSS (for lucigenin or Amplex Red assays) or protein lysis buffer (for western blot, whose ingredients are specified in section 2.9.1) with PierceTM Protease Inhibitor

Tablets, EDTA free (Thermo Scientific, United Kingdom). Homogeniser POLYTRON PT 1200E (Kinematica, Netherland) was used to cut up each sample on ice for 60 s twice. Sonifier (Branson Ultrasonics, USA) was set as Time: 8 s; Temperature: 20 °C and Amplitude: 50% for sonicating samples on ice, twice per sample.

6.2.5 Protein concentration measurement

Protein concentration measurement is described in detail in chapter 5 (section 5.2.3). The only adjustment was to increase the protein concentration standards to 0, 5, 10, 25, 50, 100 mg/ml BSA in HBSS for measuring tissue protein concentrations.

6.2.6 ROS measurement

Lucigenin chemiluminescence and DHE assays were used for measuring the effect of AngII on the $O_2^{\cdot-}$ production. The methods were detailed in sections 2.6 and 2.7. Alongside the $O_2^{\cdot-}$, Amplex red assay was also used for detecting the level of H_2O_2 production (section 2.9).

6.2.7 Western blot

Western blot was used in this study to look at the p47^{phox} KO model (p47^{phox} expression level) and the effect of AngII and KO of p47^{phox} on Nox expression and the activation of MAPK signalling pathways, in which ERK1/2, p38MAPK, and JNK were shown to have an increased level of phosphorylation in the aortas of AngII-infused and KO murine model (Li et al., 2004). The phosphorylation of a redox-sensitive marker for DNA double-strand break, H2AX was also investigated (Rothkamm et al., 2015) to understand the role of p47^{phox} and NADPH-dependent $O_2^{\cdot-}$ production upon AngII infusion on the DNA damage. The method of western blot is detailed in section 2.9.

6.2.8 Immunofluorescence

Immunofluorescence was used alongside western blot to investigate the role of p47^{phox} and the effect of AngII. The phosphorylation of redox-sensitive apoptotic molecules H2AX at Ser139/Tyr142 and ASK1 at Thr845 were examined by immunofluorescence. The detailed method is listed in section 2.10.

6.3 Results

6.3.1 The effect of AngII infusion on the blood pressure

The systolic and diastolic blood pressure of WT and p47^{phox} KO mice were measured by CODA tail-cuff system (Kent Scientific, U.S.A) after 2-week of infusion (done by the previous group and data were analysed by myself) to understand the direct effect of AngII infusion on the WT and p47^{phox} KO mice. As is shown in **Figure 6.3**, 2-week infusion of AngII increased 1) the systolic blood pressure of WT to an average of (178.2 ± 8.8) mmHg significantly, compared to 2-week infusion of saline, with an average systolic blood pressure of (122.1 ± 6.7) mmHg (* $p < 0.05$, one-way ANOVA); 2) diastolic blood pressure of WT to an average of (143.5 ± 10.9) mmHg significantly, compared to the saline-infused group, which had an average diastolic blood pressure of (100.4 ± 4.4) mmHg (* $p < 0.05$, one-way ANOVA); 3) the systolic blood pressure of p47^{phox} KO to an average of (145.9 ± 12.5) mmHg mildly, compared to 2-week infusion of saline, with an average systolic blood pressure of (128.6 ± 16.4) mmHg ($0.1 > p > 0.05$, one-way ANOVA); 4) diastolic blood pressure of p47^{phox} KO to an average of (127.3 ± 3.4) mmHg significantly, compared to the saline-infused group, which had an average diastolic blood pressure of (98.9 ± 10.7) mmHg ($\dagger p < 0.05$, one-way ANOVA).

Heart weight (HW, mg) and body weight (BW, g) ratio were also calculated, and cross-sectional areas of cardiomyocytes from each group were measured. AngII infusion significantly induced cardiac hypertrophy in WT mice as demonstrated by 1) HW/BW (mg/g) ratio, which was 5.4 ± 0.5 in AngII-infused and 4.5 ± 0.2 in saline-infused group (* $p < 0.05$, one-way ANOVA) (**Figure 6.3 C**); 2) the cross-sectional areas, which was (414 ± 60) μm^2 in AngII-infused and (341 ± 39) μm^2 in saline-infused group (* $p < 0.05$, one-way ANOVA, **Figure 6.4 A**). However, in p47^{phox} KO mice, AngII only induced mild hypertrophy based on the HW/BW ratio with AngII ($4.9 \pm$

0.3) compared with saline (4.5 ± 0.1) ($\dagger p = 0.03$, one-way ANOVA, **Figure 6.3 C**). Yet no significant change ($(285 \pm 61) \mu\text{m}^2$ with AngII in comparison to $(261 \pm 36) \mu\text{m}^2$ with saline, $0.1 > p > 0.05$) in the cardiomyocyte cross-sectional area was found (**Figure 6.4 A**). These results illustrated that AngII infusion is effective in the model set up and induced high blood pressure in WT and $p47^{\text{phox}}$ KO, and hypertrophy in WT mice.

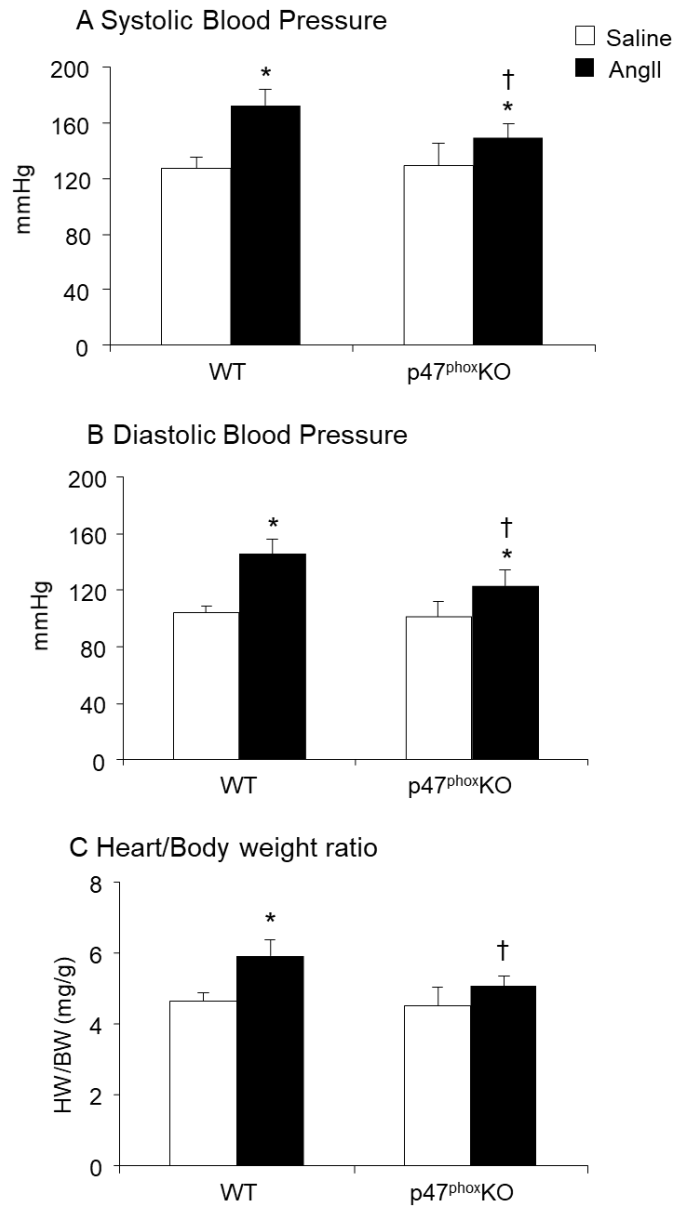


Figure 6. 3 Cardiovascular functions of WT and p47^{phox} KO mice after 2-week infusion of AngII or saline, measured by blood pressure and heart/body weight ratio.

(A) Systolic blood pressure of WT and p47^{phox} KO mice. **(B)** Diastolic blood pressure of WT and p47^{phox} KO mice. **(C)** HW/BW ratio of WT and p47^{phox} KO mice. Data were presented as Mean \pm SD. Statistical comparison between the two groups was made using one-way ANOVA. *p <0.05, significantly different from WT 2-week saline; † p <0.05, significantly different from WT 2-week AngII; # p <0.05, significantly different from KO 2-week saline.

6.3.3 The effect of AngII infusion and targeting p47^{phox} on the cardiac *in situ* O₂⁻ production measured by DHE fluorescence

Alongside the measurement of cross-sectional cardiomyocyte size, *in situ* O₂⁻ was measured by DHE fluorescence on cryosections. DHE is membrane-permeable and can bind to the chromosomes and exhibits a red fluorescent signal once oxidised. High level of fluorescent intensity indicates a high level of O₂⁻ in the tissue. At the same time, 10 mM tiron was used to scavenge ROS on the sections. **Figure 6.4 B left panel** showed representative images taken from DHE and DHE with tiron treated saline or AngII-infused WT and p47^{phox} KO cardiac sections. AngII-infused WT cardiac sections displayed a comparatively high level of bright fluorescent red, indicating a higher level of O₂⁻ production than saline-infused WT cardiac sections ($p < 0.05$). The O₂⁻ did not display any significant change in AngII-infused p47^{phox} KO sections, compare to saline. **Figure 6.4 B right panel** is the quantification of DHE fluorescent intensities displayed by different heart sections. AngII infusion had a strong effect on the O₂⁻ production in WT ($p < 0.05$, one-way ANOVA) but not p47^{phox} KO mice ($p > 0.05$, one-way ANOVA).

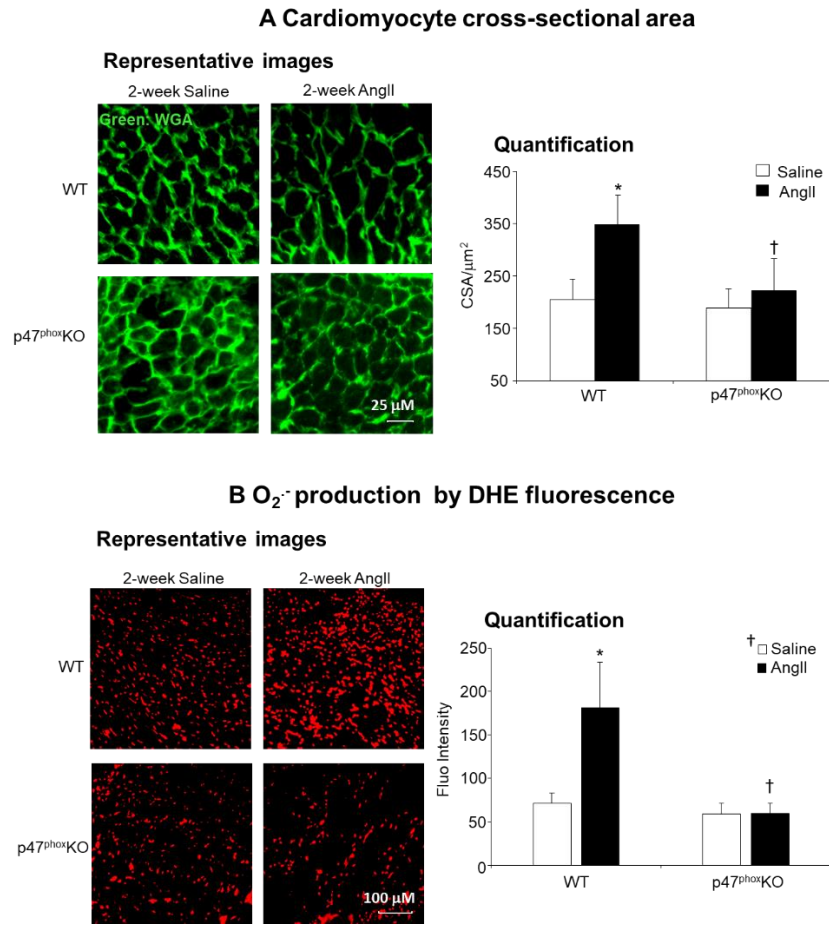


Figure 6. 4 *In situ* cardiac cross-sectional area and O₂⁻ production in AngII or saline-infused WT and p47^{phox} KO mice.

A left panel: representative images of the cardiomyocyte, stained with WGA-FITC. Images were taken under A1R confocal microscope (Nikon, Japan) (20× magnification), with the filter set to excitation/emission 495 nm/519 nm (FITC) and 358 nm/461 nm (DAPI). **A right panel:** measurement of the cardiomyocyte cross-sectional area. The cardiomyocyte cross-sectional areas were measured by ImageJ 1.50i using 10-15 images per slide. **B left panel:** representative images of oxidised DHE staining in the cardiac section. 10 mM Tiron was added before DHE as controls. Nuclei stained with oxidised DHE in red. Images were obtained under Nikon Eclipse Ti2-E inverted microscope with a red fluorescent filter, 10× magnification. **B right panel:** quantification of fluorescent intensity of DHE staining. The fluorescent intensity was calculated by measuring Mean Grey of DHE against the background using ImageJ 1.50i. 10-15 images used per slide. n=6 per group. Data were presented as Mean ± SD. Statistical comparison between the two groups was made using one-way ANOVA. *p

<0.05, significantly different from WT 2-week saline; † p <0.05, significantly different from WT 2-week AngII.

6.3.4 The effect of AngII infusion and targeting p47^{phox} on the cardiac O₂⁻ production measured by lucigenin chemiluminescence

To validate the result obtained from DHE assays and to understand the effect of AngII and KO of p47^{phox} on the O₂⁻ production, NADPH-dependent O₂⁻ production was detected by lucigenin chemiluminescence assay in a kinetic manner (**Figure 6.5 A**). Upon adding NADPH at 10 min, O₂⁻ generation climbed immediately. The O₂⁻ generation after the addition of NADPH suggested that O₂⁻ generation detected using lucigenin was NADPH-dependent. At 30 min, 10 mM Tiron, a ROS scavenger, was added and effectively inhibited the O₂⁻ generation, which confirmed the specificity of signal in this assay. Overall O₂⁻ production after adding NADPH was calculated in **Figure 6.5 B**. AngII significantly increased O₂⁻ production in WT but not p47^{phox} KO mice. Since the possible enzymatic sources of ROS include NOS, mitochondrial respiratory chain, XO and Nox, the enzymatic source of O₂⁻ generated was also investigated using different enzymatic inhibitors including L-NAME, rotenone, oxypurinol, DPI, and PEG-SOD (**Figure 6.5 C**). The increased signal detected in AngII-infused WT heart was able to be reduced by DPI, a flavoprotein inhibitor, and PEG-SOD, a superoxide dismutase. This result showed that Nox2, as a flavoprotein, is a very significant source of O₂⁻ in this study.

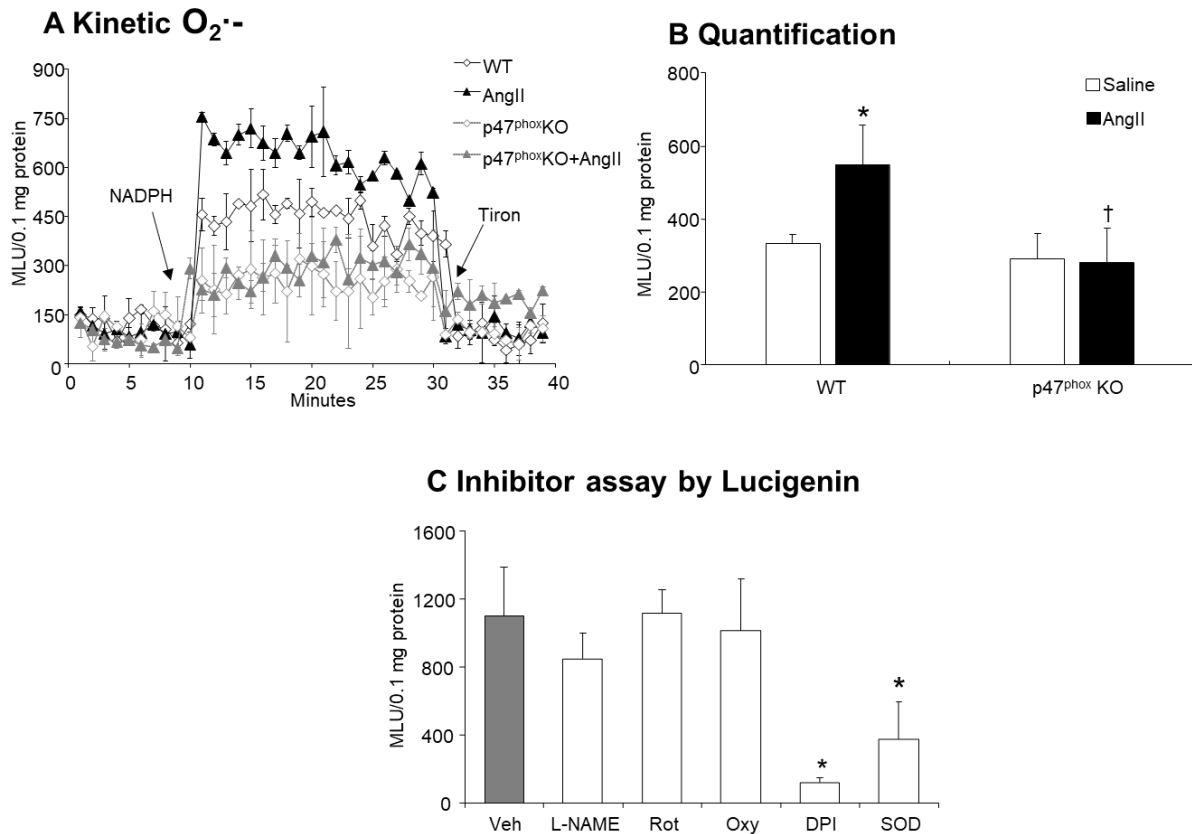


Figure 6.5 O₂⁻ production in AngII or saline-infused WT and p47^{phox} KO mouse heart.

A. Representative examples of kinetic measurement of O₂⁻ production. 0.1mM NADPH was added at 10 min. 10 mM tiron was added at 30 min, n= 3 per group. **B.** O₂⁻ production. n=6 per group. Statistical comparison between the two groups was made using one-way ANOVA. *p<0.05, significantly different from saline-infused WT; † p <0.05, significantly different from WT 2-week AngII. **C.** Enzymatic source of the O₂⁻ in AngII-infused WT heart. L-NAME: N^G-nitroarginine methyl ester, 100 mM, NOS inhibitor; Rotenone: 50 mM, mitochondrial respiratory chain inhibitor; Oxypurinol: 250 mM, XO inhibitor; DPI: diphenyleneiodonium, 20mM, flavoprotein inhibitor; PEG-SOD: 200 U/mL, polyethylene glycol, covalently linked to superoxide dismutase. n = 6 per group. Data were presented as Mean ± SD. Statistical comparison between the two groups was made using one-way ANOVA. *p <0.05, significantly different from AngII-infused WT group.

6.3.5 The effect of AngII infusion and targeting p47^{phox} on the cardiac H₂O₂ production measured by Amplex Red fluorescence

When the mammalian cells are exposed to oxidative stress, H₂O₂ is one of the major metabolic products of O₂⁻ by SOD (Lennicke et al., 2015) from the cellular self-protective mechanism (Fisher, 2009). At the same time, the other isoform of Nox, Nox4, is constitutively active due to its high *K_m* for oxygen (~18%) (Nisimoto et al., 2014) and has a significant production of H₂O₂ (discussed in section 1.3.3), the measurement of H₂O₂ would also contribute to the understanding of the role of Nox4 with AngII stimulation. In this study, H₂O₂ production in AngII-infused WT and p47^{phox} KO mice was measured by Amplex red assay. **Figure 6.6 A** is a representative standard curve of fluorescent unit displayed by different known concentrations of H₂O₂ from one Amplex Red assay. It shows that from 0.0625 μM to 2 μM H₂O₂ in the detecting system, good linearity between the concentration of H₂O₂ and the fluorescent units detected by the instrument was achieved. **Figure 6.6 B** shows a representative example of the kinetic readings of fluorescent units detected in the Amplex Red assay. Since catalase can scavenge H₂O₂, the gap in **Figure 6.6 B** represents a real-time H₂O₂ production. The signal was linear in the first 12 min. Hence the data recorded in the first 12 min was used for calculating H₂O₂ production in **Figure 6.6 C**. The quantification results in **Figure 6.6 C** showed that the AngII infusion could enhance the level of H₂O₂ production in both WT and p47^{phox} KO mice (*p* < 0.05), and this agrees partly with the fact that H₂O₂, as one of the main products from O₂⁻, increases when there is a high level of O₂⁻ production. On the other hand, the H₂O₂ increase in p47^{phox} KO (both saline and AngII-infused) could be attributed to the Nox4 functioning independent from p47^{phox}, and possibly H₂O₂ acted as a signalling molecule in response to reduced functioning of Nox2. These findings are in line with previous studies on

microglia with stimulation of amyloid- β (Geng et al., 2020), and the WT and Nox2 KO aging brain (Fan et al., 2019).

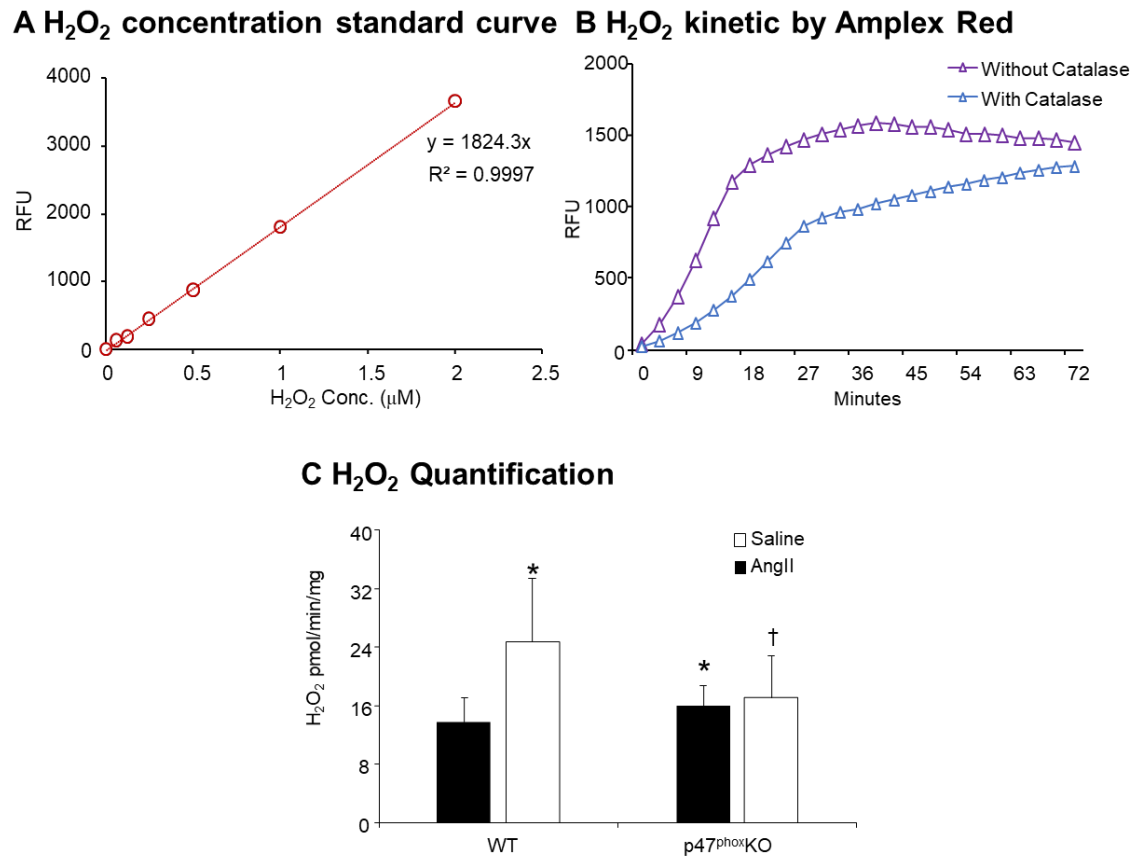


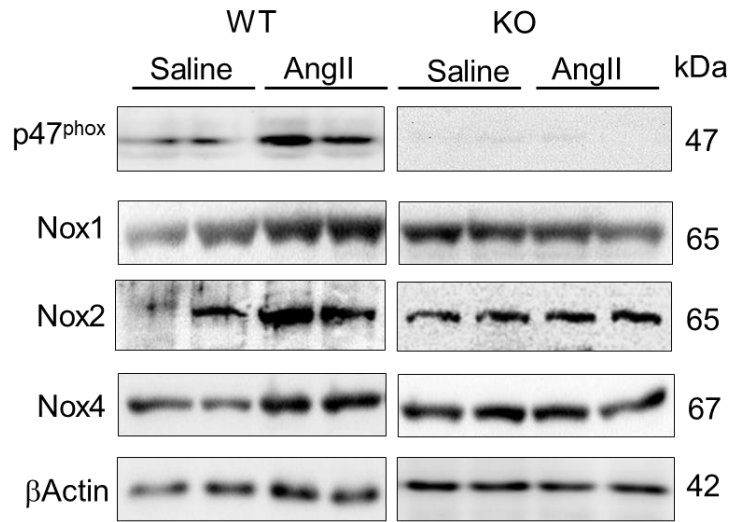
Figure 6. H₂O₂ production in saline or AngII infused WT and p47^{phox} KO mouse heart.

A. Representative example of a standard curve of the fluorescent unit against different concentrations of H₂O₂. relative fluorescent unit (RFU) was measured at c (H₂O₂) = 0, 0.0625, 0.125, 0.250, 0.500, 1.000, 2.000 μM. The curve was used to calculate H₂O₂ concentrations in the samples. **B.** A representative example of a kinetic RFU plot with or without catalase from one AngII-infused WT mice. RFU was measured every three minutes. **C.** Effect of AngII infusion on H₂O₂ production in WT and p47^{phox} KO mice. n=6 per group. Data were presented as Mean ± SD. Statistical comparisons between two groups were made using one-way ANOVA. * p < 0.05, significantly different from saline-infused WT.

6.3.6 The effect of AngII infusion and targeting p47^{phox} on the cardiac p47^{phox} and Nox expression examined by western blot

Western blot was used to examine the protein levels of p47^{phox}, Nox1, Nox2 and Nox4 in the cardiac homogenates using the AngII or saline-infused WT and p47^{phox} KO mice. **Figure 6.7 A** shows representative images on p47^{phox}, Nox1, Nox2 and Nox4 expression in AngII and saline-infused WT and p47^{phox} KO murine cardiac homogenates. The full-gel images are included at the end of this chapter as Appendix VII. Quantification of 6 different hearts per group (**Figure 6.7 B**) showed that: 1) AngII significantly increased the protein expression level of p47^{phox}, Nox1, Nox2 and Nox4 compared to saline infusion in WT mice ($p < 0.05$, one-way ANOVA); 2) yet AngII only increased the protein expression level of Nox2 in p47^{phox} KO mice mildly ($p = 0.07$, one-way ANOVA); 3) KO of p47^{phox} significantly reduced the p47^{phox} expression level in both AngII and saline-infused p47^{phox} KO mice, but significantly increased the expression of Nox1 and Nox4 compared to WT mice ($p < 0.05$, one-way ANOVA).

A Representative western blot



B Quantification

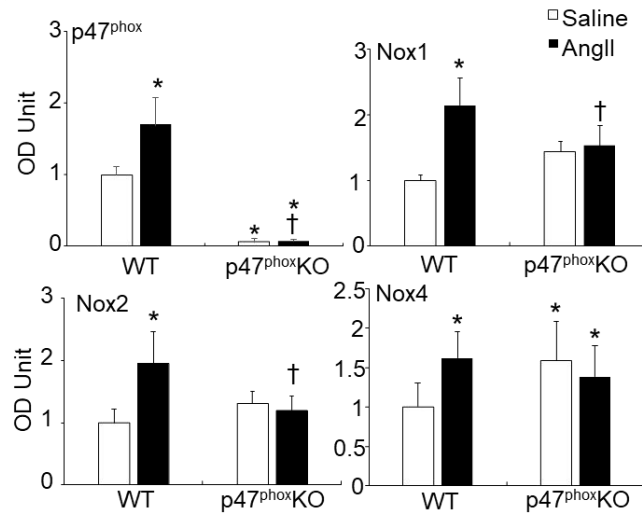


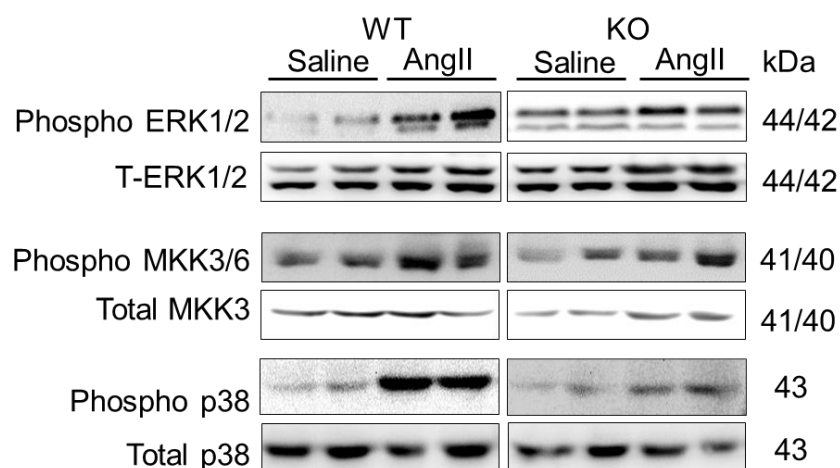
Figure 6. 7 Protein expression level of p47^{phox}, Nox1, Nox2 and Nox4 in AngII or saline-infused WT and p47^{phox} KO mice.

A Representative images of western blot analysis of p47^{phox}, Nox1, Nox2 and Nox4 in cardiac homogenates from saline or AngII-infused WT and p47^{phox} KO mice. β Actin detected in the same sample was used as a loading control. **B** the optical densities (OD) of p47^{phox}, Nox1, Nox2 and Nox4 bands were quantified using ImageJ 1.50i and normalized to the β Actin levels. Data were presented as Mean \pm SD. Statistical comparisons between two groups were made using one-way ANOVA. * p < 0.05, significantly different from WT 2-week saline; † p < 0.05, significantly different from WT 2-week AngII.

6.3.7 The effect of AngII infusion and targeting p47^{phox} on the activation of the MAPK signalling pathway examined by western blot

The activation of redox-sensitive MAPK signalling pathways has been demonstrated previously by the phosphorylation of ERK1/2, p38 and JNK in the *ex vivo* AngII incubation with WT and p47^{phox} KO murine aortic rings compared to controls. A basal increased phosphorylation level of ERK1/2, p38MAPK and JNK were discovered in p47^{phox} KO control aortic samples (Li et al., 2004). Therefore, to investigate the effect of AngII *in vivo* infusion on the activation of MAPK signalling pathways in WT and p47^{phox} KO mice, the phosphorylation of ERK1/2, mitogen-activated protein kinase kinase (MKK3/6), which was reported to be specific and only activate p38MAPK (Derijard et al., 1995; Brancho et al., 2003) and p38MAPK were examined and normalised to the corresponding total protein level by western blot. **Figure 6.8** shows the phosphorylation of ERK1/2, MKK3/6 and p38MAPK in saline or AngII-infused WT and p47^{phox} KO murine cardiac homogenates. AngII significantly increased the phosphorylation of ERK1/2, MKK3/6 and p38MAPK in WT mice ($p < 0.05$ comparing to saline-infused WT, one-way ANOVA). Moreover, these effects can be reduced or abolished in the p47^{phox} KO mice ($p < 0.05$, comparing to AngII-infused WT, one-way ANOVA). At a basal level with saline infusion, targeting p47^{phox} by KO did not affect the phosphorylation of MKK3/6, p38MAPK, or ERK1/2 significantly ($p > 0.05$, comparing to saline-infused WT, one-way ANOVA). The full-gel images for the representatives are also included in Appendix VII.

A Representative western blot



B Quantification

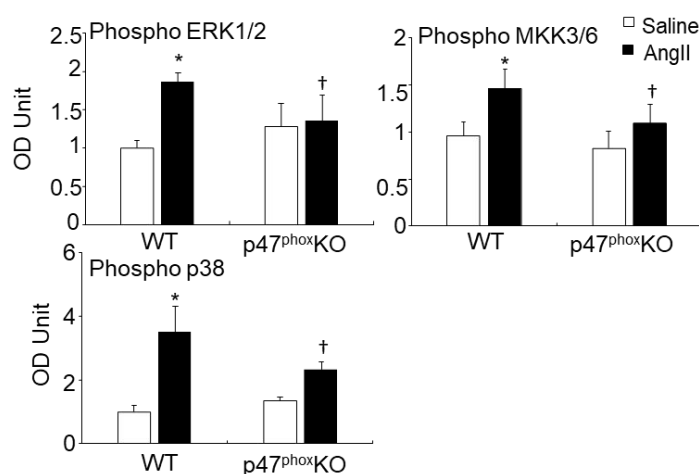


Figure 6. 8 Protein phosphorylation of ERK1/2, MKK3/6 and p38MAPK in saline or AngII infused WT and p47^{phox} KO mice.

A Representative images of western blot analysis of the phosphorylation of ERK1/2, MKK3/6 and p38MAPK in cardiac homogenates from saline or AngII-infused WT and p47^{phox} KO mice. The corresponding total protein detected in the same sample was used as a loading control. **B** the optical densities (OD) of phospho-ERK1/2, MKK3/6 and p38MAPK bands were quantified using ImageJ 1.50i and normalized to their total protein levels. Data were presented as Mean \pm SD. Statistical comparisons between two groups were made using one-way ANOVA. * $p < 0.05$, significantly different from WT 2-week saline; † $p < 0.05$, significantly different from WT 2-week AngII; # $p < 0.05$, significantly different from p47^{phox} KO 2-week saline.

6.3.8 The effect of AngII infusion and targeting p47^{phox} on phosphorylation of H2AX and ASK1

The effect of AngII on DNA damage was also investigated by looking into the phosphorylation of H2AX, a DNA double-strand breaks marker, (Kuo & Yang, 2008; Kinner et al., 2008) at Ser139, which indicates the DNA double-strand breaks in 1:1 manner, and the phosphorylation is associated with the recruiting of DNA repairing enzymes by oxidative stress (Gruosso et al., 2016). The observation of γ H2AX foci formation was seen as an indirect visualising of DNA damage in the cells (Kinner et al. 2008) but many studies have used it to score the level of DSBs (Rothkamm & Lobrich, 2003; Riballo et al., 2004; Leatherbarrow et al., 2006). Oxidative stress-related phosphorylation of H2AX has been demonstrated in human spermatozoa (Li, Yang & Huang, 2006) and leukocytes (Tanaka et al., 2006), and the formation of γ H2AX foci caused by ionising radiation has been indicated in the heart cells (Gavrilov et al., 2006) and also patients undergone paediatric cardiac catheterization (Beels et al., 2009). Therefore, in this study, phosphorylation of H2AX at Ser139/Tyr142 was used as an indication of DNA damage but the immunostaining and quantification of γ H2AX only indicated the phosphorylation of H2AX rather than the real level of DNA double-strand breaks. As is shown in **Figure 6.9 A and Figure 6.10**, AngII significantly increased the level of γ H2AX in WT mice as examined both by immunofluorescence and western blot ($p < 0.05$, compared to saline infusion with the same genetic background), suggesting a higher DNA damage level. However, KO p47^{phox} could significantly reduce the level of γ H2AX ($p < 0.05$, compared to WT mice with the same treatment).

H2AX phosphorylation by western blot

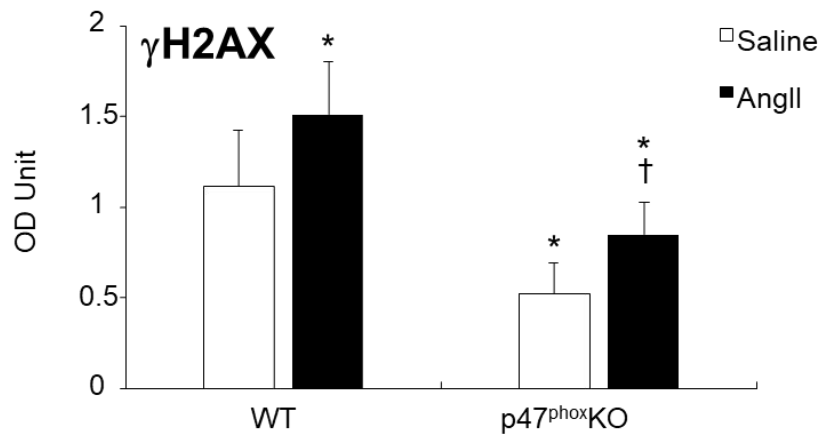
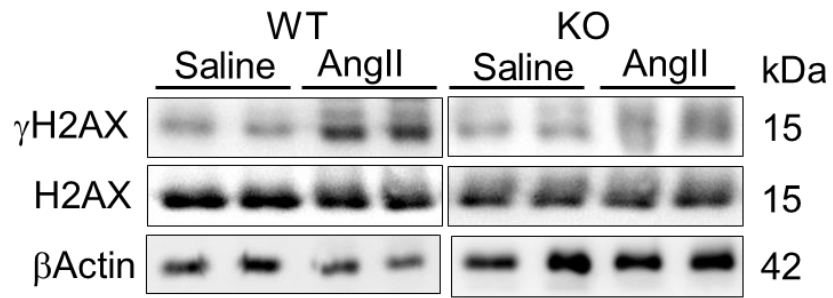


Figure 6. 9 γ H2AX detection in the AngII and saline-infused WT and p47^{phox} KO mice by western blot.

Upper: Representative images of western blot analysis of γ H2AX in cardiac homogenates from saline or AngII-infused WT and p47^{phox} KO mice. The corresponding total protein detected in the same sample was used as a loading control. Lower: OD of γ H2AX bands were quantified using ImageJ 1.50i and normalized to their total H2AX levels. Data were presented as Mean \pm SD. Statistical comparisons between two groups were made using one-way ANOVA. * $p < 0.05$, significantly different from WT 2-week saline; † $p < 0.05$, significantly different from WT 2-week AngII.

H2AX phosphorylation by immunofluorescence

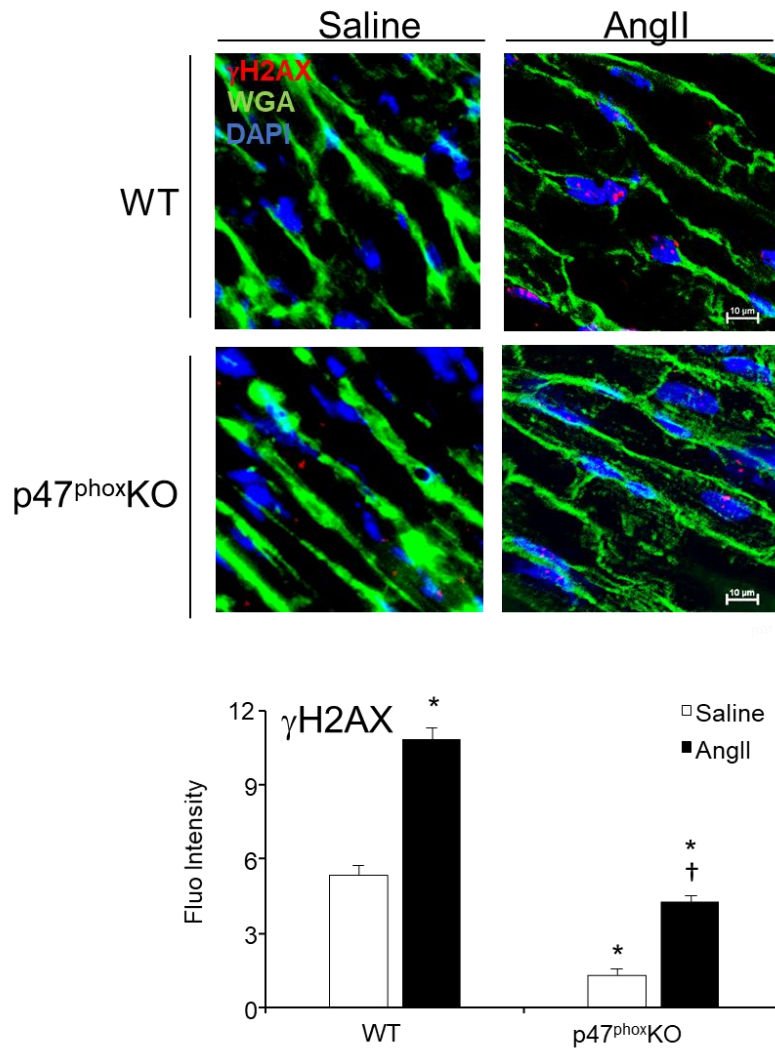


Figure 6. 10 γ H2AX detection in the AngII and saline-infused WT and p47^{phox} KO mice by immunofluorescence.

Upper: Representative images of immunofluorescence analysis of γ H2AX (Cy3 labelled, magnification: 40 \times) in the cardiac sections of saline or AngII-infused WT and p47^{phox} KO mice. Lower: Fluorescent density of γ H2AX staining was quantified using ImageJ 1.50i. Data were presented as Mean \pm SD. Statistical comparisons between two groups were made using one-way ANOVA. * p < 0.05, significantly different from WT 2-week saline; † p < 0.05, significantly different from WT 2-week AngII.

The phosphorylation of ASK1 at Thr845, as a marker for DNA damage under oxidative stress, was also examined. In this study, ASK1 was the link between oxidative

stress, and the activation of its downstream signalling molecules, including MKK3/6 and p38 (Hayakawa et al., 2012). **Figure 6.11** shows the double-immunofluorescent staining of phospho-ASK1 and Nox2. AngII significantly induced the phosphorylation of ASK1 in WT ($p < 0.05$, one-way ANOVA) but not p47^{phox} KO mice. KO p47^{phox} significantly reduced the phosphorylation of ASK1 with both saline and AngII-infusion ($p < 0.05$). This result echoes with the other DNA damage marker γ H2AX. The Nox2 expression was significantly increased in the AngII-infused WT group, but slightly in the p47^{phox} KO saline and AngII infused groups ($p = 0.06$). This result agrees with the western blot analysis of Nox2 expression in the left-ventricular cardiac homogenates.

Phosphorylation of ASK1 by immunofluorescence

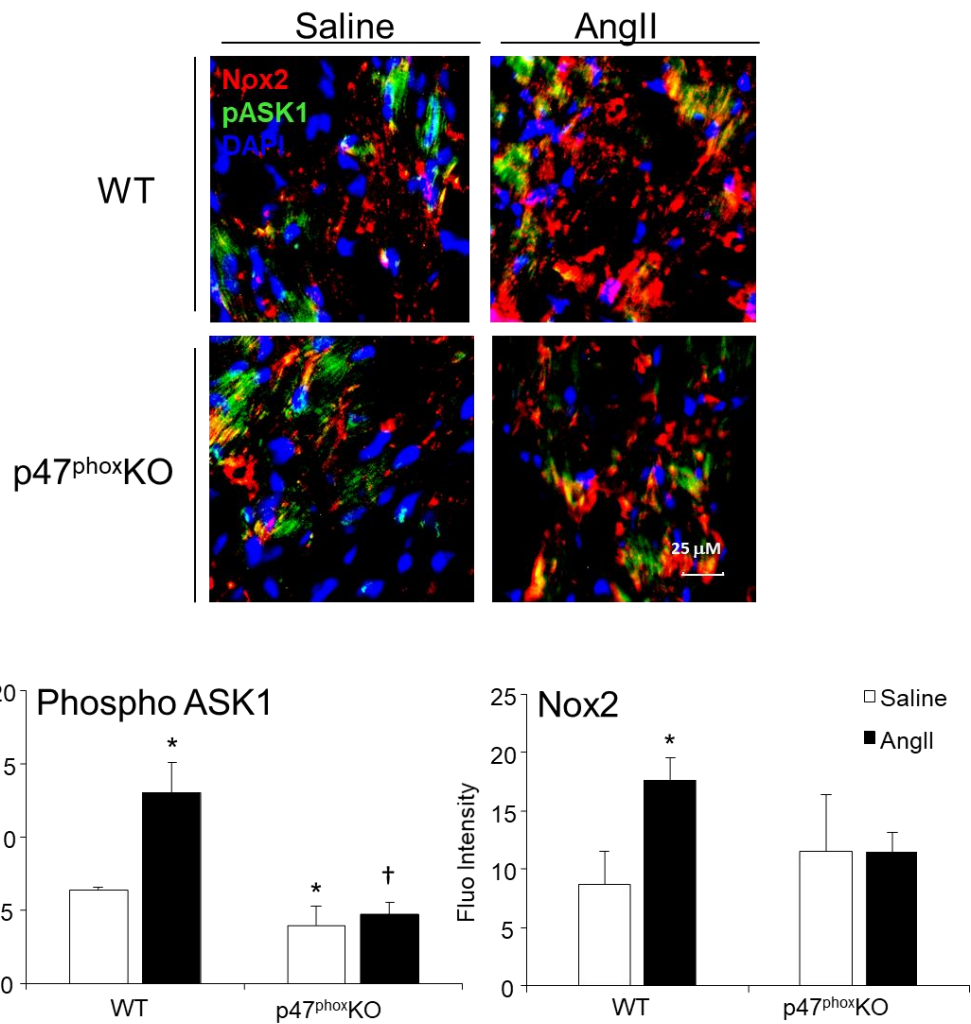


Figure 6. 11 Phosphorylation of ASK1 and Nox2 expression in the AngII and saline-infused WT and p47^{phox} KO mice, examined by immunofluorescence.

Upper: Representative images of immunofluorescence analysis of phosphorylation of ASK1 (Cy3 labelled, magnification: 20×) and the expression of Nox2 (FITC labelled, magnification 20×) in the cardiac sections of saline or AngII-infused WT and p47^{phox} KO mice. Lower: Fluorescent density of phospho-ASK1 and Nox2 staining were quantified using ImageJ 1.50i. Data were presented as Mean ± SD. Statistical comparisons between two groups were made using one-way ANOVA. * p < 0.05, significantly different from WT 2-week saline; † p < 0.05, significantly different from WT 2-week AngII.

6.4 Discussion

Cardiac hypertrophy especially left ventricle hypertrophy is one of the prevalent cardiovascular disorders that develop over a long period and can lead to life-threatening cardiac fibrosis and remodelling (Katholi & Couri, 2011). It is linked with a variety of cardiovascular conditions including ischaemia (Otterstad, 1993; Raphael et al., 2016), MI (Nepper-Christensen et al., 2017; Yuan & Leenen, 1999) and hypertension (Williams et al., 1975; Drayer, Gardin & Weber, 1983; Frohlich, 1987; Cuspidi et al., 2020). Among these conditions, hypertension is one of the most prevalent but manageable (Afridi et al., 2003; Jones et al., 2020) yet was largely neglected (Cuspidi et al., 2019; Foti et al., 2019). Hypertension caused approximately 9.4 million deaths and 7% of disease burden in 2010 (World Health Organisation, WHO), and in the U.S. hypertension was identified as the primary or contributing cause of death in about half a million cases in 2017 (Coelho et al., 2019). Research has demonstrated a close relationship between the development of hypertension, cardiac hypertrophy and the release of AngII in the human body.

AngII delivered by osmotic mini-pump has been widely used in the establishment of murine hypertension models (Iulita et al., 2018; Zimmerman et al., 2004). The effect of AngII-infusion was tested and verified by the repeated measurement of systolic and diastolic blood pressure since it is well-documented that AngII, as a vasoconstrictor, could increase the blood pressure (Catt et al., 1971; Fyhrquist, Metsarinne & Tikkanen, 1995; Crowley et al., 2006). At the same time, preload and left ventricular end-diastolic pressure, as well as the gradient between left ventricular end-diastolic pressure and arterial blood pressure were increased with elevated AngII concentration, showing positive inotropic and chronotropic effects of

AngII on the heart (Acharya et al., 2011; Broome et al., 2004; Vollmer, Meyers-Schoy & Marinelli, 1991). The increased blood pressure in p47^{phox} KO mice may have been a combined effect of AngII and the p47^{phox} KO itself considering that AngII could increase the vasoconstriction, through ROS production possibly increased by an enhanced activity of Nox1 and Nox4 (Welch, 2008). This assumption is in line with the result that Nox1 and Nox4 expression increased in the p47^{phox} KO mice with both saline and AngII-infusion, as examined by western blot in this study (section 5.3.5). At the same time, it is worth pointing out that p47^{phox} was discovered in human VSMCs (Touyz, Yao, Quinn, Pagano & Schiffrin, 2005) and murine heart (Montezano & Touyz, 2013; Patel et al., 2013) to associate with cortactin, which is responsible for the arrangement of actin filaments. Therefore, the impaired blood pressure might be related to the function of p47^{phox} in relation to contractile functions, independently from its role of Nox2 subunit. The cardiac hypertrophy in this study was examined by two methods: the HW/BW ratio and the measurement of cardiomyocyte cross-sectional areas. Hypertrophy induced in WT group was believed to be a response from hypertension and the activation of oxidative-stress sensitive signalling pathways. However, in p47^{phox} KO mice, although there was a mild increase in the blood pressure, it could be due to the complex role of p47^{phox} in the heart.

In this study, I have investigated the effect of AngII on causing cardiac oxidative stress, and if targeting p47^{phox}, the regulatory subunit of Nox2 would reduce the oxidative stress. By looking into the O₂⁻ production, the expression of NADPH oxidase, the activation of MAPK signaling pathways, and the phosphorylation of H2AX, this study showed that AngII infusion, which induced hypertension in both middle-age WT and p47^{phox} KO murine models, contributed to the pathophysiological conditions in the heart through increasing the cardiac oxidative stress. In addition,

targeting p47^{phox} affected AngII-induced cardiovascular disorders and cardiac oxidative stress.

Results of ROS production ($O_2^{\cdot-}$ and H_2O_2) by AngII or saline-infused WT and p47^{phox}KO hearts demonstrated that KO of p47^{phox} was effective in reducing the $O_2^{\cdot-}$ production upon AngII-infusion. This result is in line with (Li et al., 2004), yet KO p47^{phox} alone at basal conditions did not have a significant effect. This intriguing result was previously discussed in the p47^{phox}KO *in vitro* system (Li et al., 2002) and isolated endothelial cells from the KO mice (Li et al., 2004), in which the basal NADPH-dependent $O_2^{\cdot-}$ production significantly increased in comparison to WT mice. In this study, it was believed that the $O_2^{\cdot-}$ production in p47^{phox} KO mice might come from the impairment of Nox functioning and might be related to the deficiency of p47^{phox}.

At the same time, H_2O_2 production significantly increased by AngII infusion in WT mice as measured by Amplex Red assay, and this is very likely to be linked with the elevated $O_2^{\cdot-}$ production (Fukai & Ushio-Fukai, 2011; Zafari et al., 1998). In p47^{phox} KO mice, the H_2O_2 increase observed from both saline and AngII-infused mice might have come from the increased activities of Nox4 (as was shown by western blot in this study) (Dikalov & Nazarewicz, 2013), as a compensatory mechanism, since previous studies observed that in the VSMCs, the AngII did not change the activities of SOD or catalase (Zafari et al., 1998). Research had shown that inhibiting Nox2 using apocynin or PKC (involving in the activation of Nox2) inhibitor could reduce mitochondrial ROS production and retard mitochondrial dysfunction (Doughan, Harrison & Dikalov, 2008). Therefore, it was expected that H_2O_2 production in the p47^{phox} KO did not change as significantly as in the WT. However, since the expression of Nox4 was

increased, it could, in turn, activate the ROS production in the mitochondria (Doughan, Harrison & Dikalov, 2008).

ERK1/2 and p38 signalling pathways were reported to be activated by AngII (Berk, 1999; Griendling & Ushio-Fukai, 2000; Sano et al., 2001; Ushio-Fukai, Alexander, Akers & Griendling, 1998; Xie et al., 2001). In this study, the activation of ERK1/2, MKK 3/6 and p38 MAPK were examined. Studies have shown that there was a slight but significant increase in the level of phosphorylation of MKK3/6, p38 MAPK and ERK1/2 in the WT AngII-infused hearts in comparison to WT saline group, but in the p47^{phox} KO group, only the phosphorylation of p38 MAPK significantly increased. This could be because MAPK signaling did not depend on Nox2 solely for its activation by AngII, as previously described by (Ushio-Fukai et al., 1998) in the VSMCs. Since MKK3/6 was involved in the apoptosis signal-regulating kinase (ASK)-MKK3/6-p38 MAPK pathway (Kim et al., 2005), further studies are needed to explain the activation of MAPK signaling in the AngII-induced p47^{phox} KO mice. Despite the report on the activation of MKK3/6 by a low level of oxidative stress that did not induce the apoptosis (0.02 mM H₂O₂) in the U937 cells (Kurata, 2000), this study showed a more complex role of p47^{phox} in the cardiac MAPK/ERK signaling pathways. Li et al. (Li et al., 2004) identified the role of p47^{phox} in activating the MAPK signaling pathways in vascular endothelium, and this study expanded this effect to the hearts. Nonetheless, the effects of AngII on the activation of MAPK signaling pathways were still significantly inhibited in the p47^{phox} KO mice, which demonstrated the role of p47^{phox} under pathophysiological conditions and the therapeutic potential of targeting p47^{phox} under diseased conditions.

H2AX was also used as a DNA damage marker. AngII significantly induced the phosphorylation of H2AX on both WT and p47^{phox} KO mice. However, γ H2AX in the

p47^{phox} KO mice were not as high as in the WT. The reduced level of H2AX phosphorylation suggests that the DNA damage induced by AngII partly involve the functioning of p47^{phox}. This study shows, for the first time, a link among AngII-induced oxidative stress, p47^{phox}, phosphorylation of H2AX and DNA damage in the heart. Previous studies on H2AX have mainly been focused on radiation (Gavrilov et al., 2006; Beels et al., 2009; Gruosso et al., 2016). Recently studies from our group showed the DNA damage using γ H2AX and p53 in aging WT mice, middle-age Nox2-overexpressed mice and elderly humans (Fan et al., 2019), linking the phosphorylation of H2AX to the Nox2 functioning and the oxidative stress. Therefore, taken together, it suggests that AngII-induced O₂⁻ might have been playing a role in inducing DNA damage in heart, although might be in part.

However, one of the major limitations of this study is that the effect induced by AngII, such as the increased cardiac oxidative stress and the activation of p38 MAPK and ERK1 signalling, could be a result of hypertension rather than a direct result of hypertrophy. To overcome this, a lower dose AngII (not enough to induce cardiac hypertrophy) could be used as a new group in this study. At the same time, since previous studies revealed a more complex role a p47^{phox} than just activating of Nox2, over-expressed p47^{phox} mouse model with the treatment of AngII could also facilitate a more comprehensive understanding of p47^{phox}.

In conclusion, this study looked at the role of p47^{phox} in the AngII-induced high blood pressure and cardiac hypertrophy. Targeting p47^{phox} by KO could significantly reduce the cardiac O₂⁻ production, the activation of the p38 MAPK/ERK signalling pathway and reduce the DNA damage examined by the phosphorylation of H2AX and ASK1. However, p47^{phox} in the heart showed a more complicated role than just facilitating Nox2 to produce O₂⁻, which should not be overlooked by future research.

Chapter 7

General Discussion and Future Work

7.1 General Discussion

Up till now, many different Nox2 inhibitors have been developed. However, most of the studies have been only focusing on their effects (Sorce et al., 2017), and their PK or PK/PD relations have been potentially ignored. As an example, the invention of DPI dates back to the early 1990s (Stuehr et al., 1991), and new studies are still emerging now (Yeware et al., 2019). However, shockingly, no results on its PK parameters or PK/PD relations are available. Another example is apocynin. It was first described in 1883 by Schmiedeberg (Stefanska & Pawliczak, 2008), but it was not until recently (after 2010) that its PK properties and PK/PD relations were examined (Chandasana et al., 2015), which then boosted the improvement of its structures (Wang et al., 2013) and the research on its new derivatives (Dranka et al., 2014; Langley et al., 2017).

In the recent years, there is increasing emphasis on the involvement of preclinical PK/PD in the very early stage of the drug development (Goto et al., 2019; Lave et al., 2016). Preclinical PK/PD can facilitate the drug development process by ruling out drug candidates and solving the emerging problems as early as possible, thus reducing the cost, time and effort in this decade-lasting, \$2.8 billion (on average) process (Lindsley, 2014; Wouters, McKee & Luyten, 2020). This study examined the PK characters of apocynin (as a known control compound) as well as a novel Nox2 inhibitor (LMH001) using simulation and modelling, and their effects on reducing organ oxidative stress in a time-dependent manner. Further KO of the targeted subunit, p47^{phox}, provided insights into the signalling pathways involved in the AngII-induced

cardiac oxidative stress and hypertrophy. Nox2-mediated and related oxidative stress in AngII-induced hypertrophic heart in WT and p47^{phox} KO hearts were measured, and the AngII-induced, p47^{phox}-involved MAPK and apoptotic signalling were examined. The findings reinforce the understanding of the effect/side effect of Nox2 inhibitors targeting p47^{phox} on oxidative-stress related cardiovascular disorders.

As small-molecule Nox2 inhibitors, both apocynin and LMH001 share the similarities including short half-life, high clearance, and rapid distribution to different organs post iv bolus dosing *in vivo*. As an index for blood-brain barrier permeability, Log BB calculated for apocynin is between -0.04 to 1.0 from 1 min to 30 min. Log BB was also calculated by using the Clark's and Rishton's equations (details in section 4.3.1), Log BB of apocynin was predicted to be -0.36 (Clark's) and -0.10 (Rishton's). The calculated Log BB of apocynin is slightly lower than the observed data. The possible glycosylation might have facilitated this process (Wang et al., 2008). Glycosylation was used in the drug development for a better membrane permeability (Moradi et al., 2016). The Log BB of LMH001 was predicted to be -1.23 (Clark's) and -0.69 (Rishton's), suggesting as a small molecule, LMH001 could, to an extent, penetrate the blood-brain barrier and have access to the CNS.

Despite the investigations on the LMH001 chemical property and PK characterisation, the short half-life of LMH001 has not been addressed enough or solved. There could be interspecies differences that affect PK properties of LMH001 (Andes & Craig, 2002; Gerber et al., 1986; Vogelmann et al., 1988). However, in comparison to the existent drugs, as was demonstrated by a study on how the mouse strain differences could affect the PK parameters using on eight commercial medicines, the iv half-life in the mice ranged from 1.4 – 12.0 h (Barr et al., 2020), the $t_{1/2} = 0.04$ h of LMH001 is still relatively short. The similar arisen problem of apocynin has

encouraged the studies in its derivatives, structural modification, and formulation change, and this could also be applied to LMH001. In fact, in the patent (Patent No. WO 2013/038136 A1), there are 39 molecules, and LMH036 was also synthesised for future studies.

Concerns on the pitfalls during the development of Nox2 inhibitors have been raised (Liochev & Fridovich, 1997; Zielonka, Lambeth & Kalyanaraman, 2013; Augsburger et al., 2019; Reis et al., 2020). Therefore, using multiples methods for the measurement of PD, and evaluating the appropriate biomarker for PD analysis are essential (Goto et al., 2019; Griendling et al., 2016). O₂⁻ production measured by lucigenin chemiluminescence in the CD1 mice after iv bolus of apocynin, along with DHE and MDA assays showed it is effective in reducing brain, liver and heart oxidative stress. Moreover, the detection of LMH001 in H9C2 cells after 30 min incubation confirmed its ability to cross the cellular membrane. *in vitro* O₂⁻ and H₂O₂ production in AngII-stimulated H9C2 cells treated with different Nox2 inhibitors showed that among the treatment of 10 µM of different inhibitors (2900.7 ng/ml for LMH001, 1661.70 ng/ml for apocynin, and 1345.5 ng/ml for DPI), only LMH001 and DPI had a significant effect in reducing the O₂⁻. This result is in line with (Augsburger et al., 2019), in which it suggested that 10 µM DPI but not 300 µM apocynin was able to reduce the oxygen consumption in human neutrophils stimulated by PMA. For the first time, this study investigated a novel Nox2 inhibitor, LMH001 using a wide range of analytical chemistry, PK/PD and biochemistry method, and compared its effect with existing inhibitors. The process (including literature search, the selection of ‘control’ inhibitor, the establishment of the extraction method for the compound, HPLC-MS/MS detection method, characterisation of the chemical property, and PK/PD analysis) can be applied for future characterisation of small-molecule inhibitors.

In recent years, the interactions of p47^{phox} and p22^{phox} have emerged as a potential target for the inhibition of Nox2 activation (Hahn et al., 2011; Solbak et al., 2020). Solbak *et al.* identified eight hits targeting the SH3_A and SH3_B groove on the p47^{phox}, such as preventing the association of p47^{phox} to p22^{phox} (Solbak et al., 2020). Different from other existing Nox inhibitors, the action of these molecules is mechanism driven, therefore are predicted to have high specificity and efficacy that blocks agonist (such as AngII, result not shown in this study) induced p47^{phox} binding to p22^{phox}, a key mechanism required for Nox2 activation without effect on Nox4 or Nox5-derived ROS production. However, as discussed in chapter 5, more experiments on the LMH001 binding affinity are needed to confirm its specificity.

LMH001 showed inhibition on AngII-induced ROS production in H9C2 cells. The ROS production might also come from Nox1 as p47^{phox} is also partially involved in the regulation of Nox1 activity, and p47^{phox} also shares the structural similarity to NoxO1. This could be an added advantage of LMH001 to treat oxidative stress in the cardiovascular system, where Nox1 activation in the VSMCs is also involved in AngII-induced hypertension. However, one concern here is that without target-specific formulation or therapy, whether LMH001 would adversely target the O₂⁻ in the neutrophils. Previous experiments had shown no oxidative burst response from peripheral leukocytes (result not shown here), which might be because that larger scale of Nox2 activation was involved in the leukocyte functioning compared to the cardiovascular system. But to test this hypothesis, future experiments on determining the therapeutic window are still needed.

The research interest of this study specially lies in LMH001 treating cardiovascular diseases. Since Nox2 is globally expressed, it is essential to consider LMH001 for cardiovascular system-specific targeting formulations. One challenge here

is that, many CVDs are complex and involve multiple genes. Therefore, combining LMH001 with other medications in the formulation might be a more realistic therapy in the clinical settings, provided that there is well-informed quantification of the degree of poly-pharmacological effects of cardiovascular drugs (Li et al., 2014). On the other hand, Ebselen, a selenium with antioxidant activity, entered clinical trials for ischemic stroke (Yamaguchi et al., 1998), and recently for bipolar disorder and hypomania, affecting impulsivity and emotional processing (Kil et al., 2017; Masaki et al., 2016; Sharpley et al., 2020). LMH001, as a small molecular, has a good potential in BBB penetration as predicted by Log P and tPSA. Therefore, with *in vitro* BBB penetration models available (as discussed in chapter 4), it is worth considering the potential of LMH001 in treating neurological disorders.

Equally, since LMH compounds were also developed based on the association of p47^{phox} to p22^{phox}, looking into the p47^{phox} signalling and targeting p47^{phox} by KO in the development of AngII-induced cardiac hypertrophy could shed light on understanding the organ-specific role of p47^{phox} and side effects of targeting p47^{phox}. The p47^{phox} KO mouse model of CGD was first established by (Jackson, Gallin & Holland, 1995), disrupted by a 1.15 kb neomycin resistance cassette inserted in the sense direction into the exon 7 of Ncf1 gene. In this study, the blood pressure, heart/body weight ratio and the cross-sectional areas of cardiomyocyte size confirmed improved cardiovascular functions in the AngII-infused p47^{phox} KO mice in comparison to AngII-infused WT, and the AngII-infused p47^{phox} KO mice also had a reduced ROS production in the hearts. The investigation on p47^{phox}-signalling showed that AngII-infusion affected the activation of MAPK signalling pathways, as demonstrated by the phosphorylation of ERK1/2, p38 and MKK3/6, and the phosphorylation of ASK1 and γ H2AX (a marker for apoptosis), but this effect can be reduced by KO of p47^{phox}.

Previous research has shown in the neutrophils that activation of ERK1/2 and p38 MAPK could lead to the phosphorylation of p47^{phox}-Ser345 at primary inflammatory sites (Dang et al., 2006; Yang et al., 2008), at the same time, the generation of ROS from Nox (which involves the phosphorylation of p47^{phox}) and mitochondria being able to act as a signalling molecule to activate ERK1/2 and p38 MAPK (Yang et al., 2007; Teng et al., 2012). In this study, we promote more evidence that targeting p47^{phox} by KO can affect the activation of MAPK signalling pathways. Based on these results, LMH molecules could also be used in the saline and AngII-infused WT murine models, to study the effect of LMH on the AngII-induced cardiac hypertrophy.

On the other hand, p47^{phox} has other binding partners and functions, including mediating contractions in SMCs and cardiomyocytes. These mechanisms have not been explained/clarified fully due to a gap in the development of appropriate and effective p47^{phox} inhibitors. LMH molecules seem to be able to fill this gap if proven an effective inhibitor of p47^{phox}.

In conclusion, this study evaluated the preclinical *in vivo* PK/PD characters of a novel Nox2 inhibitor, LMH001, in comparison to apocynin (as a control inhibitor) and explored its mechanism by using AngII-infused cardiac hypertrophic WT and p47^{phox} KO murine models. This study provided evidence on the suitability of LMH001 as a Nox2 inhibitor and shed light on improvements that could be done for the future improvement of LMH molecules. The information on the function of p47^{phox} in mediating cardiac oxidative stress and the effect of targeting p47^{phox} under pathophysiological conditions are also valuable in understanding the functions of LMH001. More importantly, LMH molecules stand a bright future as a class of Nox2 inhibitors targeting the association of p47^{phox} and p22^{phox}, both in the research and clinical settings.

7.2 Future Work

This study set out to characterise the PK/PD parameters of LMH001 and to investigate the targeted p47^{phox} in AngII-infused cardiac oxidative stress. As discussed throughout the thesis, based on the results and the limitations identified, there are still many different future experiments that need to be done:

I. To investigate the possible hydrolysis and change of LMH001 *in vivo*;

The stability of LMH001 was not yet confirmed. Experiments using different simulated body fluids showed that there was a significant decrease in the detection of LMH001 in neutral and alkaline solutions. However, the exact cause is yet to be determined. In order to understand in-depth how LMH001 changes in the body, the next step could be radiolabelling of LMH001 and carrying out the PK study, thus its behaviour and distribution could be traced (Isin et al., 2012).

II. To explore the possibilities of improving the half-life of LMH001;

Like apocynin, as a small phenolic compound, LMH001 has a relatively short half-life. Addressing a problem as early as possible during drug development is crucial in terms of saving the cost and pushing it forward to reach clinical trials (Baillie, 2008). On the one hand, since LMH036 is a larger molecule, and has not got an ester group, which is a group observed in increased propensity in short half-life compounds (Gunaydin et al., 2018), and was recently synthesised, it worth exploring its chemical and PK characters in comparison to LMH001. On the other hand, as discussed in section 4.4, several ways should be used to modify the compound, with proper consultation with professional chemists.

III. To determine the tissue distribution and organ-specific effect of LMH001;

As discussed in chapter 4, the simple but essential experiments needed in this study is the measurement of LMH001 concentration in different organs in the CD1 PK model, alongside the organ specific NADPH-dependent $O_2^{\cdot-}$ generation for a better understanding of the systemic effect of LMH001.

IV. To determine the functional mechanism of LMH001;

Due to the mechanism of Nox2 inhibitors, the redox chemistry results (such as ROS level measured) are mostly used as an output or a PD biomarker (Gatto et al., 2013; Altenhofer et al., 2015; Reis et al., 2020). Despite previous results of the binding affinity studies in the cell-free system, and the results showing that LMH001 was able to penetrate the cell membrane and reduce the $O_2^{\cdot-}$ production, it is still crucial to explore the functional mechanism of LMH001 *in vivo*. The possible experiments include but not limited to the binding affinity assays, ROS-scavenging assays *in vitro*, BBB penetration using MDCKII cell model and metabolic stabilities in liver microsomes and hepatocytes.

V. To investigate the role of p47^{phox} in depth;

As discussed in chapter 6, the effect of AngII on p47^{phox} could be due to a direct effect of hypertension. Therefore, different animal models, such as a lower dose of AngII, p47^{phox} over-expression and possibly an AngII-independent model such as the deoxycorticosterone acetate (DOCA)/salt model can be used for understanding the complexity of p47^{phox} functions;

VI. To investigate the effect of LMH001 in diseased models by applying it to the AngII-induced cardiac hypertrophic models to study the role of p47^{phox};

In chapter 6, the opposing role of p47^{phox} in mediating $O_2^{\cdot-}$ production and its possible binding to different proteins such as cortactin to mediate the cardiac functions

and muscle contraction was discussed. This raised the awareness of the undiscovered possible mechanism of p47^{phox}, which might be crucial in mediating the normal functions of the cells. Therefore, if the acting mechanism of LMH001 is proven to be competitively binding to p22^{phox} thus preventing the binding of p47^{phox}, LMH001 would be able to act as an inhibitor for the in-depth study of the functions of p47^{phox} alongside p47^{phox} KO murine models in different studies looking at the function of p47^{phox}.

Appendix

Appendix I: List of Reagents

Reagent	Supplier	Catalogue No.
2',7'-Dichlorofluorescein diacetate	Sigma-Aldrich	D6883
2-mercaptoethanol	Sigma-Aldrich	M7154
Acetone	Fisher Scientific	A/0606/17
Acetonitrile (LC-MS grade)	Fisher Scientific	10001334
Acrylamide	Fisher Scientific	BPE1410-1
Ammonium acetate	Sigma-Aldrich	A1542
Ammonium persulfate (APS)	Sigma-Aldrich	A3678
Angiotensin II (AngII)	Sigma-Aldrich	A9525
Apocynin	Sigma-Aldrich	W508454
Bradford Reagent	Sigma-Aldrich	B6916
Bovine serum albumin (BSA)	Sigma-Aldrich	A2153
Bromophenol Blue	Sigma-Aldrich	161-0404
BSTFA+TMCS	Sigma-Aldrich	33154-U
Calcium chloride	Fisher Scientific	C5670
Dihydroethidium (DHE)	Sigma-Aldrich	D11347
Dimethyl sulfoxide (DMSO)	Sigma-Aldrich	D2650
Diphenyleneiodonium (DPI)	Sigma-Aldrich	D2926
Diapocynin	Sigma-Aldrich	SML0927
DAPI	Sigma-Aldrich	D9542
DMEM (Low Glucose)	Sigma-Aldrich	D5546
EDTA	Sigma-Aldrich	D/0700/53
Ethanol (HPLC grade)	Fisher Scientific	E/0650DF/17
Ethyl acetate (for HPLC)	Sigma-Aldrich	34858
Fetal bovine serum (FBS)	Sigma-Aldrich	F7524
Formic acid (for HPLC-MS)	Fisher Scientific	M/4062/17
Glacial acetic acid (HPLC grade)	Fisher Scientific	A/0400/PB15
Glycerol	Sigma-Aldrich	G5516
Glycine	Fisher Scientific	G/0800/60
H ₂ O (LC-MS grade)	Fisher Scientific	10505904
Hanks' Buffered Salt Solution (HBSS)	Gibco, ThermoFisher	14175-137
Heparin	LEO Pharma	BL110
Hydrochloric acid (ACS grade)	Sigma-Aldrich	320331
Isopentane	Fisher Scientific	9/1030/17
KH ₂ PO ₄	Sigma-Aldrich	P9791
L-Glutamine (200 mM)	Sigma-Aldrich	59202C
L-NAME	Sigma-Aldrich	N5751
Lucigenin	Sigma-Aldrich	M8010
Magnesium chloride	Sigma-Aldrich	M8266
MDA assay kit	Sigma-Aldrich	MAK085
Methanol (HPLC grade)	Fisher Scientific	M/4056/17

Methanol (LC-MS grade)	Fisher Scientific	10653963
Mowiol	Sigma-Aldrich	324590
Na ₂ PHO ₄	Fisher Scientific	N7785
NADPH	Fisher Scientific	10337241
Optical Cutting Temperature (OCT)	Pyramid Innovation	R40020-E
Oxypurinol	Sigma-Aldrich	O4502
Phosphate Buffered Saline (PBS)	Sigma-Aldrich	P4417
Paraformaldehyde	Sigma-Aldrich	P6148
PEG-SOD	Sigma-Aldrich	S9549
Potassium chloride	Sigma-Aldrich	P3911
Pierce Protease Inhibitor Tablets	Thermo Scientific	A32963
PVDF	Bio-Rad	1620177
Protein marker	Bio-Rad	1610374
Rotenone	Sigma-Aldrich	R8875
Skimmed milk	Sigma-Aldrich	70166
Sodium dodecyl sulfate (SDS)	Sigma-Aldrich	L3771
TEMED	Sigma-Aldrich	87689
Tiron	Sigma-Aldrich	89460
Triton X-100	Sigma-Aldrich	X100PC
Tris-base	Fisher Scientific	T/3710/60
Tris-HCl	Fisher Scientific	T/P631/53
Trypan Blue Solution	Sigma-Aldrich	T8154
Trypsin-EDTA Solution 10×	Sigma-Aldrich	59418C
Tween-20	Fisher Scientific	BPE337
FITC-Wheat germ agglutinin (WGA)	Sigma-Aldrich	L-4895

Appendix II: List of antibodies

Antibodies	Host Species	Dilution	Supplier	Catalogue No.
p47 ^{phox} (D-10)	Mouse	1:500	Santa Cruz	sc-17845
β -Actin (13E5)	Rabbit	1:2000	CST	4970
Nox1 (H-75)	Rabbit	1:500	Santa Cruz	sc-25545
Nox2 (H-60)	Rabbit	1:500	Santa Cruz	sc-20782
Nox2 (C-15)	Goat	1:100 (IF)	Santa Cruz	sc-5827
Nox4 (H-300)	Rabbit	1:500	Santa Cruz	sc-30141
ASK1	Rabbit	1:100 (IF)	CST	8662
phospho-ASK1 (Thr845)	Rabbit	1:100 (IF)	CST	3765
p38 MAPK (C-20)	Rabbit	1:500	Santa Cruz	sc-535
phospho p38 MAPK (Thr180/Tyr182)	Rabbit	1:1000	Sigma-Aldrich	MABS64
ERK1/2 (H-72)	Rabbit	1:500	Santa Cruz	sc-292838
phospho ERK1/2 (Thr202/Tyr204)	Rabbit	1:1000	Sigma-Aldrich	SAB4301578
H2AX	Rabbit	1:1000 and 1:100 (IF)	CST	2595
γ H2AX (Ser139/Tyr142)	Rabbit	1:1000 and 1:100 (IF)	CST	5438
anti-rabbit, HRP conjugated antibody	Goat	1:1000	Sigma-Aldrich	A3687
anti-mouse, HRP conjugated antibody	Goat	1:1000	Sigma-Aldrich	A9917
anti-rabbit, biotin- conjugated antibody	Goat	1:1000	Sigma-Aldrich	B8895
anti-goat, biotin- conjugated antibody	Rabbit	1:1000	Sigma-Aldrich	B7014
ExtrAvidin-FITC	-	1:1000	Sigma-Aldrich	E2761
ExtrAvidin-Cy3	-	1:1000	Sigma-Aldrich	E4142
anti-rabbit, FITC conjugated antibody	Goat	1:1000	Sigma-Aldrich	F0382
anti-rabbit, Cy3 conjugated antibody	Sheep	1:1000	Sigma-Aldrich	C2306

IF: Immunofluorescence. Unless specified, the dilution was for western blot analysis.

Appendix III: List of equipment

Name	Company	Model
Centrifuge	ThermoFisher	
Homogeniser	Kinematica	Polytron PT 1200E
Sonicator	Branson Ultrasonics	450 Cell Disruptor #60662
Blood pressure monitor	Kent Scientific	CODA-HT4
HPLC	Thermo Scientific	Accela LC Systems
Mass spectrometry (for LC-MS)	Thermo Scientific	LTQ-Orbitrap XL
Chemiluminescence plate reader	Molecular Devices	Spectramax L
Cryostat	Bright Instrument	Bright 5040 Cryostat
Water bath	Grant Instruments	
Fluorescent microscope	Nikon	Eclipse Ti2-E
GC	Agilent Technologies	HP6890 Series GC System Plus+
Mass spectrometry (for GC-MS)	Agilent Technologies	5973 Mass Sensitive Detect
Confocal microscope	Nikon	A1R
Colourimetric plate reader	Molecular Devices	SpectraMax 340PC
Western blot running system	Bio-rad	Mini-PROTEAN® Tetra Handcast System
Semi-dry blotting system	Bio-rad	Trans-Blot® SD
The western blot imaging system	UVP	BioSpectrum AC
Orbital shaker	Stuart	SSM1

Appendix IV: R Script for NCA Analysis

AUC-Calculation-with-PKNCA.R

Fangfei Liu

2020-06-12

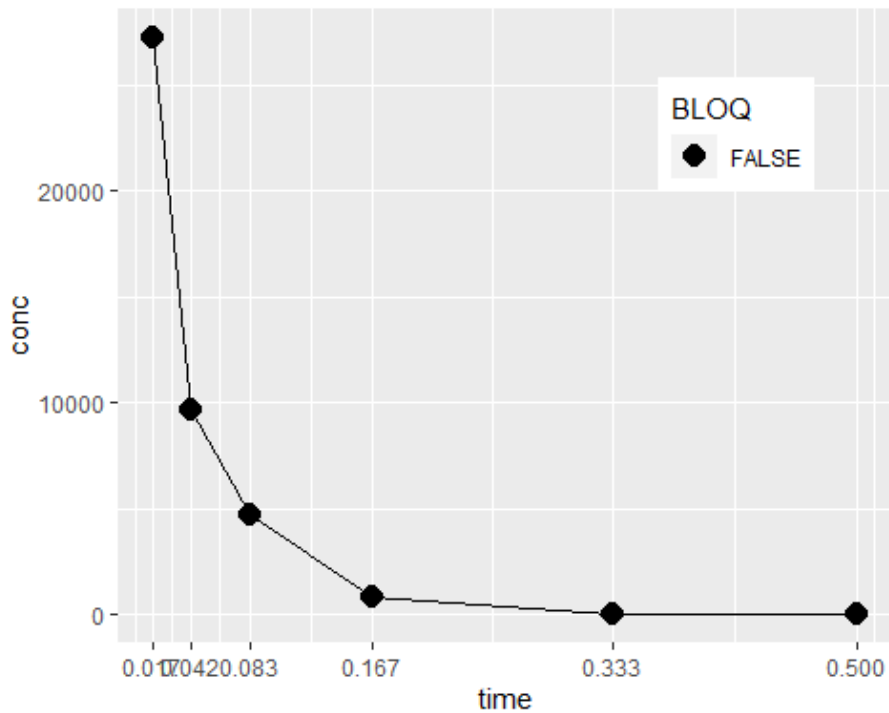
```
suppressPackageStartupMessages({
  library(PKNCA)
  library(dplyr)
  library(cowplot)
  library(knitr)
  library(ggplot2)
})

## Warning: package 'dplyr' was built under R version 3.6.3
## Warning: package 'cowplot' was built under R version 3.6.3
## Warning: package 'knitr' was built under R version 3.6.3

scale_colour_discrete <- scale_colour_hue
scale_fill_discrete <- scale_fill_hue

my_conc <- data.frame(conc=c(27271.79, 9630.83, 4650.75, 780.87, 29.68, 1
0.47),
                      time=c(0.017, 0.042, 0.083, 0.167, 0.333, 0.500),
                      subject=1)
my_conc$BLOQ <- my_conc$conc == 10
my_conc$measured <- TRUE

ggplot(my_conc,
       aes(x=time,
           y=conc,
           shape=BLOQ,
           group=subject)) +
  geom_line() +
  geom_point(size=4) +
  scale_x_continuous(breaks=my_conc$time) +
  theme(legend.position=c(0.8, 0.8))
```



```
my_dose <- data.frame(dose=c(1000000),
                      time=c(0),
                      subject=1)

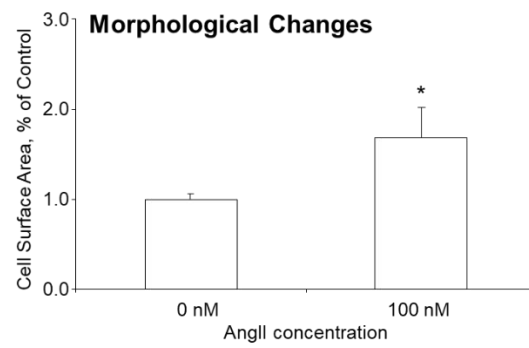
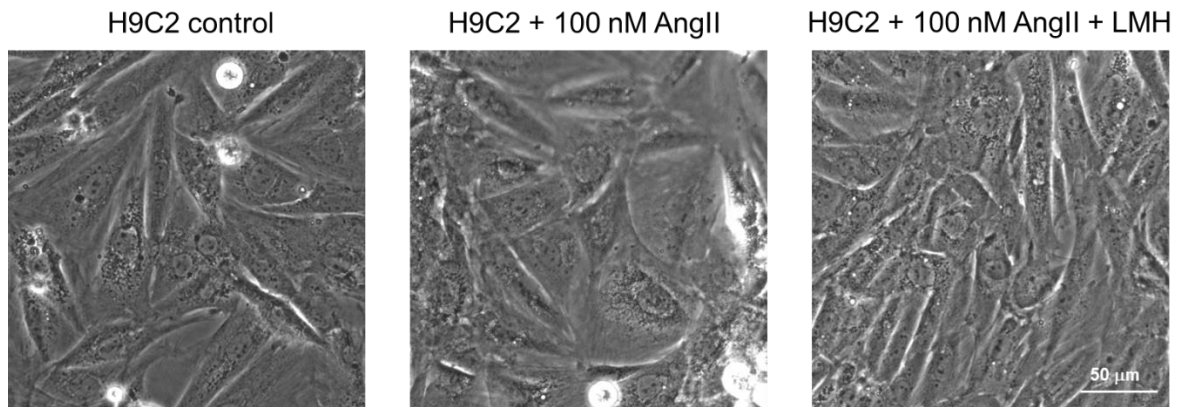
conc_obj <- PKNCConc(my_dose, conc~time|subject)
dose_obj <- PKNCAdose(my_dose, dose~time|subject)
data_obj <- PKNCAdata(data.conc=conc_obj,data.dose = dose_obj,
                     intervals=data.frame(start=0.017,
                                           end=0.500,
                                           aucall=TRUE,
                                           auclast=TRUE,
                                           aucinf.pred=TRUE,
                                           aucinf.obs=TRUE))

results_obj <- pk.nca(data_obj)
kable(as.data.frame(results_obj))
```

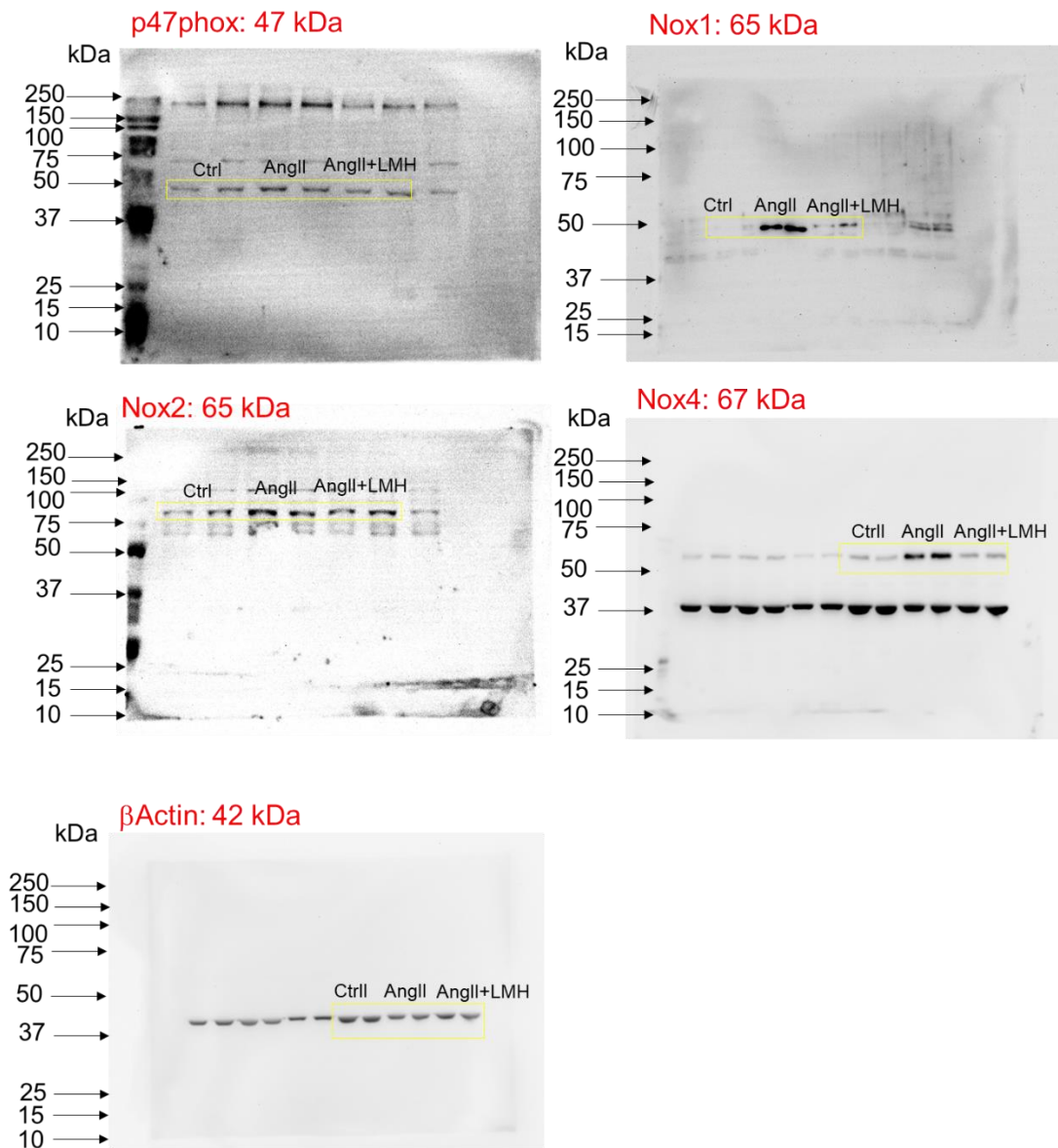
start	end	subject	PPTESTCD	PPORRES	exclude
0.017	0.5	1	auclast	927.5851496	NA
0.017	0.5	1	aucall	927.5851496	NA
0.017	0.5	1	tmax	0.001666667	NA
0.017	0.5	1	tlast	0.4830000	NA
0.017	0.5	1	clast.obs	10.4700000	NA
0.017	0.5	1	lambda.z	15.6061365	NA
0.017	0.5	1	r.squared	0.9596893	NA

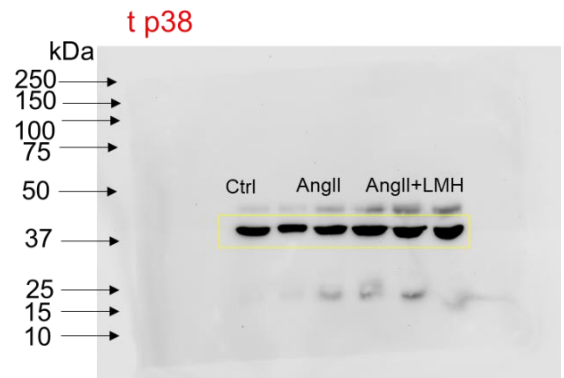
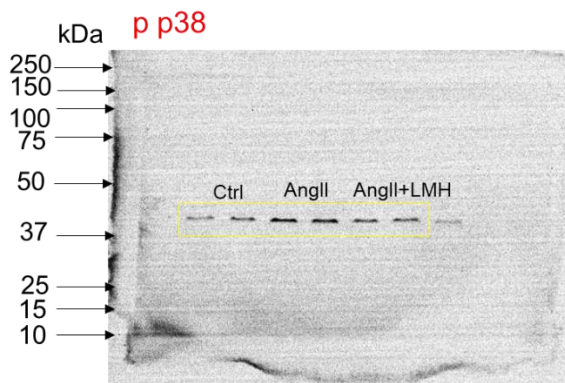
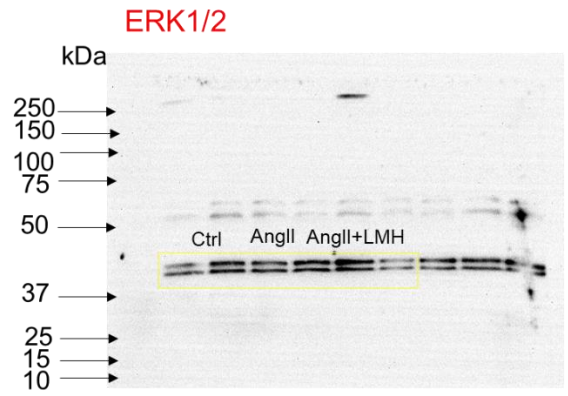
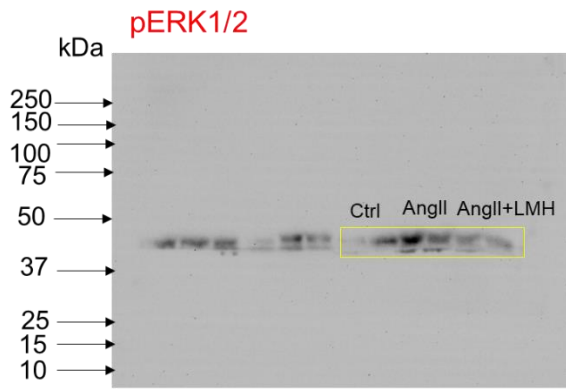
```
0.017 0.5 1 adj.r.squared      0.9462523 NA
0.017 0.5 1 lambda.z.time.first    0.0250000 NA
0.017 0.5 1 lambda.z.n.points    5.0000000 NA
0.017 0.5 1 clast.pred       5.5383321 NA
0.017 0.5 1 half.life        0.0444150 NA
0.017 0.5 1 span.ratio       10.3118222 NA
0.017 0.5 1 aucinf.obs       928.2560395 NA
0.017 0.5 1 aucinf.pred      927.9400313 NA
pk.calc.c0(conc=c(27271.79, 9630.83, 4650.75, 780.87, 29.68, 10.47),
            time=c(0.017, 0.042, 0.083, 0.167, 0.333, 0.500), time.dose = 0, c
heck = TRUE)
## [1] 55348.72
```

Appendix V: Phase-contrast of H9C2 cells

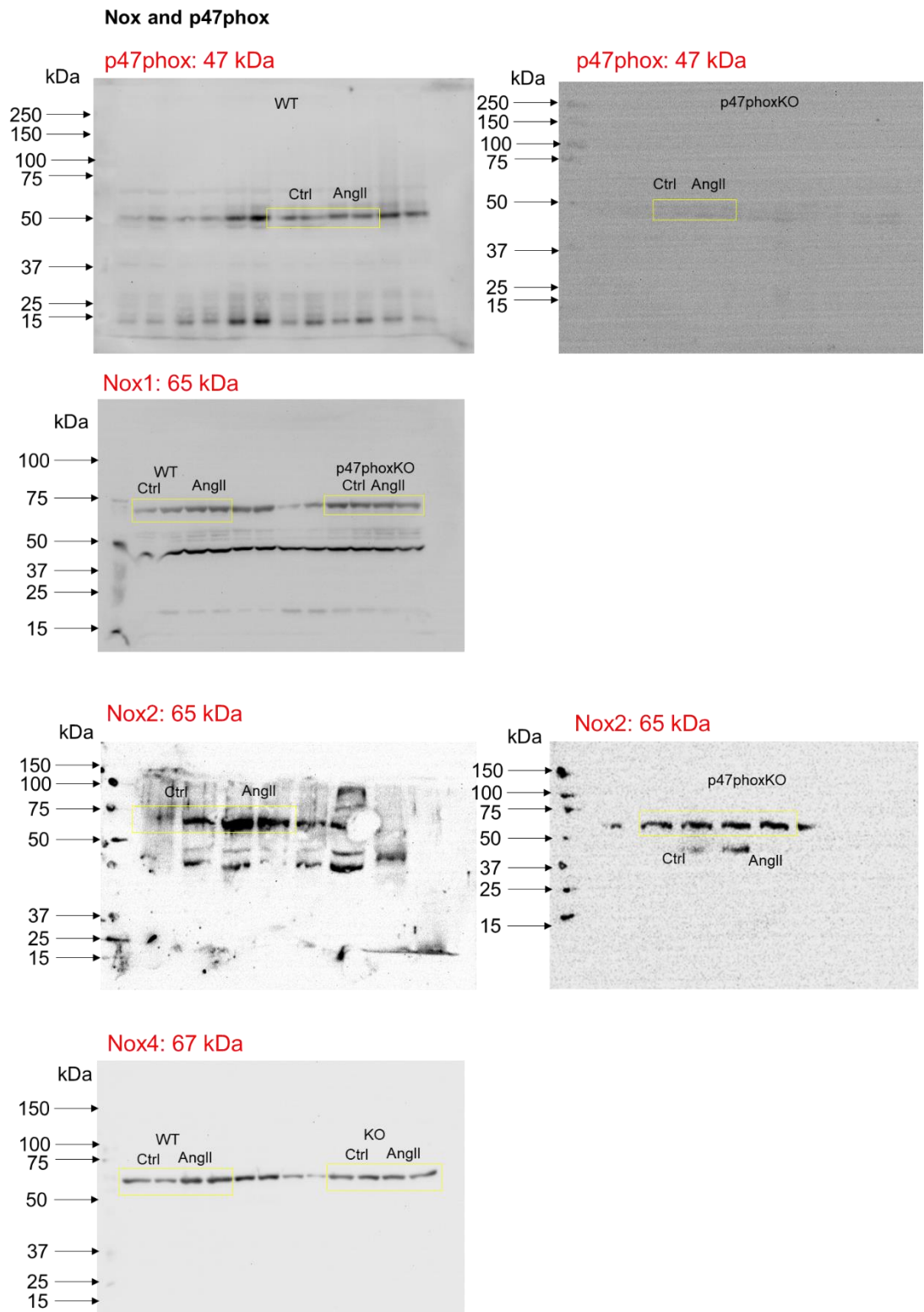


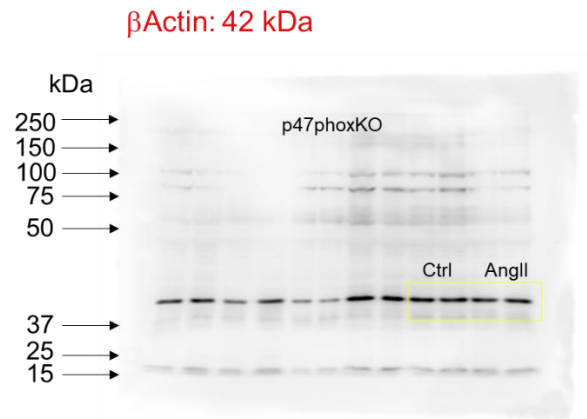
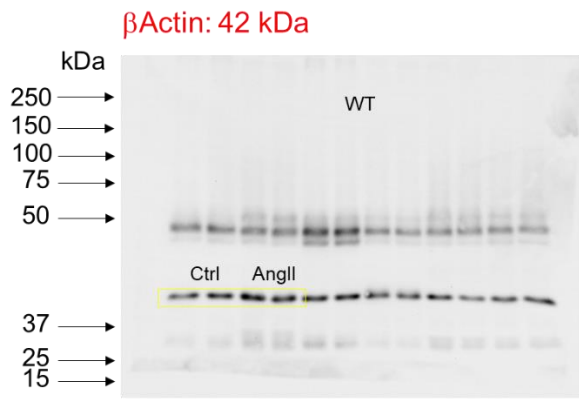
Appendix VI: Full-gel Western Blot Images for H9C2 cell Analysis





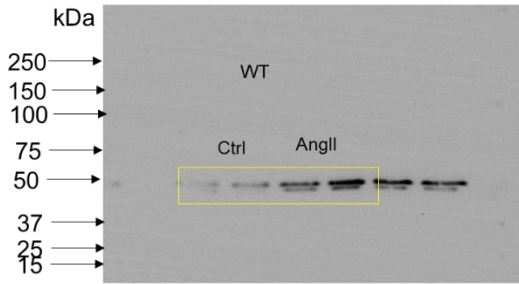
Appendix VII: Full-gel Western Blot Images for WT and KO Cardiac Homogenates



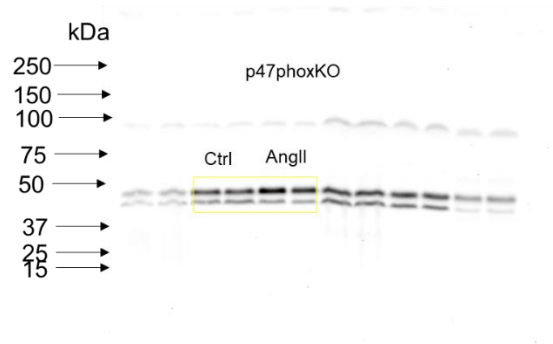


MAPK and ERK

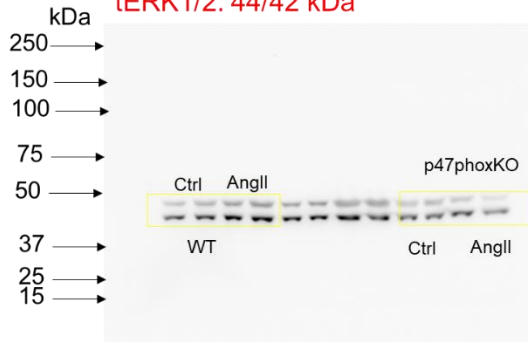
pERK1/2: 44/42 kDa



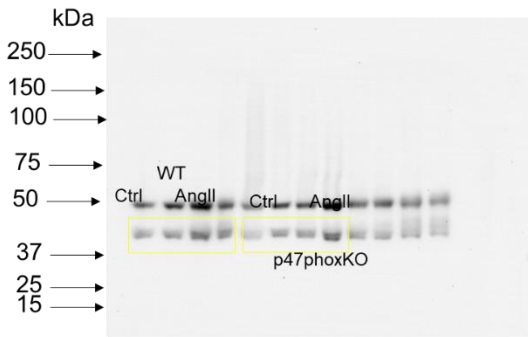
pERK1/2: 44/42 kDa



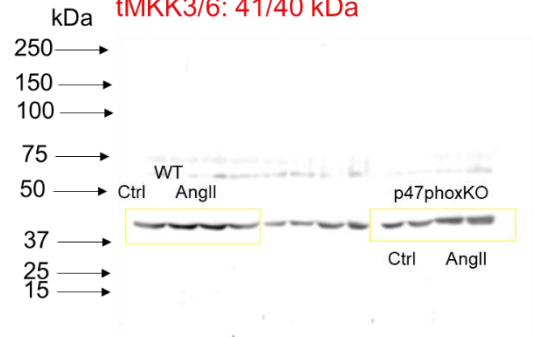
tERK1/2: 44/42 kDa



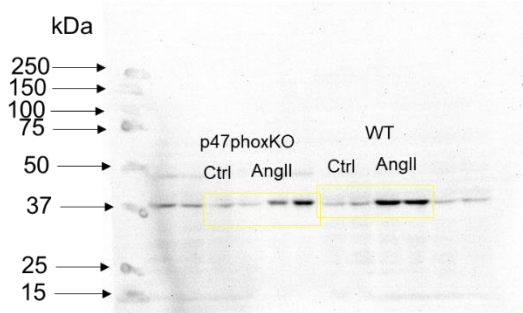
pMKK3/6: 41/40 kDa



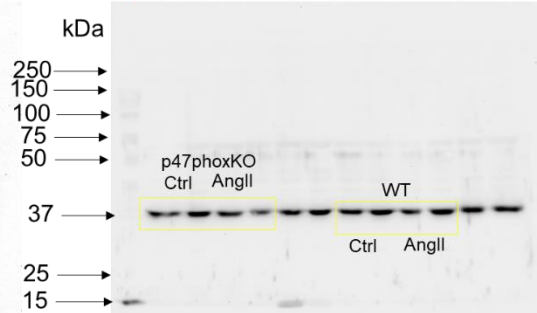
tMKK3/6: 41/40 kDa



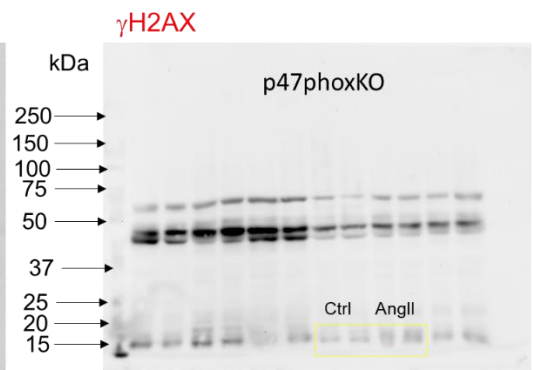
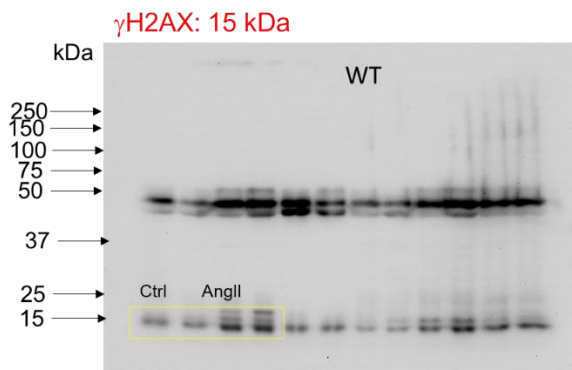
p-p38: 43 kDa



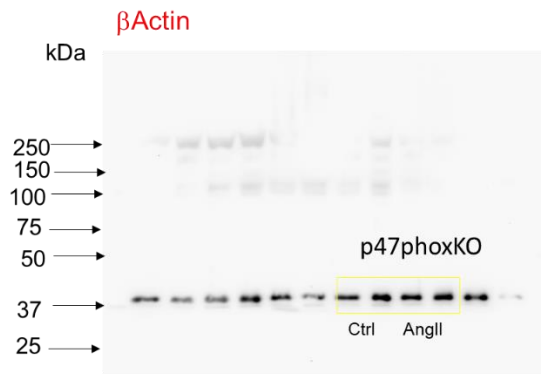
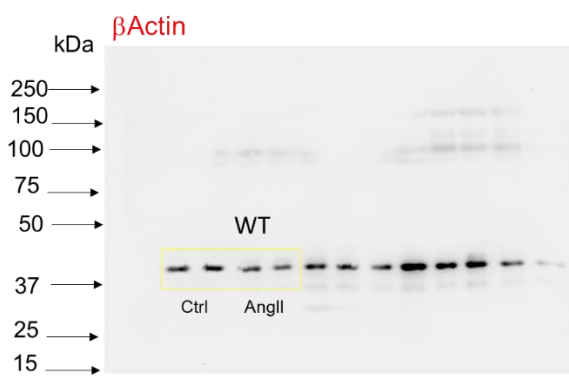
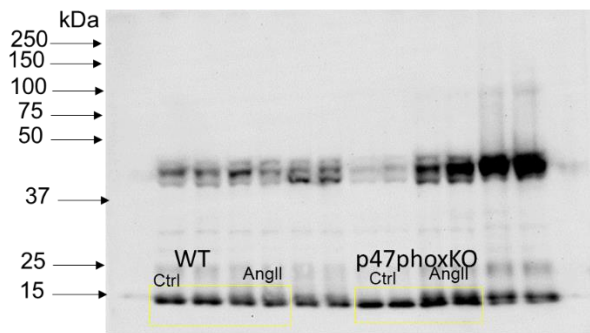
p38: 43 kDa



γ H2AX



H2AX: 15 kDa



Reference

- Abid MR, Schoots IG, Spokes KC, Wu SQ, Mawhinney C, & Aird WC (2004). Vascular endothelial growth factor-mediated induction of manganese superoxide dismutase occurs through redox-dependent regulation of forkhead and I kappa B/NF-kappa B. *Journal of Biological Chemistry* 279: 44030-44038.
- Acharya G, Huhta JC, Haapsamo M, How OJ, Erkinaro T, & Rasanen J (2011). Effect of angiotensin II on the left ventricular function in a near-term fetal sheep with metabolic acidemia. *J Pregnancy* 2011: 634240.
- Afanas'ev IB, Ostrakhovitch EA, Mikhal'chik EV, & Korkina LG (2001). Direct enzymatic reduction of lucigenin decreases lucigenin-amplified chemiluminescence produced by superoxide ion. *Luminescence* 16: 305-307.
- Afridi I, Canny J, Yao CH, Christensen B, Cooper RS, Kadiri S, *et al.* (2003). 2003 World Health Organization (WHO)/International Society of Hypertension (ISH) statement on management of hypertension. *J Hypertens* 21: 1983-1992.
- Ago T, Kitazono T, Kuroda J, Kumai Y, Kamouchi M, Ooboshi H, *et al.* (2005). NAD(P)H oxidases in rat basilar arterial endothelial cells. *Stroke* 36: 1040-1046.
- Ago T, Takeya R, Hiroaki H, Kuribayashi F, Ito T, Kohda D, *et al.* (2001). The PX domain as a novel phosphoinositide-binding module. *Biochem Biophys Res Commun* 287: 733-738.
- Aguiar C, Duarte R, & Carvalho D (2019). New approach to diabetes care: from blood glucose to cardiovascular disease. *Rev Port Cardiol* 38: 53-63.
- Al Ghoulh I, Meijles DN, Mutchler S, Zhang QM, Sahoo S, Gorelova A, *et al.* (2016). Binding of EBP50 to Nox organizing subunit p47(phox) is pivotal to cellular reactive species generation and altered vascular phenotype. *Proc Natl Acad Sci USA* 113: E5308-E5317.
- Aldieri E, Riganti C, Polimeni M, Gazzano E, Lussiana C, Campia I, *et al.* (2008). Classical inhibitors of NOX NAD(P)H oxidases are not specific. *Curr Drug Metab* 9: 686-696.
- Ali J, Camilleri P, Brown MB, Hutt AJ, & Kirton SB (2012). Revisiting the general solubility equation: in silico prediction of aqueous solubility incorporating the effect of topographical polar surface area. *J Chem Inf Model* 52: 420-428.

Allen RC (1986). Phagocytic Leukocyte Oxygenation Activities and Chemiluminescence - a Kinetic Approach to Analysis. *Method Enzymol* 133: 449-493.

Alp NJ, & Channon KM (2004). Regulation of endothelial nitric oxide synthase by tetrahydrobiopterin in vascular disease. *Arterioscl Throm Vas* 24: 413-420.

Altenhofer S, Radermacher KA, Kleikers PW, Wingler K, & Schmidt HH (2015). Evolution of NADPH Oxidase Inhibitors: Selectivity and Mechanisms for Target Engagement. *Antioxid Redox Signal* 23: 406-427.

Andes D, & Craig WA (2002). Animal model pharmacokinetics and pharmacodynamics: a critical review. *Int J Antimicrob Agents* 19: 261-268.

Arakaki N, Yamashita A, Niimi S, & Yamazaki T (2013). Involvement of reactive oxygen species in osteoblastic differentiation of MC3T3-E1 cells accompanied by mitochondrial morphological dynamics. *Biomed Res* 34: 161-166.

Arbiser JL, Petros J, Klafter R, Govindajaran B, McLaughlin ER, Brown LF, *et al.* (2002). Reactive oxygen generated by Nox1 triggers the angiogenic switch. *Proc Natl Acad Sci U S A* 99: 715-720.

Armbruster DA, & Pry T (2008). Limit of blank, limit of detection and limit of quantitation. *Clin Biochem Rev* 29 Suppl 1: S49-52.

Augsburger F, Filippova A, Rasti D, Seredenina T, Lam M, Maghzal G, *et al.* (2019). Pharmacological characterization of the seven human NOX isoforms and their inhibitors. *Redox Biol* 26: 101272.

Babior BM (1999). NADPH oxidase: an update. *Blood* 93: 1464-1476.

Baillie TA (2008). Metabolism and toxicity of drugs. Two decades of progress in industrial drug metabolism. *Chem Res Toxicol* 21: 129-137.

Ballard-Croft C, Locklar AC, Keith BJ, Mentzer RM, Jr., & Lasley RD (2008). Oxidative stress and adenosine A1 receptor activation differentially modulate subcellular cardiomyocyte MAPKs. *Am J Physiol Heart Circ Physiol* 294: H263-271.

Banerjee ER, & Henderson WR, Jr. (2012). Defining the molecular role of gp91phox in the immune manifestation of acute allergic asthma using a preclinical murine model. *Clin Mol Allergy* 10: 2.

Banfi B, Molnar G, Maturana A, Steger K, Hegedus B, Demaurex N, *et al.* (2001). A Ca²⁺-activated NADPH oxidase in testis, spleen, and lymph nodes. *Journal of Biological Chemistry* 276: 37594-37601.

Barbieri SS, Cavalca V, Eligini S, Brambilla M, Caiani A, Tremoli E, *et al.* (2004). Apocynin prevents cyclooxygenase 2 expression in human monocytes through NADPH oxidase and glutathione redox-dependent mechanisms. *Free Radic Biol Med* 37: 156-165.

Barr JT, Tran TB, Rock BM, Wahlstrom JL, & Dahal UP (2020). Strain-Dependent Variability of Early Discovery Small Molecule Pharmacokinetics in Mice: Does Strain Matter? *Drug Metab Dispos* 48: 613-621.

Barry-Lane PA, Patterson C, van der Merwe M, Hu ZY, Holland SM, Yeh ETH, *et al.* (2001). p47phox is required for atherosclerotic lesion progression in ApoE(-/-) mice. *Journal of Clinical Investigation* 108: 1513-1522.

Bartolome F, & Abramov AY (2015). Measurement of mitochondrial NADH and FAD autofluorescence in live cells. *Methods Mol Biol* 1264: 263-270.

Bedard K, & Krause KH (2007). The NOX family of ROS-generating NADPH oxidases: Physiology and pathophysiology. *Physiol Rev* 87: 245-313.

Beels L, Bacher K, De Wolf D, Werbrouck J, & Thierens H (2009). gamma-H2AX Foci as a Biomarker for Patient X-Ray Exposure in Pediatric Cardiac Catheterization Are We Underestimating Radiation Risks? *Circulation* 120: 1903-1909.

Bell RM, Cave AC, Johar S, Hearse DJ, Shah AM, & Shattock MJ (2005). Pivotal role of NOX-2-containing NADPH oxidase in early ischemic preconditioning. *Faseb J* 19: 2037-+.

Bendall JK, Cave AC, Heymes C, Gall N, & Shah AM (2002). Pivotal role of a gp91(phox)-containing NADPH oxidase in angiotensin II-induced cardiac hypertrophy in mice. *Circulation* 105: 293-296.

Benet LZ, & Zia-Amirhosseini P (1995). Basic principles of pharmacokinetics. *Toxicol Pathol* 23: 115-123.

Bensley JG, De Matteo R, Harding R, & Black MJ (2016). Three-dimensional direct measurement of cardiomyocyte volume, nuclearity, and ploidy in thick histological sections. *Sci Rep* 6: 23756.

Berk BC (1999). Angiotensin II signal transduction in vascular smooth muscle: pathways activated by specific tyrosine kinases. *J Am Soc Nephrol* 10 Suppl 11: S62-68.

Bertrand J, Comets E, & Mentre F (2008). Comparison of model-based tests and selection strategies to detect genetic polymorphisms influencing pharmacokinetic parameters. *J Biopharm Stat* 18: 1084-1102.

Bey EA, & Cathcart MK (1999). Regulation of phosphorylation and translocation of p47phox, a cytosolic component of the respiratory burst oxidase, in human monocytes. *Circulation* 100: 408-408.

Bhandarkar SS, Jaconi M, Fried LE, Bonner MY, Lefkove B, Govindarajan B, *et al.* (2009). Fulvene-5 potently inhibits NADPH oxidase 4 and blocks the growth of endothelial tumors in mice. *J Clin Invest* 119: 2359-2365.

Bhatt DL, & Pashkow FJ (2008). Introduction. Oxidative stress and heart disease. *Am J Cardiol* 101: 1D-2D.

Bodiga S, Zhong JC, Wang W, Basu R, Lo J, Liu GC, *et al.* (2011). Enhanced susceptibility to biomechanical stress in ACE2 null mice is prevented by loss of the p47(phox) NADPH oxidase subunit. *Cardiovasc Res* 91: 151-161.

Bokoch GM, & Diebold BA (2002). Current molecular models for NADPH oxidase regulation by Rac GTPase. *Blood* 100: 2692-2696.

Bonate PL, & Howard D (2004) *Pharmacokinetics in drug development*. AAPS Press: Arlington, VA.

Borchi E, Parri M, Papucci L, Becatti M, Nassi N, Nassi P, *et al.* (2009). Role of NADPH oxidase in H9c2 cardiac muscle cells exposed to simulated ischaemia-reperfusion. *J Cell Mol Med* 13: 2724-2735.

Bouin AP, Grandvaux N, Vignais PV, & Fuchs A (1998). p40(phox) is phosphorylated on threonine 154 and serine 315 during activation of the phagocyte NADPH oxidase. Implication of a protein kinase c-type kinase in the phosphorylation process. *J Biol Chem* 273: 30097-30103.

Boulanger CM, Scoazec A, Ebrahimian T, Henry P, Mathieu E, Tedgui A, *et al.* (2001). Circulating microparticles from patients with myocardial infarction cause endothelial dysfunction. *Circulation* 104: 2649-2652.

Brancho D, Tanaka N, Jaeschke A, Ventura JJ, Kelkar N, Tanaka Y, *et al.* (2003). Mechanism of p38 MAP kinase activation in vivo. *Genes Dev* 17: 1969-1978.

Braunersreuther V, Montecucco F, Asrih M, Pelli G, Galan K, Frias M, *et al.* (2013). Role of NADPH oxidase isoforms NOX1, NOX2 and NOX4 in myocardial ischemia/reperfusion injury. *J Mol Cell Cardiol* 64: 99-107.

Bravo J, Karathanassis D, Pacold CM, Pacold ME, Ellson CD, Anderson KE, *et al.* (2001). The crystal structure of the PX domain from p40(phox) bound to phosphatidylinositol 3-phosphate. *Molecular Cell* 8: 829-839.

Broome M, Haney M, Haggmark S, Johansson G, Aneman A, & Biber B (2004). Pressure-independent cardiac effects of angiotensin II in pigs. *Acta Physiol Scand* 182: 111-119.

Brown BG, Zhao XQ, Chait A, Fisher LD, Cheung MC, Morse JS, *et al.* (2001). Simvastatin and niacin, antioxidant vitamins, or the combination for the prevention of coronary disease. *N Engl J Med* 345: 1583-1592.

Burnette WN (1981). Western Blotting - Electrophoretic Transfer of Proteins from Sodium Dodecyl Sulfate-Polyacrylamide Gels to Unmodified Nitrocellulose and Radiographic Detection with Antibody and Radioiodinated Protein-A. *Anal Biochem* 112: 195-203.

Buscher B, Laakso S, Mascher H, Pusecker K, Doig M, Dillen L, *et al.* (2014). Bioanalysis for plasma protein binding studies in drug discovery and drug development: views and recommendations of the European Bioanalysis Forum. *Bioanalysis* 6: 673-682.

Byrne JA, Grieve DJ, Bendall JK, Li JM, Gove C, Lambeth JD, *et al.* (2003). Contrasting roles of NADPH oxidase isoforms in pressure-overload versus angiotensin II-induced cardiac hypertrophy. *Circ Res* 93: 802-805.

Cahill-Smith S, & Li JM (2014). Oxidative stress, redox signalling and endothelial dysfunction in ageing-related neurodegenerative diseases: a role of NADPH oxidase 2. *Br J Clin Pharmacol* 78: 441-453.

Cao M, Mao Z, Peng M, Zhao Q, Sun X, Yan J, *et al.* (2020). Extracellular cyclophilin A induces cardiac hypertrophy via the ERK/p47phox pathway. *Mol Cell Endocrinol*: 110990.

Cao TT, Chen HH, Dong Z, Xu YW, Zhao P, Guo W, *et al.* (2017). Stachydrine Protects Against Pressure Overload-Induced Cardiac Hypertrophy by Suppressing Autophagy. *Cell Physiol Biochem* 42: 103-114.

Capra V, Back M, Angiolillo DJ, Cattaneo M, & Sakariassen KS (2014). Impact of vascular thromboxane prostanoid receptor activation on hemostasis, thrombosis, oxidative stress, and inflammation. *J Thromb Haemost* 12: 126-137.

Carreno JE, Apablaza F, Ocaranza MP, & Jalil JE (2006). Cardiac hypertrophy: molecular and cellular events. *Rev Esp Cardiol* 59: 473-486.

Carrim N, Arthur JF, Hamilton JR, Gardiner EE, Andrews RK, Moran N, *et al.* (2015). Thrombin-induced reactive oxygen species generation in platelets: A novel role for protease-activated receptor 4 and GPIIb/IIIa. *Redox Biol* 6: 640-647.

Castor LRG, Locatelli KA, & Ximenes VF (2010). Pro-oxidant activity of apocynin radical. *Free Radical Bio Med* 48: 1636-1643.

Catt KJ, Zimmet PZ, Cain MD, Cran E, Best JB, & Coghlan JP (1971). Angiotensin-II Blood-Levels in Human Hypertension. *Lancet* 1: 459-&.

Cave AC, Brewer AC, Narayanapanicker A, Ray R, Grieve DJ, Walker S, *et al.* (2006). NADPH oxidases in cardiovascular health and disease. *Antioxid Redox Signal* 8: 691-728.

Chan SL, & Baumbach GL (2013). Deficiency of Nox2 prevents angiotensin II-induced inward remodeling in cerebral arterioles. *Front Physiol* 4: 133.

Chandasana H, Chhonker YS, Bala V, Prasad YD, Chaitanya TK, Sharma VL, *et al.* (2015). Pharmacokinetic, bioavailability, metabolism and plasma protein binding evaluation of NADPH-oxidase inhibitor apocynin using LC-MS/MS. *J Chromatogr B Analyt Technol Biomed Life Sci* 985: 180-188.

Chen JK, Shen CR, & Liu CL (2010). N-acetylglucosamine: production and applications. *Mar Drugs* 8: 2493-2516.

Chen K, Bai H, Arzigian M, Gao YX, Bao J, Wu WS, *et al.* (2010). Endothelial cells regulate cardiomyocyte development from embryonic stem cells. *J Cell Biochem* 111: 29-39.

Cheng G, Cao Z, Xu X, van Meir EG, & Lambeth JD (2001). Homologs of gp91phox: cloning and tissue expression of Nox3, Nox4, and Nox5. *Gene* 269: 131-140.

Chernushevich IV, Loboda AV, & Thomson BA (2001). An introduction to quadrupole-time-of-flight mass spectrometry. *Journal of Mass Spectrometry* 36: 849-865.

Chiou CT (2002) Partition and adsorption of organic contaminants in environmental systems. Wiley-Interscience: Hoboken, N.J.

Chiriaco M, Salfa I, Di Matteo G, Rossi P, & Finocchi A (2016). Chronic granulomatous disease: Clinical, molecular, and therapeutic aspects. *Pediatr Allerg Imm-Uk* 27: 242-253.

Cho KJ, Seo JM, & Kim JH (2011). Bioactive lipoxygenase metabolites stimulation of NADPH oxidases and reactive oxygen species. *Mol Cells* 32: 1-5.

Chose O, Sansilvestri-Morel P, Badier-Commander C, Bernhardt F, Tabiani DN, Rupin A, *et al.* (2008). Distinct role of nox1, nox2, and p47(phox) in unstimulated versus angiotensin II-induced NADPH oxidase activity in human venous smooth muscle cells. *J Cardiovasc Pharm* 51: 131-139.

Christensen FH, Stankevicius E, Hansen T, Jorgensen MM, Valverde VL, Simonsen U, *et al.* (2007). Flow- and acetylcholine-induced dilatation in small arteries from rats with renovascular hypertension--effect of tempol treatment. *Eur J Pharmacol* 566: 160-166.

Chung HY, Baek BS, Song SH, Kim MS, Huh JI, Shim KH, *et al.* (1997). Xanthine dehydrogenase xanthine oxidase and oxidative stress. *Age* 20: 127-140.

Chwa M, Atilano SR, Reddy V, Jordan N, Kim DW, & Kenney MC (2006). Increased stress-induced generation of reactive oxygen species and apoptosis in human keratoconus fibroblasts. *Invest Ophthalmol Vis Sci* 47: 1902-1910.

Cifuentes-Pagano E, Csanyi G, & Pagano PJ (2012). NADPH oxidase inhibitors: a decade of discovery from Nox2ds to HTS. *Cell Mol Life Sci* 69: 2315-2325.

Clark DE (1999). Rapid calculation of polar molecular surface area and its application to the prediction of transport phenomena. 2. Prediction of blood-brain barrier penetration. *J Pharm Sci* 88: 815-821.

Coelho JC, Ferretti-Rebustini REL, Suemoto CK, Leite REP, Jacob-Filho W, & Pierin AMG (2019). Hypertension is the underlying cause of death assessed at the autopsy of individuals. *Rev Esc Enferm USP* 53: e03457.

Coghill D, Banaschewski T, Zuddas A, Pelaz A, Gagliano A, & Doepfner M (2013). Long-acting methylphenidate formulations in the treatment of attention-deficit/hyperactivity disorder: a systematic review of head-to-head studies. *BMC Psychiatry* 13: 237.

Coghill D, Banaschewski T, Zuddas A, Pelaz A, Gagliano A, & Doepfner M (2015). Erratum to: Long-acting methylphenidate formulations in the treatment of attention-

deficit/hyperactivity disorder: a systematic review of head-to-head studies. *BMC Psychiatry* 15: 202.

Cohn JN, Ferrari R, & Sharpe N (2000). Cardiac remodeling--concepts and clinical implications: a consensus paper from an international forum on cardiac remodeling. Behalf of an International Forum on Cardiac Remodeling. *J Am Coll Cardiol* 35: 569-582.

Colliva A, Braga L, Giacca M, & Zacchigna S (2019). Endothelial cell-cardiomyocyte crosstalk in heart development and disease. *J Physiol*.

Condorelli G, Borello U, De Angelis L, Latronico M, Sirabella D, Coletta M, *et al.* (2001). Cardiomyocytes induce endothelial cells to trans-differentiate into cardiac muscle: implications for myocardium regeneration. *Proc Natl Acad Sci U S A* 98: 10733-10738.

Cortese S, D'Acunto G, Konofal E, Masi G, & Vitiello B (2017). New Formulations of Methylphenidate for the Treatment of Attention-Deficit/Hyperactivity Disorder: Pharmacokinetics, Efficacy, and Tolerability. *CNS Drugs* 31: 149-160.

Cranwell PB, Harwood LM, & Moody CJ (2017) *Experimental organic chemistry / Philippa B. Cranwell, Laurence M. Harwood, Christopher J. Moody*. John Wiley & Sons., Hoboken, NJ.

Crowley SD, Gurley SB, Herrera MJ, Ruiz P, Griffiths R, Kumar AP, *et al.* (2006). Angiotensin II causes hypertension and cardiac hypertrophy through its receptors in the kidney. *P Natl Acad Sci USA* 103: 17985-17990.

Cruz-Magalhaes V, Nieto-Jacobo MF, van Zijll de Jong E, Rostas M, Padilla-Arizmendi F, Kandula D, *et al.* (2018). The NADPH Oxidases Nox1 and Nox2 Differentially Regulate Volatile Organic Compounds, Fungistatic Activity, Plant Growth Promotion and Nutrient Assimilation in *Trichoderma atroviride*. *Front Microbiol* 9: 3271.

Cruzado M, Touyz RM, Tabet F, Yao GY, & Schiffrin EL (2002). Redox-dependent MAP kinase signaling by Ang II in vascular smooth muscle cells - Role of tyrosine kinase receptor transactivation. *Hypertension* 40: 434-434.

Csanyi G, Cifuentes-Pagano E, Al Ghouleh I, Ranayhossaini DJ, Egana L, Lopes LR, *et al.* (2011). Nox2 B-loop peptide, Nox2ds, specifically inhibits the NADPH oxidase Nox2. *Free Radic Biol Med* 51: 1116-1125.

Cuspidi C, Facchetti R, Bombelli M, Tadic M, Sala C, Grassi G, *et al.* (2019). High Normal Blood Pressure and Left Ventricular Hypertrophy Echocardiographic Findings From the PAMELA Population. *Hypertension* 73: 612-619.

Cuspidi C, Facchetti R, Quarti-Trevano F, Dell'Oro R, Tadic M, Grassi G, *et al.* (2020). Left ventricular hypertrophy in isolated and dual masked hypertension. *J Clin Hypertens.*

D'Addio SM, & Prud'homme RK (2011). Controlling drug nanoparticle formation by rapid precipitation. *Adv Drug Deliv Rev* 63: 417-426.

da Silva PL, Guimaraes L, & Pliego JR, Jr. (2013). Revisiting the mechanism of neutral hydrolysis of esters: water autoionization mechanisms with acid or base initiation pathways. *J Phys Chem B* 117: 6487-6497.

Dahlof B (1995). Effect of Angiotensin-II Blockade on Cardiac-Hypertrophy and Remodeling - a Review. *Journal of Human Hypertension* 9: S37-S44.

Dang DK, Shin EJ, Nam Y, Ryoo S, Jeong JH, Jang CG, *et al.* (2016). Apocynin prevents mitochondrial burdens, microglial activation, and pro-apoptosis induced by a toxic dose of methamphetamine in the striatum of mice via inhibition of p47phox activation by ERK. *J Neuroinflammation* 13: 12.

Dang PM, Stensballe A, Boussetta T, Raad H, Dewas C, Kroviarski Y, *et al.* (2006). A specific p47phox -serine phosphorylated by convergent MAPKs mediates neutrophil NADPH oxidase priming at inflammatory sites. *J Clin Invest* 116: 2033-2043.

Dang PMC, Babior BM, & Smith RM (1999). NADPH dehydrogenase activity of p67(PHOX), a cytosolic subunit of the leukocyte NADPH oxidase. *Biochemistry* 38: 5746-5753.

Davidian M, & Gallant AR (1993). The Nonlinear Mixed Effects Model with a Smooth Random Effects Density. *Biometrika* 80: 475-488.

Davis NY, McPhail LC, & Horita DA (2011). Backbone ¹H, ¹⁵N, and ¹³C resonance assignments for the NOXO1beta PX domain. *Biomol NMR Assign* 5: 139-141.

Davis NY, McPhail LC, & Horita DA (2012). The NOXO1beta PX domain preferentially targets PtdIns(4,5)P₂ and PtdIns(3,4,5)P₃. *J Mol Biol* 417: 440-453.

De Ciuceis C, Amiri F, Brassard P, Endemann DH, Touyz RM, & Schiffrin EL (2005). Reduced vascular remodeling, endothelial dysfunction, and oxidative stress in resistance arteries of angiotensin II-infused macrophage colony-stimulating factor-

deficient mice: evidence for a role in inflammation in angiotensin-induced vascular injury. *Arterioscler Thromb Vasc Biol* 25: 2106-2113.

de Mendez I, Garrett MC, Adams AG, & Leto TL (1994). Role of p67-phox SH3 domains in assembly of the NADPH oxidase system. *J Biol Chem* 269: 16326-16332.

de Waart FG, Kok FJ, Smilde TJ, Hijmans A, Wollersheim H, & Stalenhoef AF (2001). Effect of glutathione S-transferase M1 genotype on progression of atherosclerosis in lifelong male smokers. *Atherosclerosis* 158: 227-231.

Del Re DP, Yang Y, Nakano N, Cho J, Zhai P, Yamamoto T, *et al.* (2013). Yes-associated protein isoform 1 (Yap1) promotes cardiomyocyte survival and growth to protect against myocardial ischemic injury. *J Biol Chem* 288: 3977-3988.

deMendez I, Adams AG, Sokolic RA, Malech HL, & Leto TL (1996). Multiple SH3 domain interactions regulate NADPH oxidase assembly in whole cells. *Embo J* 15: 1211-1220.

deMendez I, Homayounpour N, & Leto TL (1997). Specificity of p47(phox) SH3 domain interactions in NADPH oxidase assembly and activation. *Mol Cell Biol* 17: 2177-2185.

Derijard B, Raingeaud J, Barrett T, Wu IH, Han J, Ulevitch RJ, *et al.* (1995). Independent human MAP-kinase signal transduction pathways defined by MEK and MKK isoforms. *Science* 267: 682-685.

Di-Poi N, Faure J, Grizot S, Molnar G, Pick E, & Dagher MC (2001). Mechanism of NADPH oxidase activation by the Rac/Rho-GDI complex. *Biochemistry* 40: 10014-10022.

Diatchuk V, Lotan O, Koshkin V, Wikstroem P, & Pick E (1997). Inhibition of NADPH oxidase activation by 4-(2-aminoethyl)-benzenesulfonyl fluoride and related compounds. *J Biol Chem* 272: 13292-13301.

Didichenko SA, Tilton B, Hemmings BA, Ballmer-Hofer K, & Thelen M (1996). Constitutive activation of protein kinase B and phosphorylation of p47phox by a membrane-targeted phosphoinositide 3-kinase. *Curr Biol* 6: 1271-1278.

Diebold BA, & Bokoch GM (2001). Molecular basis for Rac2 regulation of phagocyte NADPH oxidase. *Nat Immunol* 2: 211-215.

Diffie GM, Seversen EA, Stein TD, & Johnson JA (2003). Microarray expression analysis of effects of exercise training: increase in atrial MLC-1 in rat ventricles. *Am J Physiol-Heart C* 284: H830-H837.

Dikalov SI, & Nazarewicz RR (2013). Angiotensin II-induced production of mitochondrial reactive oxygen species: potential mechanisms and relevance for cardiovascular disease. *Antioxid Redox Signal* 19: 1085-1094.

Dikalova A, Clempus R, Lassegue B, Cheng G, McCoy J, Dikalov S, *et al.* (2005). Nox1 overexpression potentiates angiotensin II-induced hypertension and vascular smooth muscle hypertrophy in transgenic mice. *Circulation* 112: 2668-2676.

Dinauer MC, Curnutte JT, Rosen H, & Orkin SH (1989). A Missense Mutation in the Neutrophil Cytochrome-B Heavy-Chain in Cytochrome-Positive X-Linked Chronic Granulomatous-Disease. *Journal of Clinical Investigation* 84: 2012-2016.

Dodge JT, Jr., Brown BG, Bolson EL, & Dodge HT (1992). Lumen diameter of normal human coronary arteries. Influence of age, sex, anatomic variation, and left ventricular hypertrophy or dilation. *Circulation* 86: 232-246.

Doerries C, Grote K, Hilfiker-Kleiner D, Luchtefeld M, Schaefer A, Holland SM, *et al.* (2007). Critical role of the NAD(P)H oxidase subunit p47^{phox} for left ventricular remodeling/dysfunction and survival after myocardial infarction. *Circ Res* 100: 894-903.

Donaldson M, Antignani A, Milner J, Zhu N, Wood A, Cardwell-Miller L, *et al.* (2009). p47^(phox)-deficient immune microenvironment signals dysregulate naive T-cell apoptosis. *Cell Death and Differentiation* 16: 125-138.

Doughan AK, Harrison DG, & Dikalov SI (2008). Molecular mechanisms of angiotensin II-mediated mitochondrial dysfunction - Linking mitochondrial oxidative damage and vascular endothelial dysfunction. *Circulation Research* 102: 488-496.

Dranka BP, Gifford A, McAllister D, Zielonka J, Joseph J, O'Hara CL, *et al.* (2014). A novel mitochondrially-targeted apocynin derivative prevents hyposmia and loss of motor function in the leucine-rich repeat kinase 2 (LRRK2(R1441G)) transgenic mouse model of Parkinson's disease. *Neurosci Lett* 583: 159-164.

Drayer JIM, Gardin JM, & Weber MA (1983). Echocardiographic Left-Ventricular Hypertrophy in Hypertension. *Chest* 84: 217-221.

Drikvandi R (2017). Nonlinear mixed-effects models for pharmacokinetic data analysis: assessment of the random-effects distribution. *J Pharmacokinet Pharmacodyn* 44: 223-232.

Drummond GR, Selemidis S, Griendling KK, & Sobey CG (2011). Combating oxidative stress in vascular disease: NADPH oxidases as therapeutic targets. *Nat Rev Drug Discov* 10: 453-471.

Du JJ, Fan LM, Mai A, & Li JM (2013). Crucial roles of Nox2-derived oxidative stress in deteriorating the function of insulin receptors and endothelium in dietary obesity of middle-aged mice. *Brit J Pharmacol* 170: 1064-1077.

Dunn FG, & Pringle SD (1987). Left-Ventricular Hypertrophy and Myocardial Ischemia in Systemic Hypertension. *Am J Cardiol* 60: I19-I22.

Dutta S, & Rittinger K (2010). Regulation of NOXO1 Activity through Reversible Interactions with p22(phox) and NOXA1. *Plos One* 5.

Ebrahimian T, Li MW, Lemarie CA, Simeone SMC, Pagano PJ, Gaestel M, *et al.* (2011). Mitogen-Activated Protein Kinase-Activated Protein Kinase 2 in Angiotensin II-Induced Inflammation and Hypertension Regulation of Oxidative Stress. *Hypertension* 57: 245-254.

Eguchi K, Boden-Albala B, Jin ZZ, Rundek T, Sacco RL, Homma S, *et al.* (2008). Association between diabetes mellitus and left ventricular hypertrophy in a multiethnic population. *Am J Cardiol* 101: 1787-1791.

El-Awady MS, Rajamani U, Teng B, Tilley SL, & Mustafa SJ (2013). Evidence for the involvement of NADPH oxidase in adenosine receptors-mediated control of coronary flow using A1 and A3 knockout mice. *Physiol Rep* 1: e00070.

El-Benna J, Dang PM, Gougerot-Pocidalo MA, Marie JC, & Braut-Boucher F (2009). p47phox, the phagocyte NADPH oxidase/NOX2 organizer: structure, phosphorylation and implication in diseases. *Exp Mol Med* 41: 217-225.

El Benna J, Faust LP, & Babior BM (1994). The phosphorylation of the respiratory burst oxidase component p47phox during neutrophil activation. Phosphorylation of sites recognized by protein kinase C and by proline-directed kinases. *The Journal of biological chemistry* 269: 23431-23436.

Ellson CD, Gobert-Gosse S, Anderson KE, Davidson K, Erdjument-Bromage H, Tempst P, *et al.* (2001). PtdIns(3)P regulates the neutrophil oxidase complex by binding to the PX domain of p40(phox). *Nature Cell Biology* 3: 679-682.

Ernst LA, Gupta RK, Mujumdar RB, & Waggoner AS (1989). Cyanine Dye Labeling Reagents for Sulfhydryl-Groups. *Cytometry* 10: 3-10.

Falk E (2006). Pathogenesis of atherosclerosis. *J Am Coll Cardiol* 47: C7-12.

Fan LM, Cahill-Smith S, Geng L, Du J, Brooks G, & Li JM (2017). Aging-associated metabolic disorder induces Nox2 activation and oxidative damage of endothelial function. *Free Radic Biol Med* 108: 940-951.

Fan LM, Douglas G, Bendall JK, McNeill E, Crabtree MJ, Hale AB, *et al.* (2014). Endothelial cell-specific reactive oxygen species production increases susceptibility to aortic dissection. *Circulation* 129: 2661-2672.

Fan LM, Geng L, Cahill-Smith S, Liu F, Douglas G, McKenzie CA, *et al.* (2019). Nox2 contributes to age-related oxidative damage to neurons and the cerebral vasculature. *J Clin Invest* 129: 3374-3386.

Fan LM, & Li JM (2014). Evaluation of methods of detecting cell reactive oxygen species production for drug screening and cell cycle studies. *J Pharmacol Tox Met* 70: 40-47.

Fan LM, Teng L, & Li JM (2009). Knockout of p47 phox uncovers a critical role of p40 phox in reactive oxygen species production in microvascular endothelial cells. *Arterioscler Thromb Vasc Biol* 29: 1651-1656.

Fang JC, Kinlay S, Beltrame J, Hikiti H, Wainstein M, Behrendt D, *et al.* (2002). Effect of vitamins C and E on progression of transplant-associated arteriosclerosis: a randomised trial. *Lancet* 359: 1108-1113.

Farthing D, Karnes T, Gehr TW, March C, Fakhry I, & Sica DA (1992). External-standard high-performance liquid chromatographic method for quantitative determination of furosemide in plasma by using solid-phase extraction and on-line elution. *J Pharm Sci* 81: 569-571.

Faulkner K, & Fridovich I (1993). Luminol and Lucigenin as Detectors for O₂⁻. *Free Radical Bio Med* 15: 447-451.

Fearon IM, & Faux SP (2009). Oxidative stress and cardiovascular disease: Novel tools give (free) radical insight. *Journal of Molecular and Cellular Cardiology* 47: 372-381.

Feng Y, Cui C, Liu X, Wu Q, Hu F, Zhang H, *et al.* (2017). Protective Role of Apocynin via Suppression of Neuronal Autophagy and TLR4/NF-kappaB Signaling Pathway in a Rat Model of Traumatic Brain Injury. *Neurochem Res* 42: 3296-3309.

Fersht AR, & Kirby AJ (1967). The hydrolysis of aspirin. Intramolecular general base catalysis of ester hydrolysis. *J Am Chem Soc* 89: 4857-4863.

Finan P, Koga H, Zvelebil MJ, Waterfield MD, & Kellie S (1996). The C-terminal SH3 domain of p67phox binds its natural ligand in a reverse orientation. *J Mol Biol* 261: 173-180.

Fisher AB (2009). Redox signaling across cell membranes. *Antioxid Redox Signal* 11: 1349-1356.

Folmer V, Santos FW, Savegnago L, Brito VB, Nogueira CW, & Rocha JBT (2004). High sucrose consumption potentiates the sub-acute cadmium effect on Na⁺/K⁺-ATPase but not on delta-aminolevulinate dehydratase in mice. *Toxicology Letters* 153: 333-341.

Fontayne A, Dang PM, Gougerot-Pocidalo MA, & El-Benna J (2002). Phosphorylation of p47phox sites by PKC alpha, beta II, delta, and zeta: effect on binding to p22phox and on NADPH oxidase activation. *Biochemistry* 41: 7743-7750.

Forrester SJ, Booz GW, Sigmund CD, Coffman TM, Kawai T, Rizzo V. (2018). Angiotensin II Signal Transduction: An Update on Mechanisms of Physiology and Pathophysiology. *Physiol Rev* 98: 1627-1738.

Forrester SJ, Kikuchi DS, Hernandez MS, Xu Q, & Griendling KK (2018). Reactive Oxygen Species in Metabolic and Inflammatory Signaling. *Circ Res* 122: 877-902.

Forstermann U, Xia N, & Li H (2017). Roles of Vascular Oxidative Stress and Nitric Oxide in the Pathogenesis of Atherosclerosis. *Circ Res* 120: 713-735.

Forte M, Nocella C, De Falco E, Palmerio S, Schirone L, Valenti V, *et al.* (2016). The Pathophysiological Role of NOX2 in Hypertension and Organ Damage. *High Blood Press Cardiovasc Prev* 23: 355-364.

Foti K, Wang D, Appel LJ, & Selvin E (2019). Hypertension Awareness, Treatment, and Control in US Adults: Trends in the Hypertension Control Cascade by Population Subgroup (National Health and Nutrition Examination Survey, 1999-2016). *Am J Epidemiol* 188: 2165-2174.

Frangogiannis NG (2015). Pathophysiology of Myocardial Infarction. *Compr Physiol* 5: 1841-1875.

Frey N, Katus HA, Olson EN, & Hill JA (2004). Hypertrophy of the heart - A new therapeutic target? *Circulation* 109: 1580-1589.

Frohlich ED (1987). Cardiac hypertrophy in hypertension. *N Engl J Med* 317: 831-833.

Fukai T, & Ushio-Fukai M (2011). Superoxide dismutases: role in redox signaling, vascular function, and diseases. *Antioxid Redox Signal* 15: 1583-1606.

Funatogawa T, & Funatogawa I (2007). The bayesian bias correction method of the first-order approximation of nonlinear mixed-effects models for population pharmacokinetics. *J Biopharm Stat* 17: 381-392.

Fyhrquist F, Metsarinne K, & Tikkanen I (1995). Role of Angiotensin-Ii in Blood-Pressure Regulation and in the Pathophysiology of Cardiovascular Disorders. *Journal of Human Hypertension* 9: S19-S24.

Gabrielsson J (2016) *Pharmacokinetic and pharmacodynamic data analysis : concepts and applications*. 5th edition, revised and expanded. edn. Apotekarsocieteten: Stockholm.

Gabrielsson J, Weiner D, & Gabrielsson J (2006) *Pharmacokinetic & pharmacodynamic data analysis : concepts and applications*. 4th ed. rev. and expanded. edn. Apotekarsocieteten: [Stockholm].

Gatto GJ, Jr., Ao Z, Kears MG, Zhou M, Morales CR, Daniels E, *et al.* (2013). NADPH oxidase-dependent and -independent mechanisms of reported inhibitors of reactive oxygen generation. *J Enzyme Inhib Med Chem* 28: 95-104.

Gavrilov B, Vezhenkova I, Firsanov D, Solovjeva L, Svetlova M, Mikhailov V, *et al.* (2006). Slow elimination of phosphorylated histone gamma-H2AX from DNA of terminally differentiated mouse heart cells in situ. *Biochem Biophys Res Commun* 347: 1048-1052.

Geldenhuys WJ, Mohammad AS, Adkins CE, & Lockman PR (2015). Molecular determinants of blood-brain barrier permeation. *Ther Deliv* 6: 961-971.

Geng L, Fan LM, Liu F, Smith C, & Li J (2020). Nox2 dependent redox-regulation of microglial response to amyloid-beta stimulation and microgliosis in aging. *Sci Rep* 10: 1582.

Gerber AU, Brugger HP, Feller C, Stritzko T, & Stalder B (1986). Antibiotic therapy of infections due to *Pseudomonas aeruginosa* in normal and granulocytopenic mice: comparison of murine and human pharmacokinetics. *J Infect Dis* 153: 90-97.

Ghosh A, Langley MR, Harischandra DS, Neal ML, Jin H, Anantharam V, *et al.* (2016). Mitoapocynin Treatment Protects Against Neuroinflammation and Dopaminergic Neurodegeneration in a Preclinical Animal Model of Parkinson's Disease. *J Neuroimmune Pharmacol* 11: 259-278.

Ghosh R, Goswami SK, Feitoza LFBB, Hammock B, & Gomes AV (2016). Diclofenac induces proteasome and mitochondrial dysfunction in murine cardiomyocytes and hearts. *Int J Cardiol* 223: 923-935.

Gianni D, Diaz B, Taulet N, Fowler B, Courtneidge SA, & Bokoch GM (2009). Novel p47(phox)-related organizers regulate localized NADPH oxidase 1 (Nox1) activity. *Sci Signal* 2: ra54.

Gianni D, Taulet N, Zhang H, DerMardirossian C, Kister J, Martinez L, *et al.* (2010). A novel and specific NADPH oxidase-1 (Nox1) small-molecule inhibitor blocks the formation of functional invadopodia in human colon cancer cells. *ACS Chem Biol* 5: 981-993.

Gimenes R, Gimenes C, Rosa CM, Xavier NP, Campos DHS, Fernandes AAH, *et al.* (2018). Influence of apocynin on cardiac remodeling in rats with streptozotocin-induced diabetes mellitus. *Cardiovasc Diabetol* 17: 15.

Goncharov NV, Avdonin PV, Nadeev AD, Zharkikh IL, & Jenkins RO (2015). Reactive oxygen species in pathogenesis of atherosclerosis. *Curr Pharm Des* 21: 1134-1146.

Goto A, Abe S, Koshiha S, Yamaguchi K, Sato N, & Kurahashi Y (2019). Current status and future perspective on preclinical pharmacokinetic and pharmacodynamic (PK/PD) analysis: Survey in Japan pharmaceutical manufacturers association (JPMA). *Drug Metab Pharmacokinet* 34: 148-154.

Greco TG, Rickard LH, Weiss GS, & Petrucci RH (2007) *Experiments in General chemistry--principles & modern applications*, Petrucci, Harwood, Herring, Madura. 9th edn. Pearson Prentice Hall: Upper Saddle River, NJ.

Griendling KK, Touyz RM, Zweier JL, Dikalov S, Chilian W, Chen YR, *et al.* (2016). Measurement of Reactive Oxygen Species, Reactive Nitrogen Species, and Redox-Dependent Signaling in the Cardiovascular System: A Scientific Statement From the American Heart Association. *Circ Res* 119: e39-75.

Griendling KK, & Ushio-Fukai M (2000). Reactive oxygen species as mediators of angiotensin II signaling. *Regul Peptides* 91: 21-27.

Groemping Y, & Rittinger K (2005). Activation and assembly of the NADPH oxidase: a structural perspective. *Biochemical Journal* 386: 401-416.

Gross JrH (2004) *Mass spectrometry : a textbook*. Springer: Berlin ; New York.

Grote K, Ortmann M, Salguero G, Doerries C, Landmesser U, Luchtefeld M, *et al.* (2006). Critical role for p47phox in renin-angiotensin system activation and blood pressure regulation. *Cardiovasc Res* 71: 596-605.

Grusso T, Mieulet V, Cardon M, Bourachot B, Kieffer Y, Devun F, *et al.* (2016). Chronic oxidative stress promotes H2AX protein degradation and enhances chemosensitivity in breast cancer patients. *EMBO Mol Med* 8: 527-549.

Guengerich FP (2012). Introduction: use of radioactive compounds in drug discovery and development. *Chem Res Toxicol* 25: 511-512.

Gul R, Shawl AI, Kim SH, & Kim UH (2012). Cooperative interaction between reactive oxygen species and Ca²⁺ signals contributes to angiotensin II-induced hypertrophy in adult rat cardiomyocytes. *Am J Physiol-Heart C* 302: H901-H909.

Gunaydin H, Altman MD, Ellis JM, Fuller P, Johnson SA, Lahue B, *et al.* (2018). Strategy for Extending Half-life in Drug Design and Its Significance. *ACS Med Chem Lett* 9: 528-533.

Gunaydin H, & Houk KN (2008). Molecular dynamics prediction of the mechanism of ester hydrolysis in water. *J Am Chem Soc* 130: 15232-15233.

Gupte SA, Kaminski PM, George S, Kouznestova L, Olson SC, Mathew R, *et al.* (2009). Peroxide generation by p47(phox)-Src activation of Nox2 has a key role in protein kinase C-induced arterial smooth muscle contraction. *Am J Physiol-Heart C* 296: H1048-H1057.

Guzik TJ, Chen W, Gongora MC, Guzik B, Lob HE, Mangalat D, *et al.* (2008). Calcium-dependent NOX5 nicotinamide adenine dinucleotide phosphate oxidase contributes to vascular oxidative stress in human coronary artery disease. *J Am Coll Cardiol* 52: 1803-1809.

Guzik TJ, Mussa S, Gastaldi D, Sadowski J, Ratnatunga C, Pillai R, *et al.* (2002). Mechanisms of increased vascular superoxide production in human diabetes mellitus: role of NAD(P)H oxidase and endothelial nitric oxide synthase. *Circulation* 105: 1656-1662.

Guzik TJ, West NE, Black E, McDonald D, Ratnatunga C, Pillai R, *et al.* (2000). Vascular superoxide production by NAD(P)H oxidase: association with endothelial dysfunction and clinical risk factors. *Circ Res* 86: E85-90.

Hahn NE, Meischl C, Wijnker PJ, Musters RJ, Fornerod M, Janssen HW, *et al.* (2011). NOX2, p22phox and p47phox are targeted to the nuclear pore complex in ischemic

cardiomyocytes colocalizing with local reactive oxygen species. *Cell Physiol Biochem* 27: 471-478.

Hamman JH, Enslin GM, & Kotze AF (2005). Oral delivery of peptide drugs: barriers and developments. *BioDrugs* 19: 165-177.

Han CH, Freeman JL, Lee T, Motalebi SA, & Lambeth JD (1998). Regulation of the neutrophil respiratory burst oxidase. Identification of an activation domain in p67(phox). *J Biol Chem* 273: 16663-16668.

Han CH, & Lee MH (2000). Activation domain in P67phox regulates the steady state reduction of FAD in gp91phox. *J Vet Sci* 1: 27-31.

Hayakawa R, Hayakawa T, Takeda K, & Ichijo H (2012). Therapeutic targets in the ASK1-dependent stress signaling pathways. *Proc Jpn Acad Ser B Phys Biol Sci* 88: 434-453.

Hearn MTW (1980). High-Performance Liquid-Chromatography of Amino-Acids Peptides and Proteins .26. The Use of Reversed Phase High-Performance Liquid-Chromatography for the Structural Mapping of Polypeptides and Proteins. *J Liq Chromatogr* 3: 1255-1276.

Heart Protection Study Collaborative G (2002). MRC/BHF Heart Protection Study of antioxidant vitamin supplementation in 20,536 high-risk individuals: a randomised placebo-controlled trial. *Lancet* 360: 23-33.

Heinzel FR, Hohendanner F, Jin G, Sedej S, & Edelmann F (2015). Myocardial hypertrophy and its role in heart failure with preserved ejection fraction. *J Appl Physiol* 119: 1233-1242.

Heumuller S, Wind S, Barbosa-Sicard E, Schmidt HH, Busse R, Schroder K, *et al.* (2008). Apocynin is not an inhibitor of vascular NADPH oxidases but an antioxidant. *Hypertension* 51: 211-217.

Heymes C, Bendall JK, Ratajczak P, Cave AC, Samuel JL, Hasenfuss G, *et al.* (2003). Increased myocardial NADPH oxidase activity in human heart failure. *J Am Coll Cardiol* 41: 2164-2171.

Higuchi T, & Lachman L (1955). Inhibition of hydrolysis of esters in solution by formation of complexes. I. Stabilization of benzocaine with caffeine. *J Am Pharm Assoc Am Pharm Assoc* 44: 521-526.

Hingtgen SD, Tian X, Yang J, Dunlay SM, Peek AS, Wu Y, *et al.* (2006). Nox2-containing NADPH oxidase and Akt activation play a key role in angiotensin II-induced cardiomyocyte hypertrophy. *Physiol Genomics* 26: 180-191.

Horton RE, Yadid M, McCain ML, Sheehy SP, Pasqualini FS, Park SJ, *et al.* (2016). Angiotensin II Induced Cardiac Dysfunction on a Chip. *Plos One* 11.

Hsieh PC, Davis ME, Lisowski LK, & Lee RT (2006). Endothelial-cardiomyocyte interactions in cardiac development and repair. *Annu Rev Physiol* 68: 51-66.

Hsu WH, Yu YR, Hsu SH, Yu WC, Chu YH, Chen YJ, *et al.* (2013). The Wilms' tumor suppressor Wt1 regulates Coronin 1B expression in the epicardium. *Exp Cell Res* 319: 1365-1381.

Hu ZL, Chen J, Wei Q, & Xia Y (2008). Bidirectional actions of hydrogen peroxide on endothelial nitric-oxide synthase phosphorylation and function - Co-commitment and interplay of Akt and AMPK. *Journal of Biological Chemistry* 283: 25256-25263.

Huang CK, Zhan L, Hannigan MO, Ai Y, & Leto TL (2000). P47(phox)-deficient NADPH oxidase defect in neutrophils of diabetic mouse strains, C57BL/6J-m db/db and db/+. *J Leukoc Biol* 67: 210-215.

Huang J, & Kleinberg ME (1999). Activation of the phagocyte NADPH oxidase protein p47(phox) - Phosphorylation controls SH3 domain-dependent binding to p22(phox). *Journal of Biological Chemistry* 274: 19731-19737.

Hubackova S, Krejcikova K, Bartek J, & Hodny Z (2012). IL1- and TGFbeta-Nox4 signaling, oxidative stress and DNA damage response are shared features of replicative, oncogene-induced, and drug-induced paracrine 'bystander senescence'. *Aging (Albany NY)* 4: 932-951.

Hwang S, & Kim JK (2018). Effects of NADPH Oxidase Inhibitors and Mitochondria-Targeted Antioxidants on Amyloid beta1-42-Induced Neuronal Deaths in Mouse Mixed Cortical Cultures. *Chonnam Med J* 54: 159-166.

Infanger DW, Sharma RV, & Davisson RL (2006). NADPH oxidases of the brain: Distribution, regulation, and function. *Antioxid Redox Sign* 8: 1583-1596.

Insin EM, Elmore CS, Nilsson GN, Thompson RA, & Weidolf L (2012). Use of radiolabeled compounds in drug metabolism and pharmacokinetic studies. *Chem Res Toxicol* 25: 532-542.

Ismail HM, Scapozza L, Ruegg UT, & Dorchies OM (2014). Diapocynin, a dimer of the NADPH oxidase inhibitor apocynin, reduces ROS production and prevents force loss in eccentrically contracting dystrophic muscle. *PLoS One* 9: e110708.

Iulita MF, Vallerand D, Beauvillier M, Hauptert N, C AU, Gagne A, *et al.* (2018). Differential effect of angiotensin II and blood pressure on hippocampal inflammation in mice. *J Neuroinflammation* 15: 62.

Jackson SH, Gallin JI, & Holland SM (1995). The p47phox mouse knock-out model of chronic granulomatous disease. *J Exp Med* 182: 751-758.

Jacobson GM, Dourron HM, Liu J, Carretero OA, Reddy DJ, Andrzejewski T, *et al.* (2003). Novel NAD(P)H oxidase inhibitor suppresses angioplasty-induced superoxide and neointimal hyperplasia of rat carotid artery. *Circ Res* 92: 637-643.

Jaffre F, Callebert J, Sarre A, Etienne N, Nebigil CG, Launay JM, *et al.* (2004). Involvement of the serotonin 5-HT_{2B} receptor in cardiac hypertrophy linked to sympathetic stimulation control of interleukin-6, interleukin-1 beta, and tumor necrosis factor-alpha cytokine production by ventricular fibroblasts. *Circulation* 110: 969-974.

Jaimes EA, DeMaster EG, Tian RX, & Raji L (2004). Stable compounds of cigarette smoke induce endothelial superoxide anion production via NADPH oxidase activation. *Arterioscler Thromb Vasc Biol* 24: 1031-1036.

Jain AK, Mehra NK, & Swarnakar NK (2015). Role of Antioxidants for the Treatment of Cardiovascular Diseases: Challenges and Opportunities. *Curr Pharm Des* 21: 4441-4455.

Jang M, Cai L, Udeani GO, Slowing KV, Thomas CF, Beecher CW, *et al.* (1997). Cancer chemopreventive activity of resveratrol, a natural product derived from grapes. *Science* 275: 218-220.

Jankowski M, Broderick TL, & Gutkowska J (2020). The Role of Oxytocin in Cardiovascular Protection. *Front Psychol* 11: 2139.

Jawien W (2014). Searching for an optimal AUC estimation method: a never-ending task? *J Pharmacokinet Pharmacodyn* 41: 655-673.

Johnson DK, Schillinger KJ, Kwait DM, Hughes CV, McNamara EJ, Ishmael F, *et al.* (2002). Inhibition of NADPH oxidase activation in endothelial cells by ortho-methoxy-substituted catechols. *Endothelium* 9: 191-203.

Jones NR, McManus RJ, McCormack T, & Constanti M (2020). Diagnosis and management of hypertension in adults: NICE guideline update 2019. *Brit J Gen Pract* 70: 90-91.

Joseph LC, Kokkinaki D, Valenti MC, Kim GJ, Barca E, Tomar D, *et al.* (2017). Inhibition of NADPH oxidase 2 (NOX2) prevents sepsis-induced cardiomyopathy by improving calcium handling and mitochondrial function. *JCI Insight* 2.

Judkins CP, Diep H, Broughton BR, Mast AE, Hooker EU, Miller AA, *et al.* (2010). Direct evidence of a role for Nox2 in superoxide production, reduced nitric oxide bioavailability, and early atherosclerotic plaque formation in ApoE^{-/-} mice. *Am J Physiol Heart Circ Physiol* 298: H24-32.

Kalyanaraman B, Darley-Usmar V, Davies KJ, Dennery PA, Forman HJ, Grisham MB, *et al.* (2012). Measuring reactive oxygen and nitrogen species with fluorescent probes: challenges and limitations. *Free Radic Biol Med* 52: 1-6.

Kapoor M, Sharma N, Sandhir R, & Nehru B (2018). Effect of the NADPH oxidase inhibitor apocynin on ischemia-reperfusion hippocampus injury in rat brain. *Biomed Pharmacother* 97: 458-472.

Karaman R (2013). Prodrugs design based on inter- and intramolecular chemical processes. *Chem Biol Drug Des* 82: 643-668.

Karathanassis D, Stahelin RV, Bravo J, Perisic O, Pacold CM, Cho WW, *et al.* (2002). Binding of the PX domain of p47(phox) to phosphatidylinositol 3,4-bisphosphate and phosphatidic acid is masked by an intramolecular interaction. *Embo J* 21: 5057-5068.

Katholi RE, & Couri DM (2011). Left ventricular hypertrophy: major risk factor in patients with hypertension: update and practical clinical applications. *Int J Hypertens* 2011: 495349.

Kawai T, Forrester SJ, O'Brien S, Baggett A, Rizzo V, & Eguchi S (2017). AT1 receptor signaling pathways in the cardiovascular system. *Pharmacol Res* 125: 4-13.

Kawano M, Miyamoto K, Kaito Y, Sumimoto H, & Tamura M (2012). Noxa1 as a moderate activator of Nox2-based NADPH oxidase. *Arch Biochem Biophys* 519: 1-7.

Keiser MJ, Setola V, Irwin JJ, Laggner C, Abbas AI, Hufeisen SJ, *et al.* (2009). Predicting new molecular targets for known drugs. *Nature* 462: 175-181.

Kelly FJ (2003). Oxidative stress: its role in air pollution and adverse health effects. *Occup Environ Med* 60: 612-616.

Khan MM, & Martell AE (1967). Metal ion and metal chelate catalyzed oxidation of ascorbic acid by molecular oxygen. II. Cupric and ferric chelate catalyzed oxidation. *J Am Chem Soc* 89: 7104-7111.

Kienzl K, Sarg B, Golderer G, Obrist P, Werner ER, Werner-Felmayer G, *et al.* (2009). Proteomic Profiling of Acute Cardiac Allograft Rejection. *Transplantation* 88: 553-560.

Kil J, Lobarinas E, Spankovich C, Griffiths SK, Antonelli PJ, Lynch ED, *et al.* (2017). Safety and efficacy of ebselen for the prevention of noise-induced hearing loss: a randomised, double-blind, placebo-controlled, phase 2 trial. *Lancet* 390: 969-979.

Kim C, Kim JY, & Kim JH (2008). Cytosolic phospholipase A(2), lipoxygenase metabolites, and reactive oxygen species. *BMB Rep* 41: 555-559.

Kim SD, Moon CK, Eun SY, Ryu PD, & Jo SA (2005). Identification of ASK1, MKK4, JNK, c-Jun, and caspase-3 as a signaling cascade involved in cadmium-induced neuronal cell apoptosis. *Biochem Biophys Res Commun* 328: 326-334.

Kimes BW, & Brandt BL (1976). Properties of a clonal muscle cell line from rat heart. *Exp Cell Res* 98: 367-381.

Kimura S, Zhang GX, Nishiyama A, Shokoji T, Yao L, Fan YY, *et al.* (2005a). Mitochondria-derived reactive oxygen species and vascular MAP kinases - Comparison of angiotensin II and diazoxide. *Hypertension* 45: 438-444.

Kimura S, Zhang GX, Nishiyama A, Shokoji T, Yao L, Fan YY, *et al.* (2005b). Role of NAD(P)H oxidase- and mitochondria-derived reactive oxygen species in cardioprotection of ischemic reperfusion injury by angiotensin II. *Hypertension* 45: 860-866.

Kinner A, Wu W, Staudt C, & Iliakis G (2008). Gamma-H2AX in recognition and signaling of DNA double-strand breaks in the context of chromatin. *Nucleic Acids Res* 36: 5678-5694.

Kitajima N, Numaga-Tomita T, Watanabe M, Kuroda T, Nishimura A, Miyano K, *et al.* (2016). TRPC3 positively regulates reactive oxygen species driving maladaptive cardiac remodeling. *Sci Rep* 6: 37001.

Klees RF, De Marco PC, Salaszyk RM, Ahuja D, Hogg M, Antoniotti S, *et al.* (2006). Apocynin derivatives interrupt intracellular signaling resulting in decreased migration in breast cancer cells. *J Biomed Biotechnol* 2006: 87246.

Klein S (2010). The use of biorelevant dissolution media to forecast the in vivo performance of a drug. *AAPS J* 12: 397-406.

Knock GA, & Ward JPT (2011). Redox Regulation of Protein Kinases as a Modulator of Vascular Function. *Antioxid Redox Sign* 15: 1531-1547.

Kobayashi N, Mita S, Yoshida K, Honda T, Kobayashi T, Hara K, *et al.* (2003). Celiprolol activates eNOS through the PI3K-Akt pathway and inhibits VCAM-1 via NF-kappa B induced by oxidative stress. *Hypertension* 42: 1004-1013.

Kokubo Y, & Kamide K (2009). High-normal blood pressure and the risk of cardiovascular disease. *Circ J* 73: 1381-1385.

Kotamraju S, Tampo Y, Keszler A, Chitambar CR, Joseph J, Haas AL, *et al.* (2003). Nitric oxide inhibits H₂O₂-induced transferrin receptor-dependent apoptosis in endothelial cells: Role of ubiquitin-proteasome pathway. *Proc Natl Acad Sci U S A* 100: 10653-10658.

Kremneva E, Makkonen MH, Skwarek-Maruszewska A, Gateva G, Michelot A, Dominguez R, *et al.* (2014). Cofilin-2 Controls Actin Filament Length in Muscle Sarcomeres. *Dev Cell* 31: 215-226.

Krijnen PA, Meischl C, Hack CE, Meijer CJ, Visser CA, Roos D, *et al.* (2003). Increased Nox2 expression in human cardiomyocytes after acute myocardial infarction. *J Clin Pathol* 56: 194-199.

Kubista M, Akerman B, & Norden B (1987). Characterization of Interaction between DNA and 4',6-Diamidino-2-Phenylindole by Optical Spectroscopy. *Biochemistry* 26: 4545-4553.

Kucera J, Bino L, Stefkova K, Jaros J, Vasicek O, Vecera J, *et al.* (2016a). Apocynin and Diphenyleneiodonium Induce Oxidative Stress and Modulate PI3K/Akt and MAPK/Erk Activity in Mouse Embryonic Stem Cells. *Oxidative Medicine and Cellular Longevity*.

Kucera J, Bino L, Stefkova K, Jaros J, Vasicek O, Vecera J, *et al.* (2016b). Apocynin and Diphenyleneiodonium Induce Oxidative Stress and Modulate PI3K/Akt and MAPK/Erk Activity in Mouse Embryonic Stem Cells. *Oxid Med Cell Longev* 2016: 7409196.

Kufe DW, Holland JF, Frei E, & American Cancer Society. (2003) *Cancer medicine* 6. 6th edn. BC Decker: Hamilton, Ont. ; Lewiston, NY.

Kuhn M, Campillos M, Gonzalez P, Jensen LJ, & Bork P (2008). Large-scale prediction of drug-target relationships. *FEBS Lett* 582: 1283-1290.

Kumar R, Singh VP, & Baker KM (2009). The intracellular renin-angiotensin system in the heart. *Curr Hypertens Rep* 11: 104-110.

Kuo LJ, & Yang LX (2008). Gamma-H2AX - a novel biomarker for DNA double-strand breaks. *In Vivo* 22: 305-309.

Kurata S (2000). Selective activation of p38 MAPK cascade and mitotic arrest caused by low level oxidative stress. *J Biol Chem* 275: 23413-23416.

Kurdi M, De Mello WC, & Booz GW (2005). Working outside the system: an update on the unconventional behavior of the renin-angiotensin system components. *Int J Biochem Cell Biol* 37: 1357-1367.

Kuroda J, Ago T, Matsushima S, Zhai PY, Schneider MD, & Sadoshima J (2010). NADPH oxidase 4 (Nox4) is a major source of oxidative stress in the failing heart. *P Natl Acad Sci USA* 107: 15565-15570.

Lachman L, & Higuchi T (1957). Inhibition of hydrolysis of esters in solution by formation of complexes. III. Stabilization of tetracaine with caffeine. *J Am Pharm Assoc Am Pharm Assoc* 46: 32-36.

Laizure SC, Herring V, Hu Z, Witbrodt K, & Parker RB (2013). The role of human carboxylesterases in drug metabolism: have we overlooked their importance? *Pharmacotherapy* 33: 210-222.

Lamba M, Hutmacher MM, Furst DE, Dikranian A, Dowty ME, Conrado D, *et al.* (2017). Model-Informed Development and Registration of a Once-Daily Regimen of Extended-Release Tofacitinib. *Clin Pharmacol Ther* 101: 745-753.

Lamba M, Wang R, Fletcher T, Alvey C, Kushner Jt, & Stock TC (2016). Extended-Release Once-Daily Formulation of Tofacitinib: Evaluation of Pharmacokinetics Compared With Immediate-Release Tofacitinib and Impact of Food. *J Clin Pharmacol* 56: 1362-1371.

Lambrinidis G, Vallianatou T, & Tsantili-Kakoulidou A (2015). In vitro, in silico and integrated strategies for the estimation of plasma protein binding. A review. *Adv Drug Deliv Rev* 86: 27-45.

Langley M, Ghosh A, Charli A, Sarkar S, Ay M, Luo J, *et al.* (2017). Mito-Apocynin Prevents Mitochondrial Dysfunction, Microglial Activation, Oxidative Damage, and

Progressive Neurodegeneration in MitoPark Transgenic Mice. *Antioxid Redox Signal* 27: 1048-1066.

Lapouge K, Smith SJM, Groemping Y, & Rittinger K (2002). Architecture of the p40-p47-p67phox complex in the resting state of the NADPH oxidase - A central role for p67(phox). *Journal of Biological Chemistry* 277: 10121-10128.

Lapouge K, Smith SJM, Walker PA, Gamblin SJ, Smerdon SJ, & Rittinger K (2000). Structure of the TPR domain of p67(phox) in complex with Rac center dot GTP. *Molecular Cell* 6: 899-907.

Lassegue B, & Griendling KK (2010). NADPH oxidases: functions and pathologies in the vasculature. *Arterioscler Thromb Vasc Biol* 30: 653-661.

Lave T, Caruso A, Parrott N, & Walz A (2016). Translational PK/PD modeling to increase probability of success in drug discovery and early development. *Drug Discov Today Technol* 21-22: 27-34.

Leatherbarrow EL, Harper JV, Cucinotta FA, & O'Neill P (2006). Induction and quantification of gamma-H2AX foci following low and high LET-irradiation. *International Journal of Radiation Biology* 82: 111-118.

Lee S, Gharavi NM, Honda H, Chang I, Kim B, Jen N, *et al.* (2009). A role for NADPH oxidase 4 in the activation of vascular endothelial cells by oxidized phospholipids. *Free Radic Biol Med* 47: 145-151.

Lee ST, Chu K, Jung KH, Kim SJ, Kim DH, Kang KM, *et al.* (2008). Anti-inflammatory mechanism of intravascular neural stem cell transplantation in haemorrhagic stroke. *Brain* 131: 616-629.

Leiding JW, Marciano BE, Zerbe CS, DeRavin SS, Malech HL, & Holland SM (2013). Diabetes, Renal and Cardiovascular Disease in p47(phox^{-/-}) Chronic Granulomatous Disease. *J Clin Immunol* 33: 725-730.

Leinwand LA (2001). Calcineurin inhibition and cardiac hypertrophy: A matter of balance. *P Natl Acad Sci USA* 98: 2947-2949.

Leiva A, Fuenzalida B, Barros E, Sobrevia B, Salsoso R, Saez T, *et al.* (2016). Nitric Oxide is a Central Common Metabolite in Vascular Dysfunction Associated with Diseases of Human Pregnancy. *Curr Vasc Pharmacol* 14: 237-259.

Lennicke C, Rahn J, Lichtenfels R, Wessjohann LA, & Seliger B (2015). Hydrogen peroxide - production, fate and role in redox signaling of tumor cells. *Cell Commun Signal* 13: 39.

Leusen JH, de Boer M, Bolscher BG, Hilarius PM, Weening RS, Ochs HD, *et al.* (1994). A point mutation in gp91-phox of cytochrome b558 of the human NADPH oxidase leading to defective translocation of the cytosolic proteins p47-phox and p67-phox. *J Clin Invest* 93: 2120-2126.

Li B, Tian J, Sun Y, Xu TR, Chi RF, Zhang XL, *et al.* (2015). Activation of NADPH oxidase mediates increased endoplasmic reticulum stress and left ventricular remodeling after myocardial infarction in rabbits. *Biochim Biophys Acta* 1852: 805-815.

Li HH, Kedar V, Zhang CL, McDonough H, Arya R, Wang DZ, *et al.* (2004). Atrogin-1/muscle atrophy F-box inhibits calcineurin-dependent cardiac hypertrophy by participating in an SCF ubiquitin ligase complex. *J Clin Invest* 114: 1058-1071.

Li JJ, & Bugg TD (2007). Investigation of a general base mechanism for ester hydrolysis in C-C hydrolase enzymes of the alpha/beta-hydrolase superfamily: a novel mechanism for the serine catalytic triad. *Org Biomol Chem* 5: 507-513.

Li JM, Fan LM, Christie MR, & Shah AM (2005). Acute tumor necrosis factor alpha signaling via NADPH oxidase in microvascular endothelial cells: role of p47phox phosphorylation and binding to TRAF4. *Mol Cell Biol* 25: 2320-2330.

Li JM, Fan LM, George VT, & Brooks G (2007). Nox2 regulates endothelial cell cycle arrest and apoptosis via p21cip1 and p53. *Free Radic Biol Med* 43: 976-986.

Li JM, Gall NP, Grieve DJ, Chen M, & Shah AM (2002). Activation of NADPH oxidase during progression of cardiac hypertrophy to failure. *Hypertension* 40: 477-484.

Li JM, Mullen AM, Yun S, & Shah AM (2001). Essential role of the NADPH oxidase subunit, p47phox, in PMA-stimulated O₂⁻ production by mouse coronary microvascular endothelial cells. *Circulation* 104: 103-103.

Li JM, Mullen AM, Yun S, Wientjes F, Brouns GY, Thrasher AJ, *et al.* (2002). Essential role of the NADPH oxidase subunit p47(phox) in endothelial cell superoxide production in response to phorbol ester and tumor necrosis factor-alpha. *Circ Res* 90: 143-150.

Li JM, & Shah AM (2002). Intracellular localization and preassembly of the NADPH oxidase complex in cultured endothelial cells. *Journal of Biological Chemistry* 277: 19952-19960.

Li JM, & Shah AM (2003). Mechanism of endothelial cell NADPH oxidase activation by angiotensin II. Role of the p47phox subunit. *J Biol Chem* 278: 12094-12100.

Li JM, Wheatcroft S, Fan LM, Kearney MT, & Shah AM (2004). Opposing roles of p47phox in basal versus angiotensin II-stimulated alterations in vascular O₂-production, vascular tone, and mitogen-activated protein kinase activation. *Circulation* 109: 1307-1313.

Li P, Fu Y, Ru J, Huang C, Du J, Zheng C, *et al.* (2014). Insights from systems pharmacology into cardiovascular drug discovery and therapy. *BMC Syst Biol* 8: 141.

Li Q, Zhang W, Marden JJ, Banfi B, & Engelhardt JF (2008). Endosomal NADPH oxidase regulates c-Src activation following hypoxia/reoxygenation injury. *Biochem J* 411: 531-541.

Li YB, Zhu H, Kuppusamy P, Roubaud V, Zweier JL, & Trush MA (1998). Validation of lucigenin (bis-N-methylacridinium) as a chemilumigenic probe for detecting superoxide anion radical production by enzymatic and cellular systems. *Journal of Biological Chemistry* 273: 2015-2023.

Li Z, Yang X, Dong S, & Li X (2012). DNA breakage induced by piceatannol and copper(II): Mechanism and anticancer properties. *Oncol Lett* 3: 1087-1094.

Li ZX, Yang J, & Huang HF (2006). Oxidative stress induces H2AX phosphorylation in human spermatozoa. *Febs Letters* 580: 6161-6168.

Liang W, Oudit GY, Patel MM, Shah AM, Woodgett JR, Tsushima RG, *et al.* (2010). Role of phosphoinositide 3-kinase {alpha}, protein kinase C, and L-type Ca²⁺ channels in mediating the complex actions of angiotensin II on mouse cardiac contractility. *Hypertension* 56: 422-429.

Lindsley CW (2014). New statistics on the cost of new drug development and the trouble with CNS drugs. *ACS Chem Neurosci* 5: 1142.

Linfante I, & Wakhloo AK (2007). Brain aneurysms and arteriovenous malformations: advancements and emerging treatments in endovascular embolization. *Stroke* 38: 1411-1417.

Liochev SI, & Fridovich I (1997). Lucigenin (bis-N-methylacridinium) as a mediator of superoxide anion production. *Arch Biochem Biophys* 337: 115-120.

Lipinski B (2011). Hydroxyl Radical and Its Scavengers in Health and Disease. *Oxid Med Cell Longev*.

Liu JJ, Li DL, Zhou J, Sun L, Zhao M, Kong SS, *et al.* (2011). Acetylcholine prevents angiotensin II-induced oxidative stress and apoptosis in H9c2 cells. *Apoptosis* 16: 94-103.

Lonn E, Yusuf S, Dzavik V, Doris C, Yi Q, Smith S, *et al.* (2001). Effects of ramipril and vitamin E on atherosclerosis: the study to evaluate carotid ultrasound changes in patients treated with ramipril and vitamin E (SECURE). *Circulation* 103: 919-925.

Looi YH, Grieve DJ, Siva A, Walker SJ, Anilkumar N, Cave AC, *et al.* (2008). Involvement of Nox2 NADPH oxidase in adverse cardiac remodeling after myocardial infarction. *Hypertension* 51: 319-325.

Lopez-Acosta O, de Los Angeles Fortis-Barrera M, Barrios-Maya MA, Ramirez AR, Aguilar FJA, & El-Hafidi M (2018). Reactive Oxygen Species from NADPH Oxidase and Mitochondria Participate in the Proliferation of Aortic Smooth Muscle Cells from a Model of Metabolic Syndrome. *Oxid Med Cell Longev* 2018: 5835072.

Loukogeorgakis SP, van den Berg MJ, Sofat R, Nitsch D, Charakida M, Haiyee B, *et al.* (2010). Role of NADPH Oxidase in Endothelial Ischemia/Reperfusion Injury in Humans. *Circulation* 121: 2310-2316.

Lu JC, Cui W, Zhang HL, Liu F, Han M, Liu DM, *et al.* (2009). Additive beneficial effects of amlodipine and atorvastatin in reversing advanced cardiac hypertrophy in elderly spontaneously hypertensive rats. *Clin Exp Pharmacol Physiol* 36: 1110-1119.

Luchtefeld M, Grote K, Grothusen C, Bley S, Bandlow N, Selle T, *et al.* (2005). Angiotensin II induces MMP-2 in a p47phox-dependent manner. *Biochem Biophys Res Commun* 328: 183-188.

Lyle AN, Deshpande NN, Taniyama Y, Seidel-Rogol B, Pounkova L, Du P, *et al.* (2009). Poldip2, a novel regulator of Nox4 and cytoskeletal integrity in vascular smooth muscle cells. *Circ Res* 105: 249-259.

Lyngsie G, Krumina L, Tunlid A, & Persson P (2018). Generation of hydroxyl radicals from reactions between a dimethoxyhydroquinone and iron oxide nanoparticles. *Sci Rep-Uk* 8.

Maehara Y, Miyano K, & Sumimoto H (2009). Role for the first SH3 domain of p67phox in activation of superoxide-producing NADPH oxidases. *Biochem Biophys Res Commun* 379: 589-593.

Manea SA, Fenyo IM, & Manea A (2016). c-Src tyrosine kinase mediates high glucose-induced endothelin-1 expression. *Int J Biochem Cell B* 75: 123-130.

Mankelow TJ, Hu XW, Adams K, & Henderson LM (2004). Investigation of the contribution of histidine 119 to the conduction of protons through human Nox2. *Eur J Biochem* 271: 4026-4033.

Marin M, Gimeno C, Giner RM, Rios JL, Manez S, & Recio MAC (2017). Influence of Dimerization of Apocynin on Its Effects in Experimental Colitis. *J Agric Food Chem* 65: 4083-4091.

Marletta MA (1994). Nitric oxide synthase: aspects concerning structure and catalysis. *Cell* 78: 927-930.

Martinez-Revelles S, Avendano MS, Garcia-Redondo AB, Alvarez Y, Aguado A, Perez-Giron JV, *et al.* (2013). Reciprocal relationship between reactive oxygen species and cyclooxygenase-2 and vascular dysfunction in hypertension. *Antioxid Redox Signal* 18: 51-65.

Masaki C, Sharpley AL, Cooper CM, Godlewska BR, Singh N, Vasudevan SR, *et al.* (2016). Effects of the potential lithium-mimetic, ebselen, on impulsivity and emotional processing. *Psychopharmacology (Berl)* 233: 2655-2661.

Masano T, Kawashima S, Toh R, Satomi-Kobayashi S, Shinohara M, Takaya T, *et al.* (2008). Beneficial effects of exogenous tetrahydrobiopterin on left ventricular remodeling after myocardial infarction in rats: the possible role of oxidative stress caused by uncoupled endothelial nitric oxide synthase. *Circ J* 72: 1512-1519.

Mascher H (2012) *HPLC methods for clinical pharmaceutical analysis : a user's guide*. 1st edn. Wiley-VCH: Weinheim.

Massey KJ, Hong NJ, & Garvin JL (2012). Angiotensin II stimulates superoxide production in the thick ascending limb by activating NOX4. *Am J Physiol Cell Physiol* 303: C781-789.

Matono R, Miyano K, Kiyohara T, & Sumimoto H (2014). Arachidonic acid induces direct interaction of the p67(phox)-Rac complex with the phagocyte oxidase Nox2, leading to superoxide production. *J Biol Chem* 289: 24874-24884.

Matsukawa J, Matsuzawa A, Takeda K, & Ichijo H (2004). The ASK1-MAP kinase cascades in mammalian stress response. *J Biochem-Tokyo* 136: 261-265.

Maulik N, Sasaki H, Addya S, & Das DK (2000). Regulation of cardiomyocyte apoptosis by redox-sensitive transcription factors. *Febs Lett* 485: 7-12.

Maulik SK, & Kumar S (2012). Oxidative stress and cardiac hypertrophy: a review. *Toxicol Mech Methods* 22: 359-366.

Maulucci G, Pani G, Labate V, Mele M, Panieri E, Papi M, *et al.* (2010). Reactive Oxygen Species as Essential Mediators of Cell Adhesion and Migration. *Biophys J* 98: 576a-576a.

McNaught AD, Wilkinson A, & International Union of Pure and Applied Chemistry. (1997) *Compendium of chemical terminology : IUPAC recommendations*. 2nd edn. Blackwell Science: Oxford England ; Malden, MA, USA.

Meijles DN, Fan LM, Howlin BJ, & Li JM (2014). Molecular insights of p47phox phosphorylation dynamics in the regulation of NADPH oxidase activation and superoxide production. *J Biol Chem* 289: 22759-22770.

Meloche S, Landry J, Huot J, Houle F, Marceau F, & Giasson E (2000). P38 MAP kinase pathway regulates angiotensin II-induced contraction of rat vascular smooth muscle. *Am J Physiol-Heart C* 279: H741-H751.

Miller FJ (2009). NADPH Oxidase 4 Walking the Walk With Poldip2. *Circ Res* 105: 209-210.

Minkenbergh I, & Ferber E (1984). Lucigenin-dependent chemiluminescence as a new assay for NAD(P)H-oxidase activity in particulate fractions of human polymorphonuclear leukocytes. *J Immunol Methods* 71: 61-67.

Mita S, Kobayashi N, Yoshida K, Nakano S, & Matsuoka H (2005). Cardioprotective mechanisms of Rho-kinase inhibition associated with eNOS and oxidative stress-LOX-1 pathway in Dahl salt-sensitive hypertensive rats. *Journal of Hypertension* 23: 87-96.

Miyano K, Ueno N, Takeya R, & Sumimoto H (2006). Direct involvement of the small GTPase Rac in activation of the superoxide-producing NADPH oxidase Nox1. *Journal of Biological Chemistry* 281: 21857-21868.

Mizuki K, Takeya R, Kuribayashi F, Nobuhisa I, Kohda D, Nunoi H, *et al.* (2005). A region C-terminal to the proline-rich core of p47phox regulates activation of the phagocyte NADPH oxidase by interacting with the C-terminal SH3 domain of p67phox. *Arch Biochem Biophys* 444: 185-194.

Moens AL, Takimoto E, Tocchetti CG, Chakir K, Bedja D, Cormaci G, *et al.* (2008). Reversal of cardiac hypertrophy and fibrosis from pressure overload by tetrahydrobiopterin - Efficacy of recoupling nitric oxide synthase as a therapeutic strategy. *Circulation* 117: 2626-2636.

Molkentin JD (2004). Calcineurin-NFAT signaling regulates the cardiac hypertrophic response in coordination with the MAPKs. *Cardiovasc Res* 63: 467-475.

Monassier L, Laplante MA, Jaffre F, Bousquet P, Maroteaux L, & de Champlain J (2008). Serotonin 5-HT_{2B} receptor blockade prevents reactive oxygen species-induced cardiac hypertrophy in mice. *Hypertension* 52: 301-307.

Montezano AC, & Touyz RM (2013). Mechanosensitive regulation of cortactin by p47phox: a new paradigm in cytoskeletal remodeling. *Circ Res* 112: 1522-1525.

Moradi SV, Hussein WM, Varamini P, Simerska P, & Toth I (2016). Glycosylation, an effective synthetic strategy to improve the bioavailability of therapeutic peptides. *Chem Sci* 7: 2492-2500.

Muehlbacher M, Spitzer GM, Liedl KR, & Kornhuber J (2011). Qualitative prediction of blood-brain barrier permeability on a large and refined dataset. *J Comput Aided Mol Des* 25: 1095-1106.

Munzel T, Gori T, Keaney JF, Jr., Maack C, & Daiber A (2015). Pathophysiological role of oxidative stress in systolic and diastolic heart failure and its therapeutic implications. *Eur Heart J* 36: 2555-2564.

Murdoch CE, Alom-Ruiz SP, Wang M, Zhang M, Walker S, Yu B, *et al.* (2011). Role of endothelial Nox2 NADPH oxidase in angiotensin II-induced hypertension and vasomotor dysfunction. *Basic Res Cardiol* 106: 527-538.

Murphy MP (2009). How mitochondria produce reactive oxygen species. *Biochemical Journal* 417: 1-13.

Muthukumar K, & Nachiappan V (2010). Cadmium-induced oxidative stress in *Saccharomyces cerevisiae*. *Indian J Biochem Bio* 47: 383-387.

Nabeebaccus A, Zhang M, & Shah AM (2011). NADPH oxidases and cardiac remodelling. *Heart Fail Rev* 16: 5-12.

Nagaishi K, Adachi R, Kawanishi T, Yamaguchi T, Kasahara T, Hayakawa T, *et al.* (1999). Participation of cofilin in opsonized zymosan-triggered activation of neutrophil-like HL-60 cells through rapid dephosphorylation and translocation to plasma membranes. *J Biochem-Tokyo* 125: 891-898.

Nakamura Y, Feng Q, Kumagai T, Torikai K, Ohigashi H, Osawa T, *et al.* (2002). Ebselen, a glutathione peroxidase mimetic seleno-organic compound, as a multifunctional antioxidant - Implication for inflammation-associated carcinogenesis. *Journal of Biological Chemistry* 277: 2687-2694.

Nebigil CG, & Maroteaux L (2003). Functional consequence of serotonin/5-HT_{2B} receptor signaling in heart role of mitochondria in transition between hypertrophy and heart failure? *Circulation* 108: 902-908.

Negus SS, & Banks ML (2018). Pharmacokinetic-Pharmacodynamic (PKPD) Analysis with Drug Discrimination. *Curr Top Behav Neurosci* 39: 245-259.

Nepper-Christensen L, Lonborg J, Ahtarovski KA, Hofsten DE, Kyhl K, Ghotbi AA, *et al.* (2017). Left Ventricular Hypertrophy Is Associated With Increased Infarct Size and Decreased Myocardial Salvage in Patients With ST-Segment Elevation Myocardial Infarction Undergoing Primary Percutaneous Coronary Intervention. *J Am Heart Assoc* 6.

Nisimoto Y, Diebold BA, Cosentino-Gomes D, & Lambeth JD (2014). Nox4: a hydrogen peroxide-generating oxygen sensor. *Biochemistry* 53: 5111-5120.

Nobuhisa I, Takeya R, Ogura K, Ueno N, Kohda D, Inagaki F, *et al.* (2006). Activation of the superoxide-producing phagocyte NADPH oxidase requires co-operation between the tandem SH3 domains of p47(phox) in recognition of a polyproline type II helix and an adjacent alpha-helix of p22(phox). *Biochemical Journal* 396: 183-192.

Noguchi N, Yoshida Y, Kaneda H, Yamamoto Y, & Niki E (1992). Action of Ebselen as an Antioxidant against Lipid-Peroxidation. *Biochemical Pharmacology* 44: 39-44.

Nohl H, Kozlov AV, Gille L, & Staniek K (2003). Cell respiration and formation of reactive oxygen species: facts and artefacts. *Biochem Soc Trans* 31: 1308-1311.

Noordik JH (2004) *Cheminformatics developments : history, reviews and current research*. IOS Press ;

Distributor in the USA and Canada, IOS Press: Amsterdam
Fairfax, Va.

O'Donnell BV, Tew DG, Jones OT, & England PJ (1993). Studies on the inhibitory mechanism of iodonium compounds with special reference to neutrophil NADPH oxidase. *Biochem J* 290 (Pt 1): 41-49.

Obianom ON, Okusanya OO, Earp J, & Thway TM (2020). A Simulation Approach to Evaluate the Impact of Patterns of Bioanalytical Bias Difference on the Outcome of Pharmacokinetic Similarity Studies. *Clin Pharmacol Ther.*

Oeckler RA, Kaminski PM, & Wolin MS (2003). Stretch enhances contraction of bovine coronary arteries via an NAD(P)H oxidase-mediated activation of the

extracellular signal-regulated kinase mitogen-activated protein kinase cascade. *Circ Res* 92: 23-31.

Ohno J, Tajima Y, & Utsumi N (1986). Binding of wheat germ agglutinin in the matrix of rat tracheal cartilage. *Histochem J* 18: 537-540.

Okamura T, Okada M, Kikuchi T, Wakizaka H, & Zhang MR (2018). Kinetics and metabolism of apocynin in the mouse brain assessed with positron-emission tomography. *Phytomedicine* 38: 84-89.

Olofsen E, & Dahan A (2013). Using Akaike's information theoretic criterion in mixed-effects modeling of pharmacokinetic data: a simulation study. *F1000Res* 2: 71.

Omanwar S, Saidullah B, Ravi K, & Fahim M (2014). Modulation of Vasodilator Response via the Nitric Oxide Pathway after Acute Methyl Mercury Chloride Exposure in Rats (vol 2013, 530603, 2013). *Biomed Research International*.

Oter S, Korkmaz A, Topal T, Ozcan O, Sadir S, Ozler M, *et al.* (2005). Correlation between hyperbaric oxygen exposure pressures and oxidative parameters in rat lung, brain, and erythrocytes. *Clin Biochem* 38: 706-711.

Otterstad JE (1993). Ischaemia and left ventricular hypertrophy. *Eur Heart J* 14 Suppl F: 2-6.

Pajouhesh H, & Lenz GR (2005). Medicinal chemical properties of successful central nervous system drugs. *NeuroRx* 2: 541-553.

Palasubramaniam J, Wang X, & Peter K (2019). Myocardial Infarction-From Atherosclerosis to Thrombosis. *Arterioscler Thromb Vasc Biol* 39: e176-e185.

Palermartinez A, Panus PC, Chumley PH, Ryan U, Hardy MM, & Freeman BA (1994). Endogenous Xanthine-Oxidase Does Not Significantly Contribute to Vascular Endothelial Production of Reactive Oxygen Species. *Archives of Biochemistry and Biophysics* 311: 79-85.

Panday A, Sahoo MK, Osorio D, & Batra S (2015). NADPH oxidases: an overview from structure to innate immunity-associated pathologies. *Cell Mol Immunol* 12: 5-23.

Parajuli N, Patel VB, Wang W, Basu R, & Oudit GY (2014). Loss of NOX2 (gp91phox) prevents oxidative stress and progression to advanced heart failure. *Clin Sci (Lond)* 127: 331-340.

Park EJ, Min HY, Ahn YH, Bae CM, Pyee JH, & Lee SK (2004). Synthesis and inhibitory effects of pinosylvin derivatives on prostaglandin E2 production in lipopolysaccharide-induced mouse macrophage cells. *Bioorg Med Chem Lett* 14: 5895-5898.

Park HS, Lee SH, Park D, Lee JS, Ryu SH, Lee WJ, *et al.* (2004). Sequential activation of phosphatidylinositol 3-kinase, beta Pix, Rac1, and Nox1 in growth factor-induced production of H2O2. *Mol Cell Biol* 24: 4384-4394.

Park MY, Imajoh-Ohmi S, Nunoi H, & Kanegasaki S (1997). Synthetic peptides corresponding to various hydrophilic regions of the large subunit of cytochrome b558 inhibit superoxide generation in a cell-free system from neutrophils. *Biochem Biophys Res Commun* 234: 531-536.

Patel VB, Clarke N, Wang Z, Fan D, Parajuli N, Basu R, *et al.* (2014). Angiotensin II induced proteolytic cleavage of myocardial ACE2 is mediated by TACE/ADAM-17: a positive feedback mechanism in the RAS. *J Mol Cell Cardiol* 66: 167-176.

Patel VB, Wang Z, Fan D, Zhabyeyev P, Basu R, Das SK, *et al.* (2013). Loss of p47phox subunit enhances susceptibility to biomechanical stress and heart failure because of dysregulation of cortactin and actin filaments. *Circ Res* 112: 1542-1556.

Patti G, Melfi R, & Di Sciascio G (2005). [The role of endothelial dysfunction in the pathogenesis and in clinical practice of atherosclerosis. Current evidences]. *Recenti Prog Med* 96: 499-507.

Peluffo G, Calcerrada P, Piacenza L, Pizzano N, & Radi R (2009). Superoxide-mediated inactivation of nitric oxide and peroxynitrite formation by tobacco smoke in vascular endothelium: studies in cultured cells and smokers. *Am J Physiol-Heart C* 296: H1781-H1792.

Peng GH, Huang J, Boyd M, & Kleinberg ME (2003). Properties of phagocyte NADPH oxidase p47-phox mutants with unmasked SH3 (Src homology 3) domains: full reconstitution of oxidase activity in a semi-recombinant cell-free system lacking arachidonic acid. *Biochem J* 373: 221-229.

Peng Y, Pu JL, Tang CY, & Wu ZJ (2017). Curcumin Inhibits Heat-Induced Apoptosis by Suppressing NADPH Oxidase 2 and Activating the Akt/mTOR Signaling Pathway in Bronchial Epithelial Cells. *Cellular Physiology and Biochemistry* 41: 2091-2103.

Peshavariya H, Dusting GJ, Jiang F, Halmos LR, Sobey CG, Drummond GR, *et al.* (2009). NADPH oxidase isoform selective regulation of endothelial cell proliferation and survival. *Naunyn Schmiedebergs Arch Pharmacol* 380: 193-204.

Petrushanko IY, Lobachev VM, Kononikhin AS, Makarov AA, Devred F, Kovacic H, *et al.* (2016a). Oxidation of Ca²⁺-Binding Domain of NADPH Oxidase 5 (NOX5): Toward Understanding the Mechanism of Inactivation of NOX5 by ROS. *Plos One* 11.

Petrushanko IY, Lobachev VM, Kononikhin AS, Makarov AA, Devred F, Kovacic H, *et al.* (2016b). Oxidation of capital ES, Cyrillicsmall a, Cyrillic²⁺-Binding Domain of NADPH Oxidase 5 (NOX5): Toward Understanding the Mechanism of Inactivation of NOX5 by ROS. *PLoS One* 11: e0158726.

Physicochemical Properties, Formulation, and Drug Delivery. In *Drug Delivery*. pp 57-71.

Pigini D, Cialdella AM, Faranda P, & Tranfo G (2006). Comparison between external and internal standard calibration in the validation of an analytical method for 1-hydroxypyrene in human urine by high-performance liquid chromatography/tandem mass spectrometry. *Rapid Commun Mass Spectrom* 20: 1013-1018.

Pimentel DR, Amin JK, Xiao L, Miller T, Viereck J, Oliver-Krasinski J, *et al.* (2001). Reactive oxygen species mediate amplitude-dependent hypertrophic and apoptotic responses to mechanical stretch in cardiac myocytes. *Circ Res* 89: 453-460.

Polizio AH, Balestrasse KB, Yannarelli GG, Noriega GO, Gorzalczany S, Taira C, *et al.* (2008). Angiotensin II regulates cardiac hypertrophy via oxidative stress but not antioxidant enzyme activities in experimental renovascular hypertension. *Hypertens Res* 31: 325-334.

Pollock JD, Williams DA, Gifford MA, Li LL, Du X, Fisherman J, *et al.* (1995). Mouse model of X-linked chronic granulomatous disease, an inherited defect in phagocyte superoxide production. *Nat Genet* 9: 202-209.

Ponting CP (1996). Novel domains in NADPH oxidase subunits, sorting nexins, and PtdIns 3-kinases: Binding partners of SH3 domains? *Protein Sci* 5: 2353-2357.

Powers JC, Asgian JL, Ekici OD, & James KE (2002). Irreversible inhibitors of serine, cysteine, and threonine proteases. *Chem Rev* 102: 4639-4750.

Prosser BL, Khairallah RJ, Ziman AP, Ward CW, & Lederer WJ (2013). X-ROS signaling in the heart and skeletal muscle: stretch-dependent local ROS regulates [Ca²⁺]_i. *J Mol Cell Cardiol* 58: 172-181.

Qin F, Patel R, Yan C, & Liu W (2006). NADPH oxidase is involved in angiotensin II-induced apoptosis in H9C2 cardiac muscle cells: effects of apocynin. *Free Radic Biol Med* 40: 236-246.

Qin YY, Li M, Feng X, Wang J, Cao L, Shen XK, *et al.* (2017). Combined NADPH and the NOX inhibitor apocynin provides greater anti-inflammatory and neuroprotective effects in a mouse model of stroke. *Free Radic Biol Med* 104: 333-345.

Qiu Y, Chen Y, Zhang GGZ, Yu LX, & Mantri RV (2017) *Developing solid oral dosage forms : pharmaceutical theory & practice*. Second edition. edn. Elsevier Academic Press: Amsterdam ; Boston.

Quideau S, Deffieux D, Douat-Casassus C, & Pouysegu L (2011). Plant polyphenols: chemical properties, biological activities, and synthesis. *Angew Chem Int Ed Engl* 50: 586-621.

Raad H, Paclat MH, Boussetta T, Kroviarsky Y, Morel F, Quinn MT, *et al.* (2009). Regulation of the phagocyte NADPH oxidase activity: Phosphorylation of gp91phox/NOX2 by protein kinase C enhances its diaphorase activity and binding to Rac2, p67phox and p47phox. *Eur J Clin Invest* 39: 28-28.

Rababa'h AM, Guillory AN, Mustafa R, & Hijjawi T (2018). Oxidative Stress and Cardiac Remodeling: An Updated Edge. *Curr Cardiol Rev* 14: 53-59.

Rahman MM, Muse AY, Khan D, Ahmed IH, Subhan N, Reza HM, *et al.* (2017). Apocynin prevented inflammation and oxidative stress in carbon tetra chloride induced hepatic dysfunction in rats. *Biomed Pharmacother* 92: 421-428.

Rajagopalan S, Kurz S, Munzel T, Tarpey M, Freeman BA, Griending KK, *et al.* (1996). Angiotensin II-mediated hypertension in the rat increases vascular superoxide production via membrane NADH/NADPH oxidase activation. Contribution to alterations of vasomotor tone. *J Clin Invest* 97: 1916-1923.

Rajeswaran J, & Blackstone EH (2017). A multiphase non-linear mixed effects model: An application to spirometry after lung transplantation. *Stat Methods Med Res* 26: 21-42.

Ramotowski B, Gurbel PA, Tantry U, & Budaj A (2019). Smoking and cardiovascular diseases: paradox greater than expected? *Pol Arch Intern Med* 129: 700-706.

Rang HP (2006). The receptor concept: pharmacology's big idea. *Br J Pharmacol* 147 Suppl 1: S9-16.

Raphael CE, Cooper R, Parker KH, Collinson J, Vassiliou V, Pennell DJ, *et al.* (2016). Mechanisms of Myocardial Ischemia in Hypertrophic Cardiomyopathy: Insights From Wave Intensity Analysis and Magnetic Resonance. *J Am Coll Cardiol* 68: 1651-1660.

Reeves EP, Dekker LV, Forbes LV, Wientjes FB, Grogan A, Pappin DJC, *et al.* (2000). Direct interaction between p47(phox) and protein kinase C: evidence for targeting of protein kinase C by p47(phox) in neutrophils (vol 344, pg 859, 1999). *Biochem J* 345: 767-767.

Regier DS, Greene DG, Sergeant S, Jesaitis AJ, & McPhail LC (2000). Phosphorylation of p22phox is mediated by phospholipase D-dependent and -independent mechanisms - Correlation of NADPH oxidase activity and p22phox phosphorylation. *Journal of Biological Chemistry* 275: 28406-28412.

Reinehr R, Becker S, Eberle A, Grether-Beck S, & Haussinger D (2005). Involvement of NADPH oxidase isoforms and SRC family kinases in CD95-dependent hepatocyte apoptosis. *Hepatology* 42: 250a-250a.

Reis J, Massari M, Marchese S, Ceccon M, Aalbers FS, Corana F, *et al.* (2020). A closer look into NADPH oxidase inhibitors: Validation and insight into their mechanism of action. *Redox Biol* 32: 101466.

Riballo E, Kuhne M, Rief N, Doherty A, Smith GCM, Recio MJ, *et al.* (2004). A pathway of double-strand break rejoining dependent upon ATM, artemis, and proteins locating to gamma-H2AX foci. *Molecular Cell* 16: 715-724.

Riegelman S, Loo JC, & Rowland M (1968). Shortcomings in pharmacokinetic analysis by conceiving the body to exhibit properties of a single compartment. *J Pharm Sci* 57: 117-123.

Riggs JL (1978). Citation Classic - Isothiocyanate Compounds as Fluorescent Labeling Agents for Immune Serum. *Curr Contents*: 8-8.

Rishton GM, LaBonte K, Williams AJ, Kassam K, & Kolovanov E (2006). Computational approaches to the prediction of blood-brain barrier permeability: A comparative analysis of central nervous system drugs versus secretase inhibitors for Alzheimer's disease. *Curr Opin Drug Discov Devel* 9: 303-313.

Roberts JA, Pea F, & Lipman J (2013). The clinical relevance of plasma protein binding changes. *Clin Pharmacokinet* 52: 1-8.

Rodrigo R, Fernandez-Gajardo R, Gutierrez R, Matamala JM, Carrasco R, Miranda-Merchak A, *et al.* (2013). Oxidative stress and pathophysiology of ischemic stroke: novel therapeutic opportunities. *CNS Neurol Disord Drug Targets* 12: 698-714.

Rodriguez R, & Redman R (2005). Balancing the generation and elimination of reactive oxygen species. *P Natl Acad Sci USA* 102: 3175-3176.

Roe ND, & Ren J (2013). Oxidative activation of Ca²⁺/calmodulin-activated kinase II mediates ER stress-induced cardiac dysfunction and apoptosis. *Am J Physiol-Heart C* 304: H828-H839.

Ronis MJ, Sharma N, Vantrease J, Borengasser SJ, Ferguson M, Mercer KE, *et al.* (2013). Female mice lacking p47phox have altered adipose tissue gene expression and are protected against high fat-induced obesity. *Physiol Genomics* 45: 351-366.

Rosa CM, Gimenes R, Campos DH, Guirado GN, Gimenes C, Fernandes AA, *et al.* (2016). Apocynin influence on oxidative stress and cardiac remodeling of spontaneously hypertensive rats with diabetes mellitus. *Cardiovasc Diabetol* 15: 126.

Rosc-Schluter BI, Hauselmann SP, Lorenz V, Mochizuki M, Facciotti F, Pfister O, *et al.* (2012). NOX2-derived reactive oxygen species are crucial for CD29-induced pro-survival signalling in cardiomyocytes. *Cardiovasc Res* 93: 454-462.

Rosenblum ER, Gavaler JS, & Vanthiel DH (1989). Lipid-Peroxidation - a Mechanism for Alcohol-Induced Testicular Injury. *Free Radical Bio Med* 7: 569-577.

Ross JS, & Kesselheim AS (2015). FDA Policy and Cardiovascular Medicine. *Circulation* 132: 1136-1145.

Roth GA, Johnson C, Abajobir A, Abd-Allah F, Abera SF, Abyu G, *et al.* (2017). Global, Regional, and National Burden of Cardiovascular Diseases for 10 Causes, 1990 to 2015. *J Am Coll Cardiol* 70: 1-25.

Rothkamm K, Barnard S, Moquet J, Ellender M, Rana Z, & Burdak-Rothkamm S (2015). DNA damage foci: Meaning and significance. *Environ Mol Mutagen* 56: 491-504.

Rothkamm K, & Lobrich M (2003). Evidence for a lack of DNA double-strand break repair in human cells exposed to very low x-ray doses. *Proc Natl Acad Sci U S A* 100: 5057-5062.

Rotrosen D, Kleinberg ME, Nuno H, Leto T, Gallin JI, & Malech HL (1990). Evidence for a functional cytoplasmic domain of phagocyte oxidase cytochrome b558. *J Biol Chem* 265: 8745-8750.

Rotschafer JC, Crossley KB, Zaske DE, Russillo NJ, Strate RG, Tofte RW, *et al.* (1983). Clinical Use of a One-Compartment Model for Determining Netilmicin Pharmacokinetic Parameters and Dosage Recommendations. *Ther Drug Monit* 5: 263-267.

Rudakova EV, Boltneva NP, & Makhaeva GF (2011). Comparative analysis of esterase activities of human, mouse, and rat blood. *Bull Exp Biol Med* 152: 73-75.

Rueckschloss U, Galle J, Holtz J, Zerkowski HR, & Morawietz H (2001). Induction of NAD(P)H oxidase by oxidized low-density lipoprotein in human endothelial cells - Antioxidative potential of hydroxymethylglutaryl coenzyme a reductase inhibitor therapy. *Circulation* 104: 1767-1772.

Ruiz-Gines JA, Lopez-Ongil S, Gonzalez-Rubio M, Gonzalez-Santiago L, Rodriguez-Puyol M, & Rodriguez-Puyol D (2000). Reactive oxygen species induce proliferation of bovine aortic endothelial cells. *J Cardiovasc Pharmacol* 35: 109-113.

Saand AR, Yu F, Chen J, & Chou SH (2019). Systemic inflammation in hemorrhagic strokes - A novel neurological sign and therapeutic target? *J Cereb Blood Flow Metab* 39: 959-988.

Sacks HS, Fain JN, Cheema P, Bahouth SW, Garrett E, Wolf RY, *et al.* (2011). Depot-specific overexpression of proinflammatory, redox, endothelial cell, and angiogenic genes in epicardial fat adjacent to severe stable coronary atherosclerosis. *Metab Syndr Relat Disord* 9: 433-439.

Saleem N, Prasad A, & Goswami SK (2018). Apocynin prevents isoproterenol-induced cardiac hypertrophy in rat. *Mol Cell Biochem* 445: 79-88.

Salonen JT (2002). Clinical trials testing cardiovascular benefits of antioxidant supplementation. *Free Radic Res* 36: 1299-1306.

Salonen JT, Nyyssonen K, Salonen R, Lakka HM, Kaikkonen J, Porkkala-Sarataho E, *et al.* (2000). Antioxidant Supplementation in Atherosclerosis Prevention (ASAP) study: a randomized trial of the effect of vitamins E and C on 3-year progression of carotid atherosclerosis. *J Intern Med* 248: 377-386.

Samson RH (2008). Risk factors in vascular disease: who is really at risk and what can be done about it? Introduction. *Semin Vasc Surg* 21: 117-118.

Sandoo A, van Zanten JJ, Metsios GS, Carroll D, & Kitas GD (2010). The endothelium and its role in regulating vascular tone. *Open Cardiovasc Med J* 4: 302-312.

Sano M, Fukuda K, Sato T, Kawaguchi H, Suematsu M, Matsuda S, *et al.* (2001). ERK and p38 MAPK, but not NF-kappaB, are critically involved in reactive oxygen species-mediated induction of IL-6 by angiotensin II in cardiac fibroblasts. *Circ Res* 89: 661-669.

Sarkar S, Malovic E, Harishchandra DS, Ghaisas S, Panicker N, Charli A, *et al.* (2017). Mitochondrial impairment in microglia amplifies NLRP3 inflammasome proinflammatory signaling in cell culture and animal models of Parkinson's disease. *NPJ Parkinsons Dis* 3: 30.

Satheeshkumar K, & Mugesh G (2011). Synthesis and Antioxidant Activity of Peptide-Based Ebselen Analogues. *Chem-Eur J* 17: 4849-4857.

Sathyamoorthy M, deMendez I, Adams AG, & Leto TL (1997). p40(phox) down-regulates NADPH oxidase activity through interactions with its SH3 domain. *Journal of Biological Chemistry* 272: 9141-9146.

Sattler KJE, Galili O, Rodriguez-Porcel M, Krier JD, Lerman LO, & Lerman A (2006). Dietary reversal of experimental hypercholesterolemia improves endothelial dysfunction of epicardial arteries but not of small coronary vessels in pigs. *Atherosclerosis* 188: 301-308.

Schroder K, Helmcke I, Palfi K, Krause KH, Busse R, & Brandes RP (2007). Nox1 mediates basic fibroblast growth factor-induced migration of vascular smooth muscle cells. *Arterioscler Thromb Vasc Biol* 27: 1736-1743.

Segal AW (2008). The function of the NADPH oxidase of phagocytes and its relationship to other NOXs in plants, invertebrates, and mammals. *Int J Biochem Cell B* 40: 604-618.

Selvakumar B, Hess DT, Goldschmidt-Clermont PJ, & Stamler JS (2008). Co-regulation of constitutive nitric oxide synthases and NADPH oxidase by the small GTPase Rac. *FEBS Lett* 582: 2195-2202.

Sen CK, Packer L, & Hänninen O (2000) *Handbook of oxidants and antioxidants in exercise*. 1st edn. Elsevier: Amsterdam ; New York.

Senoner T, & Dichtl W (2019). Oxidative Stress in Cardiovascular Diseases: Still a Therapeutic Target? *Nutrients* 11.

Seredenina T, Chiriano G, Filippova A, Nayernia Z, Mahiout Z, Fioraso-Cartier L, *et al.* (2015). A subset of N-substituted phenothiazines inhibits NADPH oxidases. *Free Radic Biol Med* 86: 239-249.

Shargel L, & Yu ABC (2016) *Applied biopharmaceutics & pharmacokinetics*. Seventh edition. edn. McGraw-Hill Education: New York.

Sharma NM, Rabeler B, Zheng H, Raichlin E, & Patel KP (2016). Exercise Training Attenuates Upregulation of p47(phox) and p67(phox) in Hearts of Diabetic Rats. *Oxid Med Cell Longev*.

Sharpley AL, Williams C, Holder AA, Godlewska BR, Singh N, Shanyinde M, *et al.* (2020). A phase 2a randomised, double-blind, placebo-controlled, parallel-group, add-on clinical trial of ebselen (SPI-1005) as a novel treatment for mania or hypomania. *Psychopharmacology (Berl)* 237: 3773-3782.

Shimosegawa T, & Toyota T (1994). NADPH-diaphorase activity as a marker for nitric oxide synthase in neurons of the guinea pig respiratory tract. *Am J Respir Crit Care Med* 150: 1402-1410.

Shrestha P, Yun JH, Ko YJ, Kim M, Bae YS, & Lee W (2017). C-terminal tail of NADPH oxidase organizer 1 (Noxo1) mediates interaction with NADPH oxidase activator (Noxa1) in the NOX1 complex. *Biochem Biophys Res Commun* 490: 594-600.

Sipkens JA, Krijnen PAJ, Hahn NE, Wassink M, Meischl C, Smith DEC, *et al.* (2011). Homocysteine-induced cardiomyocyte apoptosis and plasma membrane flip-flop are independent of S-adenosylhomocysteine: a crucial role for nuclear p47(phox). *Mol Cell Biochem* 358: 229-239.

Sipkens JA, Krijnen PAJ, Meischl C, Cillessen SAGM, Smulders YM, Smith DEC, *et al.* (2007). Homocysteine affects cardiomyocyte viability: concentration-dependent effects on reversible flip-flop, apoptosis and necrosis. *Apoptosis* 12: 1407-1418.

Sirker A, Murdoch CE, Protti A, Sawyer GJ, Santos CX, Martin D, *et al.* (2016). Cell-specific effects of Nox2 on the acute and chronic response to myocardial infarction. *J Mol Cell Cardiol* 98: 11-17.

Smiljanec K, Mbakwe AU, Ramos-Gonzalez M, Pohlig RT, & Lennon SL (2020). Antioxidant cocktail following a high-sodium meal does not affect vascular function in young, healthy adult humans: a randomized controlled crossover trial. *Nutr Res* 79: 13-22.

Smith BG, Tibby SM, Qureshi SA, Rosenthal E, & Krasemann T (2012). Quantification of temporal, procedural, and hardware-related factors influencing radiation exposure during pediatric cardiac catheterization. *Catheter Cardiovasc Interv* 80: 931-936.

Smith DA, Beaumont K, Maurer TS, & Di L (2018). Relevance of Half-Life in Drug Design. *J Med Chem* 61: 4273-4282.

Solbak SMO, Zang J, Narayanan D, Hoj LJ, Bucciarelli S, Softley C, *et al.* (2020). Developing Inhibitors of the p47phox-p22phox Protein-Protein Interaction by Fragment-Based Drug Discovery. *J Med Chem* 63: 1156-1177.

Sorce S, & Krause KH (2009). NOX Enzymes in the Central Nervous System: From Signaling to Disease. *Antioxid Redox Sign* 11: 2481-2504.

Sorce S, Stocker R, Seredenina T, Holmdahl R, Aguzzi A, Chio A, *et al.* (2017). NADPH oxidases as drug targets and biomarkers in neurodegenerative diseases: What is the evidence? *Free Radic Biol Med* 112: 387-396.

Sovari AA, Iravanian S, Dolmatova E, Jiao Z, Liu H, Zandieh S, *et al.* (2011). Inhibition of c-Src Tyrosine Kinase Prevents Angiotensin II-Mediated Connexin-43 Remodeling and Sudden Cardiac Death. *J Am Coll Cardiol* 58: 2332-2339.

Spiteller G (1985). Combination of Chromatographic-Separation Methods with Mass-Spectrometry - a Modern Technique for Studying Metabolism. *Angew Chem Int Edit* 24: 451-465.

Stasia MJ (2016). CYBA encoding p22(phox), the cytochrome b558 alpha polypeptide: gene structure, expression, role and physiopathology. *Gene* 586: 27-35.

Stefanska J, & Pawliczak R (2008). Apocynin: molecular aptitudes. *Mediators Inflamm* 2008: 106507.

Stolk J, Hiltermann TJ, Dijkman JH, & Verhoeven AJ (1994). Characteristics of the inhibition of NADPH oxidase activation in neutrophils by apocynin, a methoxy-substituted catechol. *Am J Respir Cell Mol Biol* 11: 95-102.

Stuehr DJ, Fasehun OA, Kwon NS, Gross SS, Gonzalez JA, Levi R, *et al.* (1991). Inhibition of Macrophage and Endothelial-Cell Nitric-Oxide Synthase by Diphenyleneiodonium and Its Analogs. *Faseb Journal* 5: 98-103.

Suh SW, Gum ET, Hamby AM, Chan PH, & Swanson RA (2007). Hypoglycemic neuronal death is triggered by glucose reperfusion and activation of neuronal NADPH oxidase. *J Clin Invest* 117: 910-918.

Szilagyi JT, Mishin V, Heck DE, Jan YH, Aleksunes LM, Richardson JR, *et al.* (2016). Selective Targeting of Heme Protein in Cytochrome P450 and Nitric Oxide Synthase by Diphenyleneiodonium. *Toxicological Sciences* 151: 150-159.

Takeya R, Ueno N, Kami K, Taura M, Kohjima M, Izaki T, *et al.* (2003). Novel human homologues of p47phox and p67phox participate in activation of superoxide-producing NADPH oxidases. *J Biol Chem* 278: 25234-25246.

Tampo Y, Kotamraju S, Chitambar CR, Kalivendi SV, Keszler A, Joseph J, *et al.* (2003). Oxidative stress-induced iron signaling is responsible for peroxide-dependent oxidation of dichlorodihydrofluorescein in endothelial cells: role of transferrin receptor-dependent iron uptake in apoptosis. *Circ Res* 92: 56-63.

Tamura M, Itoh K, Akita H, Takano K, & Oku S (2006). Identification of an actin-binding site in p47phox an organizer protein of NADPH oxidase. *FEBS Lett* 580: 261-267.

Tanaka T, Halicka HD, Traganos F, & Darzynkiewicz Z (2006). Phosphorylation of histone H2AX on ser 139 and activation of ATM during oxidative burst in phorbol ester-treated human leukocytes. *Cell Cycle* 5: 2671-2675.

Tardiff JC (2006). Cardiac hypertrophy: stressing out the heart. *Journal of Clinical Investigation* 116: 1467-1470.

Tedeschi D, Rizzi A, Biscaglia S, & Tumscitz C (2020). Acute myocardial infarction and large coronary thrombosis in a patient with COVID-19. *Catheter Cardiovasc Interv.*

Tehrani S, Tomasevic N, Weed S, Sakowicz R, & Cooper JA (2007). Src phosphorylation of cortactin enhances actin assembly. *P Natl Acad Sci USA* 104: 11933-11938.

Teixeira G, Szyndralewicz C, Molango S, Carnesechi S, Heitz F, Wiesel P, *et al.* (2017). Therapeutic potential of NADPH oxidase 1/4 inhibitors. *Br J Pharmacol* 174: 1647-1669.

Tejero J, & Stuehr D (2013). Tetrahydrobiopterin in nitric oxide synthase. *Iubmb Life* 65: 358-365.

Teng L, Fan LM, Meijles D, & Li JM (2012). Divergent effects of p47(phox) phosphorylation at S303-4 or S379 on tumor necrosis factor-alpha signaling via TRAF4 and MAPK in endothelial cells. *Arterioscler Thromb Vasc Biol* 32: 1488-1496.

Thakur S, Du J, Hourani S, Ledent C, & Li JM (2010). Inactivation of adenosine A2A receptor attenuates basal and angiotensin II-induced ROS production by Nox2 in endothelial cells. *The Journal of biological chemistry* 285: 40104-40113.

Thatcher SE (2017) *The renin-angiotensin-aldosterone system : methods and protocols.* Humana Press : Springer: New York, NY.

Thomas SR, Chen K, & Keaney JF, Jr. (2002). Hydrogen peroxide activates endothelial nitric-oxide synthase through coordinated phosphorylation and dephosphorylation via

a phosphoinositide 3-kinase-dependent signaling pathway. *J Biol Chem* 277: 6017-6024.

Thum T, Fraccarollo D, Schultheiss M, Froese S, Galuppo P, Widder JD, *et al.* (2007). Endothelial nitric oxide synthase uncoupling impairs endothelial progenitor cell mobilization and function in diabetes. *Diabetes* 56: 666-674.

Tickner J, Fan LM, Du J, Meijles D, & Li JM (2011). Nox2-derived ROS in PPAR γ signaling and cell-cycle progression of lung alveolar epithelial cells. *Free Radic Biol Med* 51: 763-772.

Timmis A, Townsend N, Gale C, Grobbee R, Maniadakis N, Flather M, *et al.* (2018). European Society of Cardiology: Cardiovascular Disease Statistics 2017. *Eur Heart J* 39: 508-579.

Touyz RM, Chen X, Tabet F, Yao G, He G, Quinn MT, *et al.* (2002). Expression of a functionally active gp91phox-containing neutrophil-type NAD(P)H oxidase in smooth muscle cells from human resistance arteries: regulation by angiotensin II. *Circ Res* 90: 1205-1213.

Touyz RM, Yao G, Quinn MT, Pagano PJ, & Schiffrin EL (2005). p47phox associates with the cytoskeleton through cortactin in human vascular smooth muscle cells - Role in NAD(P)H oxidase regulation by angiotensin II. *Arterioscl Throm Vas* 25: 512-518.

Touyz RM, Yao GY, & Schiffrin EL (2003). c-Src induces phosphorylation and translocation of p47phox: Role in NAD(P)H oxidase-mediated superoxide generation by Ang II in human vascular smooth muscle cells. *Arterioscl Throm Vas* 23: A5-A5.

Tsai KH, Wang WJ, Lin CW, Pai PY, Lai TY, Tsai CY, *et al.* (2012). NADPH oxidase-derived superoxide Anion-induced apoptosis is mediated via the JNK-dependent activation of NF-kappa B in cardiomyocytes exposed to high glucose. *Journal of Cellular Physiology* 227: 1347-1357.

Turner MW, & Shields JG (1984). Immunofluorescence in Medical Science - Kawamura, a, Aoyama, Y. *Immunol Today* 5: 210-211.

Ueyama T, Lekstrom K, Tsujibe S, Saito N, & Leto TL (2007). Subcellular localization and function of alternatively spliced Nox1 isoforms. *Free Radic Biol Med* 42: 180-190.

Uhrovic J (2014). Strategy for determination of LOD and LOQ values--some basic aspects. *Talanta* 119: 178-180.

Ungvari Z, Csiszar A, Edwards JG, Kaminski PM, Wolin MS, Kaley G, *et al.* (2003). Increased superoxide production in coronary arteries in hyperhomocysteinemia: role of tumor necrosis factor- α , NAD(P)H oxidase, and inducible nitric oxide synthase. *Arterioscler Thromb Vasc Biol* 23: 418-424.

UniProt C (2019). UniProt: a worldwide hub of protein knowledge. *Nucleic Acids Res* 47: D506-D515.

Usatyuk PV, Romer LH, He DH, Parinandi NL, Kleinberg ME, Zhan S, *et al.* (2007). Regulation of hyperoxia-induced NADPH oxidase activation in human lung endothelial cells by the actin cytoskeleton and cortactin. *Journal of Biological Chemistry* 282: 23284-23295.

Ushio-Fukai M, Alexander RW, Akers M, & Griendling KK (1998). p38 mitogen-activated protein kinase is a critical component of the redox-sensitive signaling pathways activated by angiotensin II - Role in vascular smooth muscle cell hypertrophy. *Journal of Biological Chemistry* 273: 15022-15029.

Verbon EH, Post JA, & Boonstra J (2012). The influence of reactive oxygen species on cell cycle progression in mammalian cells. *Gene* 511: 1-6.

Vilar S, Chakrabarti M, & Costanzi S (2010). Prediction of passive blood-brain partitioning: straightforward and effective classification models based on in silico derived physicochemical descriptors. *J Mol Graph Model* 28: 899-903.

Violi F, Carnevale R, Loffredo L, Pignatelli P, & Gallin JI (2017). NADPH Oxidase-2 and Atherothrombosis: Insight From Chronic Granulomatous Disease. *Arterioscler Thromb Vasc Biol* 37: 218-225.

Vogelman B, Gudmundsson S, Leggett J, Turnidge J, Ebert S, & Craig WA (1988). Correlation of antimicrobial pharmacokinetic parameters with therapeutic efficacy in an animal model. *J Infect Dis* 158: 831-847.

Vollmer RR, Meyers-Schoy SA, & Marinelli RR (1991). Mechanisms involved in angiotensin II induced increases in cardiac output in pithed rats. *Clin Exp Hypertens A* 13: 1433-1445.

Wang K, Li L, Song Y, Ye X, Fu S, Jiang J, *et al.* (2013). Improvement of pharmacokinetics behavior of apocynin by nitrone derivatization: comparative pharmacokinetics of nitrone-apocynin and its parent apocynin in rats. *PLoS One* 8: e70189.

Wang Q, Smith RE, Luchtefeld R, Sun AY, Simonyi A, Luo R, *et al.* (2008). Bioavailability of apocynin through its conversion to glycoconjugate but not to diapocynin. *Phytomedicine* 15: 496-503.

Wang Y, Zhang Y, Ding G, May HI, Xu J, Gillette TG, *et al.* (2017). Temporal dynamics of cardiac hypertrophic growth in response to pressure overload. *Am J Physiol Heart Circ Physiol* 313: H1119-H1129.

Waterman KC, Adami RC, Alsante KM, Antipas AS, Arenson DR, Carrier R, *et al.* (2002). Hydrolysis in pharmaceutical formulations. *Pharm Dev Technol* 7: 113-146.

Watkins SJ, Borthwick GM, Oakenfull R, Robson A, & Arthur HM (2012). Angiotensin II-induced cardiomyocyte hypertrophy in vitro is TAK1-dependent and Smad2/3-independent. *Hypertens Res* 35: 393-398.

Welch WJ (2008). Angiotensin II-Dependent Superoxide Effects on Hypertension and Vascular Dysfunction. *Hypertension* 52: 51-56.

Wells JI (1988) *Pharmaceutical preformulation : the physicochemical properties of drug substances*. Ellis Horwood.

Wen Y, Ahmad F, Mohri Z, Weinberg PD, & Leake DS (2019). Cysteamine inhibits lysosomal oxidation of low density lipoprotein in human macrophages and reduces atherosclerosis in mice. *Atherosclerosis* 291: 9-18.

Wientjes FB, Reeves EP, Soskic V, Furthmayr H, & Segal AW (2001). The NADPH oxidase components p47(phox) and p40(phox) bind to moesin through their PX domain. *Biochem Biophys Res Commun* 289: 382-388.

Wilhelmi V, Fischer U, Weighardt H, Schulze-Osthoff K, Nickel C, Stahlmecke B, *et al.* (2013). Zinc Oxide Nanoparticles Induce Necrosis and Apoptosis in Macrophages in a p47phox- and Nrf2-Independent Manner. *Plos One* 8.

Wilkinson BL, & Landreth GE (2006). The microglial NADPH oxidase complex as a source of oxidative stress in Alzheimer's disease. *J Neuroinflamm* 3.

Williams D, Gorwit J, Crawford M, Garza G, Orourke R, & Karliner J (1975). Left-Ventricular Function in Hypertrophy Due to Systemic Hypertension. *Circulation* 52: 56-56.

Williams FM (1985). Clinical significance of esterases in man. *Clin Pharmacokinet* 10: 392-403.

Williams MS, & Kwon J (2004). T cell receptor stimulation, reactive oxygen species, and cell signaling. *Free Radic Biol Med* 37: 1144-1151.

Wills ED, Gillham B, Papachristodoulou DK, & Thomas JH (1997) *Wills' biochemical basis of medicine*. 3rd edn. Butterworth-Heinemann: Oxford ; Boston.

Wilson L, Butcher C, Finan P, & Kellie S (1997). SH3 domain-mediated interactions involving the phox components of the NADPH oxidase. *Inflammation Research* 46: 265-271.

Wind S, Beuerlein K, Eucker T, Muller H, Scheurer P, Armitage ME, *et al.* (2010). Comparative pharmacology of chemically distinct NADPH oxidase inhibitors. *Br J Pharmacol* 161: 885-898.

Wouters OJ, McKee M, & Luyten J (2020). Estimated Research and Development Investment Needed to Bring a New Medicine to Market, 2009-2018. *JAMA* 323: 844-853.

Wray DW, Nishiyama SK, Harris RA, & Richardson RS (2008). Angiotensin II in the elderly - Impact of angiotensin II type 1 receptor sensitivity on peripheral hemodynamics. *Hypertension* 51: 1611-1616.

Wu R, Laplante MA, & de Champlain J (2005). Cyclooxygenase-2 inhibitors attenuate angiotensin II-induced oxidative stress, hypertension, and cardiac hypertrophy in rats. *Hypertension* 45: 1139-1144.

Wu RF, Gu Y, Xu YC, Nwariaku FE, & Terada LS (2003). Vascular endothelial growth factor causes translocation of p47phox to membrane ruffles through WAVE1. *J Biol Chem* 278: 36830-36840.

Wu RF, Ma Z, Liu Z, & Terada LS (2010). Nox4-derived H₂O₂ mediates endoplasmic reticulum signaling through local Ras activation. *Mol Cell Biol* 30: 3553-3568.

Xie Z, Pimental DR, Lohan S, Vasertriger A, Pligavko C, Colucci WS, *et al.* (2001). Regulation of angiotensin II-stimulated osteopontin expression in cardiac microvascular endothelial cells: role of p42/44 mitogen-activated protein kinase and reactive oxygen species. *J Cell Physiol* 188: 132-138.

Xu S, Liu Z, & Liu P (2013). HDL cholesterol in cardiovascular diseases: the good, the bad, and the ugly? *Int J Cardiol* 168: 3157-3159.

Yamaguchi T, Sano K, Takakura K, Saito I, Shinohara Y, Asano T, *et al.* (1998). Ebselen in acute ischemic stroke: a placebo-controlled, double-blind clinical trial. Ebselen Study Group. *Stroke* 29: 12-17.

Yan Z, & Caldwell G (2004) *Optimization in drug discovery : in vitro methods*. Humana Press: Totowa, N.J.

Yang CS, Lee HM, Lee JY, Kim JA, Lee SJ, Shin DM, *et al.* (2007). Reactive oxygen species and p47phox activation are essential for the Mycobacterium tuberculosis-induced pro-inflammatory response in murine microglia. *J Neuroinflammation* 4: 27.

Yang CS, Shin DM, Lee HM, Son JW, Lee SJ, Akira S, *et al.* (2008). ASK1-p38 MAPK-p47phox activation is essential for inflammatory responses during tuberculosis via TLR2-ROS signalling. *Cell Microbiol* 10: 741-754.

Yang W, Liu Z, Xu Q, Peng H, Chen L, Huang X, *et al.* (2017). Involvement of vascular peroxidase 1 in angiotensin II-induced hypertrophy of H9c2 cells. *J Am Soc Hypertens* 11: 519-529 e511.

Yang XZ, Chang Y, & Wei W (2016). Endothelial Dysfunction and Inflammation: Immunity in Rheumatoid Arthritis. *Mediat Inflamm*.

Yau JW, Teoh H, & Verma S (2015). Endothelial cell control of thrombosis. *BMC Cardiovasc Disord* 15: 130.

Yeware A, Gamble S, Agrawal S, & Sarkar D (2019). Using diphenyliodonium to induce a viable but non-culturable phenotype in Mycobacterium tuberculosis and its metabolomics analysis. *PLoS One* 14: e0220628.

Yoshinaga S, Kohjima M, Ogura K, Yokochi M, Takeya R, Ito T, *et al.* (2003). The PB1 domain and the PC motif-containing region are structurally similar protein binding modules. *Embo Journal* 22: 4888-4897.

Yost RA, & Enke CG (1978). Selected Ion Fragmentation with a Tandem Quadrupole Mass-Spectrometer. *J Am Chem Soc* 100: 2274-2275.

Yu LX, DeLeo FR, Biberstine-Kinkade KJ, Renee J, Nauseef WM, & Dinauer MC (1999). Biosynthesis of flavocytochrome b(558) - gp91(phox) is synthesized as a 65-kDa precursor (p65) in the endoplasmic reticulum. *Journal of Biological Chemistry* 274: 4364-4369.

Yu LX, Zhen L, & Dinauer MC (1997). Biosynthesis of the phagocyte NADPH oxidase cytochrome b(558) - Role of heme incorporation and heterodimer formation in maturation and stability of gp91(phox) and p22(phox) subunits. *Journal of Biological Chemistry* 272: 27288-27294.

Yu W, Wu J, Cai F, Xiang J, Zha W, Fan D, *et al.* (2012). Curcumin alleviates diabetic cardiomyopathy in experimental diabetic rats. *PLoS One* 7: e52013.

Yu W, Zha WL, Ke ZQ, Min Q, Li CR, Sun HR, *et al.* (2016). Curcumin Protects Neonatal Rat Cardiomyocytes against High Glucose-Induced Apoptosis via PI3K/Akt Signalling Pathway. *J Diabetes Res.*

Yuan B, & Leenen FHH (1999). Cardiac hypertrophy and mortality following acute myocardial infarction in rats. *Faseb Journal* 13: A1077-A1077.

Yun MR, Im DS, Lee JS, Son SM, Sung SM, Bae SS, *et al.* (2006). NAD(P)H oxidase-stimulating activity of serum from type 2 diabetic patients with retinopathy mediates enhanced endothelial expression of E-selectin. *Life Sci* 78: 2608-2614.

Yuzawa S, Suzuki NN, Fujioka Y, Ogura K, Sumimoto H, & Inagaki F (2004a). A molecular mechanism for autoinhibition of the tandem SH3 domains of p47(phox), the regulatory subunit of the phagocyte NADPH oxidase (vol 9, pg 443, 2004). *Genes to Cells* 9: 609-609.

Zafari AM, Ushio-Fukai M, Akers M, Yin Q, Shah A, Harrison DG, *et al.* (1998). Role of NADH/NADPH oxidase-derived H₂O₂ in angiotensin II-induced vascular hypertrophy. *Hypertension* 32: 488-495.

Zhang D, Hu XM, Qian L, Chen SH, Zhou H, Wilson B, *et al.* (2011). Microglial MAC1 receptor and PI3K are essential in mediating beta-amyloid peptide-induced microglial activation and subsequent neurotoxicity. *J Neuroinflamm* 8.

Zhang M, Perino A, Ghigo A, Hirsch E, & Shah AM (2013). NADPH oxidases in heart failure: poachers or gamekeepers? *Antioxid Redox Signal* 18: 1024-1041.

Zhang M, Prosser BL, Bamboye MA, Gondim ANS, Santos CX, Martin D, *et al.* (2015). Contractile Function During Angiotensin-II Activation: Increased Nox2 Activity Modulates Cardiac Calcium Handling via Phospholamban Phosphorylation. *J Am Coll Cardiol* 66: 261-272.

Zhang M, & Shah AM (2014). ROS signalling between endothelial cells and cardiac cells. *Cardiovasc Res* 102: 249-257.

Zhang TT, Wang YL, Jin B, Li T, & Ma C (2019). Plasma pharmacokinetics of isorhapontigenin, a novel derivative of stilbenes, in mice by LC-MS/MS method. *J Asian Nat Prod Res* 21: 895-904.

Zhou W, Zhan Y, Virbasius JV, He DD, Song X, & Pomerleau DP (2003). The p40phox and p47phox PX domains of NADPH oxidase target cell membranes via direct and indirect recruitment by phosphoinositides. *Faseb J* 17: A1319-A1320.

Zi M, Stafford N, Prehar S, Baudoin F, Oceandy D, Wang X, *et al.* (2019). Cardiac hypertrophy or failure? - A systematic evaluation of the transverse aortic constriction model in C57BL/6NTac and C57BL/6J substrains. *Curr Res Physiol* 1: 1-10.

Zielonka J, Lambeth JD, & Kalyanaraman B (2013). On the use of L-012, a luminol-based chemiluminescent probe, for detecting superoxide and identifying inhibitors of NADPH oxidase: a reevaluation. *Free Radic Biol Med* 65: 1310-1314.

Zimmerman MC, Lazartigues E, Sharma RV, & Davisson RL (2004). Hypertension caused by angiotensin II infusion involves increased superoxide production in the central nervous system. *Circ Res* 95: 210-216.